In-situ and *Ex-situ* Microscopy and Spectroscopy Study of Catalytic Materials

by

Shuyi Zhang

A dissertation submitted in partial fulfillment
of the requirements for the degree of
Doctor of Philosophy
(Materials Science and Engineering)
in the University of Michigan
2017

Doctoral Committee:

Professor Emmanoul Kioupakis, Co-Chair
Professor Xiaoqing Pan, Co-Chair
Professor Mark A. Barteau
Adjunct Professor George W. Graham

Dedication

This dissertation is dedicated to my family, my mentors and all who have supported me in the past years. It is dedicated to those who have true interests in the fantastic world of microstructures and pursuing the scientific understanding behind them.

Acknowledgements

First and foremost, I would like to give my greatest thanks to my advisers Xiaoqing Pan and George W. Graham. Dr. Pan supervised my research from microscopy perspective and provided crucial opinions at important moments. I found all his critics and insights very valuable not only for my PhD study but also for the rest of my life. Dr. Graham supervised me from catalysis perspective and have been working with me on every single detail of my research. He is a very kind mentor, always willing to give me comfort and thoughtful advice whenever I feel panic, unconfident or lost. Dr. Kioupakis also offered a lot of genuine advice and support throughout the years regarding science and career options. Dr. Barteau has been very candid of his opinion and helped me transform into a more confident and independent researcher.

Besides my great committee members, I was very lucky to have the chance to collaborate with a lot of great minds in the field of catalysis. Dr. Matteo Cargnello (Stanford University) not only provided me the most well-made samples but also tremendous heartfelt encouragement and genuine advice to help me concur any difficulties in research. His perfectionism and enthusiasm in research acts as a lighthouse when I am searching in the dark. Dr. Phillip N. Christopher (University of California at Riverside) is another important collaborator who inspired me with a lot of insightful ideas. Dr. Philipp Plessow's (Stanford University) great contribution comprised the theoretical calculation in Chapter II. Other collaborators that I feel grateful working with

include but not limited to Dr. Ray Gorte (University of Pennsylvania) and his student Tzia Ming Onn, Dr. Zhenmeng Peng and his student Changlin Zhang.

I am, of course, indebted to all the senior researchers who have taught me different kinds of valuable techniques and skills. Dr. Masahiro Kawasaki (JEOL) has been an incredible resource of advanced microscopy techniques. It's his 30 years' experience and expertise that make a lot of challenging experiment exceptional. And we were able to take some very impressive data under extremely demanding conditions. Dr. Larry Allard (Oak Ridge National Laboratory) hosted me in ORNL and showed me *in-situ* gas reaction for the first time in my life. He is always enthusiastic with research and his countless stories happened in his life. Brad Carpenter and Ben Jacobs (both from Protochips) have provided tremendous assistance in troubleshooting and maintaining the gas cell system. I truly appreciate Brad's instantaneous reply at any time even after work.

I would like to thank all the members of Pan group that I have met and worked with. Dr. Michael B. Katz, Dr. Peng Gao and Dr. Yi Zhang taught me everything in the world of microscopy including sample preparation, instrument operation and data analysis. Mingjie Xu always impressed me with his in depth knowledge in mechanics and kept a cheerful and genial atmosphere in the lab. He and Wei Cai always help me with gas change and maintenance of the gas cell. Sheng Dai has spent a lot of time in the dark TEM room with me and I hope all his work will go well in the future. Besides those who have worked with me intensively, I would like to thank the rest of students and postdocs including Christopher Nelson, Sungjoo Kim, Jake Jokisaari, Kui Zhang, Linze Li, Minghao Fang, Xianfeng Du, Baihai Li, Lin Xie, Pei Lei and Chang Zhou.

Almost all my data were collected in Electron Microbeam Analysis Laboratory (now named as Michigan Center for Materials Characterization). Dr. Kai Sun and Dr. Haiping Sun are great consultants for most of the problems that I experienced including instrumental optimization, experimental methods and other related questions. It's the great dedication of all the staff members in EMAL including John Mansfield, Bobby Kerns, Kai Sun, Haiping Sun and Beverly Clampit that make mine and other researchers' work possible.

Last but not least, I feel grateful for the generous support of funding agencies including Ford Motor Company under a University Research Proposal grant and the National Science Foundation under grants CBET-1159240 and DMR-0723032. I truly appreciate the financial support offered by the department in my last semester.

Contents

List of Figures

List of Tables

List of Appendices

Chapter I

Introduction and Background

1.1 Heterogeneous Catalyst

Catalysis was first termed by Baron J. J. Berzelius to account for the increase in the rate of a chemical reaction due to the participation of catalyst which will not be consumed during the reaction. A broader definition of catalysts including materials not only change the reaction rate (either increase or decrease) but also the selectivity of the product. Heterogeneous catalysts are distinguished from homogeneous catalysts by the different phases involved in chemical reaction.[1] Homogeneous catalysts are present in the same phases as reactants and products, while heterogeneous catalysts are present in a different phase. Most of the heterogeneous catalysts used in industry are solids which consisted of metal nanoparticles (NPs) on oxide supports and the reactants are gases or liquids.[2] Heterogeneous catalysts are easier to separate from the product stream that aids in the creation of continuous chemical processes and more tolerant of harsh operating conditions than their homogeneous analogues.

The presence of catalyst usually can provide an alternative reaction pathway to create products from reactants. If the energy barriers of the catalytic path are much lower than the barriers of the noncatalytic path, significant enhancements in the reaction rate can be realized through the use of catalyst. The catalysis processes are usually accomplished through four essential steps. First,

reaction molecules are adsorbed onto the surface of the catalytic nanoparticles. Second, these adsorbates undergo bond rearrangement to form intermediate product through reactant dissociation. Third, the reaction intermediates interact on the surface to form product molecules. Last, these product molecules are then desorbed from the surface returning the catalyst to its original configuration.[3] For example, G. Ertl [4] proposed the thermochemical kinetic profile depicted in Figure 1.1. For the platinum-catalyzed CO oxidation according to the overall reaction $CO + \frac{1}{2}O_2 \rightarrow CO_2$. The first step in the profile represents the adsorption of CO and O_2 on the surface of Pt nanoparticles, followed by dissociation of O_2 into O_{ads} single atoms which will combine with CO to form the final product CO_2. The final step in the catalytic reaction is desorption of adsorbed CO_2 into the gas phase. Due to the high stability of the O_2 molecules, the noncatalytic pathway is extremely slow at normal temperature. The participation of Pt nanoparticles (NPs) facilitate the reaction by providing a low energy path to dissociate dioxygen and form the product CO_2.

1.2 The advantages of using STEM and EELS in Catalytic Materials

Changing the structure and composition of the catalyst surface can dramatically alter the activation energies of the elementary steps in the process resulting in an increase or a decrease in the reaction rate. Moreover, competing low-energy reaction pathways may lead to the creation of different products lowering the selectivity of the catalysts. To achieve high selectivity in the chemical conversion process for the desired products, the surface of the catalyst must be controlled so that the adsorbate interactions are directed along the desired reaction pathway. Therefore, elucidating the relationship between surface structure and catalytic activity is crucial to design better catalyst for crucial transformation. Different with other characterization technique that usually provide the average information of the ensemble, Transmission Electron Microscope (TEM) is the only atomic

resolution tool that can allow the location, shape and structure of individual nanoparticles dispersed on an irregular high surface area support to be directly observed. For this reason, electron microscopy is a critical tool for characterization of heterogeneous catalysts. Atomic resolution phase contrast microscopy in a conventional TEM has been extensively used to study the structure and morphology of a wide variety of catalysts. [5,6] However, strong diffraction contrast created by the underlying support materials in bright field TEM significantly suppress the visibility of small particles on top of them. Indeed, from a historical point of view, the need to identify the location of heavy metal particles or single atoms on low-atomic number supports was a primary motivation for the development of high-angle annular dark-field (HAADF) Scanning Transmission Electron Microscopy (STEM) imaging – the so-called Z-contrast imaging approach.[7-10] Z-contrast imaging technique could completely suppress diffraction contrast that usually result in the confusion of data interpretation. The contrast of very small metal NPs, ~1-2nm in diameter, can be dramatically enhanced comparing to bright filed image and atomic scale structure can be clearly unraveled.

STEM combines the principles of TEM and Scanning Electron Microscopy (SEM). A highly-focused electron probe is raster-scanned across the material, and various types of transmitted electrons are collected as a function of position as shown in Figure 1.2. The transmitted electrons scattered at high angle with respect to the optical axis can be collected to form chemically sensitive, atomic number (Z) contrast images, while electrons scattered at low angle can be collected to form diffraction or phase contrast image. Those images are formed by elastically scattered electrons. Electrons that have lost a measurable amount of energy when passing through the sample can be used to form Electron Energy Loss Spectra. The x-rays generated can be collected with an Energy-

Dispersive X-ray Spectroscopy (EDS) detector and used to form high spatial resolution compositional maps.

Electron energy loss spectroscopy (EELS) is another powerful technique for determining the physico-chemical properties of catalytic materials on the nanometer scale. It can be employed to provide information not only on elemental composition but also on the electronic structure of materials.[11] The high-loss portion of the spectrum above about 50 eV contains information from inelastic interactions with the inner or core shells. When the electron beam transfers sufficient energy to a K, L, M, N, or O shell electron to knock it out of the attractive field of the nucleus, inner-shell ionization will occur. Because the energy loss is characteristic of each element involved, the signal, called "edge", is direct source of elemental information. The shape of the edge is related to bonding effect or chemical environment of the element, and is termed Energy-Loss Near-Edge structure (ELNES).[12]

1.3 Motivation and Recent Developments of *In-Situ* Microscopy

In general, the catalyst operates in a liquid or a gas environment at elevated pressure and temperature, and their structure and composition are likely to change under reactive environments. Conventional microscopy characterization under high vacuum conditions may provide results which are either misleading or difficult to interpret unambiguously. To solve this problem, STEM should ideally be performed under conditions identical to those found in the reactor. A general instrumental requirement for *in-situ* gas reaction is to keep a high gas pressure around the sample region and high vacuum around the electron source. So far, it can be achieved through two different methods:

- Environmental TEM (ETEM): Differential pumping system is used to maintain a pressure difference between the sample area and the gun. A typical ETEM and a schematic of the vacuum system is shown in Figure 1.3.
- Microelectromechanical Systems (MEMS) based closed cell technique: Gas is confined around the sample region by using MEMS based E-Chips with thin electron transparent windows. A typical gas holder from Protochips is shown in Figure 1.4.

In ETEM, a series of differential pumping stages are employed to create a large pressure difference between the sample area and the rest of the microscope. This is accomplished by inserting a series of differential pumping apertures into the microscope column and adding additional pumping capacity to remove the gas that leaks through the differential pumping apertures. ETEM has been developed for several decades and recent technology developments have enabled new research in the study of nanomaterials in gaseous environments.[13-19] Nowadays, ETEM become very robust with pressures of up to 20 mbar without damaging the FEG and the resolution is comparable with regular aberration corrected TEM.[3]

However, at the same time researchers start to realize some inherent disadvantages of ETEM in real application. First, aberration corrected TEMs are extremely dedicated instruments that can easily cost a few million dollars. ETEM requires modification of the column architecture and the additional pumping systems, which make it more prohibitive to most researchers. Second, the pressure can only go up to 1-2 % of 1 atm for gases easy to pump, while the upper pressure limit can be 2–4 times lower for gases like H_2. This huge pressure gap can result in an inherent discrepancy between *in-situ* and *ex-situ* observations. Third, because the electron path length in

the gas containing area is on the order of millimeter, ionization of the gas is another issue need to be considered. According to the plot in Figure 1.5, for 27mm gas path (assuming sample is located in the middle of the pole piece with a total length of 54mm), the probability for 200-kV electron to be scattered at 10 Torr O_2 is about 10% and increase to 60% at 100 Torr. This indicate that the significant electron gas interaction cannot be neglected due to the long distance of gas path inside the ETEM. On the other hand, in a cell with 40um gap, the probability of gas scattering is only 10% at 1 atm. This demonstrates the advantage of a suitably designed window cell for high-pressure applications.

In the MEMS based gas cell technique, samples and gases are sandwiched between two pieces of amorphous SiN membranes, thus high vacuum can be maintained for the rest part of the microscope. This system usually includes a gas manifold, a specially designed TEM holder, E-chips and software controller. Since the only modification is on the TEM holder, the price is much cheaper than an ETEM and thus make *in-situ* TEM technique more accessible. Moreover, it can be incorporated into most of the mainstream microscopes. The primary advantage of gas cell technique comparing to ETEM is the high pressure application-it can achieve atomic resolution at 1 atm with minimum gas ionization, thus the pressure gap can be entirely eliminated. The main disadvantage of gas cell technique is that imaging and spectroscopy capabilities will be compromised by the additional scattering due to the amorphous membrane. Besides, the gas cell holder is usually single tilt and the sample geometry is constrained. There is also a risk of membrane rupture, even though the amount of gas in the cell is very little (on the order of 10^{-6} L), additional precautions is still necessary to protect the field emission source.

1.4 Objectives of this Dissertation

The goal of my PhD work can be divided into two parts. One is developing and improving *in-situ* gas cell technique with a startup company Protochips through a beta site program. A prototype instrument was installed in Michigan Center for Material Characterization ($(MC)^2$) before the commercial version is available to the market for testing and development. The second objective is to investigate structural and chemical changes in a variety of catalytic materials through *in*-situ microscopy and spectroscopy techniques with direct information acquired under working conditions. These structural changes will be related to their corresponding catalytic properties, aiming to provide new insights of the underlying mechanisms. Major materials systems studied in this thesis include strong metal support interaction in Pd or Rh NPs supported on TiO_2, structural evolution of Pd@CeO_2 core shell catalyst, sintering mechanism of Pt NPs supported on high-surface-area alumina, atomic-scale insight into the self-regenerative process of Rh-$CaTiO_3$ and Pt-$CaTiO_3$. Other computation techniques including Density Function Theory (DFT is conducted by Philipp N. Plessow) and multislice simulation are also employed to understand the mechanisms of the observed phenomena.

1.5 References

1. Davis, M. E.; Davis, R. J., *Fundamentals of chemical reaction engineering*. Courier Corporation: 2012.

2. Rothenberg, G., *Catalysis: concepts and green applications*. John Wiley & Sons: 2015.

3. Pennycook, S. J.; Nellist, P. D., *Scanning transmission electron microscopy: imaging and analysis*. Springer Science & Business Media: 2011.

4. Anderson, J. R.; Boudart, M., *Catalysis: science and technology*. Springer Science & Business Media: 2012; Vol. 11.

5. Gontard, L. C.; Chang, L. Y.; Hetherington, C. J.; Kirkland, A. I.; Ozkaya, D.; Dunin-Borkowski, R. E. *Angew. Chem.* **2007,** 119, 3757-3759.

6. Thomas, J. M.; Gai, P. L. *Advances in catalysis* **2004,** 48, 171-227.

7. Datye, A. K. *J. Catal.* **2003,** 216, 144-154.

8. Liu, J. *J. Electron Microsc.* **2005,** 54, 251-278.

9. Blom, D. A.; Bradley, S.; Sinkler, W.; Allard, L. *Microsc. Microanal.* **2006,** 12, (S02), 50-51.

10. Treacy, M.; Rice, S. *Journal of Microscopy* **1989,** 156, 211-234.

11. Egerton, R. *Rep. Prog. Phys.* **2008,** 72, 016502.

12. Williams, D. B.; Carter, C. B., The transmission electron microscope. In *Transmission electron microscopy*, Springer: 1996; pp 3-17.

13. Baldi, A.; Narayan, T. C.; Koh, A. L.; Dionne, J. A. *Nature materials* **2014,** 13, 1143-1148.

14. Helveg, S.; Lopez-Cartes, C.; Sehested, J.; Hansen, P. L.; Clausen, B. S.; Rostrup-Nielsen, J. R.; Abild-Pedersen, F.; Nørskov, J. K. *Nature* **2004,** 427, 426-429.

15. Hansen, P. L.; Wagner, J. B.; Helveg, S.; Rostrup-Nielsen, J. R.; Clausen, B. S.; Topsøe, H. *Science* **2002,** 295, 2053-2055.

16. Sharma, R.; Crozier, P. A., Environmental transmission electron microscopy in nanotechnology. In *Handbook of microscopy for nanotechnology*, Springer: 2005; pp 531-565.

17. Jinschek, J. *Chem. Commun.* **2014,** 50, 2696-2706.

18. Crozier, P. A.; Hansen, T. W. *MRS Bull.* **2015,** 40, 38-45.

19. Yoshida, H.; Kuwauchi, Y.; Jinschek, J. R.; Sun, K.; Tanaka, S.; Kohyama, M.; Shimada, S.; Haruta, M.; Takeda, S. *Science* **2012,** 335, 317-319.

20. Allard, L. F.; Overbury, S. H.; Bigelow, W. C.; Katz, M. B.; Nackashi, D. P.; Damiano, J. *Microsc. Microanal.* **2012,** 18, 656-666.

21. Vendelbo, S.; Elkjær, C.; Falsig, H.; Puspitasari, I.; Dona, P.; Mele, L.; Morana, B.; Nelissen, B.; van Rijn, R.; Creemer, J. *Nature materials* **2014,** 13, 884-890.

22. Li, Y.; Zakharov, D.; Zhao, S.; Tappero, R.; Jung, U.; Elsen, A.; Baumann, P.; Nuzzo, R. G.; Stach, E.; Frenkel, A. *Nature communications* **2015,** 6, 8583.

23. Zhang, S.; Chen, C.; Cargnello, M.; Fornasiero, P.; Gorte, R. J.; Graham, G. W.; Pan, X. *Nature communications* **2015,** 6, 8778.

24. Zhang, S.; Plessow, P. N.; Willis, J. J.; Dai, S.; Xu, M.; Graham, G. W.; Cargnello, M.; Abild-Pedersen, F.; Pan, X. *Nano Lett.* **2016,** 16, 4528–4534.

25. Matsubu, J. C.; Zhang, S.; DeRita, L.; Marinkovic, N. S.; Chen, J. G.; Graham, G. W.; Pan, X.; Christopher, P. *Nat Chem* **2016,** advance online publication.

26. Zhang, S.; Cargnello, M.; Cai, W.; Murray, C. B.; Graham, G. W.; Pan, X. *J. Catal.* **2016,** 337, 240-247.

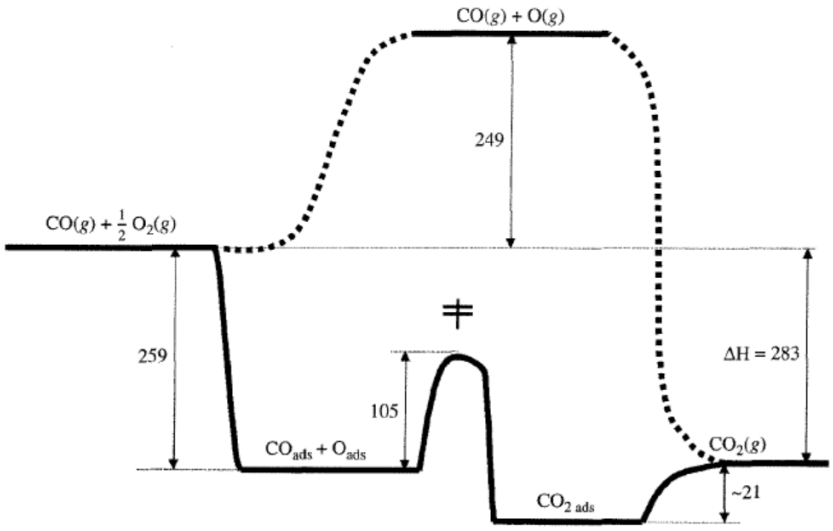

Figure 1.1 Schematic energy diagram of CO oxidation with (solid line) and without and Pt catalyst (dashed line). All energies are given in kJ mol^{-1}. Based on data presented in reference 4.

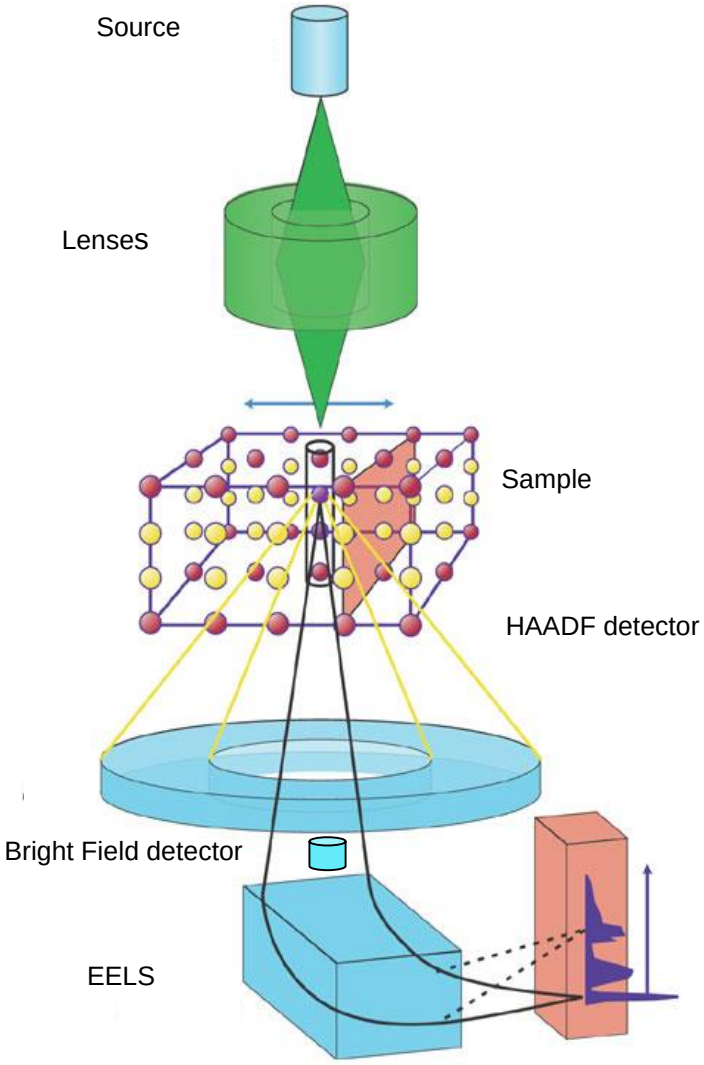

Figure 1.2 Schematic of STEM system showing the relevant components.

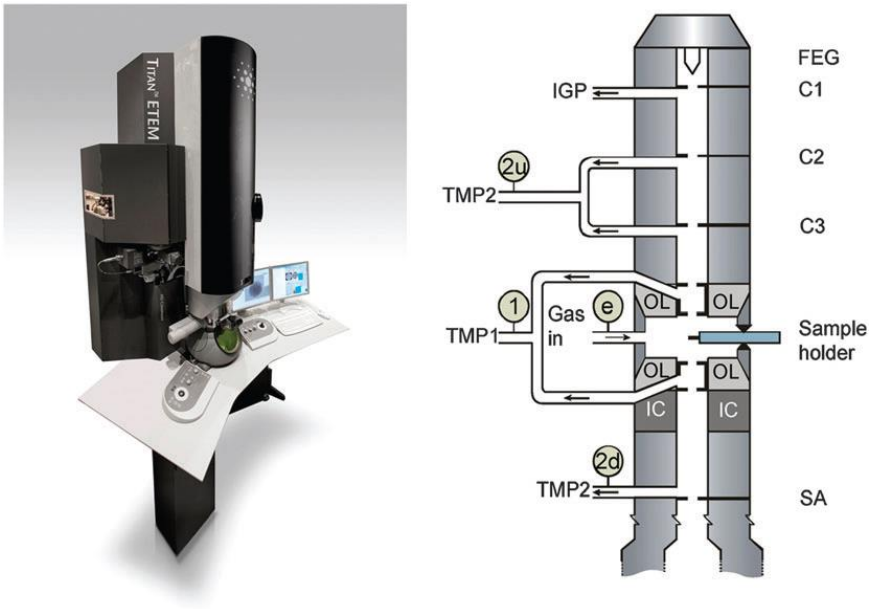

Figure 1.3 A FEI Titan ETEM G_2 (left) and a sketch of the vacuum system highlighting the pressure-limiting apertures at the stages of the objective lens (OL), the condenser lenses (first (C1), second (C2) and third (C3)) and the selected area (SA) aperture. (Based on images from Reference 17).

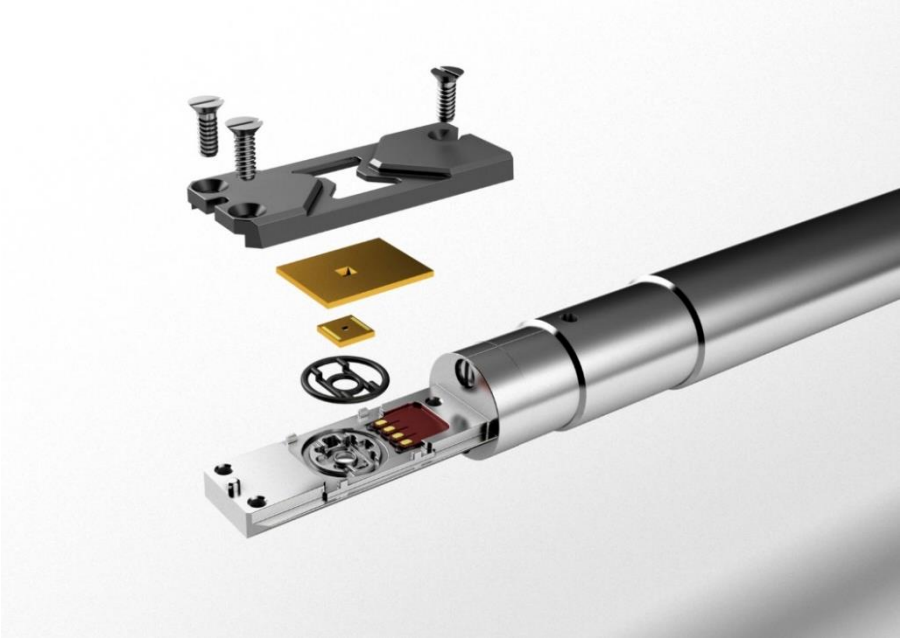

Figure 1.4 Protochips Atmosphere system with butterfly design.

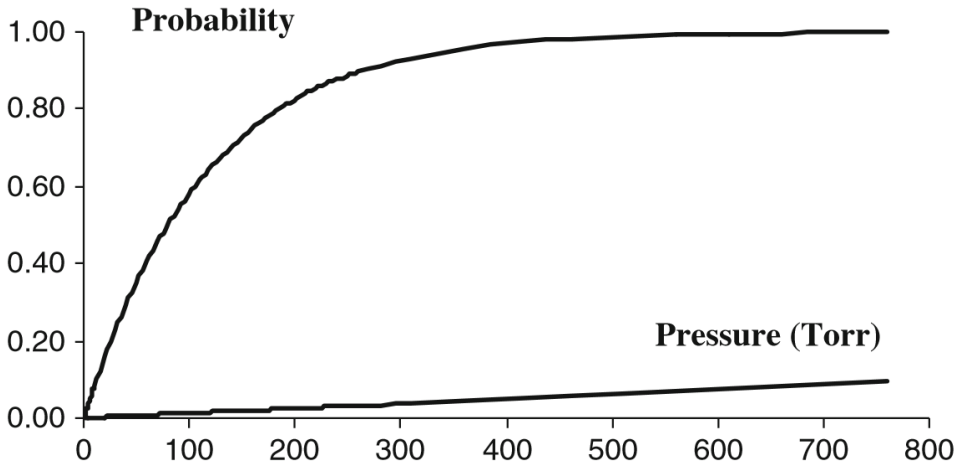

Figure 1.5 Probability of electron being scattered once by column of O_2 gas as a function of pressure. Upper curve-gas path length 27mm; lower curve-gas path length 40um. (Based on data from reference 3.)

Chapter II

Strong Metal Support Interaction (SMSI), Classical and Adsorbate Mediated

2.1 Background and Previous Research

Transition-metal nanoparticles (NPs) in oxide-supported metal catalysts play the leading role in promoting heterogeneous catalytic reactions, but the oxide often plays a critical supporting role, affecting both activity and selectivity.[1-3] The term Strong Metal Support Interaction (SMSI) originated with Tauster and co-workers, who used it to describe the dramatic suppression of H_2 and CO chemisorption by transition metal NPs supported on TiO_2 following a H_2-reduction treatment at around 500 °C.[4] Initially, both electronic effect (A perturbation of the electronic structure of the metal catalyst, originating from an interaction between the cluster and the oxide support) and steric effects (A physical covering of metal particles by a thin layer of reduced oxide support, blocking active catalytic sites at metal surfaces) were considered in attempts to understand the phenomenon,[5] but a series of early surface science and *ex-situ* TEM studies eventually demonstrated that a thin TiOx layer forms on the metal NPs, physically blocking the interaction of gas molecules with their surfaces.[6-9]

Studies regarding the nature and structure of the overlayers have been realized mainly through surface science techniques under ultra-high vacuum (UHV) and Transmission Electron Microscopy (TEM). Scanning Tunneling Microscopy (STM) provided atomic scale structural

information on a variety of model catalysts where metal nanoparticles including Pd or Pt are sputtered onto the single crystalline oxide substrate followed by high temperature annealing under UHV[10, 11] or in an inverse regime where different amounts Ti are sputtered on to flat metal surface.[12] The structures have been interpreted mostly as a single TiO_x (x~1) layer with large and complex unit cells (~100 $Å^2$) on the fcc(111)-planes of metal single crystalline surfaces. Only one report identified a possible double layer structure.[13] Due to the top-down nature of STM images, it is however hard to clearly discern the metal-oxide interface and to unequivocally establish the thickness of the reduced oxide layer. Furthermore, UHV annealing may be able to create a reducing condition but the lowest oxygen potential that can be achieved is still much higher than reduction under H_2 atmosphere. Electron microscopy data in this sense is a viable complement to STM studies. TEM studies revealed that a thin reduced oxide layer, typically a few angstrom thick, can migrate onto a Rh, Pt or Pd particle after reduction in H_2 at 500°C,[7-9, 14] and that the clean Rh surfaces can be recovered via oxidation at 300°C.[15] Similar phenomenon was also found in CeO_2 [14] and $Ce_{0.80}Tb_{0.2}O_{2-x}$.[16] Among the TEM work on TiO_2, amorphous surface layer is usually observed except one study reported that crystalline TiOx layer was found on Pt (111) facets but rough or disordered on other facets.[8] The discrepancy is likely due to the instability of the surface layer upon exposure to air, consequently *ex-situ* transmission electron microscopy (TEM) has its own limitations as to provide a structure that is representative of the catalyst under working condition. A systematic *in-situ* TEM study that can provide the aspired atomically resolved information at ambient pressure where appropriate experimental techniques are used is clearly needed to understand the mechanism of SMSI. Classical SMSI part was published in *Nano Letters* **16**, 4528 (2016). Absorbate-Mediated part was published in *Nature Chemistry* (2016). doi:10.1038/nchem.2607.

2.2 Methods

2.2.1 Material Synthesis

*Monodispersed Pd/TiO_2, Pt/TiO2, Au/TiO_2 samples**

The supported catalyst systems were prepared by deposition of pre-formed metal nanocrystals onto commercial titania P25 (Sigma-Aldrich). Pd and Pt nanocrystals were synthesized according to reference,[17] whereas Au nanocrystals followed reference.[18] The conditions for making different nanocrystals were:

- **Pd nanocrystals:** A mixture of 0.25 mmol $Pd(acac)_2$, 2.5 mmol oleylamine, 1.25 mmol trioctylphosphine, 1.25 mmol oleic acid, 6.6 mL 1-octadecene, 3.4 mL 1-tetradecene, reaction at 290 °C for 15 minutes.
- **Pt nanocrystals**: A mixture of 0.25 mmol $Pt(acac)_2$, 2.0 mmol oleylamine, 0.5 mmol trioctylphosphine, 4.0 mmol oleic acid, 10 mL of trioctylamine were reacted at 30 °C for 30 minutes.
- **Au nanocrystals:** A mixture of 100 mg $HAuCl_4$, 10 mL oleylamine (80-90%, Acros), 10 mL tetraline, were dissolved and reacted at room temperature with a solution of 0.5 mmol of tributylamine borane complex (Sigma-Aldrich) in 1 mL oleylamine and 1 mL tetraline. The purified nanocrystals dissolved in hexanes at appropriate concentrations were added to a stirred solution of titania P25 in toluene (40 mL) in order to obtain a final loading of 0.5 wt. % in metal. The samples were left stirring for 30 minutes. Powders were collected by centrifugation, dried overnight and the organic ligands removed following a fast thermal treatment in a furnace at 700 °C for 30 seconds.

These samples were synthesized by Joshua Willis.

*Rh/ TiO_2 impregnated catalyst**

Six weight loadings of Rh (0.2%, 0.5%, 1%, 2%, 4%, and 6%) were deposited on TiO_2 (Evonik-P25), to produce total sample masses of 1g each, using an impregnation technique. The necessary mass of ($Rh(NO_3)_3 \cdot xH_2O$, Sigma-Aldrich-#83750) for each weight loading was dissolved in an evaporation dish with 2mL of distilled water. TiO_2 was mixed with the aqueous Rh solution using a stir rod until homogeneous, dried at 95 °C for 4 h, ground with a mortar and pestle, and calcined in a tube furnace at 450 °C in air for 4 h. All reductions of the samples were performed in-situ prior to the kinetic and characterization analyses.

* These samples were synthesized by John C. Matsubu.

2.2.2 Catalytic Measurements (Rh_TiO_2)*

All CO_2 reduction reaction rates and selectivity were measured using 15−20 mg of catalyst at 200 °C in a 1/4" OD borosilicate packed bed reactor operating at atmospheric pressure and running under differential reactor conditions (conversion of limiting reagent <5%) with the effluent quantified by online gas chromatography (GC, SRI MG #3). CO_2 was separated from other gases using a Hayesep D column, while H_2, N_2, CH_4, and CO were separated using a molecular sieve (MS13X) packed column. The separated gases were then quantified using a flame ionization detector (FID) and a thermal conductivity detector (TCD). The total reactant flow rate in all studies was 100 standard cm^3 per minute (sccm). Gases were delivered via Teledyne mass flow controllers.

The standard experimental procedure for all data shown in **2.3.2** was as follows:

- Reduction: Pure H_2 flow (20 sccm) over catalyst at 450 °C for 1 hour
- Reactivity Assay: Reduce temperature to 200 °C and flow 1 sccm CO_2, 1sccm H_2, 98 sccm He for reactivity assay of reduced material for 4 hours. Reported CO and CH_4 production

rates are associated with steady-state measurements obtained by averaging 5 GC injections over the final hour.

- A-SMSI Formation: Increase temperature to 250 °C and change flow rates to 20 sccm CO_2, 2 sccm H_2, and 78 sccm He for 4 hours.
- Reactivity Assay: Reduce temperature to 200 °C and flow 1 sccm CO_2, 1sccm H_2, 98 sccm He for reactivity assay of reduced material for 4 hours. Reported CO and CH_4 production rates are associated with steady-state measurements obtained by averaging 5 GC injections over the final hour.
- Re-Reduction: Increase temperature to 450 °C and switch environment to pure H_2 flow (20 sccm) for 4 hours.

*These measurements were conducted by John C. Matsubu.

2.2.3 Density Functional Theory Calculations*

DFT-calculations have been carried out with Quantum Espresso[19] using ultrasoft pseudopotentials[20] and Fermi-Dirac smearing with k_BT = 0.1 eV, except for gas-phase molecules, where integer occupation numbers have been enforced. The energy cut-off for the plane wave expansion of wave function (density) was 500 eV (5000 eV). We have used H_2 and H_2O as reference gas-phase molecules and the O_2-reference was obtained using its experimental binding energy corrected by the zero-point energy: $E(O_2) = E(H_2O) – E(H_2) + 2.75$ eV. Γ-centered k-point sampling was used in all cases. Generally we employed a kpoint-density roughly corresponding to (12×12×1) per (1×1)-Pd-fcc(111) surface unit cell. This has been found to give sufficiently converged energies (see below). Slabs were separated by about 16 Å and the dipole correction has

additionally been used to reduce the artificial interaction between slabs[21]. All presented number have been obtained using non spin-polarized calculations. We have thoroughly tested many structures for spin-polarized solutions. However, despite using strongly magnetic guesses for the initial wave function, all converged solutions were non-magnetic. This is in agreement with calculations reported for TiOx overlayers[13, 22]. To avoid convergence issues with surface energies, they were calculated using the 'linear-fit' method, e.g. the bulk reference energy was obtained by linear regression of the total slab-energies with respect to the number of layers. The free energy of solids and surfaces is approximated by their electronic energies. Free energies of gas phase molecules were obtained using the usual corrections from statistical thermodynamics for translation, (harmonic) oscillation and (rigid) rotation.

*DFT calculation was conducted by Philipp N. Plessow.

2.2.4 *In-situ* Microcopy and Spectroscopy

In-situ Microscopy and EELS

In-situ TEM was conducted on a JEOL 3100-R05 microscope with double Cs-correctors operated at 300 kV using the Protochips Atmosphere system, and Electron Energy Loss Spectroscopy (EELS) was utilized to probe the chemical nature of the amorphous overlayer and acquired with Gatan #965 Quantum Imaging Filter (GIF). The Ti valence was quantified by using Multiple Linear Least Square (MLLS) Fitting within Digital Micrograph Software. This involves forming a model function consisting of a linear combination of the two normalized reference spectra ($SrTiO_3$ and $LaTiO_3$) and then fit that model to the experimental spectrum by adjusting the coefficient of each linear term to minimize the square deviation between the model and data. The

purity of the gases used in the in situ experiment was 99.9995%. All reported temperatures are based on the Protochips calibration.

6% Rh/TiO_2 sample sintered at 800 ˚C for 3h in N_2 in a tube furnace. To trigger the A-SMSI layer, the sample was then treated in $20CO_2$:$2H_2$ for 4 hours. To trigger classical SMSI layer, the sample was treated under 5%H_2/Ar at 550 ˚C for 10mins in the gas cell.

*In-situ DRIFTS Measurements (Rh_TiO_2)**

DRIFTS measurements were executed to identify how the various treatments explored in this study impact the species adsorbed on the catalyst surface. Generally, catalysts were loaded into a Harrick Praying Mantis high temperature reaction chamber (ZnSe windows) mounted inside of a Thermo Scientific Praying Mantis diffuse reflectance adapter, attached to a Thermo Scientific Nicolet iS10 FT-IR spectrometer with a MCT-A detector. Measurements were taken with 128 scans, 4 cm-1 resolution, and a 30-40 SLM N_2 purge of the spectrometer and Praying Mantis adapter box that started at the same time as the reduction. Gases were flowed to the reaction chamber using Teledyne mass flow controllers. Typically, 10 mg of the catalyst sample was packed on top of 100 mg of α-alumina. The reactor effluent was routed to the GC to monitor reactivity of the catalyst and ensure consistent behavior with experiments performed in the glass reactors.

After loading the catalysts in the reactor, the following steps were taken for the DRIFTS cycling experiments to identify how the species on the catalyst surface under reaction conditions (1%CO_2:1%H_2:98%He, 180 °C) following reduction and A-SMSI formation, and the reversibility of this process, (Figure 2, Supplementary Figs 28-30):

1. Reduction: Pure H_2 flow (20 sccm) over sample at 350 °C* for 1 hour

2. FTIR Background: Changed temperature to 180 °C* and collected background spectrum in H_2.

3. Reactivity Assay: Changed flows to 1 sccm CO_2, 1 sccm H_2, 98 sccm He and allowed the system 20 minutes to reach steady state prior to collecting a spectrum of the reduced material in reaction conditions.

4. A-SMSI Formation: Changed temperature to 210 °C* and flowrates to 20 sccm CO_2, 2 sccm H_2, and 78 sccm He for 16 hours* to induce A-SMSI formation.

5. Reactivity Assay: Changed temperature to 180 °C* and flowrates to 1 sccm CO_2, 1 sccm H_2, 98 sccm He and allowed the system 20 minutes to reach steady state prior to collecting a spectrum of the catalyst in reaction conditions and the ASMSI state.

6. Re-Reduction: Pure H_2 flow (20 sccm) over sample at 350 °C* for 4 hour.

7. Reactivity Assay: Changed temperature to 180 °C* and flowrates to 1sccm CO_2, 1sccm H_2, 98 sccm He and allowed the system 20 minutes to reach steady state prior to collecting a spectrum of the re-reduced catalyst.

*In-situ DRIFTS were conducted by John C. Matsubu.

Note: The A-SMSI formation step was performed for 16 hours in the DRIFTS studies instead of 4 hours used in the reactivity studies due to a lower temperature at the top of the catalyst bed (where IR spectra are collected from) compared to the set-point temperature of the catalyst bed. Later temperature calibration indicated the surface of the catalyst was approximately 210 °C rather than the 250 °C used in the kinetic reactor for A-SMSI formation. The 200 °C sampling temperature was also found to only be approximately 180 °C. The 450 °C reduction temperature was later determined to actually be 350 °C. Based on the robustness and consistency of the observed

reactivity changes and accompanied changes in absorbed species in the FTIR experiments, these small temperature differences had no impact on the experimental results or conclusions drawn from the experiments.

*In-Situ X-ray Absorption Spectroscopy**

EXAFS experiments were performed at Beamline 2-2 at the Stanford Synchrotron Radiation Lightsource (SSRL), SLAC National Accelerator Laboratory, Stanford, California. A double-crystal Si (220) monochromator was used to scan X-ray energy from -100 to 200 eV and -200 eV to 1300 eV relative to the Rh K-edge (23,220 eV) for XANES and EXAFS spectra, respectively. About 20 mg of 2% Rh/TiO2 catalyst was placed in 2.4 mm OD quartz tubes and into a resistance heating-capable Claussen cell with gas flowing through the powder. Data were recorded for untreated sample at room temperature, at 400 °C in H_2 flow for reduced catalyst and at 250 °C with 20%CO_2/2%H_2/78%He flow all at 20 mL/min. Although the XAS data were obtained in both transmission and fluorescence modes, only transmission spectra are presented. Rh foil was placed between the transmission and reference X-ray detectors and measured simultaneously with the nanoparticle samples for X-ray energy calibration and data alignment. Data processing and analysis were performed using the IFEFFIT package. The amplitude and phase photoelectron scattering functions for the first nearest neighbor (1NN) photoelectron path were calculated using the FEFF6 program and used to fit the EXAFS equation in R-space and derive the photoelectron energy origin correction $\Delta E0$, and structural parameters (N, R, and σ 2) of the systems. S02 was obtained by an independent bulk-metal fit of the Rh foil in which the coordination number of the first nearest neighbor bonds was fixed at 12 (as expected for a face-centered-cubic lattice), and its value of 0.86 was used in the fits of all nanoparticle samples.

* *In-Situ* X-ray Absorption Spectroscopy was conducted by John C. Matsubu.

2.3 Results and Discussion

2.3.1 Classical SMSI

Electron Beam consideration

We are aware that beam effects could possibly create artifacts. All the images were taken with a significantly reduced probe current, ~7 pA, while the probe current for normal STEM imaging is between 50-100 pA [23, 24]. To minimize beam effect, Chi et al. used 20 pA probe current to study in-situ surface faceting of metal particles of similar size [25]. Our probe size is estimated to be about 0.8 Å, which is typical for state-of-the-art aberration corrected STEM (1.3 Å after the membrane), before crossing the membrane of the cell. Our current density is 4 $pA/Å^2$, about 1 to 2 orders of magnitude lower than typical values [26]. Our electron dose could go up to 10^4 $e/Å^2$ to acquire the highest quality image, but we immediately reduced it to less than 100 $e/Å^2$ after image acquisition. One direct way to identify the occurrence of electron beam damage is to record images of the same area before and after irradiation and compare the contrast under the same imaging conditions. No change was found when the samples were illuminated with the same conditions for prolonged time, as shown in the figures below. At a relatively higher oxygen potential (H_2 (4.7 vol. %)/O_2 (5.7 vol. %)/Ar, μ_O~ -0.9eV), the surfaces of Pd particles stayed clean at 500 °C during 20 min observation, as shown in Figure 2.1. At lower oxygen potential (H_2 (5 vol. %)/Ar, μ_O< -3.7 eV), an amorphous layer starts to migrate onto the particles at temperatures around 250 °C. (Due to electron beam induced contamination in the gas cell, we couldn't get high quality images below 250 °C in order to clearly identify the presence of surface layer migration. A more obvious amorphous layer can

be observed at 300 °C, as shown in Figure S2.) During 15 min observation at 250 °C under H_2 (5 vol. %)/Ar at 1 atm, no change was observed, as shown in Figure 2.2.

Finally, when the temperature was raised to 500 °C under the same gas atmosphere (H_2 (5 vol. %)/Ar at 1 atm), two crystalline layers were instantaneously formed, and they were observed to be very stable under the beam illumination for 90 min, as shown in Figure 2.3.

2.3.1.2 Reversible surface layer formation

Representative sequential Annular Bright Field (ABF) images of an individual Pd nanocrystal supported on TiO_2 under reducing and oxidizing atmospheres are reported in Figure 2.4 A-F. The Pd particles were examined *ex-situ* at room temperature before performing *in-situ* experiments, and they all exhibited clean surfaces, as shown in Figure 2.5. Under reducing conditions (H_2 (5 vol. %)/Ar at 1 atm) at 250 °C shown in A, an amorphous layer starts to form on the particles, arguably through diffusion of reduced TiO_x species from the support to the particle surface, starting from the metal-support boundary (see arrows in Figure 2.4A). When the temperature is increased to 500 °C under the same conditions, the amorphous layer crystallizes to form a bilayer that is almost epitaxial with the Pd(111) plane (Figure 2.4C and higher magnification images in Figure 2.4 G-H). About 90% of all the Pd particles observed are covered by the bilayer structure. The lattice spacing is ~2.9 Å for the lower layer and 3.0 Å for the top layer, and the overlayer follows ABCABC stacking of the underneath Pd along [111] direction. The comparison between ABF (Figure 2.4G) and high angle annular dark field (HAADF) (Figure 2.4H), where the image contrast is the opposite and brightness in the latter case is proportional to atomic number, confirms that the surface layer is composed of a material with lower atomic number than Pd. When the gas atmosphere is changed to oxidizing (150 Torr O_2) and the temperature decreased to 250 °C, the

ordered surface oxide layer gradually becomes amorphous and dissociates, resulting in slightly enhanced contrast in the background (Figure 2.4 D-E). This situation is essentially unaffected upon heating to 500 °C (Figure 2.4E). When the cell was pumped and filled back with H_2 (5 vol. %)/Ar at 1 atm, the particle was again covered by the crystalline bilayer (Figure 2.4F) and becomes faceted. The above experiments clearly demonstrate the reversible nature of the formation and dissociation of the surface layer under reducing and oxidizing gas compositions, respectively. The electron energy-loss spectroscopic (EELS) scan shown in Figure 2.4 I, taken *in situ* under 5% H_2/Ar at 500 °C, along the line ABCD, confirms that this surface layer is TiO_x. From the TiO_2 support (measuring point A) to the Pd nanoparticle (measuring point B), the fine structure of Ti shows features typical of the transition from 4+ to 3+, based on reference spectra from TiO_2 and $LaTiO_3$, though a precise determination of the stoichiometry of the surface layer is not feasible with the present data. (Measuring point D was chosen in a region without any sample as a background reference.) Corresponding experiments performed on a Pd/Al_2O_3 sample showed no evidence of overlayers, as shown in Figure 2.6.

The influence of oxygen chemical potential on the structure of overlayers

The crystalline TiO_x double layer has rarely been observed, and we therefore performed theoretical investigations to better understand its nature and stability. Using DFT, we explored different stoichiometries, compositions, and geometries to identify the potentially most stable candidate structures. In general, the reaction involved in forming TiO_x/Pd(hkl) from the TiO_2 support and metallic Pd nanocrystals under exposure to H_2 can be written as:

$$TiO_2 + (2\text{-}x)H_2 + Pd(hkl) \rightarrow TiO_x/Pd(hkl) + (2\text{-}x)H_2O \qquad (1)$$

If one assumes that H_2O is in equilibrium with H_2 and O_2, this is equivalent to:

$$TiO_2 + Pd(hkl) \rightarrow TiO_x/Pd(hkl) + (2-x)/2\ O_2 \qquad (2)$$

As explicitly written in eq. (1), the free energy of a given structure depends only on temperature and oxygen partial pressure. Since the amount of Ti supplied by the supporting titania is sufficient to fully cover the particles, and since the surface area does not change significantly, the most stable surface is that which minimizes the free energy per surface area and not per formula unit of reaction shown in (1) or (2). T and $p(O_2)$ can be further related to the chemical potential of oxygen, μ_O, as the only variable. Plotting the free energy of formation of different structures against μ_O therefore allows us to study the relative stability of different thin surface structures under varying conditions. Furthermore, we found the hydrogenated surface layer is energetically unfavorable as shown in Figure 2.7.

According to our calculations summarized in Figure 2.7, a double layer resulting from stacking two hexagonal k-phase Ti_2O_3 layers [27] in the sequence Pd-Ti-O-Ti-O is the thermodynamically most stable phase at $\mu_O < -3.7$ eV, while a single layer k-phase is expected to be stable between $-3.7\ eV < \mu_O < -2.8$ eV. At $\mu_O > -2.8$ eV, the Pd particles are expected to be clean. Although single and double layer structures have the same stoichiometry ($TiO_{1.5}$), the transition is predicted to occur because the double layer has a higher density per area. Therefore, the oxygen deficiency per area is higher and so is the slope of the free energy per area with respect to μ_O.

The oxygen chemical potential at which the double layer has been found experimentally, as shown in Fig. 2.7B, $\mu_O \leq$ -3.7 eV (this value representing an estimated upper limit), is in agreement with the range expected theoretically (< -3.7 eV). Note that the oxygen pressure corresponding to this chemical potential is much lower than the estimated upper bound in a UHV chamber, and therefore the double layer should not be easily observable under UHV conditions [10-12]. In order to observe the predicted transition from double to single layer experimentally, the mixture of gases was varied to increase the oxygen chemical potential. Using an initial composition of H_2 (4.9 vol. %)/O_2 (2 vol. %)/Ar at 1 atm, we indeed observed the formation of a monolayer, shown in Figure 2.7C. The conditions correspond to a chemical potential of $\mu_O \sim$ -2.8 eV if the gas is fully equilibrated. This is also in agreement with the range of stability expected theoretically. Clean particles are observed under more oxidizing conditions with an initial gas mixture of H_2 (4.7 vol. %)/O_2 (5.7 vol. %)/Ar at 1 atm and 500 °C, shown in Figure 2.7D. Upon equilibration of the gas, this corresponds to $\mu_O \sim$ -0.9 eV and is therefore fully in the range expected theoretically. Thus, the influence of gas composition on the surface structure is clearly demonstrated through DFT calculation and *in situ* observation. It worth noting that a single layer of TiO rock phase is competitive with the double layer of Ti_2O_3 at lower μ_O based on DFT calculation result but not experimentally observed. Within the accuracy of our calculations this does certainly not rule out the existence of the Ti_2O_3 double layer phase, but TiO becomes more stable when the oxygen partial potential is low enough.

We have computed the thermodynamic stability of k-phase single and double layers of TiO_x in the (1×1)/(2×2) super cell on Pt and Au, as well as Pd. Generally, both overlayers are stable on Pd and Pt and unstable on Au, as shown in the table 2.1.

The validity of this combined experimental-theoretical approach is further demonstrated by corresponding results from the comparative systems, Pt/TiO_2, which is similar to Pd/TiO_2, and Au/TiO_2, which does not exhibit stable overlayers under our conditions, as shown in Figure 2.8-2.10.

Shape change induced by the formation of surface layer

Finally, we consider Pd NP shape changes that may occur under the influence of the SMSI effect. As shown in Figure 2.11, a round-to-facetted particle transformation appears to coincide with the formation of the crystalline double layer. A more dramatic shape change occurs upon encapsulation of the Pd NP by a single layer, as shown by the HAADF-STEM images in Figure 2.11A-F (corresponding ABF images are in Figure 2.11A'-F'). The shape of the particle originally appears to be a truncated octahedron with rounded corners (Figure 2.11A and 2.11A'. (110) truncations are shown between two adjacent (111) facets while high index planes exist between (111) and (100) facets. After heating at 400 °C for 25 minutes, causing the single TiO_x overlayer to form on the particle, (111) facets expand, (100) shrink, and (110) and other high-index facets are fully lost, as shown in the sequence of Figure 2.11B(B')-F(F'). Following published methods [28], we calculated the ratio of (111) to (100) surface areas. This ratio changes from 1.08 (Figure 2.11A) to 1.27 when the temperature is increased to 500 °C (Figure 2.11G). The origin of this shape change is related to surface energy considerations. The extension of the two facets is inversely proportional to their surface energy, i.e. the lower the surface energy the more stable and more extended the facet is ($A_{111}/A_{100} = \gamma_{100}/\gamma_{111}$). The adhesion energy between Pd facets and TiO_x overlayer per Pd atom is negative ($\gamma_{adh} \sim -0.2$ eV) and thus reduces the overall surface energy. Since the (111) facet shows a lower surface energy compared to both (100) and (110), $\gamma_{111} = 82$

meV, γ_{100} = 94 meV and γ_{110} = 99 meV (computed values), the TiO_x overlayer results in a net increase of the ratio of the unperturbed surface energies $\gamma_{100}/\gamma_{111}$, considering a similar adhesion energy for both facets:

$$\gamma_{100}/\gamma_{111} < (\gamma_{100} + \gamma_{adh})/(\gamma_{111} + \gamma_{adh}) \quad (3)$$

Therefore, reduced surface energy due to the overlayer results in an increased value of $A_{111}/A_{100} = \gamma_{100}/\gamma_{111}$. In the same way, the reduced surface energy may have a more pronounced effect on (110) or the other surfaces of higher energies and directly lead to suppression, which explains the origin of shape change. Another example showing the dynamic shape change accompanied with the crystallization of the surface layer can be found in Figure 2.12; about 60% of the covered Pd particles observed exhibited such a change in shape. A schematic demonstrating the shape change of the particle, from round to faceted, due to net increase of the ratio A_{111}/A_{100} and elimination of (110) plane is shown in Figure 2.11G. During the dynamic sharp change, the formation of steps occurs on (111) plane in Figure 2.11 C'-E', suggesting the shape change is achieved through surface migration of Pd atoms between (111) and (100) facets.

2.3.2 Adsorbate-Mediated SMSI

*Effect of in-situ pre-*treat*ments on CO_2-reduction catalysis*

In a recent analysis of TiO_2-supported Rh (Rh/TiO_2) catalysts for the reduction of CO_2 by H_2, Matsubu. et al. observed a dynamic decrease in the rate of CH_4 production and increase in the rate of CO production when operating at CO_2:H_2 ratios greater than 1[29]. A complete cycle is shown in Figure 2.14 A for 6% Rh/TiO_2, in which the CH_4 selectivity decreased from 98% after reduction

(450 °C for four hours) to 11% after $20CO_2:2H_2$ treatment and returned to 98% CH_4 selectivity after re-reduction (450 °C for four hours). The influence of the $20CO_2:2H_2$ treatment on CO_2-reduction selectivity was tested for various Rh weight loadings on TiO_2 shown in Figure 2.14 B Consistently, the $20CO_2:2H_2$ treatment decreased CH_4 production and increased CO production, which was reversible on re-reduction. A low CH_4 selectivity on catalysts with a lower Rh weight loading after reduction was caused by high concentrations of isolated Rh-atom active sites. The largest selectivity changes were observed for higher Rh weight loadings that predominantly consist of Rh-nanoparticle active sites, which suggests that the $20CO_2:2H_2$ treatment modified the reactivity of Rh nanoparticles rather than single atoms.

Changes in adsorbates on Rh and TiO_2.

In-situ diffuse-reflectance infrared Fourier transform spectroscopy (DRIFTS) was used to examine the effect of $20CO_2:2H_2$ treatment on the species adsorbed on Rh and TiO_2 under the reaction conditions. Figure 2.15 shows in situ DRIFT spectra acquired from 2% Rh/TiO_2 under the reaction conditions ($1\%CO_2:1\%H_2:98\%$He and 200°C) after reduction, $20CO_2:2H_2$ treatment and re-reduction. Under the reaction conditions, the DRIFT spectrum of the reduced catalyst shows CO linearly bound to Rh at the top (2,046 cm^{-1}) and bridge (1,880 cm^{-1}) sites and a low adsorbate coverage on TiO_2, aside from H_2O (1,620 cm^{-1}), in agreement with previous reports [30, 31]. After $20CO_2:2H_2$ treatment, the switch in CO_2-reduction selectivity correlated with a ~50 cm^{-1} redshift in the frequency of the linear- and bridge-bound CO stretching modes and a twofold decrease in the integrated area of the linear-bound CO stretch. $20CO_2:2H_2$ treatment also introduced a high coverage of formate (HCO_2, 2,973, 2,923, 2,853, 1,531 and 1,351 cm^{-1}) and a bicarbonate-like species (HCO_3, 1,444 cm^{-1}) on the TiO_2 surface [32], which were only observed under reaction

conditions following the $20CO_2$:$2H_2$ treatment. Re-reduction of the catalyst regenerated spectral characteristics of the freshly reduced catalyst, consistent with the regenerated reactivity shown in Figure 2.14. To identify whether the ~50 cm^{-1} redshift and decreased intensity of the linear CO stretching mode were simply caused by a decrease in CO coverage on Rh, CO_2 was removed from the reactant stream to leave H_2 to react with the adsorbates. After removal of CO_2 from the reactant stream, CO stretches redshifted ~35–40 cm^{-1} as the CO coverage decreased on both the reduced and $20CO_2$:$2H_2$-treated catalysts. This is shown quantitatively in Figure 2.15, in which the reduced and $20CO_2$:$2H_2$-treated catalysts exhibit a similar decrease in the CO stretching frequency in H_2 flow. The coverage-dependent redshift in the CO stretching frequency of 35 –40 cm^{-1} is consistent with the effect of reduced dipole coupling on nanoparticle-catalyst surfaces, which indicates that the $20CO_2$:$2H_2$-treatment-induced 50 cm^{-1} redshift (Fig. 2a) 3 in the CO stretching frequency was not caused by a change in 4 local CO coverage.

The origin of the 50 cm^{-1} shift in the CO stretching frequency was probed further by executing a temperature-programmed desorption (TPD) in He after the coverage-dependent experiment (spectra 6–8 in Figure 2.15). The HCO_x species desorbed from TiO_2 above ~300°C with a simultaneous blueshift in frequency of the remaining linearly bound CO by ~35 to ~1,996 cm^{-1}, almost identical to the frequency observed at low coverage on the reduced catalyst (Figure 2.15c). Catalyst performance was tested after the HCO_x species were desorbed from the $20CO_2$:H_2-treated sample and the reactivity was restored to the behavior of the original reduced catalyst state. Correlation between the removal of HCO_x species from TiO_2 and the blueshift in the CO stretching frequency, combined with the return of the reduced catalyst reactivity, demonstrates that the modified reactivity induced by $20CO_2$:$2H_2$ treatment is mediated by interactions between HCO_x

and the TiO_2 support. The similarity between the influence of $20CO_2$:$2H_2$ and formic acid treatments on the reactivity of Rh/TiO_2 catalysts suggests the existence of an A-SMSI state in which a high coverage of HCO_x.

Direct visualization of surface layer

To visualize directly the $20CO_2$:$2H_2$-induced TiO_2 structural transformation, fresh 2% Rh/TiO_2 catalyst was first examined in the Atmosphere gas cell after 4hrs heating under $20CO_2$:$2H_2$ at 250 ºC. As shown in the Figure 2.16, a very thin amorphous layer was found to cover almost all the surface of Rh and TiO_2 support. The size of the particles, ~2nm in diameter, indicating the thickness of the amorphous layer is too thin to be clearly visualized in the gas cell with 80nm membrane.

To enhance the contrast of the surface layers and suppress any possible artifact induced by the electron beam, the fresh 6% Rh/TiO_2 sample was pre-sintered at 800 °C in N_2 to increase the Rh particle size from 1–3 nm to 10–50 nm. The sintered catalyst was evaluated for reactivity after reduction and $20CO_2$:$2H_2$ treatment, and CH_4 selectivity decreased from 97% after reduction to 4% after $20CO_2$:$2H_2$ treatment. This almost identical influence of $20CO_2$:$2H_2$ treatment on the sintered and unsintered 6% Rh/TiO_2, with large differences in Rh particle sizes, strongly supports the mechanism of HCO_x-mediated migration of TiO_x onto Rh, because the charge-transfer mechanism without overlayer formation would have been suppressed by the increased particle size in the sintered catalyst. *In-situ* STEM analyses were executed both during reduction and $20CO_2$:$2H_2$ treatment of the sintered 6% Rh/TiO_2 catalyst to compare the overlayers of classical SMSI and A-SMSI. After treatment at 550°C in 5%H_2/N_2, conditions known to form the classical

SMSI state, a crystalline bilayer of TiO_x quickly formed as a conformal coating on large crystalline Rh particles, similar to what we observed on Pd and Pt, showing in Figure 2.17a. In contrast, after $20CO_2$:$2H_2$ treatment for four hours at 250°C an amorphous overlayer on Rh was observed to form (Figure 2.17b). More examples of A-SMSI layer are shown in Figure 2.18. *In-situ* electron energy-loss spectroscopy (EELS) measurements with a 1.0–1.5 Å spot size focused at various locations on the overlayer directly proved that Ti was present in the amorphous overlayer formed from $20CO_2$:$2H_2$ treatment shown in Figure 2.19. Ti in the amorphous overlayer was found to exist in a combination of Ti^{3+} (∼30%) and Ti^{4+} (∼70%) oxidation states, quantified using Multiple Linear Least Square (MLLS) method.

2.4 Summary

2.4.1 Classical SMSI

In order to actually capture the dynamic formation process of the SMSI overlayer and truly understand its structure, we employ *in-situ* ambient pressure scanning TEM (STEM), supported by density functional theory (DFT), on high-surface area Pd/TiO_2, Pd/Al_2O_3, Pt/TiO_2 and Au/TiO_2 catalysts, thus providing unprecedented detail at the atomic scale. Under SMSI state, an amorphous TiOx layer is initially formed at low temperature (∼300 °C) in a reducing atmosphere, followed by crystallization into an ordered layer epitaxial with the Pd(111) surface at ∼500 °C. With reference to well-known properties of the SMSI, the amorphous layer corresponds to the state produced by low temperature reduction (LTR), whereas the crystalline layer corresponds to the state produced by high-temperature reduction (HTR): the overlayer formed by LTR is gas permeable, but the overlayer formed by HTR is very effective in blocking access of gas molecules to the underlying metal surface. We demonstrate that the reduced oxide is one or two atomic layers thick, depending on the reactive gas atmosphere, which we adjust by controlling H_2 and O_2 partial

pressures in a MEMS-based closed TEM gas cell. We also show that crystallization of the overlayers is accompanied by a reconstruction of the underlying Pd nanocrystal facets as a result of surface energy minimization. Both DFT calculation and in-situ TEM studies confirm that SMSI state can form on Pd/TiO_2, Pt/TiO_2 but not Pd/Al_2O_3 and Au/TiO_2.

2.4.2 Adsorbate-Mediated SMSI

Through a combination of *in-situ* microscopy and spectroscopy, it has been demonstrated that HCO_x adsorbates on TiO2-supported Rh catalysts can induce oxygen vacancy formation in the support and drive the formation of an A-SMSI overlayer on Rh. The A-SMSI overlayer is porous (which enables access for the reactants to interact with the Rh surface) and stable under humid reaction conditions. The existence of the A-SMSI overlayer locally modifies the selectivity of the underlying Rh-nanoparticle surface, which opens new avenues for tuning and controlling the reactivity of supported metal catalysts.

2.4.3 Comparison of Classical and A-SMSI overlayers

The formation mechanisms and characteristics of the A-SMSI overlayers proposed, and the classical SMSI overlayer described by Tauster, [4] are schematically depicted in Figure 2.10. In both overlayers, migration of the support onto the catalytically active metal is induced by the oxygen-vacancy formation in the support. For the SMSI overlayer formation, H_2 treatment at 30 ∼500°C induces oxygen-vacancy formation in the support, which drives the formation of an impermeable, crystalline and fully reduced metal–oxide overlayer on flat facets of metal particles. Formation of the A-SMSI overlayer is mediated by the high coverage of HCO_x on the support at 150–300°C, which causes oxygen vacancy formation and drives the formation of a gas permeable and partially

reduced metal oxide overlayer on the catalytically active metal. For classical SMSI overlayers formed with TiO_2, the overlayer is oxidized rapidly in the humid environment of the CO_2 +H_2 reaction, which causes recession of the support off the metal and a negating influence on the catalytic reactivity of the underlying metal. However, the A-SMSI overlayers derived from TiO_2 are stable under humid reaction conditions, which enables the overlayer to influence strongly the reactivity of the catalytically active metal. A-SMSI overlayer locally modifies the reactivity of the underlying Rh-nanoparticle surface, which opens new avenues for tuning and controlling the reactivity of supported metal catalysts.

2.5 References

1. Henry, C. R. *Surf. Sci. Rep.* **1998,** 31, 231-325.
2. Farmer, J. A.; Campbell, C. T. *Science* **2010,** 329, 933-936.
3. Green, I. X.; Tang, W.; Neurock, M.; Yates, J. T. *Science* **2011,** 333, 736-739.
4. Tauster, S.; Fung, S.; Garten, R. *J. Am. Chem. Soc.* **1978,** 100, 170-175.
5. Kao, C.-C.; Tsai, S.-C.; Chung, Y.-W. *J. Catal.* **1982,** 73, 136-146.
6. Bracey, J. D.; Burch, R. *J. Catal.* **1984,** 86, 384-391.
7. Logan, A. D.; Braunschweig, E. J.; Datye, A. K.; Smith, D. J. *Langmuir* **1988,** 4, 827-830.
8. Datye, A.; Kalakkad, D.; Yao, M.; Smith, D. J. *J. Catal.* **1995,** 155, (1), 148-153.
9. Liu, J. *Microsc. Microanal.* **2004,** 10, 55-76.
10. Bennett, R.; Pang, C.; Perkins, N.; Smith, R.; Morrall, P.; Kvon, R.; Bowker, M. *The Journal of Physical Chemistry B* **2002,** 106, 4688-4696.
11. Barcaro, G.; Agnoli, S.; Sedona, F.; Rizzi, G. A.; Fortunelli, A.; Granozzi, G. *The Journal of Physical Chemistry C* **2009,** 113, 5721-5729.

12. Sedona, F.; Rizzi, G. A.; Agnoli, S.; Llabrés i Xamena, F. X.; Papageorgiou, A.; Ostermann, D.; Sambi, M.; Finetti, P.; Schierbaum, K.; Granozzi, G. *The Journal of Physical Chemistry B* **2005,** 109, 24411-24426.

13. Dulub, O.; Hebenstreit, W.; Diebold, U. *Phys. Rev. Lett.* **2000,** 84, 3646.

14. Bernal, S.; Calvino, J.; Cauqui, M.; Gatica, J.; Larese, C.; Omil, J. P.; Pintado, J. *Catal. Today* **1999,** 50, 175-206.

15. Braunschweig, E. J.; Logan, A. D.; Datye, A. K.; Smith, D. J. *J. Catal.* **1989,** 118, 227-237.

16. Gatica, J. M.; Baker, R. T.; Fornasiero, P.; Bernal, S.; Blanco, G.; Kašpar, J. *The Journal of Physical Chemistry B* **2000,** 104, 4667-4672.

17. Cargnello, M.; Doan-Nguyen, V. V.; Gordon, T. R.; Diaz, R. E.; Stach, E. A.; Gorte, R. J.; Fornasiero, P.; Murray, C. B. *Science* **2013,** 341, 771-773.

18. Peng, S.; Lee, Y.; Wang, C.; Yin, H.; Dai, S.; Sun, S. *Nano research* **2008,** 1, 229-234.

19. Giannozzi, P.; Baroni, S.; Bonini, N.; Calandra, M.; Car, R.; Cavazzoni, C.; Ceresoli, D.; Chiarotti, G. L.; Cococcioni, M.; Dabo, I. *J. Phys.: Condens. Matter* **2009,** 21, 395502.

20. Vanderbilt, D. *Physical Review B* **1990,** 41, 7892-7895.

21. Bengtsson, L. *Physical Review B* **1999,** 59, 12301-12304.

22. Barcaro, G.; Sedona, F.; Fortunelli, A.; Granozzi, G. *The Journal of Physical Chemistry C* **2007,** 111, 6095-6102.

23. Batson, P. E. *Microsc. Microanal.* **2008,** 14, 89-97.

24. Krivanek, O. L.; Dellby, N.; Murfitt, M. F.; Chisholm, M. F.; Pennycook, T. J.; Suenaga, K.; Nicolosi, V. *Ultramicroscopy* **2010,** 110, 935-945.

25. Chi, M.; Wang, C.; Lei, Y.; Wang, G.; Li, D.; More, K. L.; Lupini, A.; Allard, L. F.; Markovic, N. M.; Stamenkovic, V. R. *Nature communications* **2015,** 6, 8925.

26. Lupini, A.; Krivanek, O.; Dellby, N.; Nellist, P.; Pennycook, S. In *Developments in Cs-corrected STEM*, CONFERENCE SERIES-INSTITUTE OF PHYSICS, 2001; Philadelphia; Institute of Physics; 1999: pp 31-34.

27. Surnev, S.; Vitali, L.; Ramsey, M.; Netzer, F.; Kresse, G.; Hafner, J. *Physical Review B* **2000,** 61, 13945.

28. Nolte, P.; Stierle, A.; Jin-Phillipp, N.; Kasper, N.; Schulli, T.; Dosch, H. *Science* **2008,** 321, 1654-16529.

29. Matsubu, J. C.; Yang, V. N.; Christopher, P. *J. Am. Chem. Soc.* **2015,** 137, 3076-3084.

30. Henderson, M.; Worley, S. *The Journal of Physical Chemistry* **1985,** 89, 1417-1423.

31. Karelovic, A.; Ruiz, P. *J. Catal.* **2013,** 301, 141-153.

32. Bando, K. K.; Sayama, K.; Kusama, H.; Okabe, K.; Arakawa, H. *Applied Catalysis A: General* **1997,** 165, 391-409.

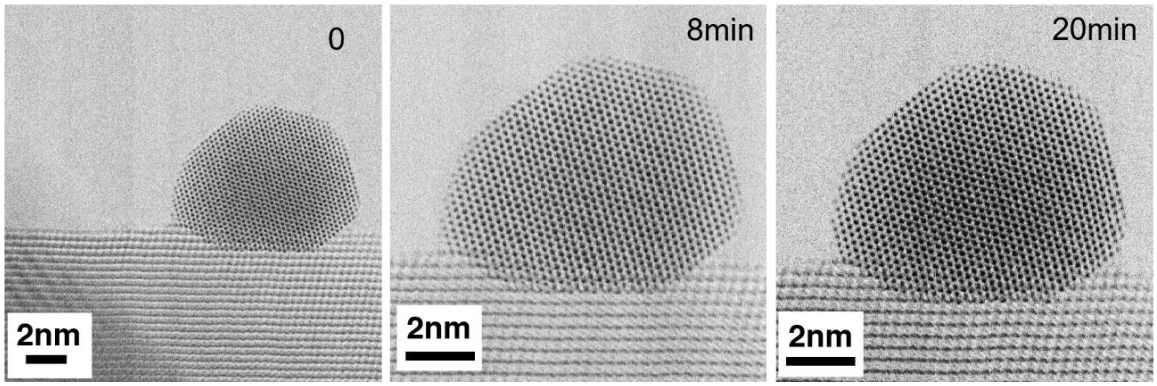

Figure 2.1 ABF images showing that no amorphous layer migrate onto the particle under H_2 (4.7 vol. %)/O_2 (5.7 vol. %)/Ar at 500 °C during 20mins electron beam illumination. (Images are from *Nano Letters* **16**, 4528 (2016).)

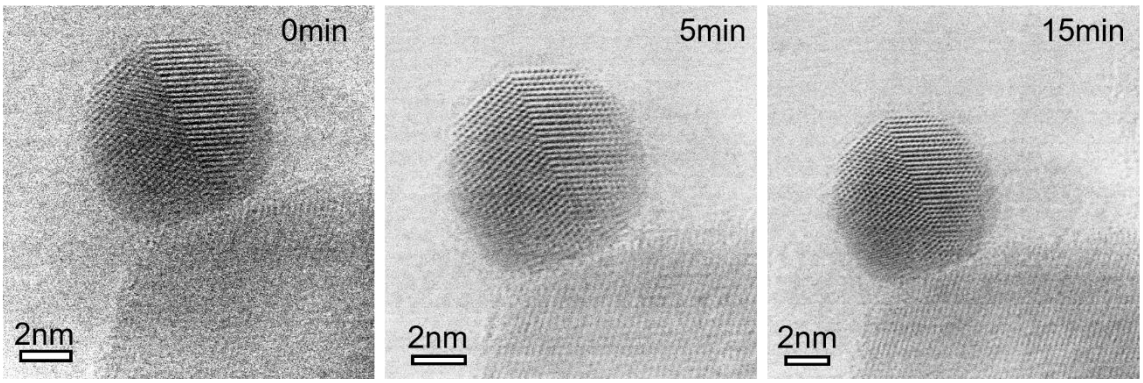

Figure 2.2 ABF images showing that an amorphous layer start to form on the surface of the particle at 250 °C under H_2 (5 vol. %)/Ar at 1 atm and no changes have been observed in the images taken at varied time. (Images are from *Nano Letters* **16**, 4528 (2016).)

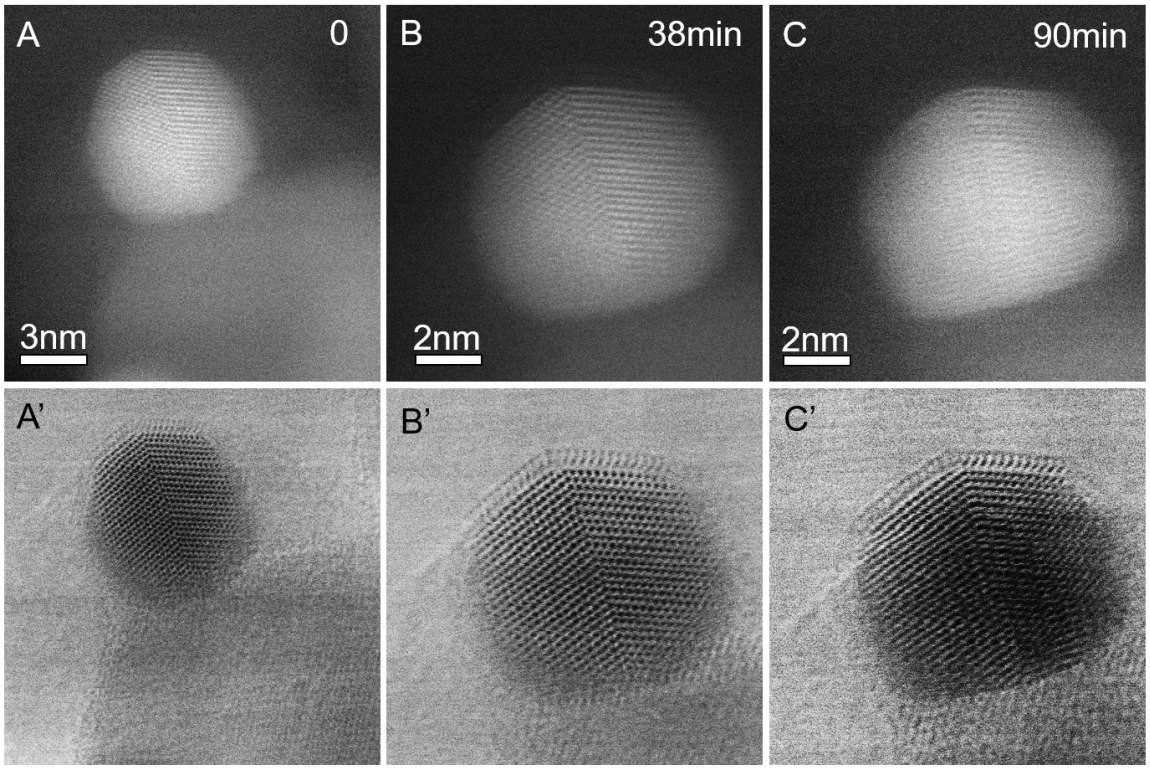

Figure 2.3 Pair of HAADF and ABF images showing that no structural damage can be discerned in the images taken at varied time up to 90 mins of illumination at 500 °C under H_2 (5 vol. %)/Ar at 1 atm. (Images are from *Nano Letters* **16**, 4528 (2016).)

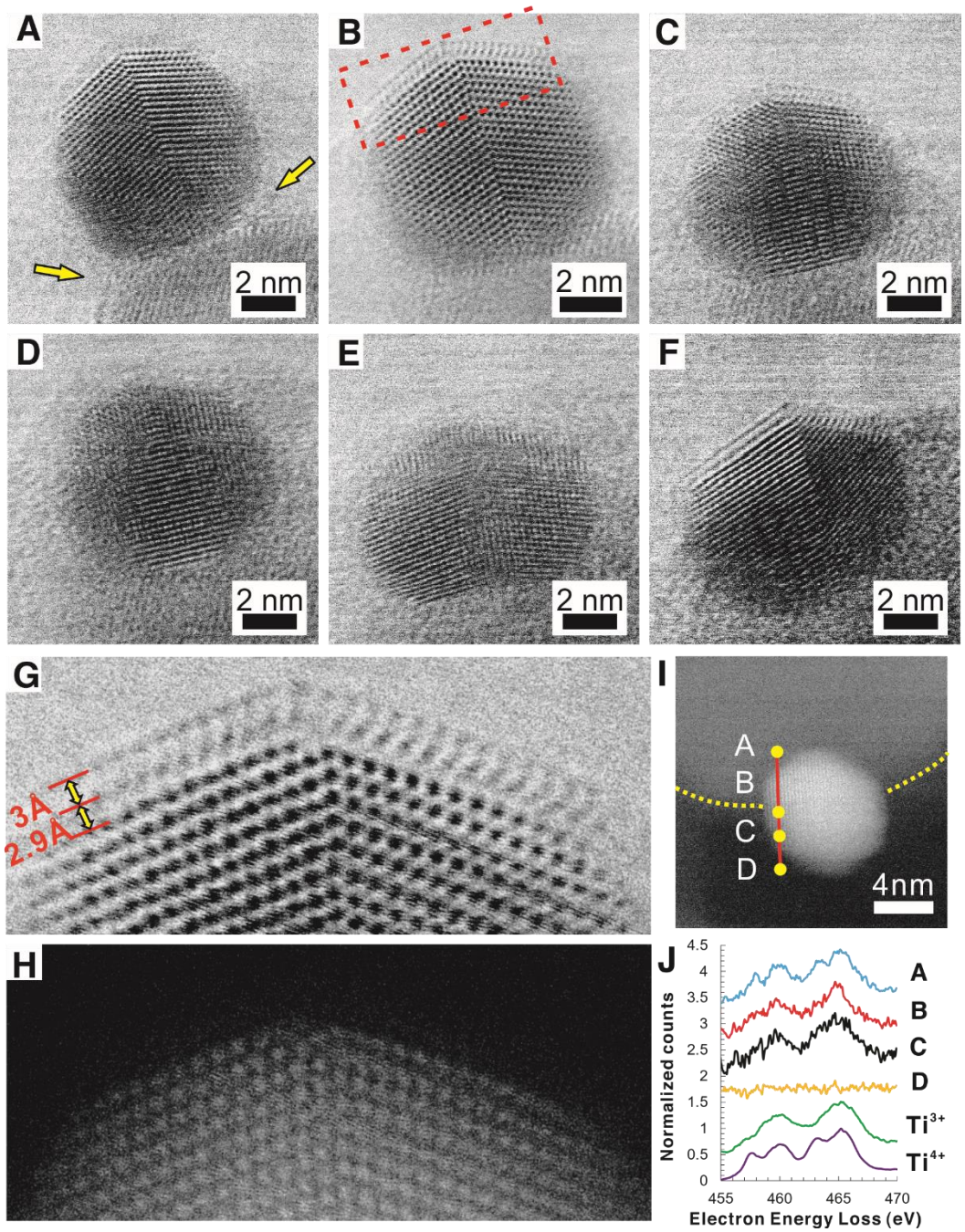

Figure 2.4. Reversible formation of the TiO_x overlayer on Pd nanocrystal in Pd/TiO_2. Sequential *in situ* observations, first under reducing conditions (H_2 (5 vol. %)/Ar at 1 atm) of the Pd/TiO_2 sample at 250 °C (A), then 500 °C for 10 min (B); next under oxidizing conditions (150 Torr O_2) at 250 °C for 8 minutes (C), then 15 minutes (D), and then at a final stable state at 500 °C (E); and finally under reducing conditions again (H_2 (5 vol. %)/Ar at 1 atm) at 500 °C for 5 minutes (F). (G, H) are higher magnification ABF and HAADF images, respectively, of a section of part (B) showing the TiO_x double layer. (I, J) EELS spectra extracted from a line scan of another particle, shown in (I), under H_2 (5 vol. %)/Ar at 1 atm and 500 °C, and Ti^{3+} and Ti^{4+} reference spectra acquired from $LaTiO_3$ and TiO_2. (Images are from *Nano Letters* **16**, 4528 (2016).)

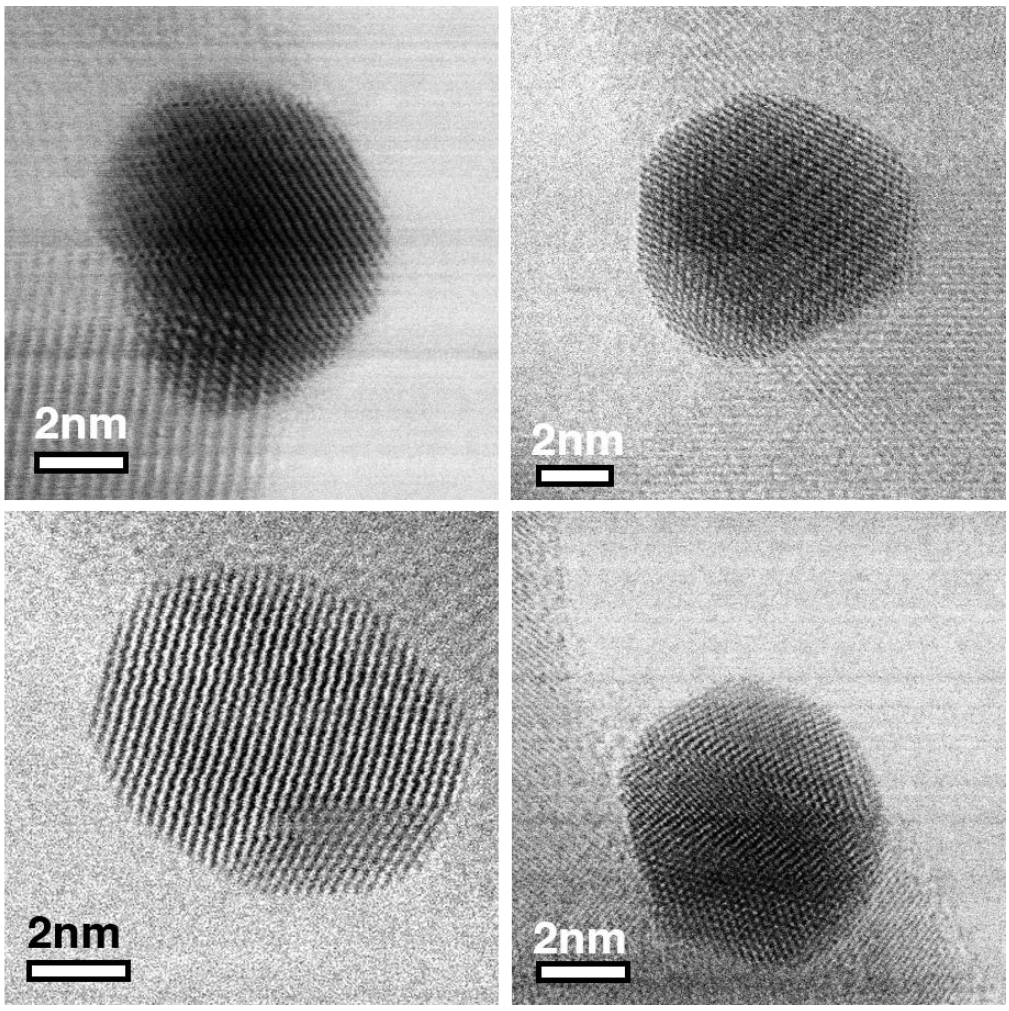

Figure 2.5 *Ex-situ* BF STEM images showing that the surfaces of the Pd particles are initially (i.e., before conducting the in-situ experiments) clean at room temperature. (Images are from *Nano Letters* **16**, 4528 (2016).)

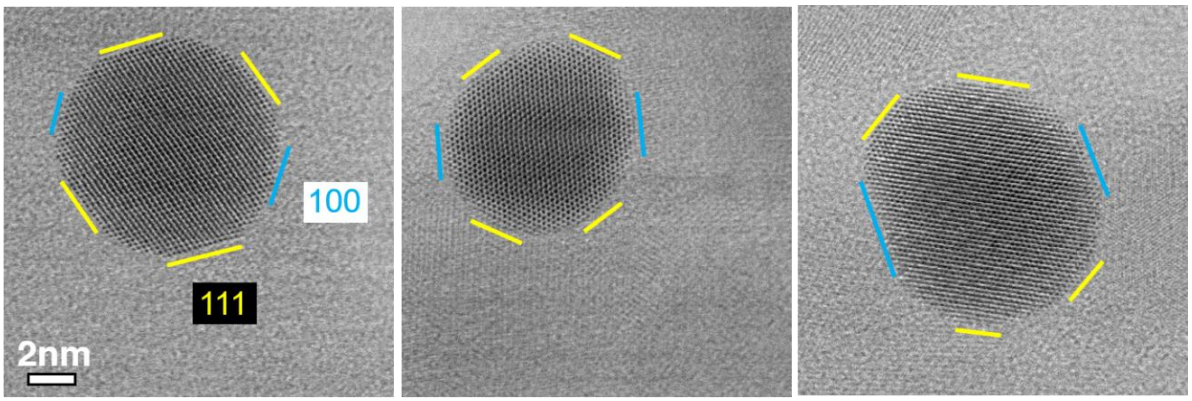

Figure 2.6 ABF STEM images showing that no change occurred when Pd/Al_2O_3 was heated under H_2 (5 vol. %)/Ar at 1 atm at 500 °C. The shape of the Pd nanoparticle is a truncated octahedron with smooth truncation between the two major facets, (111) and (100). (Images are from *Nano Letters* **16**, 4528 (2016).)

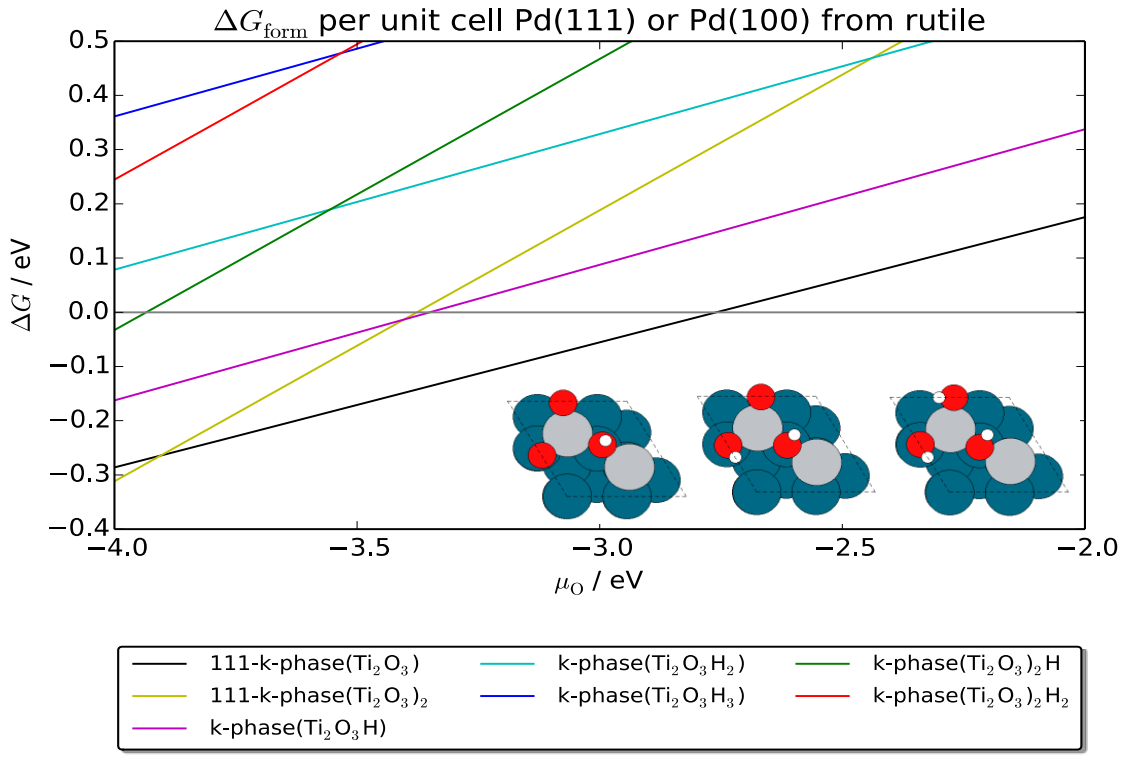

Figure 2.7. Stability of hydrogenated single and double layers. Structural models are shown in an inset. (Images are from *Nano Letters* **16**, 4528 (2016), data is calculated by Philipp N. Plessow)

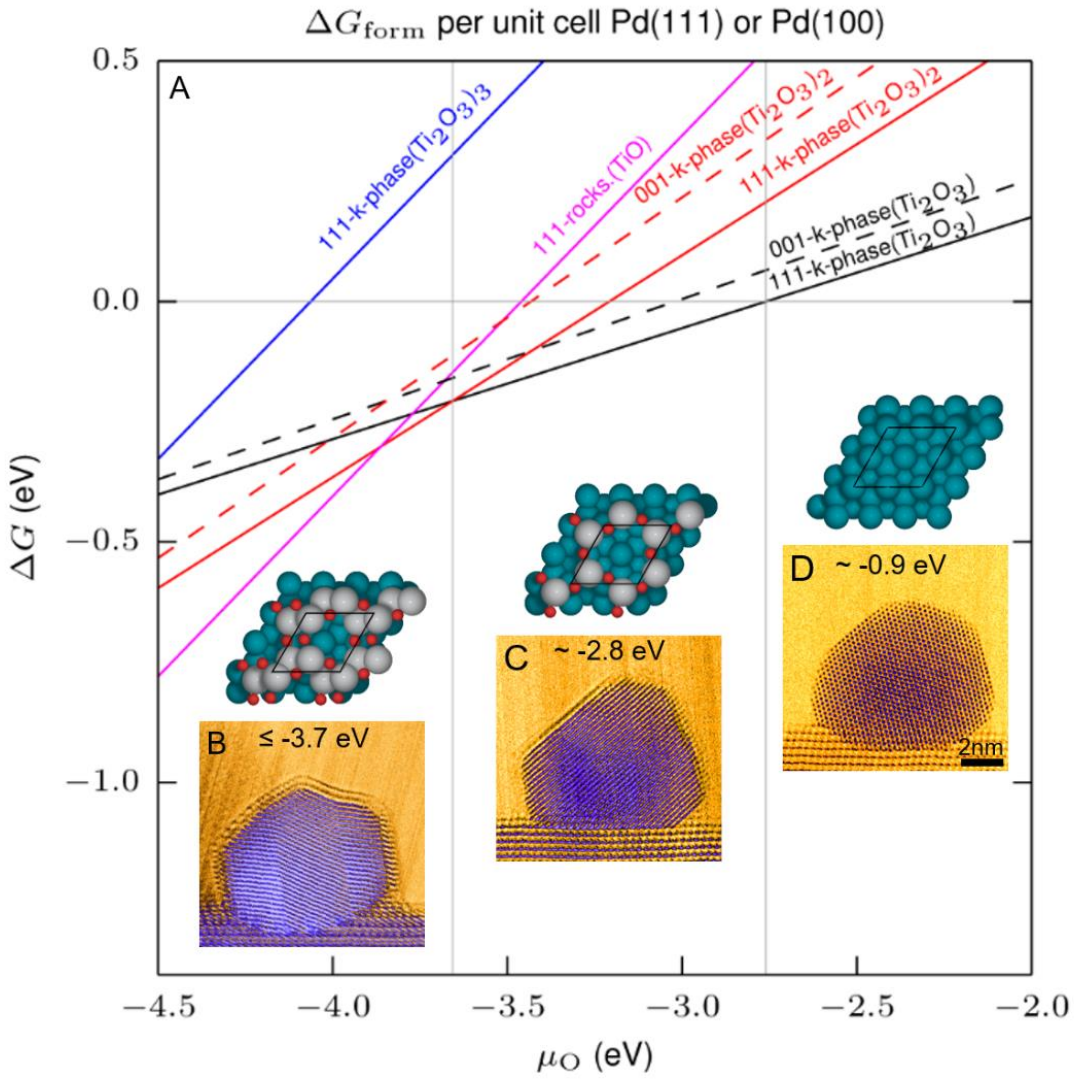

Figure 2.8. Theoretical calculations and experimental evidence of free energy *G* for different TiO_x phases on Pd(111) or Pd(100) surfaces as a function of oxygen chemical potential μ_O. (A) Calculated energy diagram (B) TiO_x/Pd double layer found under H_2 (5 vol. %)/Ar at 1 atm total pressure and 500 °C. (C) TiO_x/Pd single layer found under H_2 (4.9 vol. %)/O_2 (2 vol. %)/Ar at 1 atm total pressure and 500 °C. (D) No layer was observed under H_2 (4.7 vol. %)/O_2 (5.7 vol. %)/Ar at 1 atm total pressure and 500 °C. The top-down views of the corresponding structures of the experimentally-observed surface layers are shown above the TEM images. Pd is in dark green, Ti in grey and Oxygen in red. (Images are from *Nano Letters* **16**, 4528 (2016), energy diagram is calculated by Philipp N. Plessow)

Table 2.1. Comparison of the stability of the k-phase single and double layers of TiO_x on the (111) facets of different metals on at μ_O = -3.7 eV. Free energies of formation are given in eV. (Data is from *Nano Letters* **16**, 4528 (2016), calculated by Philipp N. Plessow)

	single	double
Au	0.04	0.18
Pd	-0.23	-0.19
Pt	-0.32	-0.40

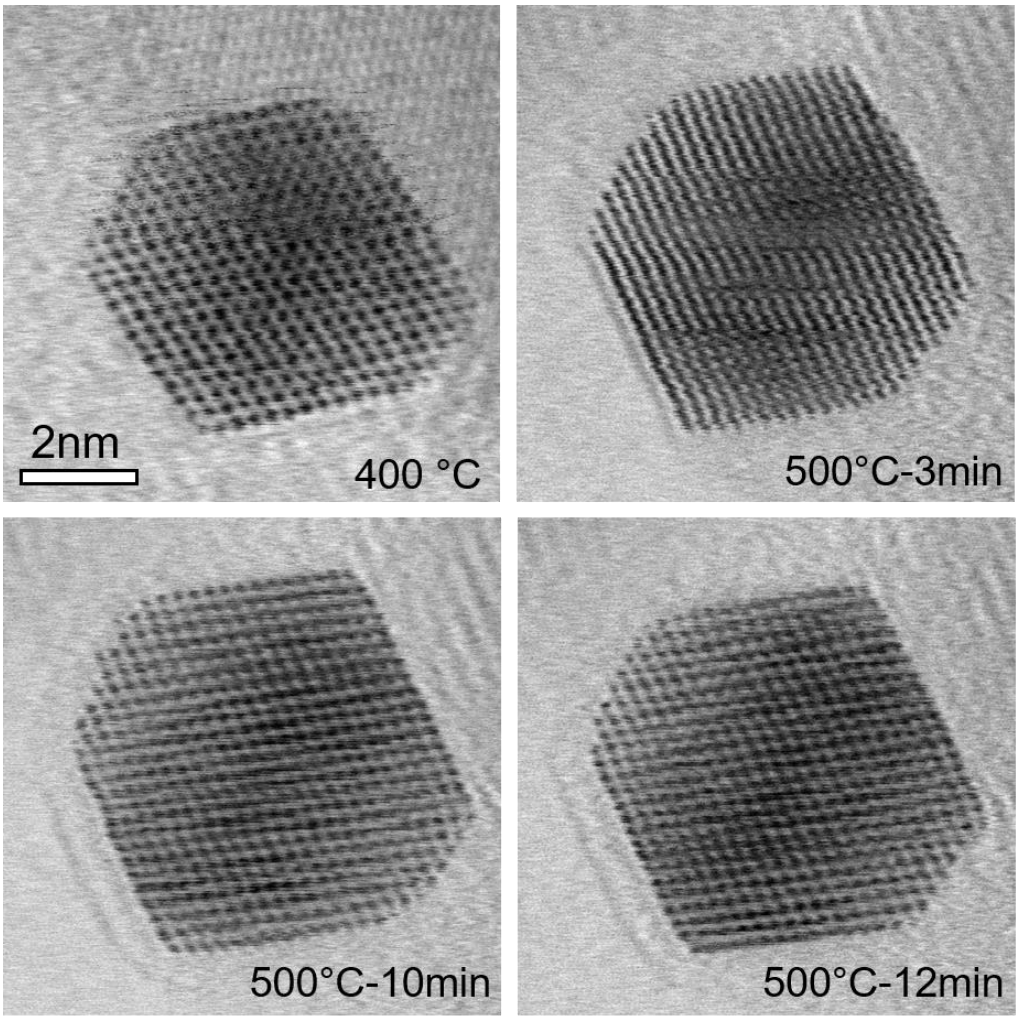

Figure 2.9. ABF images showing the formation of TiO_x double layer on Pt particles in Pt/TiO_2 under H_2 (5 vol. %)/Ar at 1 atm.(Images are from *Nano Letters* **16**, 4528 (2016))

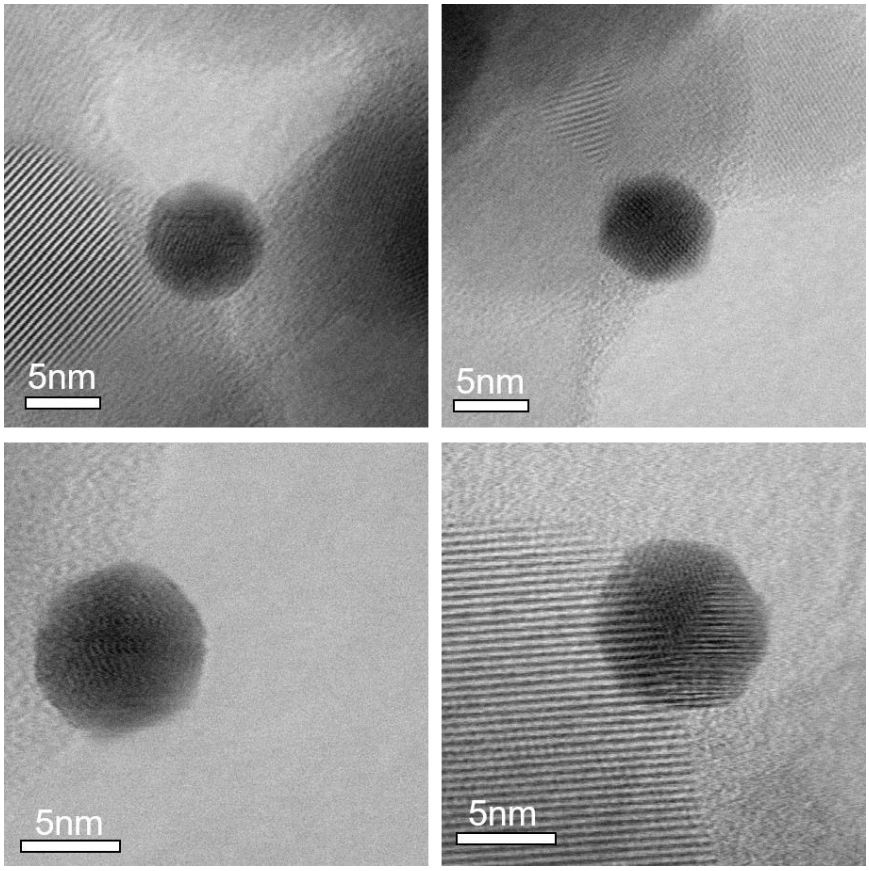

Figure 2.10. ABF images showing that the surface of Au particles in Au/TiO_2 are clean after 1 h heating under H_2 (5 vol. %)/Ar at 1 atm at 500 °C. (Images are from *Nano Letters* **16**, 4528 (2016))

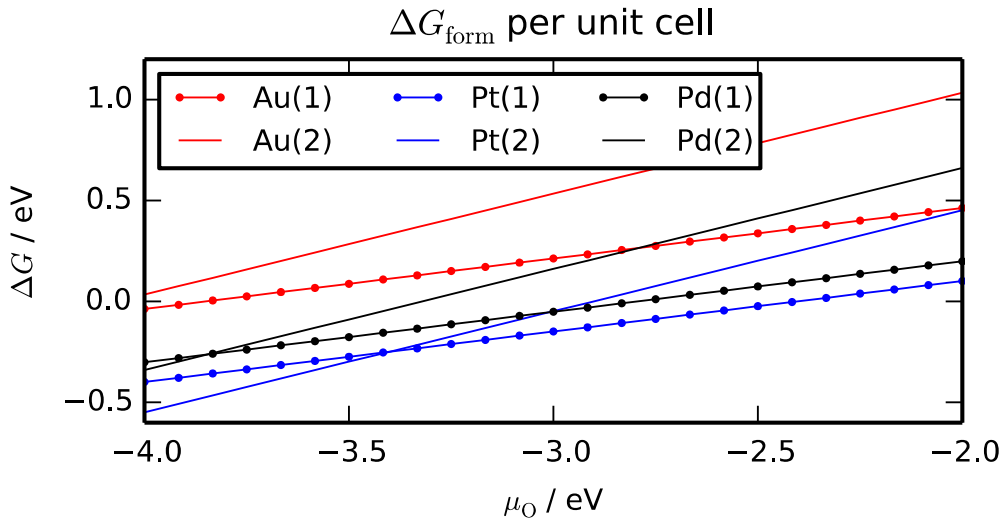

Figure 2.11. Stability of k-phase single and double-layer TiOx structures supported on (111) Au, Pd and Pt. The number of layers is given in parentheses. (Data is from *Nano Letters* **16**, 4528 (2016), calculated by Philipp N. Plessow)

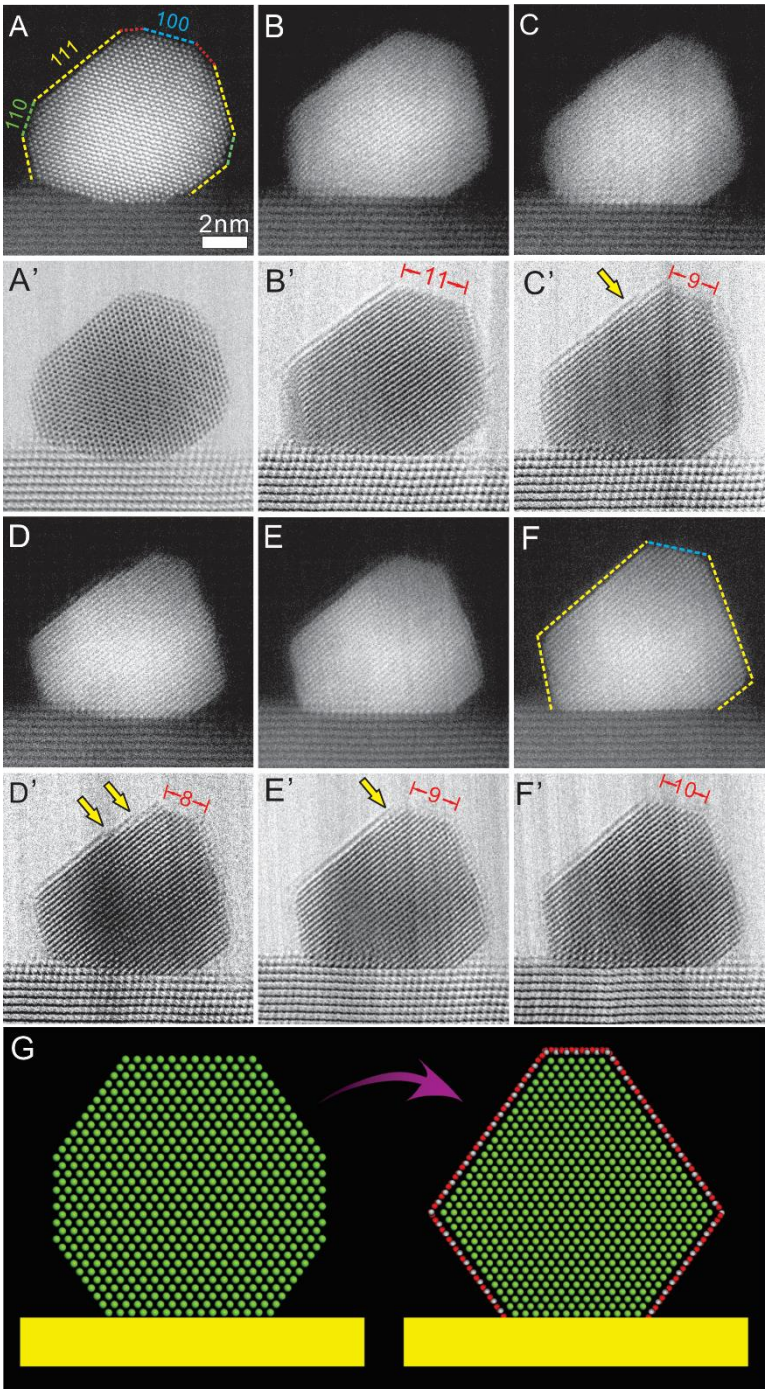

Figure 2.12. Dynamic shape change of a single Pd nanocrystal supported on TiO_2 during overlayer formation. (A-F) HAADF and (A'-F') corresponding BF STEM images of Pd/TiO_2 under H_2 (4.9 vol. %)/O_2 (2 vol. %)/Ar 1 atm at 400 °C (A), 400 °C for 25 minutes (B), 400 °C for 30 minutes (C), 500 °C for 3 minutes (D), 500 °C for 22 minutes (E) and 500 °C final stable state (F). Corresponding surface energy ratios $\gamma_{100}/\gamma_{111}$ are 1.08, 1.24, 1.26, 1.27, 1.31, 1.27 for A-F, respectively. (G) A schematic showing the round-to-facetted shape transformation of the particle. Pd is green, O in red and Ti in grey. (Images are from *Nano Letters* **16**, 4528 (2016), calculated by Philipp N. Plessow)

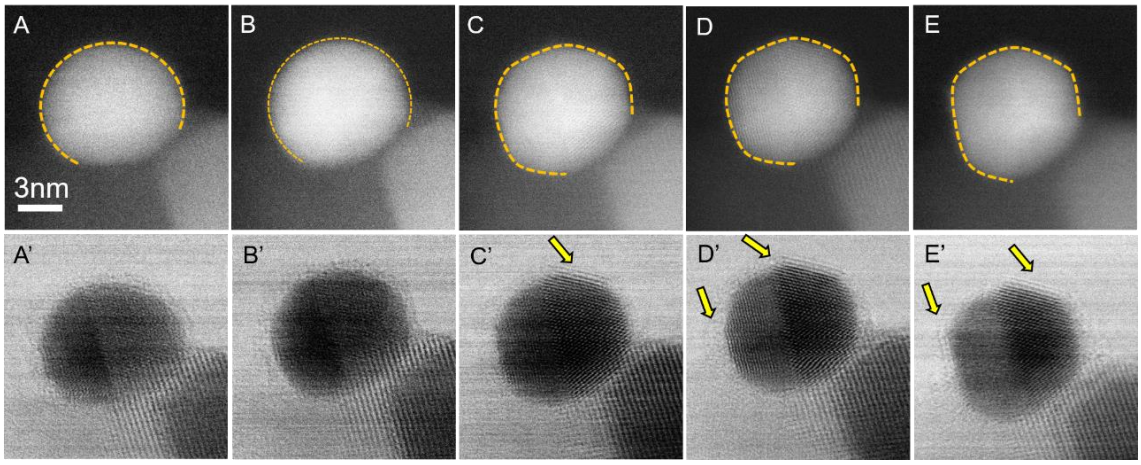

Figure 2.13. Dynamic process showing the disorder to order transition accompanied by the faceting of the particle under 760 Torr 5%H_2/N_2 (A) 300 °C (B) 400 °C 2 min (C) 400 °C 15 min (D) 400 °C 47 min (E) 500 °C. (Images are from *Nano Letters* **16**, 4528 (2016), calculated by Philipp N. Plessow)

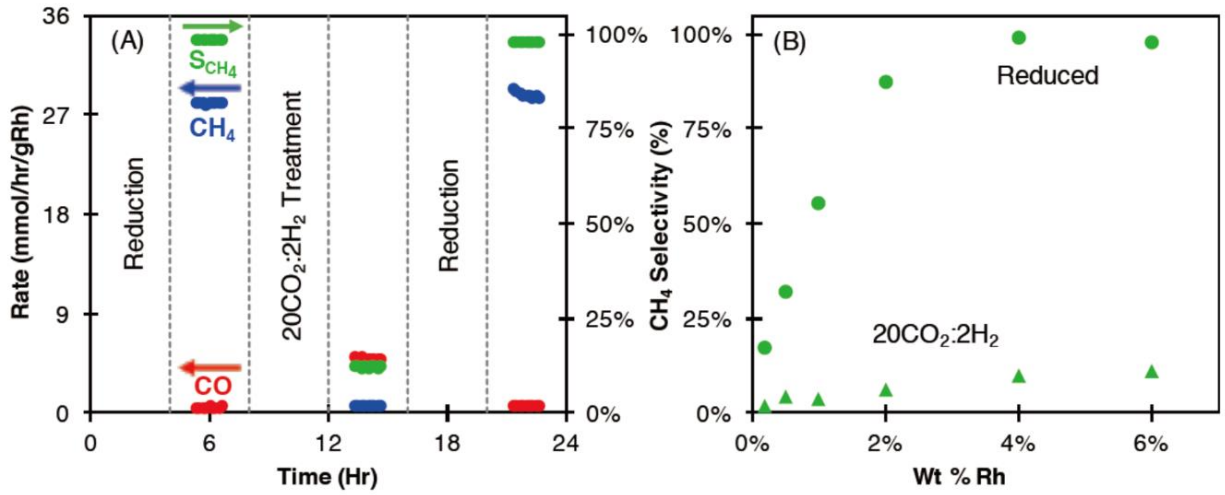

Figure 2.14 5 A, Rate of CO and CH_4 production and selectivity to CH_4 over 6% Rh/TiO_2 measured at 200 °C with a feed composition of 1% CO_2, 1%H_2 and 98% He, after treatments with pure H_2 at 450 °C for four hours (reduction) and then 20CO2:2H2 at 250 °C for four hours. Between treatments, CH_4 selectivity was reversibly controlled from 98 to 11%. B, Effect of $20CO_2:2H_2$ treatment on CH_4 selectivity as a function of Rh weight loading (%).(Data is from "Adsorbate-mediated strong metal–support interactions in oxide-supported Rh catalysts." Nature Chemistry, published online, taken by John Matsubu)

"

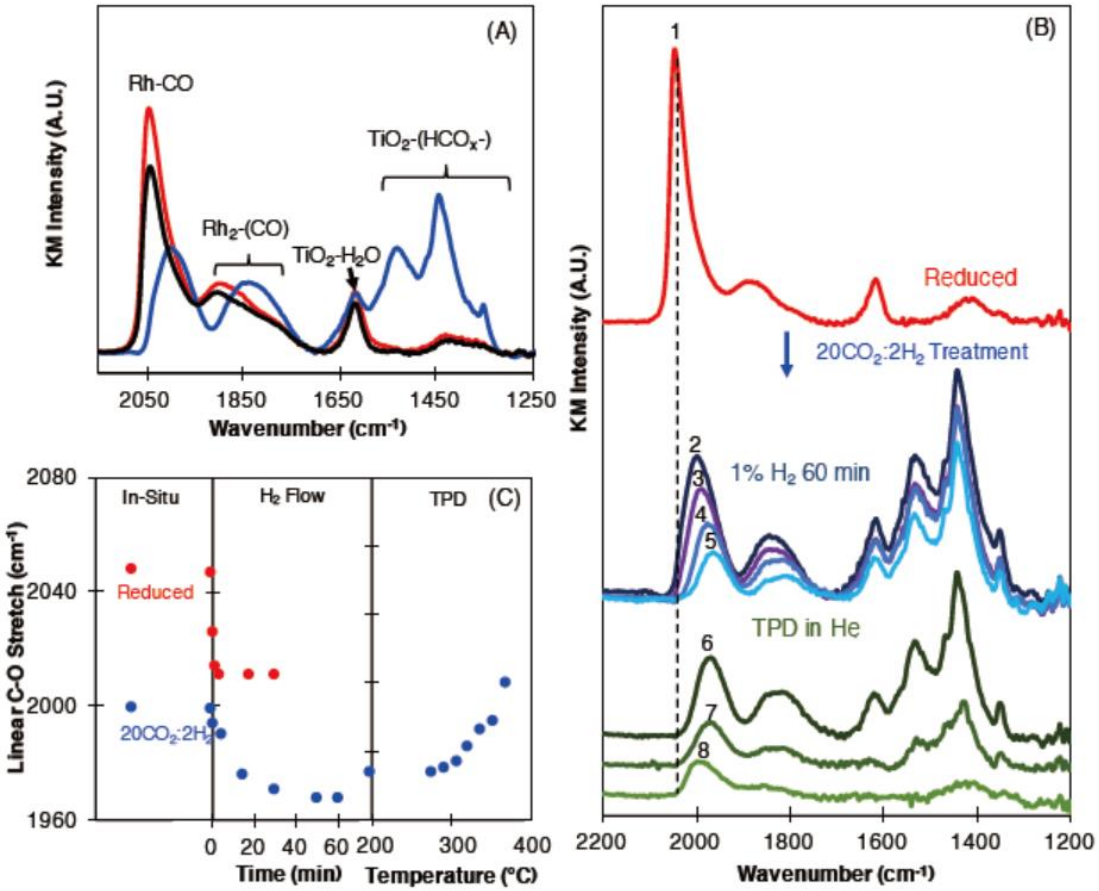

Figure 2.15 Infrared analysis of selectivity switch. A, *In-situ* DRIFT spectra collected from 2% Rh/TiO_2 at the reaction conditions (180 °C, 1% CO_2, 1% H_2, 98% He) for reduced (red), $20CO_2$:$2H_2$-treated (blue) and re-reduced (black) catalysts. On $20CO_2$:$2H_2$ treatment, the CO stretching frequency of linear and bridge Rh-carbonyl groups decreased by 50 cm^{-1}, their intensity dropped twofold and TiO_2-bound HCOx species appeared. Re-reduction reversed all the effects of the $20CO_2$:H_2 treatment. B, DRIFT spectra of 2% Rh/TiO_2 under the reaction conditions after reduction (spectrum 1), after $20CO_2$:$2H_2$ treatment (spectrum 2) and CO_2 flow removed (only 1% H_2) for 5, 15 and 60 minutes (spectra 3–5). Spectra 6–8 were collected during TPD in He at 213, 312 and 370 °C, respectively, immediately after the collection of spectrum 5. The vertical dotted line represents the CO stretch frequency on a reduced 2% Rh catalyst under the reaction conditions. Corresponding increases in the carbonyl stretching frequency with HCO_x desorption suggest they are related. C, Peak positions of the linear CO stretching frequency during the experiments shown in Fig. 2b. The reduced (red) and $20CO_2$:$2H_2$-treated (blue) catalysts exhibited a similar decrease in CO stretching frequency in H_2 flow, which suggests that the shift in carbonyl frequency in A did not result from a decrease in CO coverage.(Data is from "Adsorbate-mediated strong metal–support interactions in oxide-supported Rh catalysts." Nature Chemistry, published online, taken by John Matsubu)

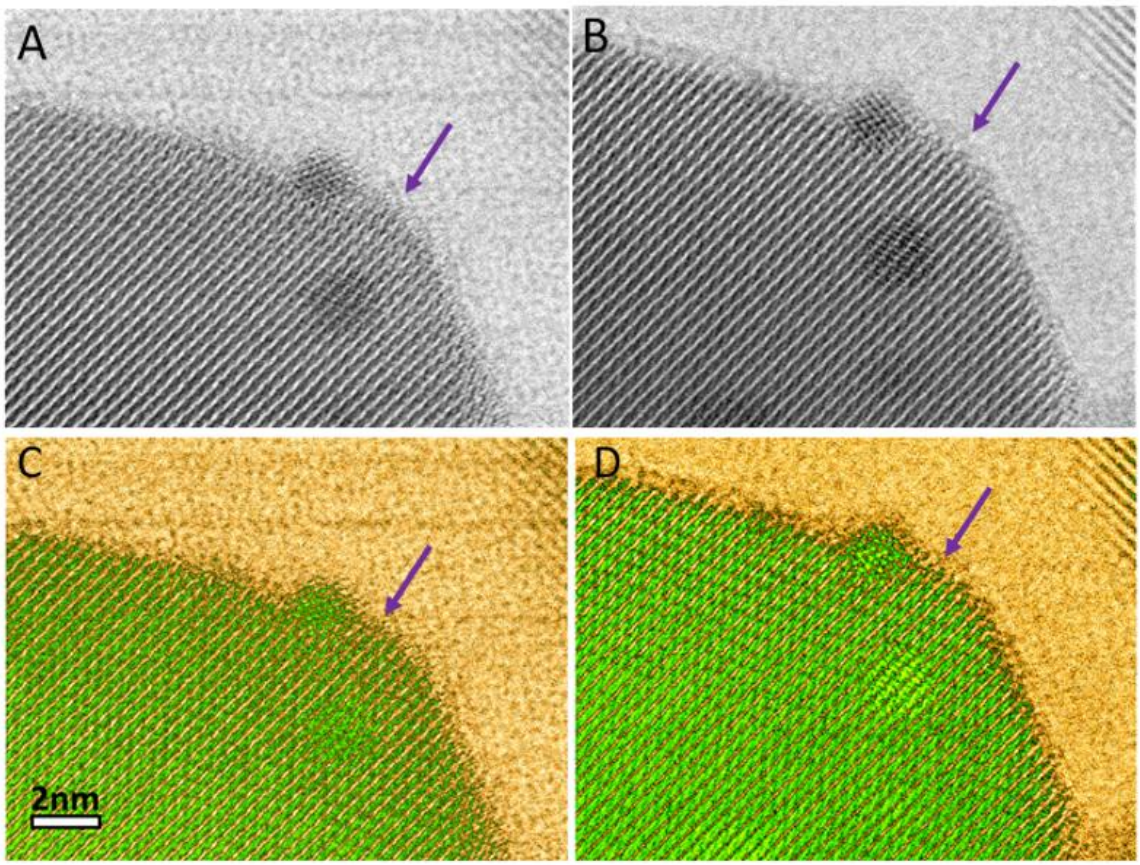

Figure 2.16 *In-situ* bright field STEM (BF-STEM) images of 2%Rh/TiO_2 A) after 1 hour of H_2 reduction and B) 3 hours of $20CO_2$:$2H_2$ treatment. C, D) are A,B with false coloring to emphasize the A-SMSI overlayer. The formation of the comprehensive low-contrast overlayer is pointed out by the arrows in B and D and lack thereof in A and C. (Data is from "Adsorbate-mediated strong metal–support interactions in oxide-supported Rh catalysts." Nature Chemistry, published online)

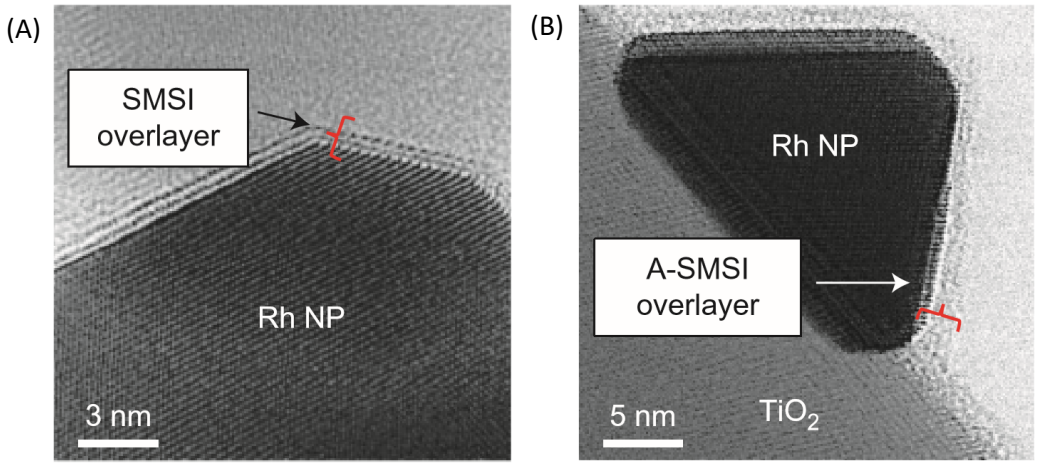

Figure 2.17 Visualizing SMSI and A-SMSI states. a,b, In situ STEM images of sintered 6% Rh/TiO_2 after treatment in 5% H_2 and 95% N_2 at 550°C for ten minutes (a), which induced the formation of a TiO_x SMSI crystalline bilayer, and after treatment in $20CO_2$:$2H_2$ at 250°C for three hours (b), which caused the formation of an amorphous A-SMSI overlayer. The images were collected at atmospheric pressure. (Data is from "Adsorbate-mediated strong metal–support interactions in oxide-supported Rh catalysts." Nature Chemistry, published online)

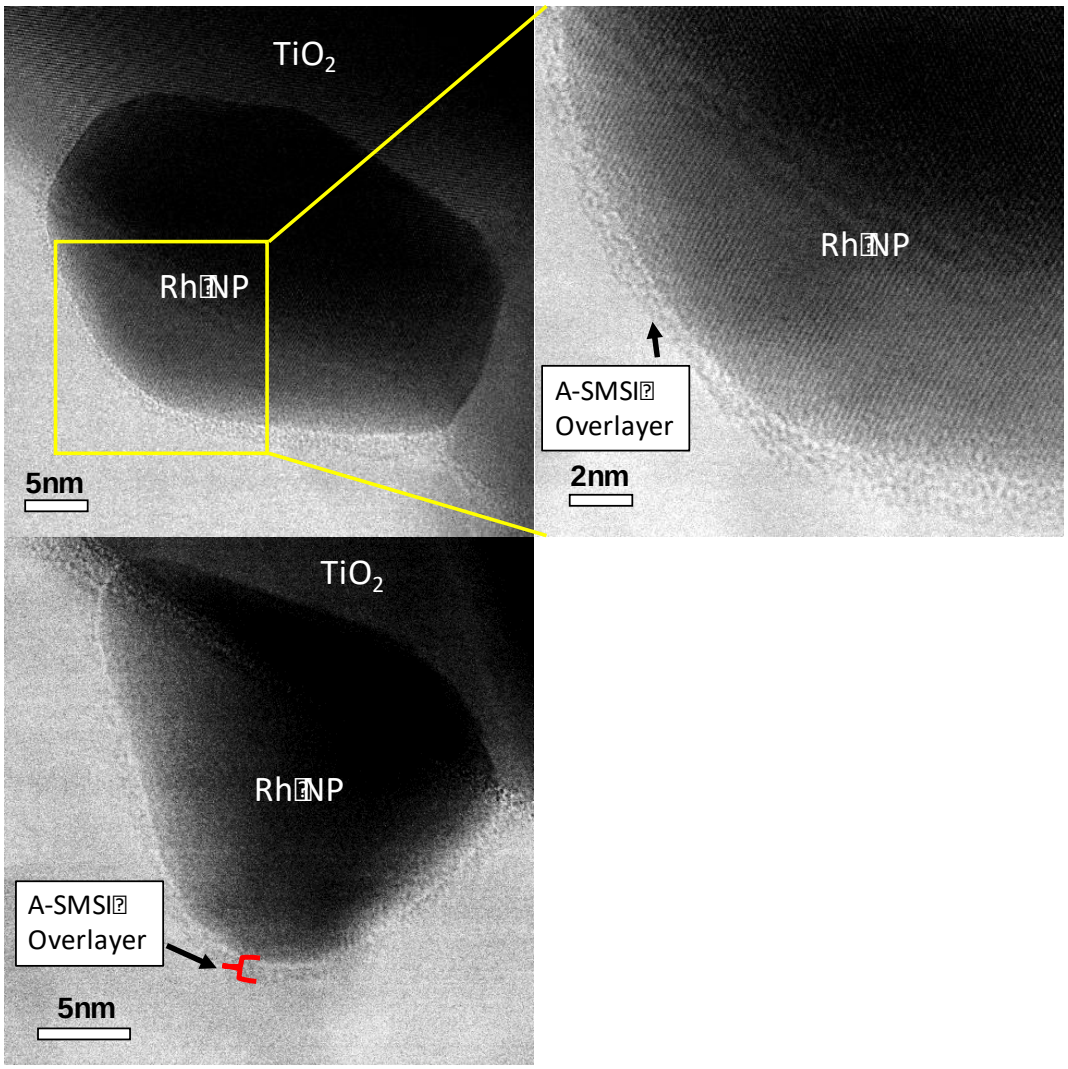

Figure 2.18. More examples showing the amorphous A-SMSI overlayer denoted by the red bracket is observed on the Rh nanoparticles (NP) after 4hrs treatment under $20CO_2$:$2H_2$: $78N_2$. These images, along, with Figure 2.17 suggest that treating a Rh/TiO_2 with the $20CO_2$:$2H_2$ treatment reduces the TiO_2 support, causing migration onto Rh and formation of an overlayer covering the Rh NP's via a different mechanism than the typical high temperature H_2 induced SMSI. (Data is from "Adsorbate-mediated strong metal–support interactions in oxide-supported Rh catalysts." Nature Chemistry, published online)

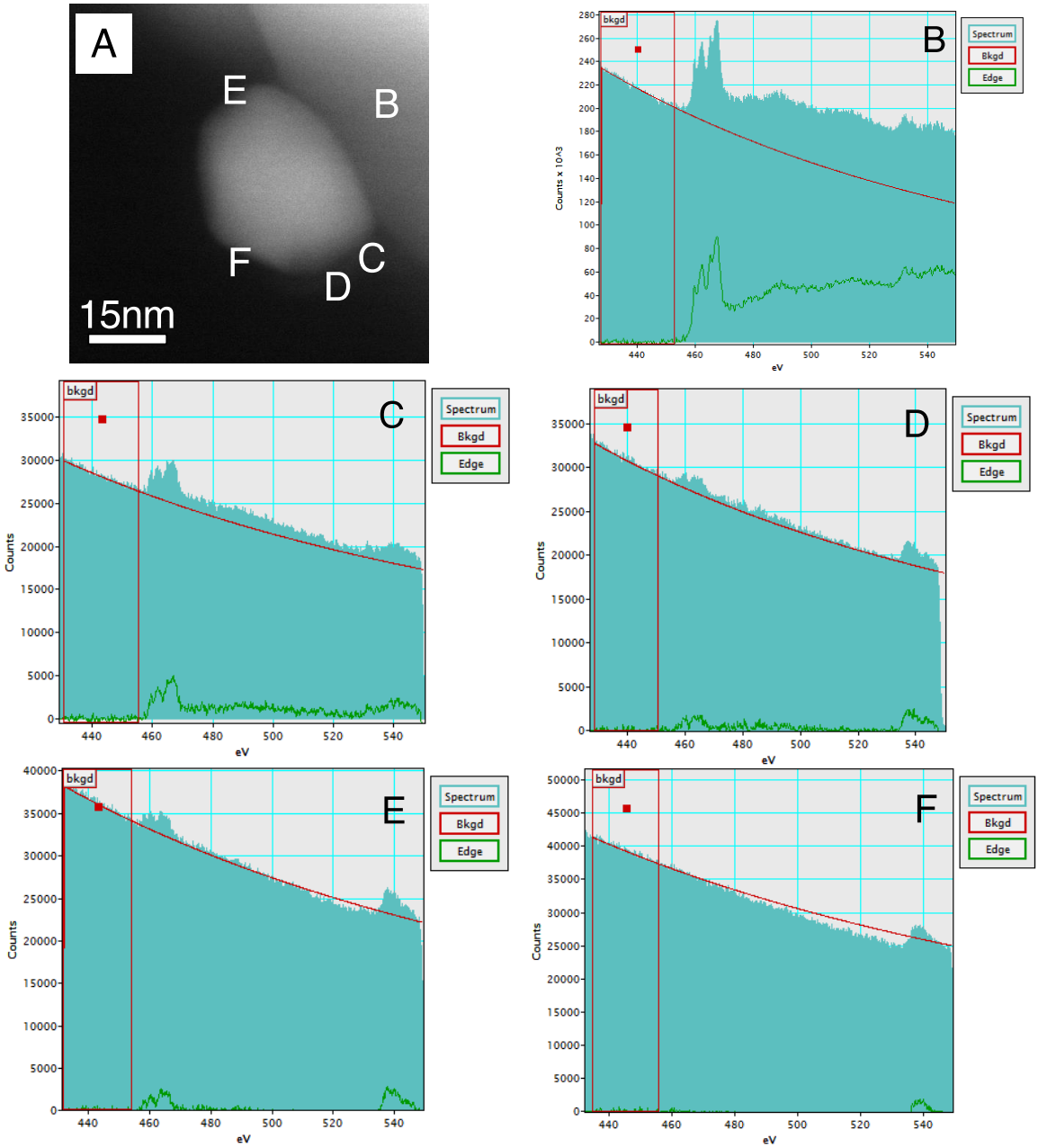

Figure 2.19 *In-situ* HAADF image and corresponding EELS data on different spots. (A) HAADF image of (800 ˚C-sintered) 6% Rh/TiO_2 sample, after 250 ˚C 20CO_2:2H_2 conditions for 4 hours. This HAADF image serves as a map for EELS analysis with the letters (B-F) identifying the position of collected EELS spectra in (B-F). The EELS spot size is 1-1.5 Angstroms. B) Ti L edge showing Ti^{4+} in the TiO_2 support. C) Ti present on the shoulder of the particle. Multiple Linear Least Squares (MLLS) fitting based on standard spectra from $SrTiO_3$ and $LaTiO_3$ indicated that 31% of the Ti was Ti^{3+} and 69% was Ti^{4+}. There was a Ti L edge also found on spots D and E, but not on F. The particle may have been partially covered or the concentration of Ti on the top of the particle (F) may have been below the detection limit of experimental configuration. Note: the sample was enclosed in two pieces of membrane with a total thickness of 80nm, likely attenuating the EELS signal. (Data is from "Adsorbate-mediated strong metal–support interactions in oxide-supported Rh catalysts." Nature Chemistry, published online.)

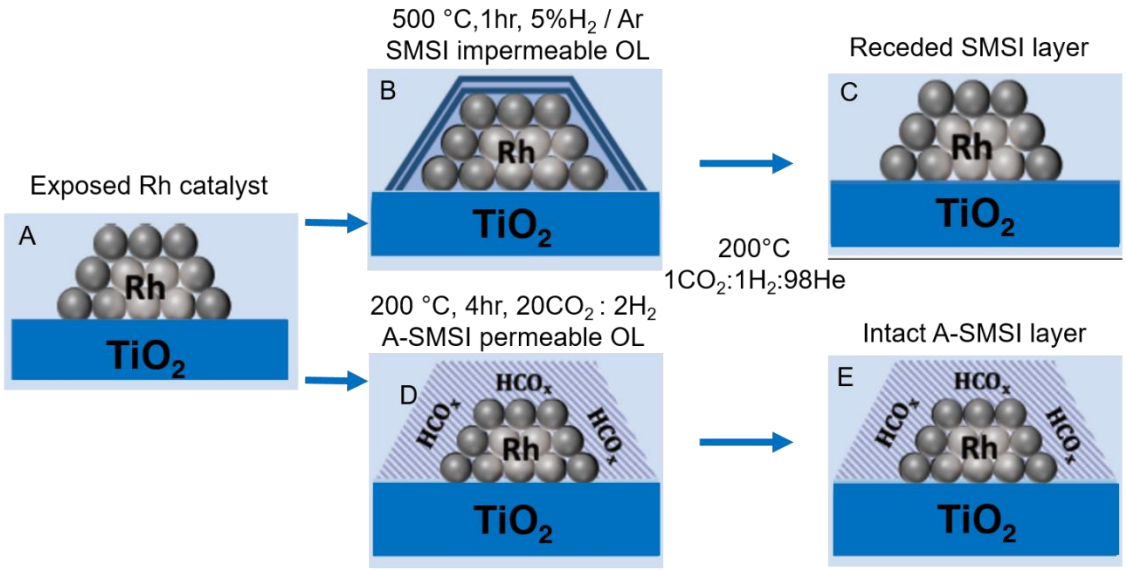

Figure 2.20 Comparison of SMSI and A-SMSI overlayer structure formation and stability. A, Schematic showing bare Rh particles on TiO_2 or Nb_2O_5 with exposed Rh sites that favour CH_4 production. B, Rh/TiO_2 after treatment with high-temperature (500°C) H_2 forms an impermeable SMSI overlayer. C, TiO_x SMSI overlayer recedes off Rh when exposed to CO_2-reduction conditions because of H_2O-induced re-oxidation of TiO_x to TiO_2. The catalytic behaviour in C is nearly identical to that in A. D, $20CO_2$:$2H_2$-treated catalyst that forms a permeable A-SMSI overlayer composed of TiO_x species and HCO_x. E, The stable A-SMSI overlayer under CO_2-reduction conditions modifies the Rh catalytic behavior. OL, overlayer. (Data is from "Adsorbate-mediated strong metal–support interactions in oxide-supported Rh catalysts." Nature Chemistry, published online)

Chapter III

Dynamic structural evolution of $Pd@CeO_2$ core shell catalyst

3.1 Introduction

Methane (CH_4) is the largest constituent of natural gas and is widely used in power generation and in other heating applications. However, it's also a greenhouse gas with an effect that is 20 times higher than that of CO_2. Current emissions-control catalysts are ineffective at reducing concentrations of CH_4 at low temperature and results in the emission of toxic nitrogen oxides (NO_x) and CO at high temperature.

Over the past several years, attention has increasingly been focused on efforts to engineer catalysts at the nanometer scale. These efforts have succeeded in generating a number of interesting and significant results, both in terms of the ability to synthesize new materials and to realize novel functionality. A recent example is the solution-based assembly of units composed of a Pd core and CeO_2 shell[1], which when homogeneously deposited onto a functionalized-alumina support, yield a unique methane combustion catalyst[2].

Core–shell structures, such as noble-metal (Ag, Au, Pd, Pt) particles in a carbon sphere[3], Pt@CoO yolk/shell nanoparticles[4], $Pt@mSiO_2$[5], and Au nanoparticles in hollow ZrO_2[6] and hollow SiO_2[7] spheres, comprise a broad class of nano-engineered catalysts. In cases where a solid metal core is encapsulated in an oxide shell, the goal has usually been to isolate the metal particles from each

other, in order to avoid sintering, while keeping active sites accessible. In the case of the Pd@CeO_2 catalyst[1, 2, 8], another goal was to ensure intimate contact between a central Pd nanoparticle and a surrounding shell, made of comparably sized CeO_2 nanocrystals, in order to promote more efficient total oxidation of methane.

Cargnello et al.[2] reported a unique core shell catalyst where one Pd nanocrystal forms the core and eleven CeO_2 nanocrytals form the shell. The preorganised core shell structure was further deposited onto hydrophobic alumina through Si-O-Al bonding and the corresponding schematic is shown in Figure 3.1. The Pd@CeO_2/H-Al_2O_3 catalysts exhibit exceptional catalytic performance for combustion of CH_4 ($CH_4 + 2O_2 \rightarrow CO_2 + 2H_2O$) when compared with two references sample. One is 1 wt % Pd on a CeO_2 support, prepared by optimized incipient wetness impregnation (denoted as Pd/CeO_2-IWI). The other is prepared by impregnation of Pd (at 1 wt %) and CeO_2 (at 9 wt %) from their nitrate salts onto pristine alumina (denoted as Pd/CeO_2/Al_2O_3-IMP). Pd@CeO_2/H-Al_2O_3 catalyst achieved complete conversion of CH_4 for a gas stream of 0.5 volume % CH_4 and 2.0 volume % O_2 in Ar at a space velocity of 200,000 ml g^{-1} $hour^{-1}$ at about 400°C as shown in Figure 3.2. By comparison, all the other reference samples achieved complete CH_4 conversion only above 700°C, more than 300°C higher than that found with the Pd@CeO_2/H-Al_2O_3 catalyst. Even when compared to state-of-the-art Pd/CeO_2 systems under the same reaction conditions, the temperature of complete conversion is decreased by more than 130°C. The authors attribute the enhanced reactivity of the Pd@CeO_2/H-Al_2O_3 catalyst to the strong Pd-CeO_2 interaction of the core-shell Pd@CeO_2 units.

In an attempt to better understand the connection between structure and activity, we have performed a more detailed electron microscopy study of supported Pd@CeO_2, including planar forms of the catalyst, using state-of-the-art *ex-situ* and *in-situ* transmission electron microscopy (TEM) with sub-angstrom resolution. Our results reveal a wholly unexpected structural transformation that occurs upon air calcination at temperatures between 500 and 800 °C, in which a new phase of very highly dispersed palladium and ceria in intimate contact is formed. Based on the newly found structure, we propose an alternative explanation for the exceptional catalytic properties. This piece of work was published on Nat Commun 2015, **6**, 7778.

3.2 Experimental Methods

3.2.1 Material Synthesis*

The preparation of Pd@CeO_2 and its deposition onto Si-functionalized surfaces of Sasol TH100/150 alumina and yttria-stabilized zirconia single crystals was performed as described previously[2, 8]. All samples were initially calcined in laboratory air for 5h at either 500 or 800°C. The short (30min) 800°C *ex-situ* air calcination treatment, subsequently performed on the high surface-area sample that had initially been calcined at 500°C, was done using compressed air.

*Sample were synthesized by Chen Chen and Matteo Cargnello

3.2.2 TEM Specimen Preparation

High-surface-area samples were suspended in methanol with sonication and drop cast onto lacy carbon-on-copper grids (Pella). Cross-sectional and plan-view specimens of model planar samples were prepared by standard sample preparation methods. The model planar sample was first glued to a silicon sacrificial layer to protect the surface before diamond saw sectioning into small pieces,

followed by mechanical polishing with diamond lapping film and low-angle (3°) Ar ion milling at 3kV to electron transparency. Plan-view specimens were mechanically polished and ion milled from the substrate side only, thus no surface damage can be created.

3.2.3 Microscopy Characterization

Specimens were examined in a spherical aberration (C_S)-corrected JEOL JEM-2100F operated at 200keV, equipped with EDS detectors and Gatan image filters for EELS acquisition. *In-situ* observation was carried out on the same microscope using the Protochips Atmosphere system, which consists of a micro-electrical-mechanical systems (MEMS)-based closed cell, a heating holder and a gas delivery manifold. The sample was situated between two SiN windows, each of 30–50nm in thickness, with a 5mm gap in between. The purity of oxygen used in the in situ experiment was 99.9995%. All reported temperatures are based on the Protochips calibration.

3.3 Results and Discussion

3.3.1 High-Surface-Area Supported Pd@CeO_2 Samples

High-angle annular dark field (HAADF) images, obtained by scanning transmission electron microscopy (STEM) of a sample of Pd@CeO_2 supported on high-surface-area Si-functionalized Al_2O_3, following air calcination at 500 °C for 5h, are shown in Figure 3.3. Bright features of order 10 nm across, seen in Figure 3.3, are more clearly resolved in images taken at progressively higher magnification, Figure 3.3 b, c, which show that they consist of clusters of particles, each about 2-3 nm in diameter. Although the particles usually appear in clusters, of varying size and shape, some are also individually dispersed, such as those indicated by the arrow in Figure 3.3b. X-ray energy dispersive spectroscopy (EDS) (Figure 3.4) showed that clusters typically contain O, Al,

Si, Pd, and Ce, but the Pd/Ce ratio was found to vary from cluster to cluster. Lattice fringes, when evident, can usually be related to CeO_2.

For comparison, images obtained from a sample calcined in air at 800 °C for 5h are shown in Figure 3.3d-f. Although the low magnification images, Figure 3.3 a and d, look similar, images taken at progressively higher magnification, Figure 3.3e, f, show that the bright features are each comprised of only a few (1-3) larger (5-20 nm across) particles. Very small (less than 1 nm across) features, indicated by arrows in Figure 3.3f, were also observed. Pd typically did not appear in EDS spectra, taken at random points, shown in Figure 3.5, though some very large (10s of nm across) palladium particles were found.

3.3.2 Model Planar Supported Pd@CeO_2 Samples

In an attempt to simplify the characterization of the system, we examined samples of Pd@CeO_2 supported on the Si-functionalized surface of single crystals of yttria-stabilized zirconia (YSZ). A low magnification plan-view image of a sample air calcined at 500 °C for 5h, shown in Figure 3.6, indicates that the surface is fully coated by a layer of material. Progressively higher magnification images, shown in Figure 3.6b, c, reveal a relatively open structure of randomly packed particles, each 2-3 nm across. Lattice spacing, when observed, is usually characteristic of CeO_2, though spacing corresponding to Pd was occasionally found, as indicated in Figure 3.6c. Cross-sectional images, shown in Figure 3.6d-f, establish that the layer coating the surface is generally uniform in thickness and consists mainly of single particles of ceria (and some palladium), each about 2-3 nm across. The 1-2 nm apparent gap between this layer and the YSZ surface is due to the Si interlayer, according to EDS. EDS results, obtained from somewhat thicker regions of the layer, also

confirmed the composition of palladium and ceria particles, inferred on the basis of lattice spacing, as shown in Figure 3.6f. The valence state of Ce in this sample is 3+, according to EELS (Figure 3.7 a,b).

Plan-view images of a sample air calcined at 800 °C for 5h, shown in Figure 3.8 a-c, provide evidence of two distinct types of features, one with relatively large dimensions, and the other with very small dimensions. The large features are typically 10-20 nm across. EDS confirmed that the brighter parts of these features (some of which are indicated by arrows in Figure 3.8b), typically 10 nm across, are comprised of palladium, with ceria comprising the remainder (Figure 3.9). The number of Pd-containing features is relatively small, as shown in Figure 3.8b. In addition to these features, the lower magnification images, Figure 3.8 a,b, reveal that the surface has one of two distinct appearances, regions of either uniform low or high brightness (in HAADF). The large features are typically found at either the boundaries or entirely within the regions of low brightness, which are rich in Si (Figure 3.10). The very small features, less than 1 nm across, are usually uniformly dispersed in areas of high brightness, as shown in Figure 3.8c. Cross-sectional bright field (BF) images of this sample, such as that in Figure 3.8d, show that most of the 10-20 nm ceria and palladium particles are covered by a thick layer rich in Si, according to EDS. The valence state of Ce in this sample is 4+ (Figure 3.7 c, d).

3.3.3 High-Surface-Area Supported Pd@CeO_2 samples – Extended Calcination and *In-Situ* Observations

The presence of very small (1 nm across) features, found in both samples calcined at 800 °C but in neither of the samples calcined at 500 °C, prompted an examination of the effect of a short (30

min) 800 °C *ex-situ* air calcination treatment on the high-surface-area supported Pd@CeO_2 sample that had been calcined at 500 °C. Surprisingly, this treatment caused the entire sample to become covered by a very high population of atomic-scale species that were not initially present. A comparison of the sample before and after the extended calcination is shown in Figure 3.11 a,b.

In order to better understand this process and the other transformations that occur in samples calcined at elevated temperatures, we conducted an *in-situ* calcination treatment with 150 Torr of pure oxygen (comparable to the 20% concentration of oxygen in air at atmospheric pressure) in the TEM, using a novel sealed gas cell sample holder. For temperatures below 500 °C, typical clusters of 2-3 nm particles (mostly ceria nanocrystals) remained totally stable, but when the temperature reached 500 °C, a drastic structural transformation, shown in the sequential set of images in Figure 3.11c, commenced. The atoms on the corners of the smaller and more isolated particles first became mobile and started to leave the cluster. As indicated by the solid and dashed yellow arrows on the images at 7 and 10 minutes, respectively, a relatively small particle then began to dissociate into a "cloud" of atomic-scale species, followed by the dissociation of three more non-overlapping particles, indicated by the circles on images at 10 and 22 minutes. With increasing time, more crystallites shrank and dissociated, as indicated by other pairs of arrows of the same color on the sequential images in Figure 3.11c, until the majority of particles in this cluster had transformed into atom "clouds" after about an hour. Since the alumina surface was Si-functionalized, it seems likely that a silica layer is involved in the stabilization of these atomic-scale "clouds". In fact, atom "clouds" were not observed in analogous experiments performed on samples that did not contain Si (Figure 3.12).

As the temperature of the sample in the gas cell was increased toward 650 °C, other dynamical processes were also observed, as shown in Figure 3.13. In this example, the two particles in the dashed square are initially of equal size, with the lower one surrounded by a "cloud". The contraction of the "cloud", accompanied by the growth of the lower particle with time can be clearly seen in the sequential images between 15-21 minutes. Concurrently, the particle appears to rotate and change shape in an attempt to minimize its surface energy, until it finally becomes a truncated octahedron bound by eight planes (the lowest surface energy plane) and six planes. This state is well accepted as the most stable shape for CeO_2 nanoparticles of this size[9, 10]. Eventually, the two crystallites coalesce, driven by the tendency to lower overall surface energy. Many such examples of particle coalescence were observed, resulting in CeO_2 particles of 5-10 nm in diameter. However, very small (1-2 nm) features, similar to those observed in samples after *ex-situ* calcination at 800 °C for 5h, remained throughout the sample, as shown in Figure 3.13b. The total heating time of the *in-situ* experiment was about 250 minutes (Figure 3.14).

3.3.4 Discussion

In our attempt to better characterize Pd@CeO_2 supported on Si-functionalized alumina, the use of a novel *in-situ* electron microscopy technique has allowed us to observe the dynamics of structural transformations that occur under an oxidizing atmosphere. *Ex-situ* examination of samples calcined for 5h at 500 °C show that the Pd@CeO_2 structures are initially formed of a mixture of 2-3 nm palladium and ceria crystallites, generally in close proximity, where Pd is hard to unequivocally discern by lattice spacing or contrast difference. Samples calcined for 5h at 800 °C contain both large palladium and ceria particles, typically 5-20 nm across, as well as very small entities, less than 1 nm across, most likely derived from ceria, but possibly also including

palladium. A short *ex-situ* calcination of the 500 °C sample at 800 °C generates many atomic species, well dispersed on the support.

Observations made on the model planar sample calcined at 800 °C show that large numbers of the very small entities may coexist with the large ceria and palladium particles. These observations also suggest that a highly dispersed form of atomic-scale species may have appeared first, and that the larger particles subsequently grew by consumption of this material in their immediate vicinities. This suggestion is supported by comparison of the number of Ce atoms that would have occupied regions of low brightness, assuming these regions originated from a monolayer of ceria particles, 2-3 nm in diameter, and the number of Ce atoms contained in the large ceria particles within their perimeters. As an example, these numbers agree to within a factor of 2 for the region indicated by the oval in Fig. 3b: $3x10^5$ Ce corresponding to a monolayer of ceria particles covering the low brightness region vs. $5x10^5$ Ce within the large ceria particles.

Such a scenario is actually demonstrated by the *in-situ* observations, where dynamic processes were followed in real time: Single atoms are released by smaller crystallites at 500 °C in 150 Torr oxygen and then stabilize in the form of atom "clouds" with low mobility, where silica likely plays some role, either structurally or chemically. However, the "clouds" become energetically unfavorable at higher temperature. Atomic species or clusters either add onto some relatively larger particles in close proximity, or nucleate into the very small entities if a large particle is not nearby. The above *in-situ* results thus provide insight into the formation of the atomic-scale species and the very small entities observed in samples after *ex-situ* calcination. Although the origin of this phenomenon is not yet fully understood, we propose that it essentially reflects the

thermodynamic favorability of compound formation between the ceria nanocrystals, which exhibit significant Ce^{3+} character, and the silica in close proximity. The stability of Ce^{3+} in these particles under oxidizing conditions may be related to excess oxygen vacancies in nano-scale ceria, which has been reported by several groups[8, 11-13]. Similar arguments have been made concerning the surface-to-bulk ratio and valence state change from 4+ to 3+ when the thickness of the wall of ceria nanotubes change from 10 nm to 5 nm[13]. In any case, initiation of such a reaction between ceria and silica could be facilitated by the lower cohesive energy of the ceria particles, arising both from their high surface area and excess surface oxygen vacancies. It has been shown in other studies that one such compound, $Ce_{9.33}(SiO_4)_6O_2$, tends to gradually decompose back into a mixture of nano-scale ceria and silica as temperature is increased to about 800 °C in air[14, 15]. Such decomposition and phase separation is consistent with our observation of the eventual growth of large particles and the appearance of Si-rich deposits around them in the model planar sample calcined at 800 °C.

While it is clear that the very small entities exist in both powder and model planar catalyst samples, calcined at 800 °C, we propose that a high concentration of the atom-scale species, seen most clearly in the model planar sample, is also present in the powder sample. In contrast, the 2-3 nm ceria and palladium particles do not survive the 800 °C calcination treatment. The structure of supported $Pd@CeO_2$ thus evolves as shown in Figure 3.15, according to all of our new observations. At the low temperature extreme, this structure bears some resemblance to the core-shell structure, since 2-3 nm particles of ceria and palladium may be intimately mixed together, but at the high temperature extreme, which corresponds closely to the calcination treatment used for the previously reported methane combustion experiments (850 °C)[2], the structure consists of

essentially two distinct forms, a mixture of coarse particles of ceria and palladium, that should be characterized by conventional catalytic behavior, and a new structure in which ceria, palladium, and silica are all present in a very highly dispersed form. It would thus appear that the unique catalytic properties arise from the new structure. A question that remains unanswered is the precise composition and structure of the material comprised of the atomic-scale species. It has been reported that Pd-doped ceria-zirconia, or ionic Pd incorporated into the surface of ceria, can inhibit the PdO-Pd transformation[16-18], which plagues the conventional methane combustion catalyst[2]. It is possible that the material in our newly found structure contains ionic Pd bonded to ceria in such a fashion. Post-reaction TEM examination, or *in-situ* TEM studies performed under methane combustion conditions, could provide useful tests of this hypothesis.

3.4 Summary

In an attempt to better understand the connection between structure and activity, we perform a detailed electron microscopy study of supported $Pd@CeO_2$, including planar forms of the catalyst, using state-of-the-art *ex-situ* and *in-situ* transmission electron microscopy (TEM) with sub-angstrom resolution. Our results reveal an unexpected structural transformation that occurs upon air calcination at temperatures between 500°C and 800°C, in which a phase of very highly dispersed palladium and ceria in intimate contact is formed, which may be account for the unique catalytic property. This finding may open new perspectives about the origin of the activity of this catalyst.

3.5 References

1. Cargnello, M.; Wieder, N. L.; Montini, T.; Gorte, R. J.; Fornasiero, P. *J. Am. Chem. Soc.* **2009,** 132, (4), 1402-1409.

2. Cargnello, M.; Jaén, J. D.; Garrido, J. H.; Bakhmutsky, K.; Montini, T.; Gámez, J. C.; Gorte, R.; Fornasiero, P. *Science* **2012,** 337, 713-717.

3. Sun, X.; Li, Y. *Angew. Chem. Int. Ed.* **2004,** 43, 597-601.

4. Yin, Y.; Rioux, R. M.; Erdonmez, C. K.; Hughes, S.; Somorjai, G. A.; Alivisatos, A. P. *Science* **2004,** 304, 711-714.

5. Joo, S. H.; Park, J. Y.; Tsung, C. K.; Yamada, Y.; Yang, P.; Somorjai, G. A. *Nat Mater* **2009,** 8, 126-31.

6. Arnal, P. M.; Comotti, M.; Schüth, F. *Angew. Chem.* **2006,** 118, 8404-8407.

7. Lee, J.; Park, J. C.; Song, H. *Adv. Mater.* **2008,** 20, 1523-1528.

8. Adijanto, L.; Bennett, D. A.; Chen, C.; Yu, A. S.; Cargnello, M.; Fornasiero, P.; Gorte, R. J.; Vohs, J. M. *Nano Lett.* **2013,** 13, 2252-7.

9. Wang, Z. L.; Feng, X. *The Journal of Physical Chemistry B* **2003,** 107, (49), 13563-13566.

10. Zhang, F. *J. Appl. Phys.* **2004,** 95, 4319.

11. Reddy, B. M.; Khan, A.; Lakshmanan, P.; Aouine, M.; Loridant, S.; Volta, J.-C. *The Journal of Physical Chemistry B* **2005,** 109, 3355-3363.

12. Tschöpe, A. *J. Electroceram.* **2005,** 14, 5-23.

13. Han, W.-Q.; Wu, L.; Zhu, Y. *J. Am. Chem. Soc.* **2005,** 127, 12814-12815.

14. Kępiński, L.; Wołcyrz, M.; Marchewka, M. *J. Solid State Chem.* **2002,** 168, 110-118.

15. Rocchini, E.; Trovarelli, A.; Llorca, J.; Graham, G. W.; Weber, W. H.; Maciejewski, M.; Baiker, A. *J. Catal.* **2000,** 194, 461-478.

16. Primavera, A.; Trovarelli, A.; de Leitenburg, C.; Dolcetti, G.; Llorca, J. *Stud. Surf. Sci. Catal.* **1998,** 119, 87-92.

17. Priolkar, K.; Bera, P.; Sarode, P.; Hegde, M.; Emura, S.; Kumashiro, R.; Lalla, N. *Chem. Mater.* **2002,** 14, 2120-2128.

18. Colussi, S.; Gayen, A.; Farnesi Camellone, M.; Boaro, M.; Llorca, J.; Fabris, S.; Trovarelli, A. *Angew. Chem. Int. Ed.* **2009,** 48, 8481-8484.

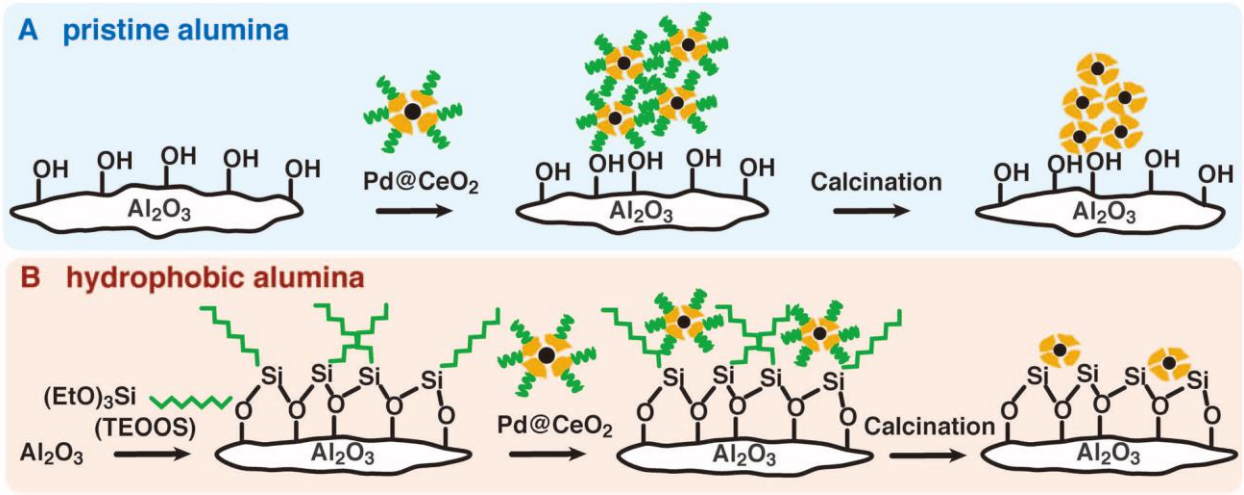

Figure 3.1 Schematic representation of the agglomeration of $Pd@CeO_2$ structures when using the pristine alumina (A) and their deposition as single units after treatment of the same support with triethoxy(octyl)silane (TEOOS) (B).(Figure is extracted from Cargnello, M et al., P. *Science* **2012,** 337, 713-717 with permission).

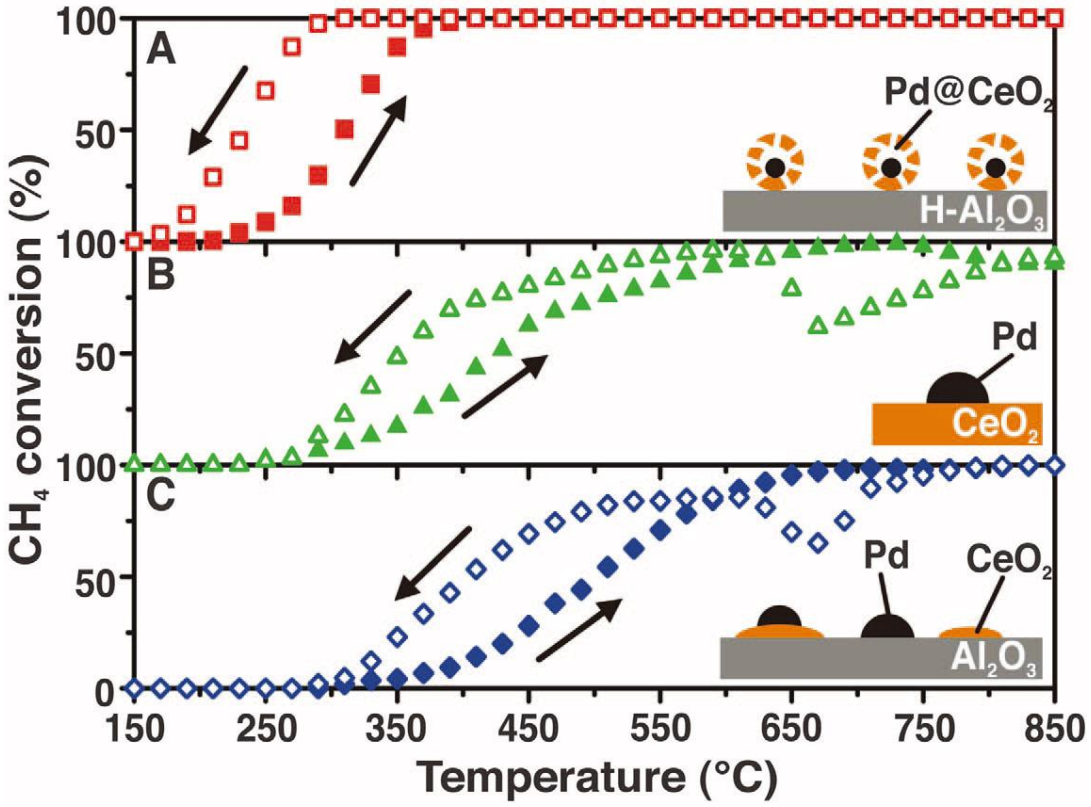

Figure 3.2 Heating and cooling (10°C min^{-1}) light-off curves of CH_4 conversion against the temperature for the three catalyst formulations used. (A) Pd@CeO_2/H-Al_2O_3 core-shell catalyst, (B) Pd/CeO_2-IWI, and (C) Pd/CeO_2/Al_2O_3-IMP (Data is extracted from Cargnello, M et al., P. *Science* **2012,** 337, 713-717 with permission.)

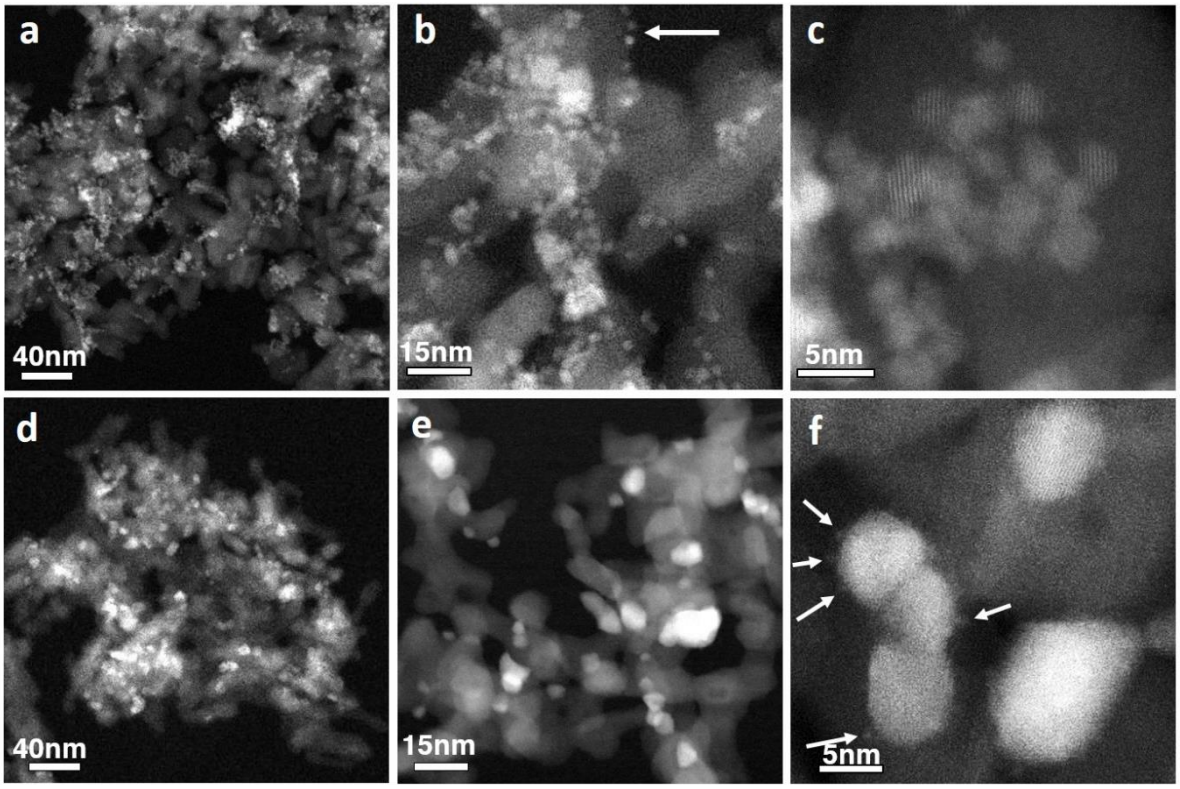

Figure 3.3 HAADF images of the high-surface-area alumina-supported Pd@CeO_2 sample. (a-c) calcined at 500 °C and (d-f) calcined at 800 °C, both for 5h. The brighter features are either Pd or CeO2 particles while the darker background is Al_2O_3.
(Images are from Nat Commun 2015, **6**, 7778.)

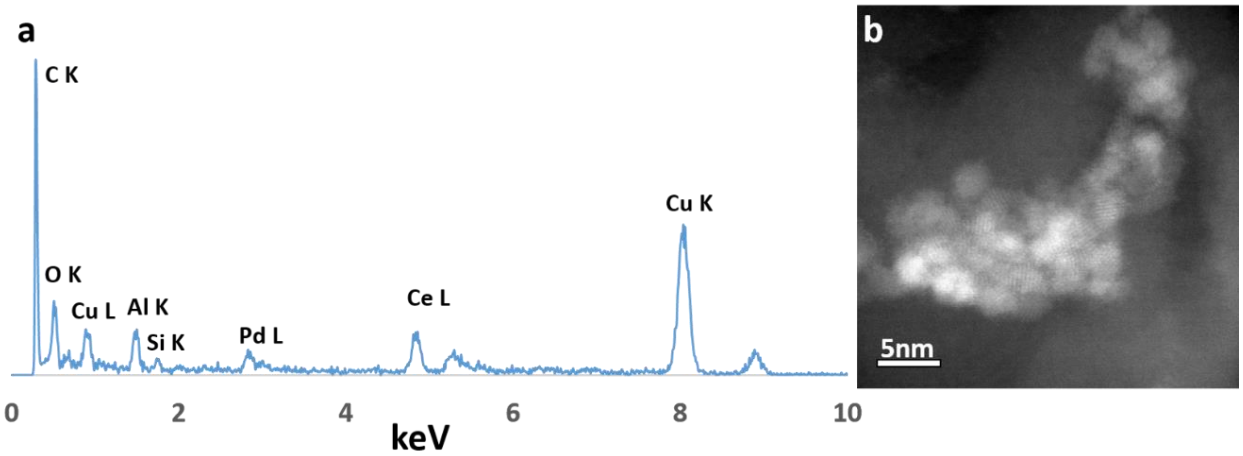

Figure 3.4 A typical EDS spectrum showing the composition of the high-surface-area Si-functionalized Al_2O_3 -supported Pd@CeO_2 sample calcined at 500 °C. The spectrum in (a) was acquired from the region shown in the HAADF image in (b). (The Cu signal arises from the TEM grid, which may also be the source of C.) (Images are from Nat Commun 2015, **6**, 7778.)

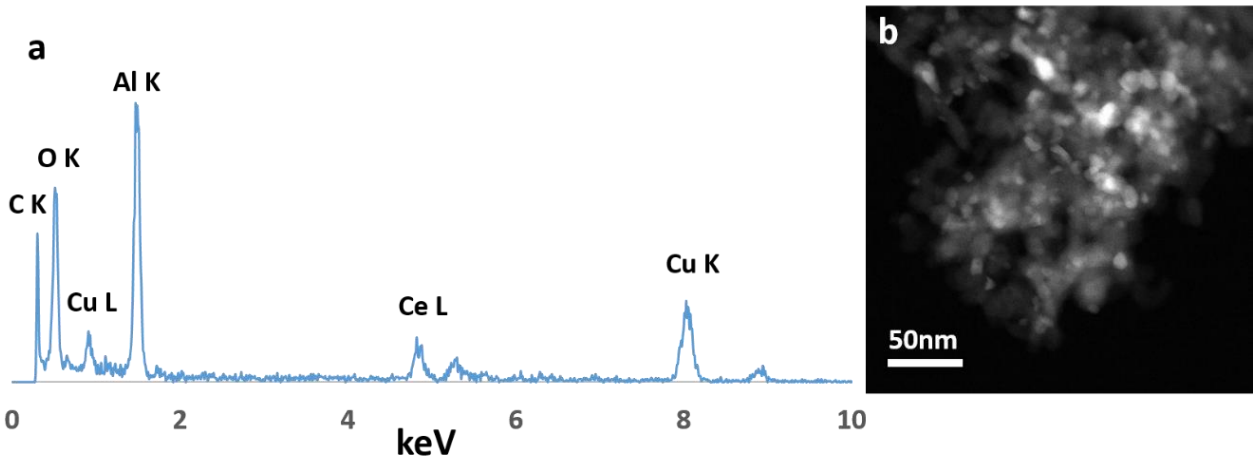

Figure 3.5 A typical EDS spectrum showing the composition of the high-surface-area Si-functionalized Al_2O_3 -supported Pd@CeO_2 sample calcined at 800 °C. The spectrum in (a) was acquired from the region shown in the HAADF image in (b). (Images are from Nat Commun., 2015, **6**, 7778.)

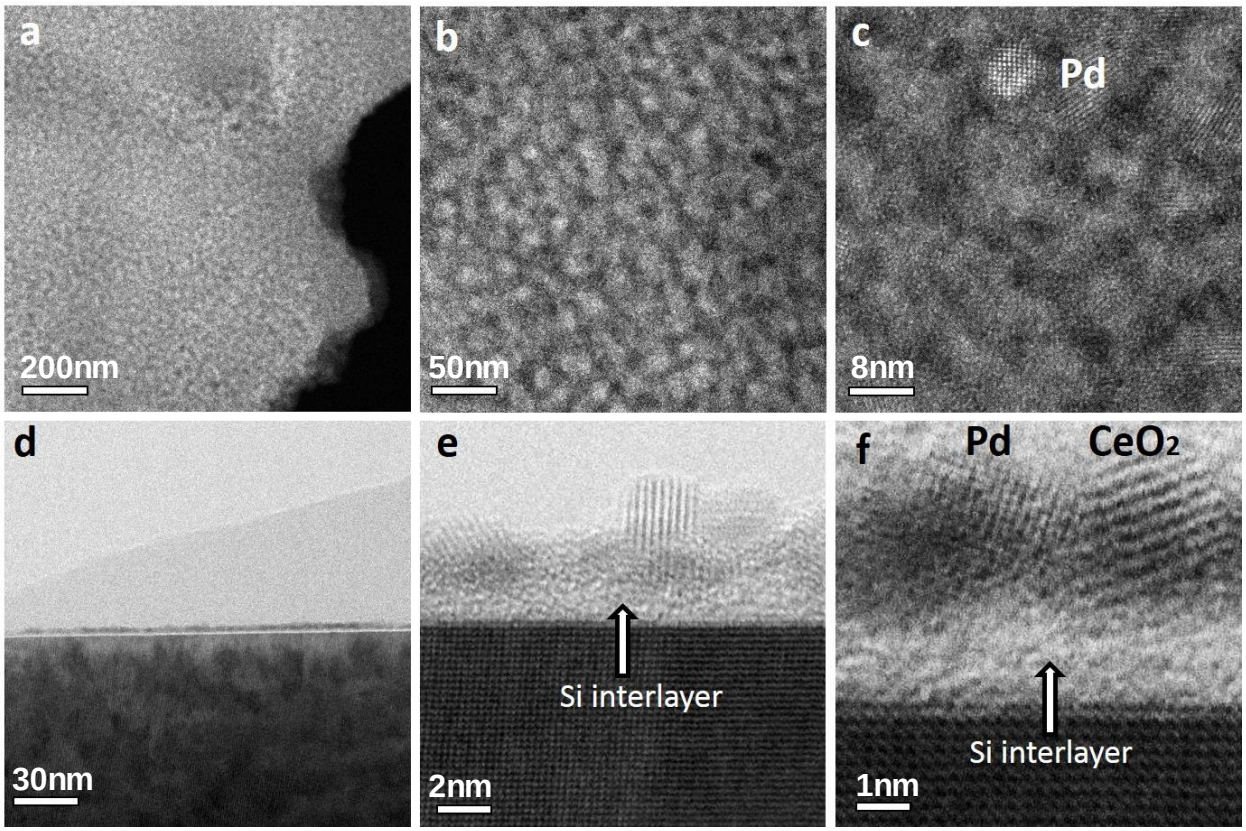

Figure 3.6 Images of the model planar YSZ-supported Pd@CeO_2 sample calcined at 500 °C. (a–c) Plan-view HAADF images and (d–f) cross-sectional bright-field images. Scale bars, 40nm (a), 8nm (b), 3nm (c), 30nm (d), 2nm (e) and 1nm (f). (Images are from Nat Commun., 2015, **6**, 7778.)

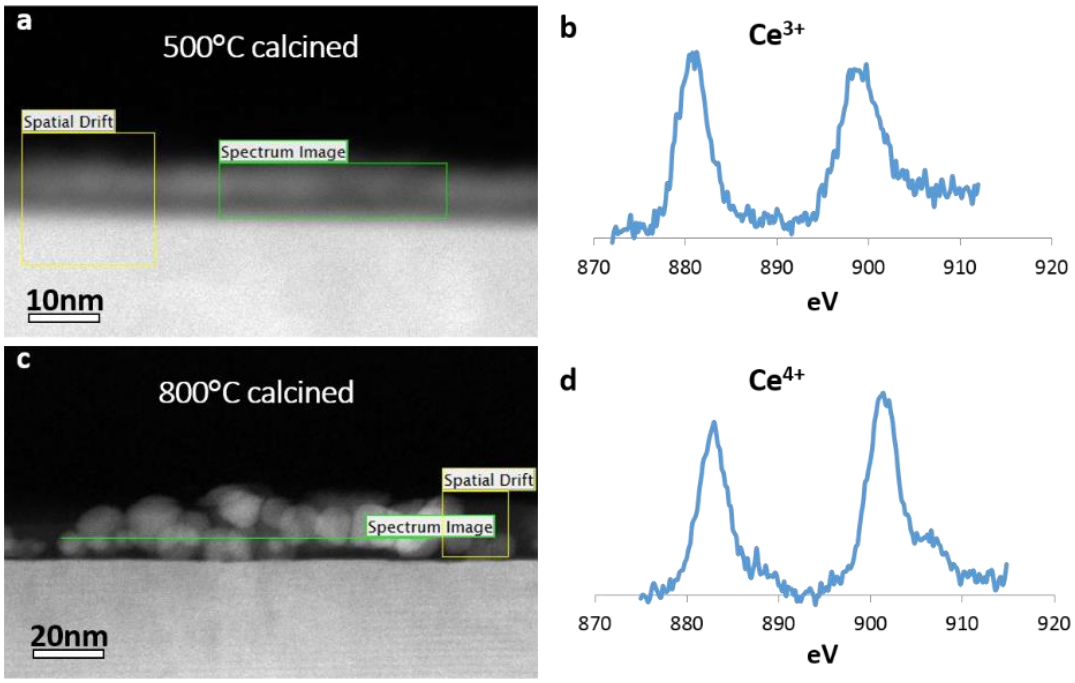

Figure 3.7 EELS spectra from cross-sectional specimens of model planar Si-functionalized YSZ-supported Pd@CeO_2 samples calcined at 500 °C and 800 °C, showing the typical 3+ and 4+ spectral signatures. The spectrum in (b) and (d) is extracted from the square or line labeled as "spectrum image" in (a) and (c), respectively. (Images are from Nat Commun., 2015, **6**, 7778.)

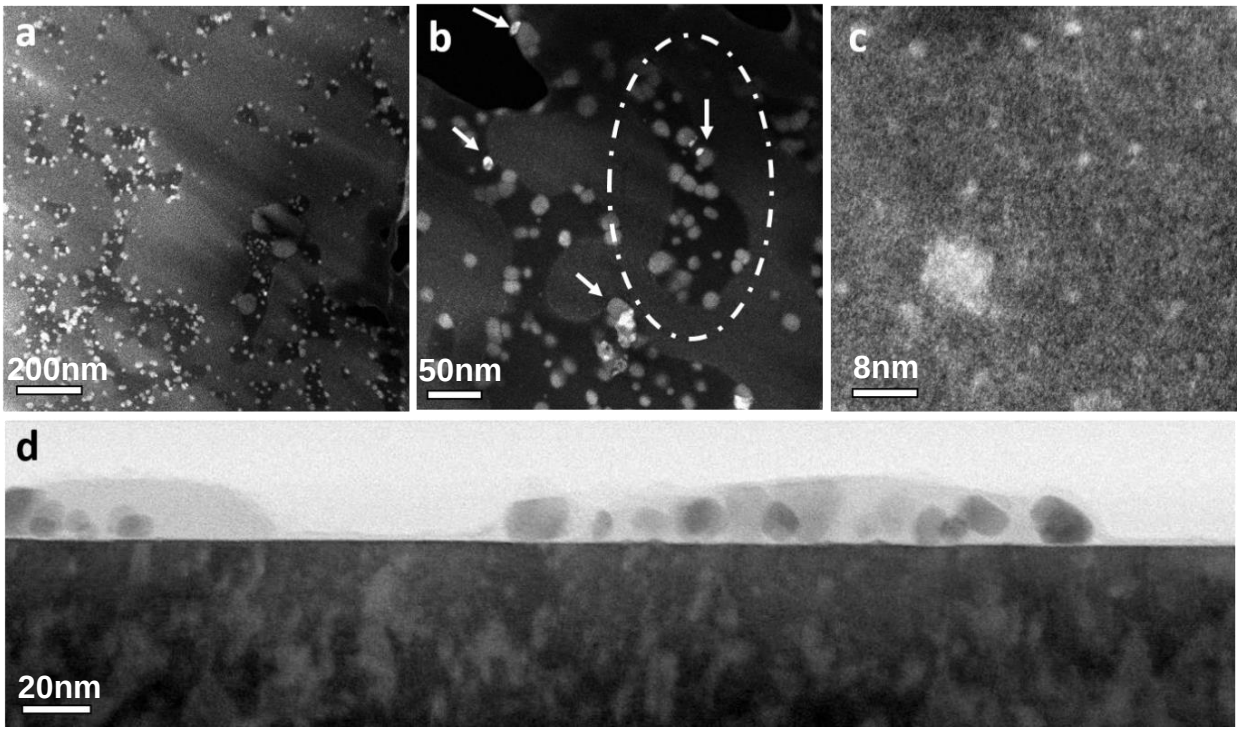

Figure 3.8 Images of the model planar YSZ-supported Pd@CeO2 sample calcined at 800 °C. (a-c) plan-view HAADF images and (d) cross-sectional BF image. The region encircled by the oval was used to calculate the number of Ce atoms, as detailed in the discussion section. Scale bars, 200 nm (a), 50 nm (b), 8 nm (c), 20 nm (d). (Images are from Nat Commun., 2015, **6**, 7778.)

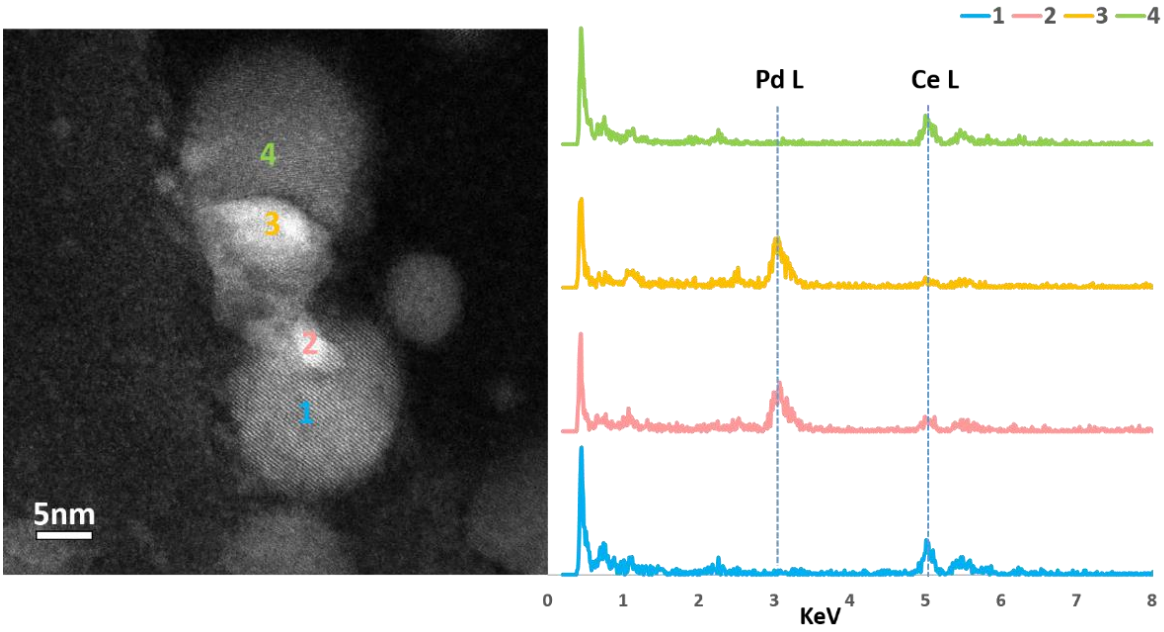

Figure 3.9 Typical EDS spectra showing the chemical composition of large particles in a plan-view specimen of the model planar Si-functionalized YSZ-supported Pd@CeO_2 sample calcined at 800 °C. The corresponding spots where the spectra were taken are marked in the HAADF image on the left. Generally, the brighter parts are rich in Pd, while the darker parts are rich in ceria. (Images are from Nat Commun., 2015, **6**, 7778.)

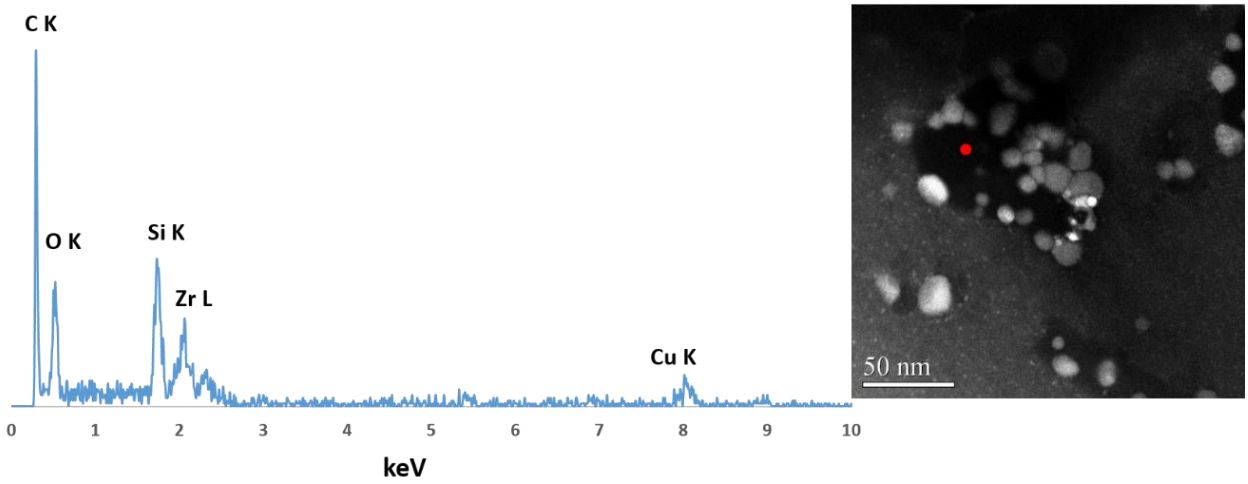

Figure 3.10 Typical EDS spectrum showing that the low brightness region of the plan-view specimen of the model planar Si-functionalized YSZ-supported Pd@CeO_2 sample calcined at 800 °C is rich in Si. The region where the spectrum was taken is marked by a red spot on the HAADF image at the right. This result corresponds well with similar results from cross-sectional specimens showing that the large particles are covered by a thick layer, rich in Si (Figure 3.8d). (Images are from Nat Commun., 2015, **6**, 7778.)

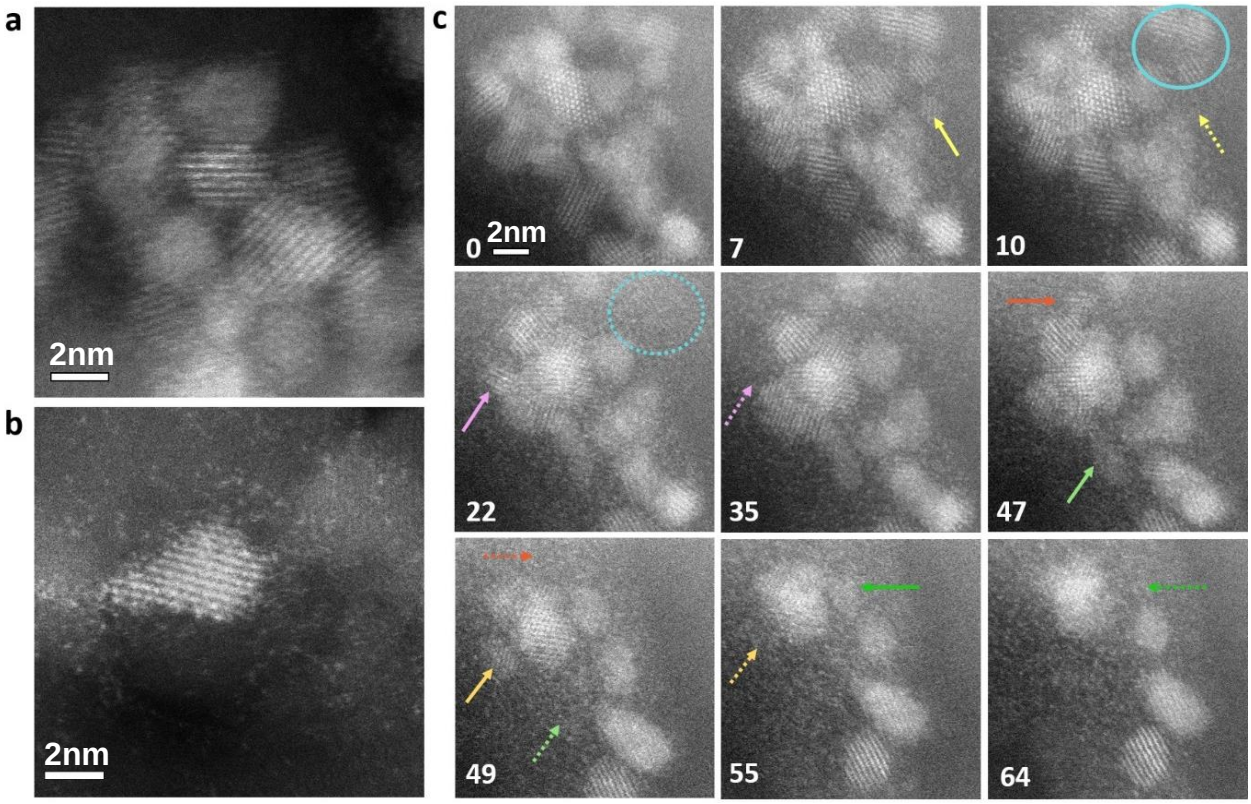

Figure 3.11 Formation of atomic species during extended calcination – *ex-situ* and *in-situ* observations. (a) Sample calcined at 500 °C (b) Sample calcined at 500 °C after 30 min extended ex-situ calcination at 800 °C, showing that a large number of atomic-scale species were generated. (c) Sequential images showing the dissociation of 2-3 nm particles and the formation of atom "clouds" during in-situ calcination at 500 °C in 150 Torr O_2. Elapsed time, in minutes, is indicated on the lower left corner of each image. Arrows of the same color are used to indicate the gradual disappearance of the small crystallites. (Images are from Nat Commun., 2015, **6**, 7778.)

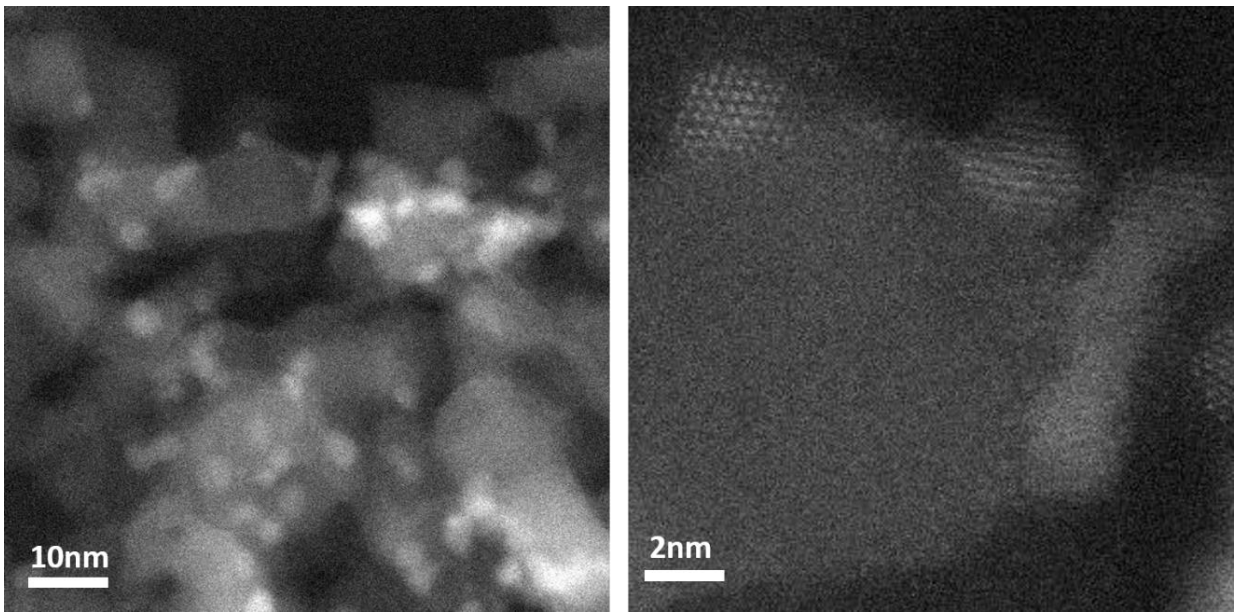

Figure 3.12 HAADF images acquired from Si-free sample at 500 °C in 150 Torr O_2. Atom "clouds" were not observed around the ceria particles, which are also typically larger than those in the Si-containing sample. Particles showing lattice fringes are CeO_2. (Images are from Nat Commun., 2015, **6**, 7778.)

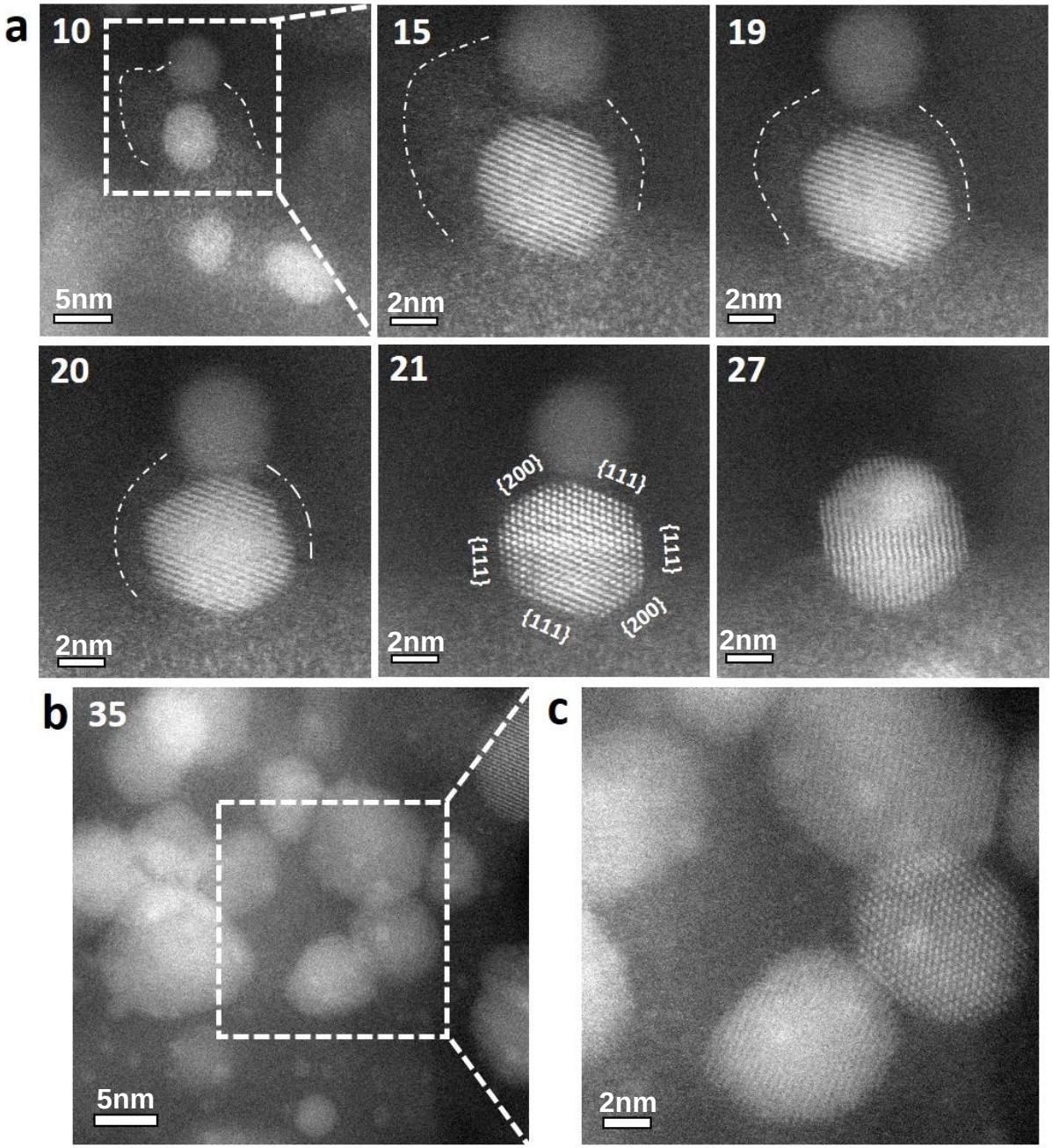

Figure 3.13 *In-situ* observation of disappearance of atom "cloud", particle growth, coalescence, and appearance of sub-nm features. (a) Sequential images taken at 650 °C in 150 Torr O_2, showing the gradual disappearance of an atom "cloud" accompanied by the growth of a particle in its close vicinity, followed by particle coalescence. The dashed line is used to delineate the periphery of the atom "cloud". The spacing between (111) lattice planes in the larger particle labeled "21", 3.1 Å, confirms it is CeO_2. (b) Appearance of sub-nm features in an image taken at a different area. Elapsed time, in minutes, is indicated on the upper left corner of each image. (Images are from Nat Commun., 2015, **6**, 7778.)

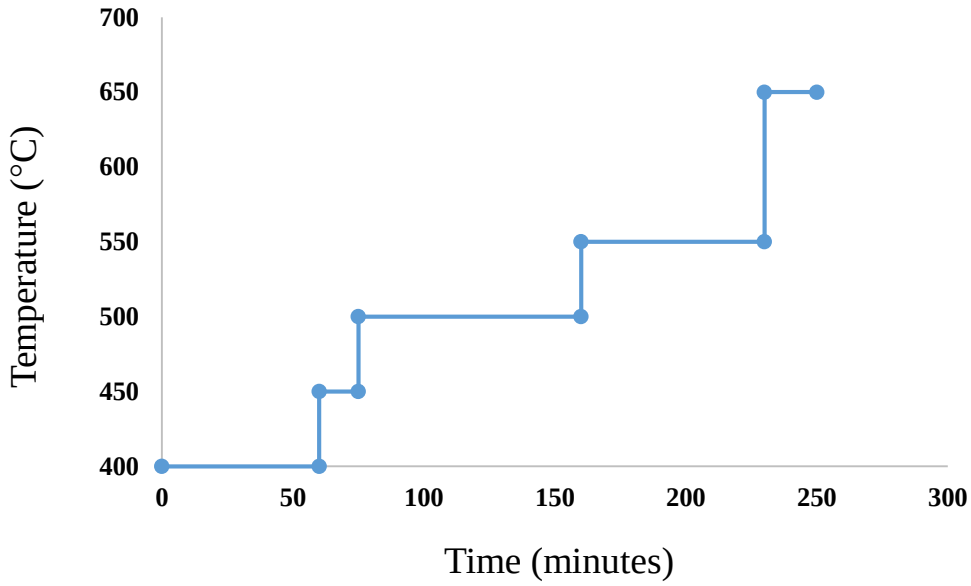

Figure 3.14 Heating profile during the *in-situ* observations. The *in-situ* calcination started at a nominal temperature of 400 °C and ended at 650 °C, with total heating time of about 250 min. (Images are from Nat Commun., 2015, **6**, 7778.)

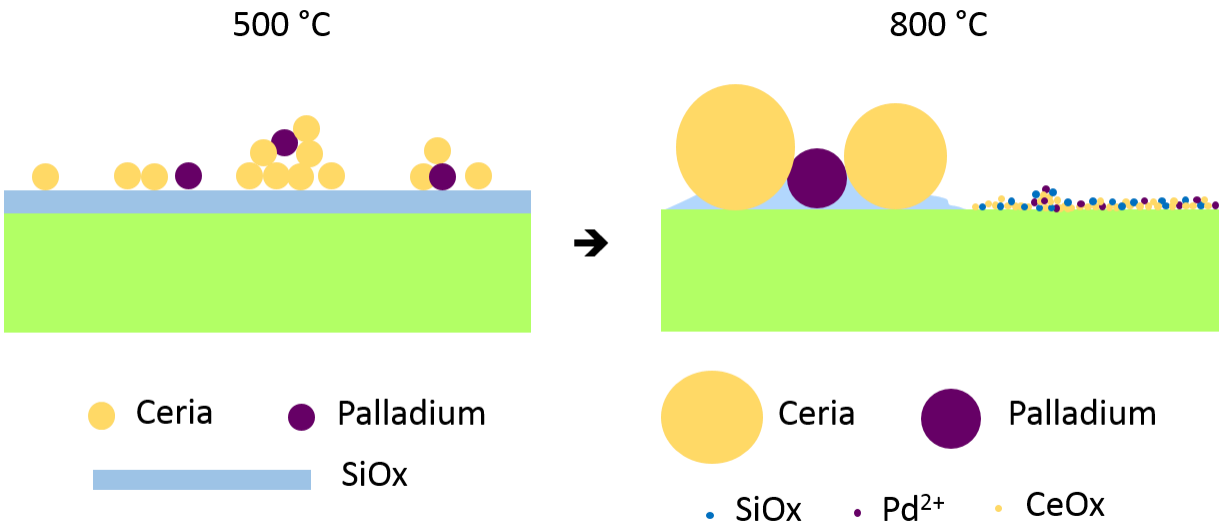

Figure 3.15 Overall structural transformation of Pd@CeO_2 core shell structure. Schematic showing that the original clusters of 2-3 nm particles evolve into a mixture of 5-20 nm particles and a new structure containing Ce, Pd, Si and O in a very highly dispersed form. (Images are from Nat Commun., 2015, **6**, 7778.)

Chapter IV

Sintering Mechanism of Pt Nanoparticles Supported on High-Surface-Area Alumina

4.1 Introduction and Background

Supported transition metal nanoparticles (NPs) find widespread applications in catalysts,[1-5] sensors,[6, 7] fuel cells,[8-10] and several other energy conversion devices.[6, 11, 12] In many of these applications, stable materials that sustain high temperatures without losing active surface area are required. This need is particularly important when precious metals are used, due to their dwindling supply and increasing demand that require NP growth over time to be mitigated as much as possible. The understanding of mechanisms involved in the growth of supported metal NPs is thus crucial, and despite the large body of work, still not complete. In particular, a detailed atomistic description of the processes taking place under conditions that are closest to the final applications is still missing.

The ability to clearly differentiate between the two most commonly mentioned deactivation phenomena, Ostwald ripening (OR) and particle migration and coalescence (PMC), is important to the design of more stable catalysts. Difficulty arises from the fact that samples in which particle size distributions are broad do not easily allow for discrimination between the two mechanisms, in which on one side single atom species participate in the particle growth (OR), and on the other the

entire particles merge to produce larger ones (PMC). Various observation techniques have been exploited in this sense. Indirect techniques, such as chemisorption or X-ray diffraction, typically applied to large ensembles of NPs, provide only averaged information about particle size distributions (PSDs). Direct measurement of PSDs by transmission electron microscopy (TEM), on the other hand, is plagued by the uncertainty of conclusions drawn from severely limited sample size in highly heterogeneous samples. Further, the validity of using the shape of the PSD to discriminate between the two main growth processes, has been questioned because similar log-normal distributions can satisfactorily fit both mechanisms of growth.[13] Efforts to characterize these processes on model supports using the environmental TEM, which allows for real-time observation, have been reported and greatly advanced the fundamental understanding,[14-18] but the material and pressure gaps inherent in such work still raise questions about whether the results hold true for conditions closer to realistic applications.

In the present study, we employ a recently developed *in-situ* TEM technique,[19-21] which can be used at atmospheric pressure, to identify the separate contributions of OR and PMC to the growth of mono-dispersed Pt NPs in high-surface-area Pt/Al_2O_3 catalysts under reducing conditions. The use of this technique on realistic samples eliminates both pressure and material gaps, thus allowing us to directly observe both processes separately in real time. Further, the use of mono-dispersed Pt NPs not only allows for the suppression of OR, as recently shown on a model planar support,[22] but also demonstrates the utility of this approach for controlling growth rates of supported metal NPs for potentially realistic applications. This piece of work was published in Journal of Catalysis, **2016**, 337, 240-247.

4.2 Experimental Methods

4.2.1 Material Synthesis*

Pt nanocrystals were synthesized by following established procedure with minor modifications.[5] All syntheses were performed using standard Schlenk techniques. $Pt(acac)_2$ (98%, Acros Organics) was used as metal precursor. Trioctylamine (TOA, 97%) was purchased from Acros. Oleylamine (OLAM, 70%), trioctylphosphine (TOP, 97%) and oleic acid (OLAC, 90%) were purchased from Sigma-Aldrich and used as received. 0.2 mmol of $Pt(acac)_2$ were mixed with oleylamine (2 mmol), oleic acid (8 mmol) in TOA (10 mL) and evacuated at RT for 5 minutes. Trioctylphosphine (0.1 mmol for smaller particles, 0.5 mmol for larger ones) was then added and the mixture evacuated further and heated to 120 °C for 30 minutes. The flask was flushed with nitrogen and heated very quickly (~ 40 °C min^{-1}) to 250 °C (smaller particles) or 350 °C (larger particles). After 30 minutes of reaction under continuous stirring, the solution was cooled to room temperature. The particles were isolated by addition of isopropanol and centrifugation (8000 rpm, 3 minutes). No size selection procedures were employed. The particles were soluble in low-polar solvents (hexanes, toluene, chloroform, THF) and were finally dissolved in toluene or hexanes for further analysis. It was found that a small volume of OLAM (50 μL) was generally needed to ensure the complete redissolution of the particles.

The high surface area alumina (Sasol TH100-150) was calcined to 900 °C for 24 h, and therefore stable under the condition utilized in our study. Stock solutions at known concentrations of Pt were prepared in hexanes and slowly added to a mixture of 200 mg of calcined alumina powder well dispersed in toluene (15 mL) by sonication. Adsorption of the particles occurs instantaneously, and the powder is isolated by centrifugation and dried at 120 °C overnight. Samples were prepared

with final nominal Pt loading of 0.5 wt% (0.25 wt% for each size in the mixed-size sample). Removal of the ligands was performed on the dried samples by following a fast thermal treatment at 700 °C for 30 s as recently reported.[23]

*Sample were prepared by Joshua Willis and Matteo Cargnello.

4.2.2 Microscopy Characterization

In-situ observations were carried out with a double spherical aberration-corrected microscope (JEOL JEM-3100R05) operated at 300 kV in combination with the closed gas cell system (Protochips Atmosphere^{TM}) we used in previous study.

Beam effects were first studied on samples *ex-situ*. With a probe current of 20 pA and magnification above 8M, pixel time about 16us, corresponding electron dose is about 4.6×10^4 $e^-/Å^2$ two beam-induced artifacts were apparent. First, some particles immediately began to rotate under the beam, and surface disordering/annealing was also observed, mostly on 2 nm particles, as shown in Figure 4.1. Second, the beam was found to significantly facilitate coalescence of particles in close proximity, shown in Figure 4.2.

In order to avoid such beam effects, we reduced the probe current to 10 pA and kept the magnification below 2M, corresponding to electron dose less than 1000 $e^-/Å^2$. As shown in Figure 4.3, we were then able to scan the same region for 90 min without observing any change in particle size and number.

These same beam conditions were thus adopted for the *in-situ* experiment, where 8-10 areas were selected for analysis, and each area was imaged 4-5 times at 600 °C, 700 °C and 800 °C, at a magnification of about 1M. Each image has 1024×1024 pixels, with a dwell time at each pixel of about 20 μs, corresponding electron dose less than 1000 $e^-/Å^2$. The sample was then shifted to the next area where another image was taken. None of the samples showed any change after 10 hours of continuous heating, 5 hours at 600 °C and 5 hours at 700 °C. At 800 °C, where we did observe changes immediately after the temperature was increased, the beam was valved off between image acquisitions in order to further reduce any possible beam effect.

4.2.3 Particle Size Measurement

A total of 233, 320 and 314 NPs were counted for small, large, and mixed sized samples, respectively, by hand using Digital Micrograph™ software. The microscope has a point resolution of 0.047 nm, and the images were acquired at 0.13-0.24 nm/pixel. Error bars are defined as ± 1 pixel length. An example is shown in Figure 4.4. In this case, an average was made when the horizontal and vertical lengths are different.

4.3 Results and Discussion

Pt NPs, either 2.2±0.4 nm (referred to as "small") or 4.4±0.2 nm (referred to as "large") in diameter, or a mixture thereof (referred to as "mixed") were prepared and supported on high-surface-area alumina. Based on alumina surface area and the nominal Pt loading, the expected NP areal density was ~10^{-3} nm^{-2} in the small and mixed samples and roughly ten times smaller in the large sample, though local variations in particle density were found in some regions of the sample. For the purposes of this study, regions with comparable densities were selected for detailed

observation. The measured average areal density of NPs for the small, large and mixed samples analyzed below was 12.6×10^{-4} nm^{-2}, 6.9×10^{-4} nm^{-2} and 10.6×10^{-4} nm^{-2} (7.9×10^{-4} nm^{-2} for NPs smaller than 3 nm), respectively.

A low-magnification high-angle annular dark field (HAADF) image of the as-synthesized small, large and mixed NP samples are shown in Figure 4.5 a-c. Atomic resolution HAADF images of individual large and small Pt NPs are shown in Figures 4.5 d, e. These images were taken *ex-situ*, with the NP sample supported on a carbon grid.

Samples were heated under 760 Torr of forming gas (5 vol% H_2 in N_2) at 600 °C, 700 °C, and 800 °C, for 5 h at each temperature, inside the gas cell in the microscope. Sequential images of 6-10 different areas in each sample were taken 4-5 times at each temperature. These images were taken with an electron beam diameter about 0.1nm and a probe current of 10pA, and the beam was valved off between image acquisitions, in order to avoid possible beam effects. Histograms of PSDs measured from such images at the conclusion of the treatments at 700 and 800 °C are shown in Figure 4.6, together with the initial PSDs that were measured at 300 °C. As shown in Figure 4.6a, no significant change occurred in the PSD of the small NP sample until 800 °C, after which the mean particle size had increased by 0.5 nm, ~23%. By contrast, the PSD of the large NP sample remained basically unaffected throughout the entire experiment, as shown in Figure 4.6b. The largest change in PSD, by far, occurred in the mixed NP sample, where most of the small NPs disappeared during the 5 h at 800 °C, as shown in Figure 4.6c. It is important to emphasize that our initial (and final, when stationary) PSDs are truly representative of the entire sample due to the high uniformity of the particles, a situation which has been exploited in previous work.[5] The large change between the initial and final PSDs in the mixed NP sample, compared with the others,

thus strongly suggests that OR has been drastically limited through size selection. Dynamic observation in real time, however, is needed for undisputable evidence of the NP growth mechanisms.

Sequential HAADF images, such as those shown in Figure 4.7, provide direct evidence of the disappearance of the small NPs in the mixed sample. The artifact induced by high dose electron beam and the procedures to avoid them are detailed in Experimental Methods. An example of the disappearance of a NP is indicated by the red arrow in Figure 4.7, and an example of the shrinking of another NP is indicated by the yellow arrow. It is important to note that the shrinking particles in Figure 4.7 is representative of the small particles in the mixed sample. A plot showing the changes in the particle size (radius) as a function of time for four NPs, two shrinking and two disappearing, is shown in the bottom left panel of Figure 4.7. Even though particle migration was also observed in the case of some small NPs, at the current particle densities the distance between particles ensures that PMC is almost completely suppressed (see also below). Thus, OR has to be the dominant mechanism of NP growth in the mixed NP sample under our conditions of NP density and environment.

The process of OR involves detachment of atoms from NPs, Fickian diffusion on the support, and deposition onto a different NP.[24] Because the energy barrier for detachment of a single Pt atom from a NP onto the alumina support (~2.5 eV) is much higher than the diffusion barrier of Pt atoms on alumina (0.2-0.5 eV), we employ Equation 1 in the interface-transfer-limiting regime, as in previous work, [17, 25] in order to analyze our observations:

$$\frac{dr}{dt} = \frac{K}{r}\left[\exp\left(\frac{R}{r^*}\right) - \exp\left(\frac{R}{r}\right)\right] \qquad (1)$$

where

$$K = \frac{2}{a}\frac{\nu_p \Omega sin\theta}{(2 - 3cos\theta + cos\theta^3)}\exp(-\frac{E_{OR}}{k_B T})$$

and

$$R = \frac{2\gamma\Omega}{k_B T}$$

Here r is the radius of a given NP at time t, and r^*, known as the critical radius, is the equilibrium value, below which particles shrink and above which they grow. R, called capillary length, is in the range of 2.8-5.6 nm at 800 °C, given that $\boldsymbol{k_B}$ is the Boltzmann constant, T is temperature, $\boldsymbol{\Omega}$ is the atomic volume of Pt (0.015 nm^3), and γ is the surface tension of Pt (in the range of 1.4-2.8N/m),[26] ν_P is the thermal vibration frequency of Pt atoms in the lattice (taken as 10^{14} Hz),[17] θ is the contact angle between the Pt NP and the support (taken as 90°), a is the Pt interatomic distance, and E_{OR} is the activation energy of OR.

In previous studies, simplifications to Equation 1 have been made, either by Gibbs-Thomson linearization[24] or by omitting the first exponential term within the bracket,[17] which corresponds to a NP in equilibrium with a far-field surface atom concentration. Those approximations are valid when r is much larger than the capillary length, R, in the former case or when r^* is much larger than r in the latter case. Here, two models are fitted. In model A, the full equation was integrated numerically and fitted to the experimental data in Figure 4.7, allowing γ and E_{OR} to vary. Although r* changes with time slightly, we assumed it remains constant over the 1500 second interval at the beginning of the 800 °C portion of our experiment, during which the data in Figure 3 was obtained, and took 2 nm as its value, which is in the range of 1.5-2.3 nm, estimated by the arithmetic average of the measured r according to a prescription previously applied in the interface-controlled regime.[25] The best fit gave K=9.6×10^{-6} and R=4.96 nm, which corresponds to γ=2.45 N/m. In model B, the first exponential part containing r* is ignored and the best fit gave K=9.8×10^{-6},

R=4.59, corresponding to γ=2.27 N/m. Both models gave an activation energy of 364 kJ/mol. The results are shown in Figure 4.8.

Conceptually, E_{OR} can be expressed as $E_{OR} = \Delta H_s - E_{ad} + E_d$, where ΔH_s is the sublimation enthalpy of Pt (~565 kJ mol^{-1}),[27] E_{ad} is the Pt atom adsorption energy (~2-2.5 eV in vacuum),[28] and E_d is the energy barrier for Pt atoms to migrate on the alumina support (~0.2-0.5 eV in vacuum).[28] Thus, the activation energy is within the range of 340-420 kJ mol^{-1}, which agrees with the activation energy extracted from our NP shrinking rate. Although the parameters used in this analysis may not be uniquely determined, the fact that they are at least reasonable provides confidence that it correctly captures the essential characteristics of OR.

To further illustrate the effect of NP size on the phenomenon of OR, the initial NP shrinking rates for different combinations of r and r^*, computed by Equation 1 with all the other parameters given above, are listed in Table 4.1. As shown in the table, the shrinking rate for a NP with diameter of $2r$ = 2 nm increases significantly as $2r^*$ increases from 2.2 nm to 5 or 10 nm. Because the equilibrium radius r* can be estimated as an arithmetic mean radius in the interface controlled regime, the difference between r and r* corresponds to the width of PSD, demonstrating that OR is suppressed when the PSD is relatively narrow. For larger NPs, with $2r|2r^*$ combinations of 5|10, 5|20, and 5|50, OR is not as prominent, due to the temperature dependence of the capillary length, R, and thus the width of the PSD is less relevant. These results clearly demonstrate how OR reflects the difference of surface energy, expressed as 2γΩ/r, between small and large NPs, which drastically increases with decreasing size. Our observations are thus in agreement with previous

findings that OR is a dominant NP growth mechanism in samples containing particles 2-5 nm in diameter.[15]

Histograms showing the evolution of the PSD of the mixed NP sample at 800 °C, together with a summary plot of average NP size versus time, are shown in Figure 4. The most significant change in the PSD occurs in the first 110 min, and a change in slope is also found at 110 min in the plot of average NP size versus time, corresponding to a decreased growth rate for times greater than 110 min. Since OR is the dominant mechanism, the decrease in growth rate may be compared with the NP shrinking rate that was derived above. At the beginning of the 800 °C portion of the experiment, taking an r|r* combination of 0.9|2, we obtain an initial NP shrinking rate of -2.5×10^{-3} nm/s, while after 110 min, taking an $r|r^*$ combination of 1.2|2, we obtain a rate of -4.0×10^{-4} nm/s, lower by ~6 times. We therefore propose that the decrease in growth rate with time is due to the fact that smaller particles, which are the primary driving force for the decrease of surface area, are depleted in the process of OR, therefore providing further support for this mechanism of deactivation.

Histograms showing the evolution of the PSD of the mixed NP sample at 800 °C, together with a summary plot of average NP size versus time, are shown in Figure 4.9. The most significant change in the PSD occurs in the first 110 min, and a change in slope is also found at 110 min in the plot of average NP size versus time, corresponding to a decreased growth rate for times greater than 110 min. Since OR is the dominant mechanism, the decrease in growth rate may be compared with the NP shrinking rate that was derived above. At the beginning of the 800 °C portion of the experiment, taking an $r|r^*$ combination of 0.9|2, we obtain an initial NP shrinking rate of $-2.5\times10^{-}$

^{3} nm/s, while after 110 min, taking an $r|r^{*}$ combination of 1.2|2, we obtain a rate of -4.0×10^{-4} nm/s, lower by ~6 times. We therefore propose that the decrease in growth rate with time is due to the fact that smaller particles, which are the primary driving force for the decrease of surface area, are depleted in the process of OR, therefore providing further support for this mechanism of deactivation.

Based on the comparison of tens of sequential images taken on the small sample, we found that no change in NP number and size could be discerned in regions of relatively low density, $\sim14\times10^{-4}$ nm^{-2}, after the full 15 h experiment, as shown in Figure 4.10, thus confirming that OR has been drastically limited under these conditions. On the other hand, clear evidence of particle migration over distances of ~20 nm was observed. Since this distance is much less than the inter-particle spacing in these low-density regions, coalescence could not occur, either. For example, the particles indicated by yellow arrows in Figure 4.10 were clearly diffusing around at 800 ºC, but they didn't shrink or coalesce with other particles nearby. However, in other regions with somewhat higher local NP density ($\sim20\times10^{-4}$ nm^{-2}), PMC is clearly taking place, as indicated by the red circles in Figure 4.11. Calculation confirms that the additive volume of the four particles shown in Figure 6(f), for example, is equal to that of the single particle shown in Figure 6(h).

Since OR has been drastically limited in low density regions of the small (and large) NP samples, the slight shift to larger size observed in the small NP sample at 800 °C is mostly attributed to PMC. The overall process of PMC can be divided into two steps, random migration followed by collision-induced coalescence.[24] Since the time required for coalescence is much shorter than that needed for migration in this case, particle migration is the rate-controlling step. It arises from the

random motion of the supported NPs due to the rapid atomic diffusion on their surfaces. The mobility of supported NPs thus decreases rapidly with increasing NP size.[24] By taking 20 nm as an average migration distance ($2\sqrt{D_{NP}t}$) of the small NPs, based on a series of sequential images recorded over a 5 h period at 800 °C, we deduce that the particle diffusion coefficient, D_{NP}, is on the order of 10^{-17} cm^2 s^{-1}. In the classical model, D_{NP} can be expressed as $0.301D_s(\frac{a}{r})^4$ for spherical particles, where D_s is the surface atom diffusion coefficient, r is the NP radius, and a is the atomic spacing.[24] Surprisingly, the measured D_{NP} is 5 orders of magnitude smaller than the classical model predicts.[24, 29] We speculate that the large discrepancy may be due to the geometry of the support and the specific bonding between the alumina support and the Pt NPs, also observed in other similar systems.[18,30] The contribution of PMC to particle coarsening in this case is thus much smaller than expected. The strong dependence of D_{NP} on the NP size further implies that the large particles are almost immobile (since the calculated migration distance is less than the diameter), and this was indeed confirmed by sequential HAADF images, such as those shown in Figure 4.12. Although the size dependence of the particle diffusion coefficient can provide useful knowledge in controlling the PMC rate through optimization of particle loading, further investigation of particle diffusion in real catalysts is clearly needed, given the discrepancy between experiment and theory revealed here.

4.4 Summary

In summary, through a unique combination of novel *in-situ* atomic resolution transmission electron microscopy performed at elevated temperatures under atmospheric pressure conditions on size selected Pt NPs supported on high-surface-area Al_2O_3, we have been able to cleanly separate and individually characterize the processes of OR and PMC under reducing conditions. Further, our

work suggests that OR can be efficiently limited through the use of monodisperse NPs with narrow PSD in real catalysts, though fluctuations limit the time over which this situation persists, as shown by recent Monte Carlo simulations.[31] The contribution of PMC was found to be much smaller than expected, based on the classical model for particle diffusion coefficient. In principle, it should be possible to also limit PMC by the appropriate choice of NP size. We therefore provide useful general guidelines for the preservation of high catalyst dispersion with extended time in use.

4.5 References

1. Gates, B. *Chem. Rev.* **1995,** 95, 511-522.

2. Bunluesin, T.; Gorte, R.; Graham, G. *Applied Catalysis B: Environmental* **1998,** 15, 107-114.

3. Campbell, C. T.; Parker, S. C.; Starr, D. E. *Science* **2002,** 298, 811-4.

4. Galvis, H. M. T.; Bitter, J. H.; Khare, C. B.; Ruitenbeek, M.; Dugulan, A. I.; de Jong, K. P. *Science* **2012,** 335, 835-838.

5. Cargnello, M.; Doan-Nguyen, V. V.; Gordon, T. R.; Diaz, R. E.; Stach, E. A.; Gorte, R. J.; Fornasiero, P.; Murray, C. B. *Science* **2013,** 341, 771-773.

6. Tian, Y.; Tatsuma, T. *Chem. Commun.* **2004**, 1810-1811.

7. Lu, J.; Do, I.; Drzal, L. T.; Worden, R. M.; Lee, I. *ACS nano* **2008,** 2, 1825-1832.

8. Joo, S. H.; Choi, S. J.; Oh, I.; Kwak, J.; Liu, Z.; Terasaki, O.; Ryoo, R. *Nature* **2001,** 412, 169-172.

9. Liu, Z.; Ling, X. Y.; Su, X.; Lee, J. Y. *The Journal of Physical Chemistry B* **2004,** 108, 8234-8240.

10. Alayoglu, S.; Nilekar, A. U.; Mavrikakis, M.; Eichhorn, B. *Nature materials* **2008,** 7, 333-338.

11. Aricò, A. S.; Bruce, P.; Scrosati, B.; Tarascon, J.-M.; Van Schalkwijk, W. *Nature materials* **2005,** 4, 366-377.

12. White, R. J.; Luque, R.; Budarin, V. L.; Clark, J. H.; Macquarrie, D. J. *Chem. Soc. Rev.* **2009,** 38, 481-494.

13. Datye, A. K.; Xu, Q.; Kharas, K. C.; McCarty, J. M. *Catal. Today* **2006,** 111, 59-67.

14. DeLaRiva, A. T.; Hansen, T. W.; Challa, S. R.; Datye, A. K. *J. Catal.* **2013,** 308, 291-305.

15. Hansen, T. W.; DeLaRiva, A. T.; Challa, S. R.; Datye, A. K. *Acc. Chem. Res.* **2013,** 46, 1720-1730.

16. Behafarid, F.; Pandey, S.; Diaz, R. E.; Stach, E. A.; Cuenya, B. R. *Phys. Chem. Chem. Phys.* **2014,** 16, 18176-84.

17. Challa, S. R.; Delariva, A. T.; Hansen, T. W.; Helveg, S.; Sehested, J.; Hansen, P. L.; Garzon, F.; Datye, A. K. *J. Am. Chem. Soc.* **2011,** 133, 20672-5.

18. Simonsen, S. B.; Chorkendorff, I.; Dahl, S.; Skoglundh, M.; Sehested, J.; Helveg, S. *J. Am. Chem. Soc.* **2010,** 132, 7968-7975.

19. Allard, L. F.; Wittig, J. E.; Chi, M.; More, K. L.; Bigelow, W. C.; Damiano, J.; Nackashi, D. P. *Microsc. Microanal.* **2013,** 19, (S2), 1474-1475.

20. Vendelbo, S.; Elkjær, C.; Falsig, H.; Puspitasari, I.; Dona, P.; Mele, L.; Morana, B.; Nelissen, B.; van Rijn, R.; Creemer, J. *Nature materials* **2014,** 13, 884-890.

21. Zhang, S.; Chen, C.; Cargnello, M.; Fornasiero, P.; Gorte, R. J.; Graham, G. W.; Pan, X. *Nature communications* **2015,** 6, 7778.

22. Wettergren, K.; Schweinberger, F. F.; Deiana, D.; Ridge, C. J.; Crampton, A. S.; Rotzer, M. D.; Hansen, T. W.; Zhdanov, V. P.; Heiz, U.; Langhammer, C. *Nano Lett.* **2014,** 14, 5803-9.

23. Cargnello, M.; Chen, C.; Diroll, B. T.; Doan-Nguyen, V. V.; Gorte, R. J.; Murray, C. B. *J. Am. Chem. Soc.* **2015**, 137, 6906-6911.

24. Wynblatt, P.; Gjostein, N. *Prog. Solid State Chem.* **1975,** 9, 21-58.

25. Houk, L. R.; Challa, S. R.; Grayson, B.; Fanson, P.; Datye, A. K. *Langmuir* **2009,** 25, 11225-11227.

26. Overbury, S.; Bertrand, P.; Somorjai, G. *Chem. Rev.* **1975,** 75, 547-560.

27. Arblaster, J. W. *Platinum Met. Rev.* **2005,** 49, 141-149.

28. Aaron Deskins, N.; Mei, D.; Dupuis, M. *Surf. Sci.* **2009,** 603, 2793-2807.

29. Schumacher, D.; Seeger, A.; Härlin, O. *physica status solidi (b)* **1968,** 25, 359-371.

30. Mei, D.; Kwak, J. H.; Hu, J.; Cho, S. J.; Szanyi, J.; Allard, L. F.; Peden, C. H. *The Journal of Physical Chemistry Letters* **2010,** 1, 2688-2691.

31. Zhdanov, V. P.; Schweinberger, F. F.; Heiz, U.; Langhammer, C. *Chem. Phys. Lett.* **2015,** 631, 21-25.

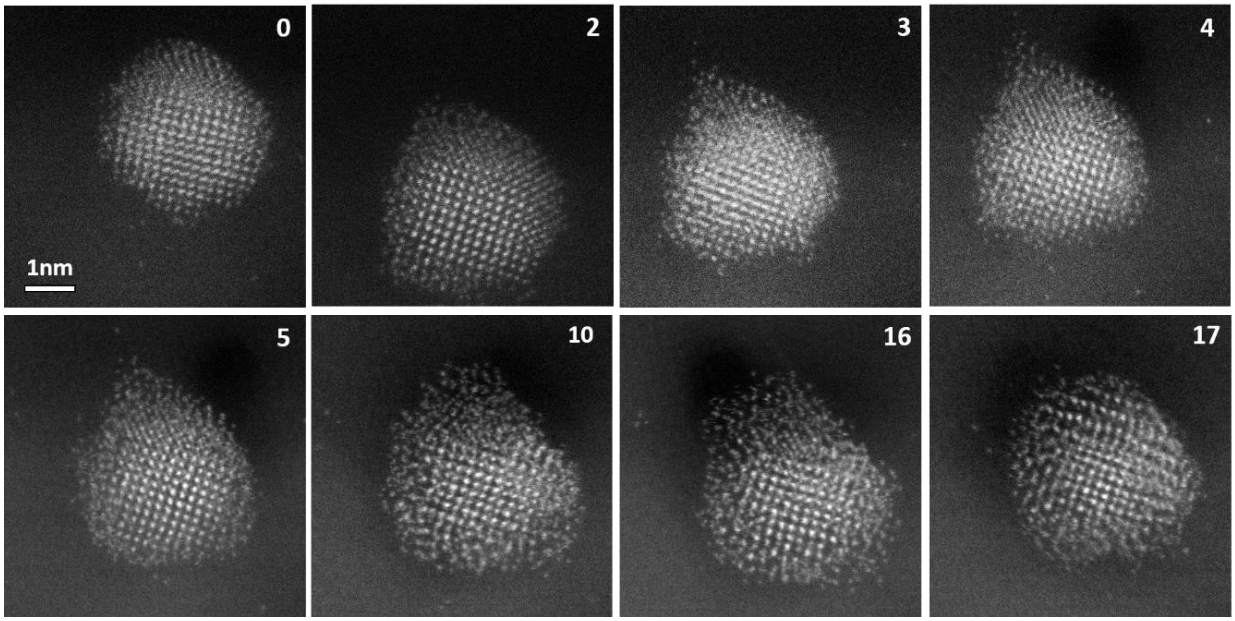

Figure 4.1. Sequential images showing beam-induced surface disorder/annealing. Elapsed time, in minutes, is indicated in the upper right corner of each image. (Images are from Journal of Catalysis, **2016**, 337, 240-247)

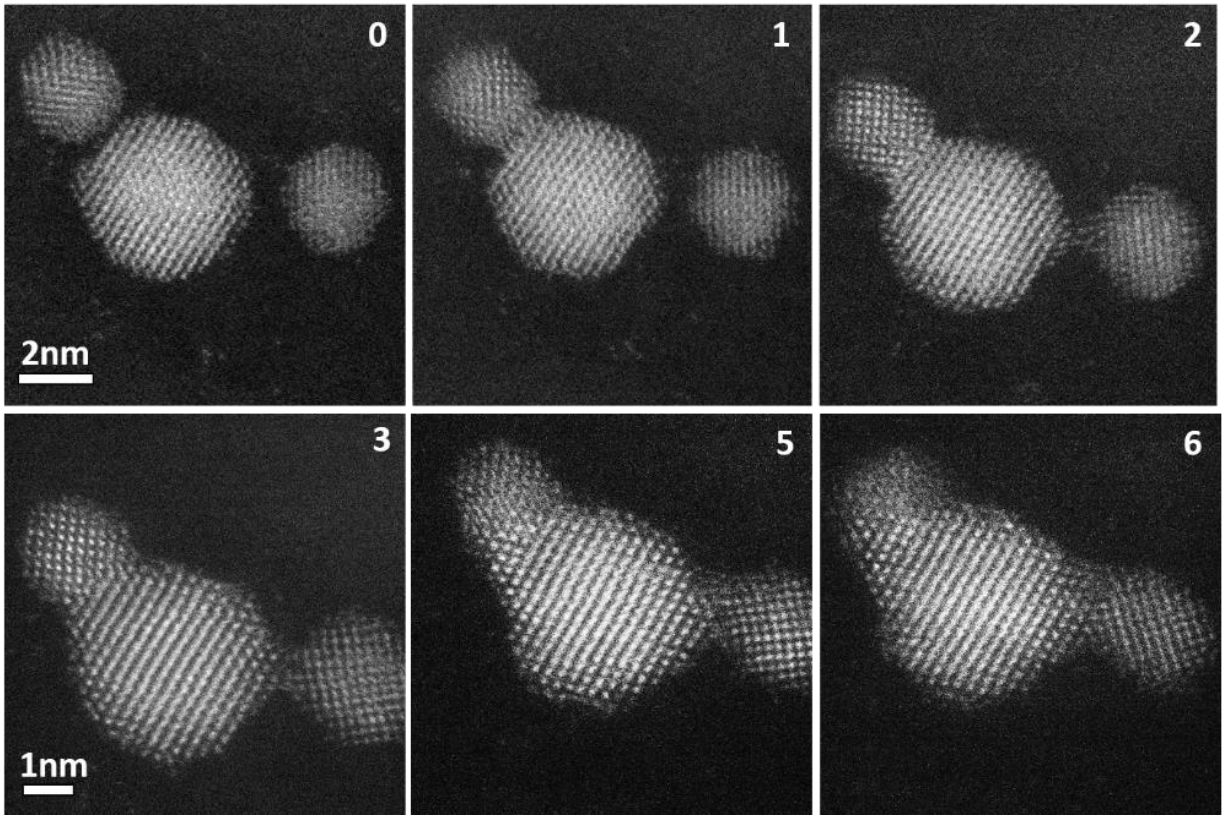

Figure 4.2. Sequential images showing beam-induced particle coalescence. Elapsed time, in minutes, is indicated in the upper right corner of each image. (Images are from Journal of Catalysis, **2016**, 337, 240-247)

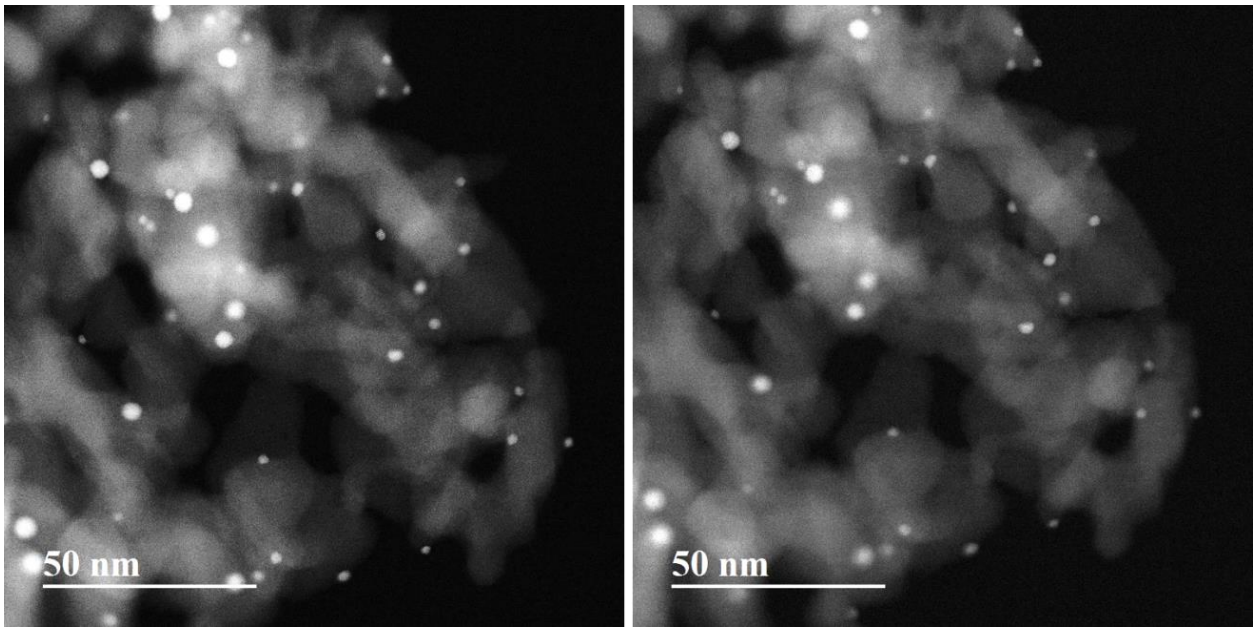

Figure 4.3. Comparison of initial (left) and final (right) images under continuous illumination at 1.2M for 90 min. No obvious change in particle size/shape or coalescence of particles in close proximity is evident. (Images are from Journal of Catalysis, **2016**, 337, 240-247)

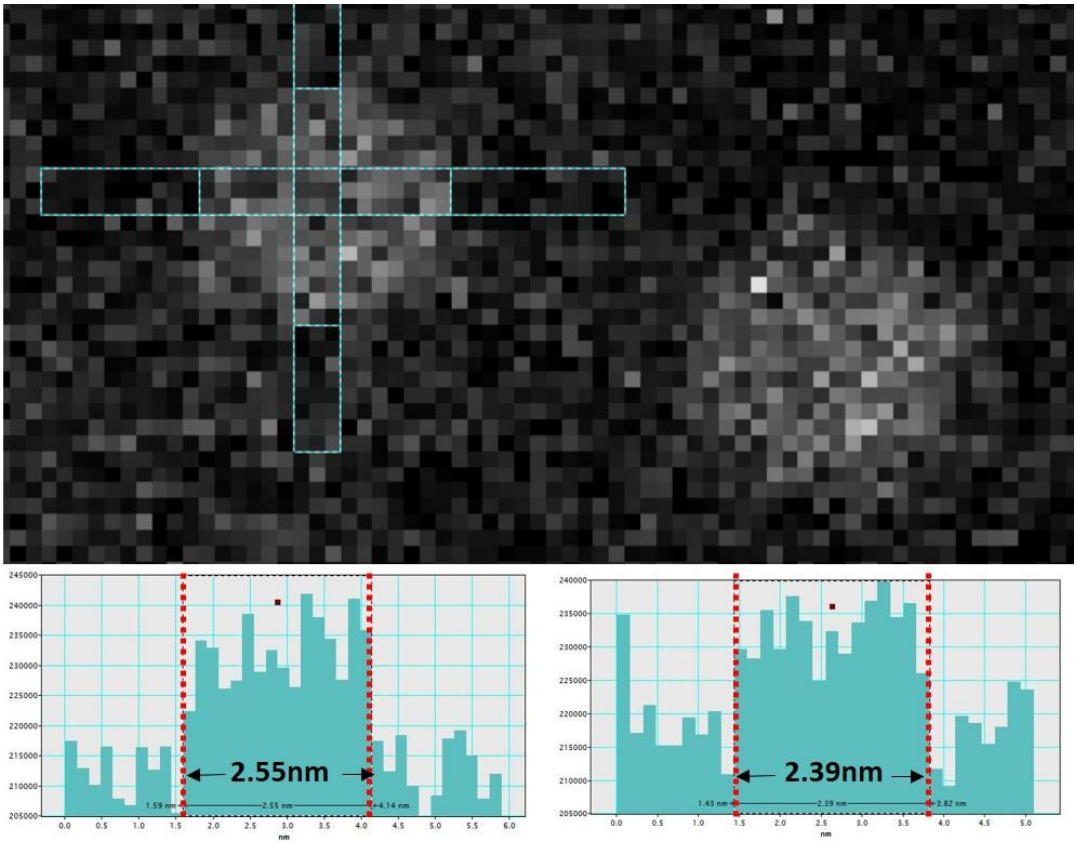

Figure 4.4 Enlarged HAADF images showing the measurement of the particle size. The diameter for the particle being measured is determined as 2.47 nm, an average of the vertical and horizontal length. (Images are from Journal of Catalysis, **2016**, 337, 240-247)

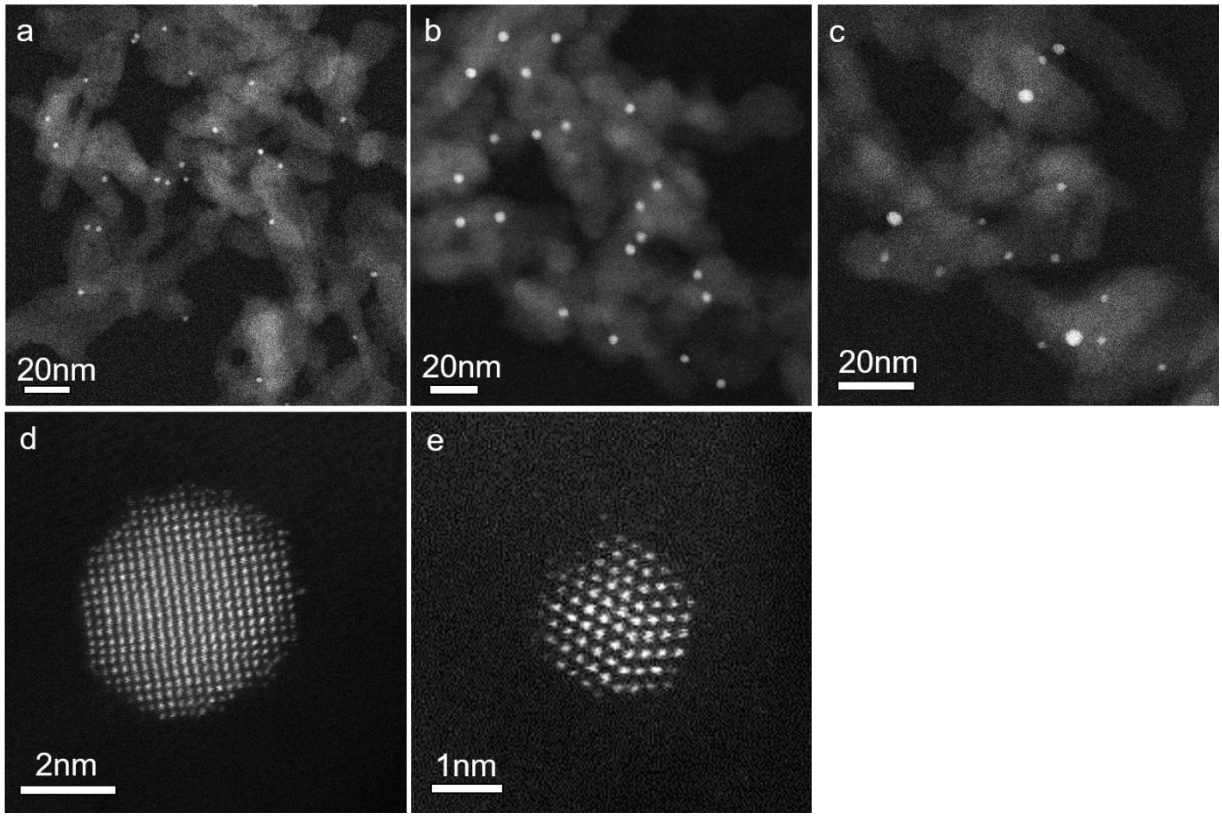

Figure 4.5 HAADF images of the as-prepared small (a), large (b) and mixed (d) NP sample and individual large (d) and small (e) Pt NPs. (Images are from Journal of Catalysis, **2016**, 337, 240-247)

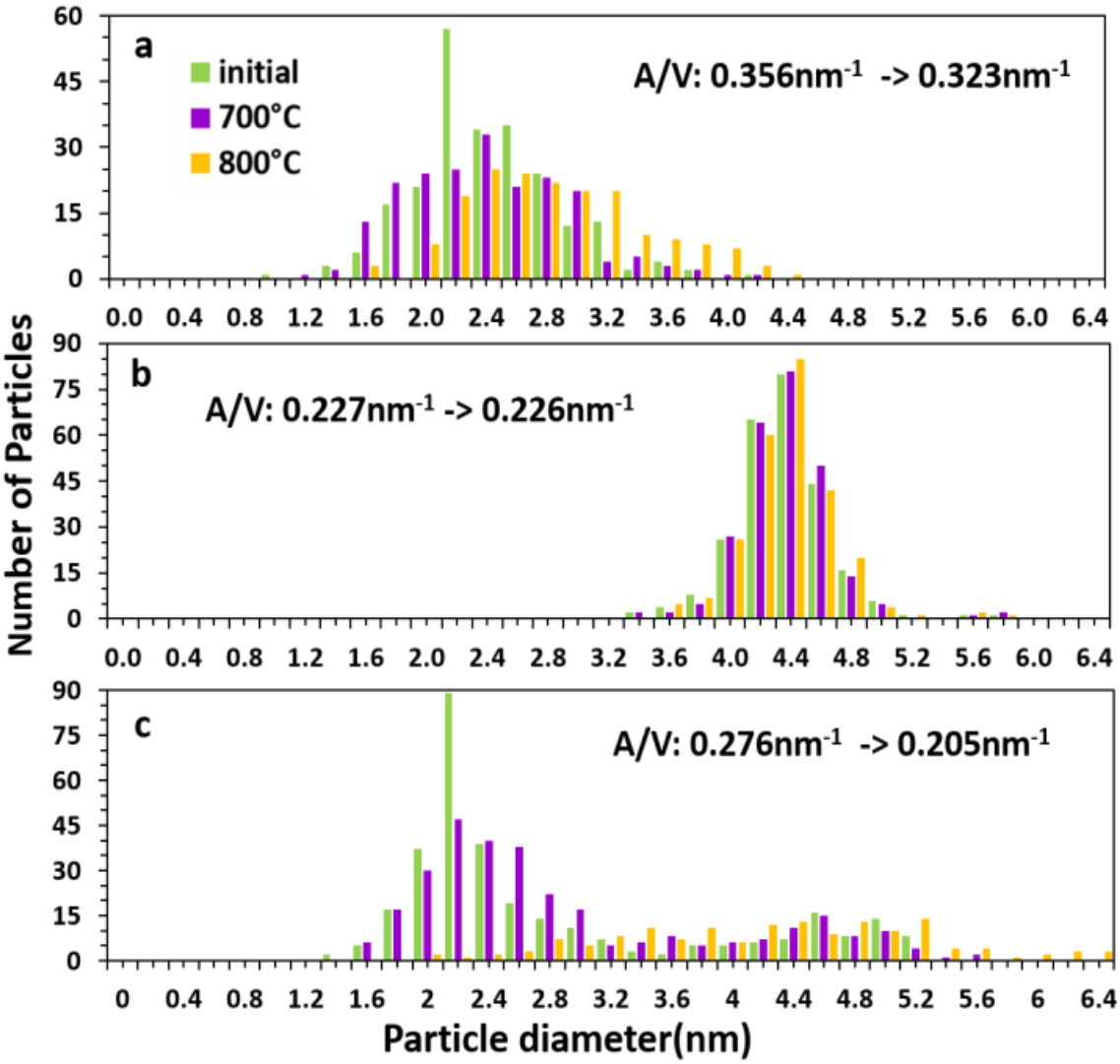

Figure 4.6 Pt PSDs of the small (a), large (b) and mixed (c) NP samples obtained from HAADF images taken during in-situ observation at the indicated temperatures. The area-to-volume ratios (A/V), assuming hemispherical NPs, computed from initial and final PSDs, are also shown for each sample. (Images are from Journal of Catalysis, **2016**, 337, 240-247).

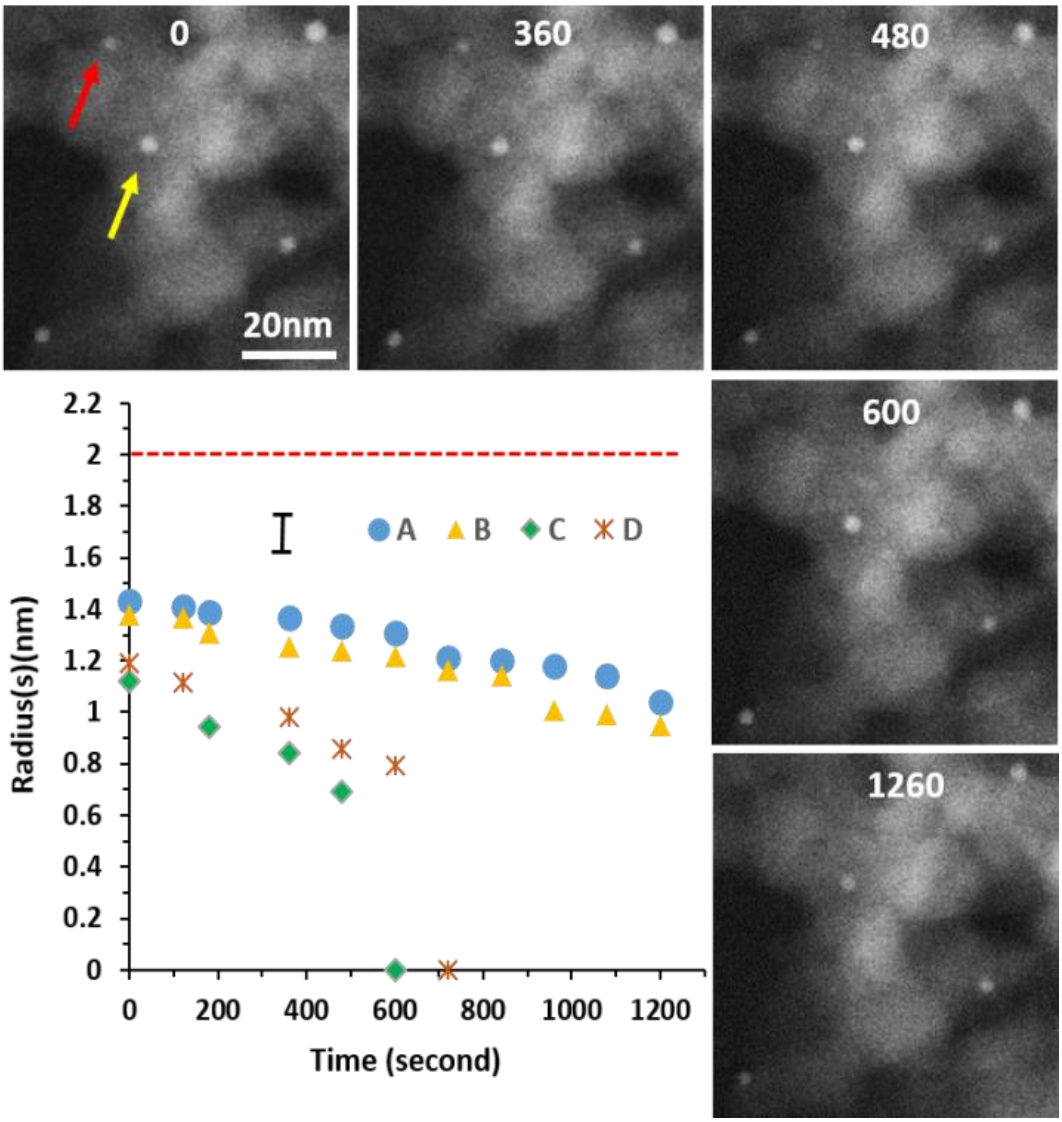

Figure 4.7 Sequential images showing the gradual shrinking and disappearance of the small NPs in the mixed NP sample. Elapsed time, in seconds, is indicated on the top of each HAADF image, taken at 800 °C. A plot showing the radius of four NPs as a function of time is shown in the bottom left. The dashed line corresponds to the value of r^* used in fitting, as discussed in SI. The error bar for all points is ±0.07 nm, as shown on the plot. (Images are from Journal of Catalysis, **2016**, 337, 240-247)

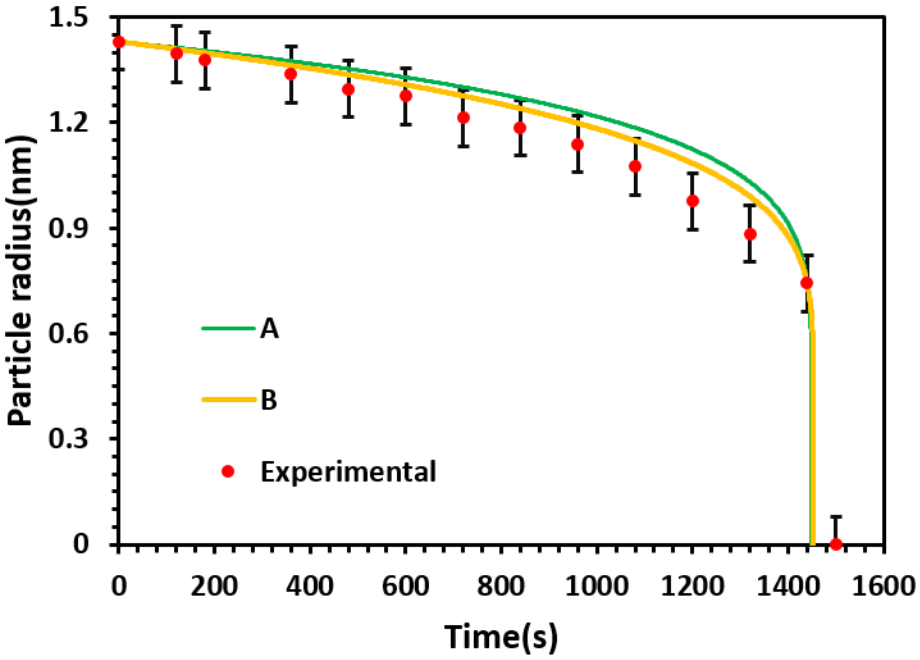

Figure 4.8 A plot comparing the fitted and experimental results of the particle radius change with time. "Green" curve corresponds to model A, "Orange" corresponds to model B, and red dots correspond to the averaged shifted experimental data. (Images are from Journal of Catalysis, **2016**, 337, 240-247)

Table 4.1 Initial NP shrinking rates (dr/dt) for various combinations of 2r and $2r^*$. (Images are from Journal of Catalysis, **2016**, 337, 240-247)

*2r|2r**	2|2.2	2|5	2|10	5|10	5|20	5|50
dr/dt (10^{-4}nm/s)	-5.0	-13	-13.4	-0.17	-0.22	-0.23

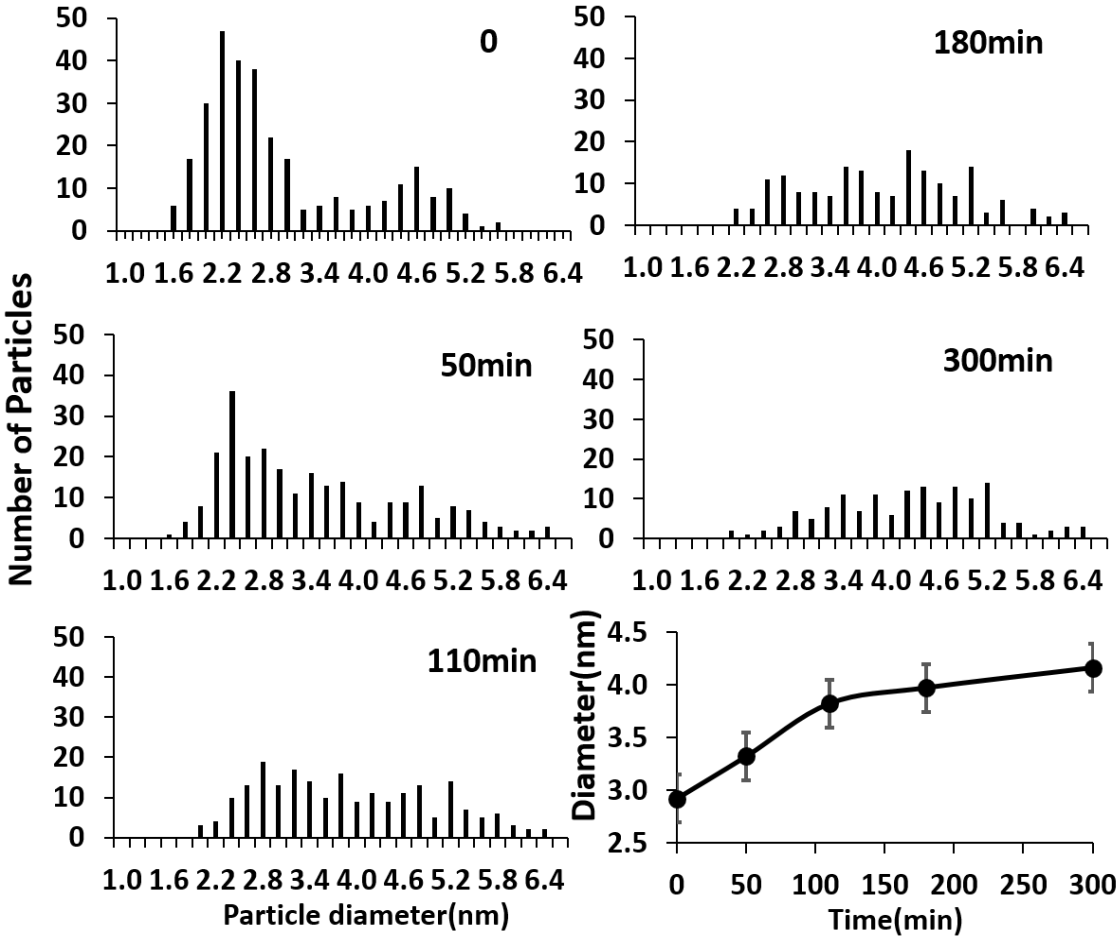

Figure 4.9 Pt PSDs of the mixed NP sample obtained after 0, 50 min, 110 min, 180 min, and 300 min from *in-situ* observations during heating at 800 °C. The time dependence of average NP size is shown in the bottom right panel. (Images are from Journal of Catalysis, **2016**, 337, 240-247).

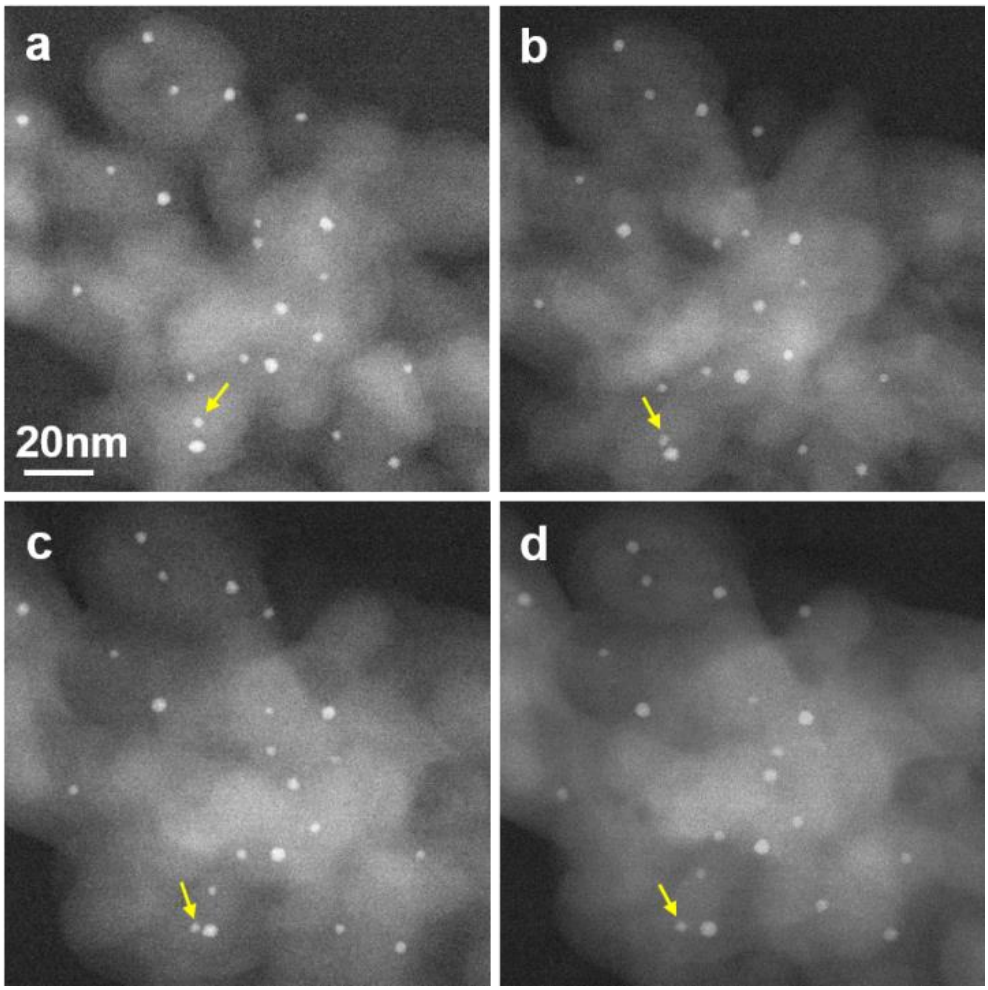

Figure 4.10 Sequential HAADF images showing an area of the small NP sample with relatively low ($14x10^{-4}$ nm^{-2}) NP density. (a-d) were acquired at 0 (at the end of 700 °C), 1, 3.5 and 5 hours at 800 °C. (Images are from Journal of Catalysis, **2016**, 337, 240-247)

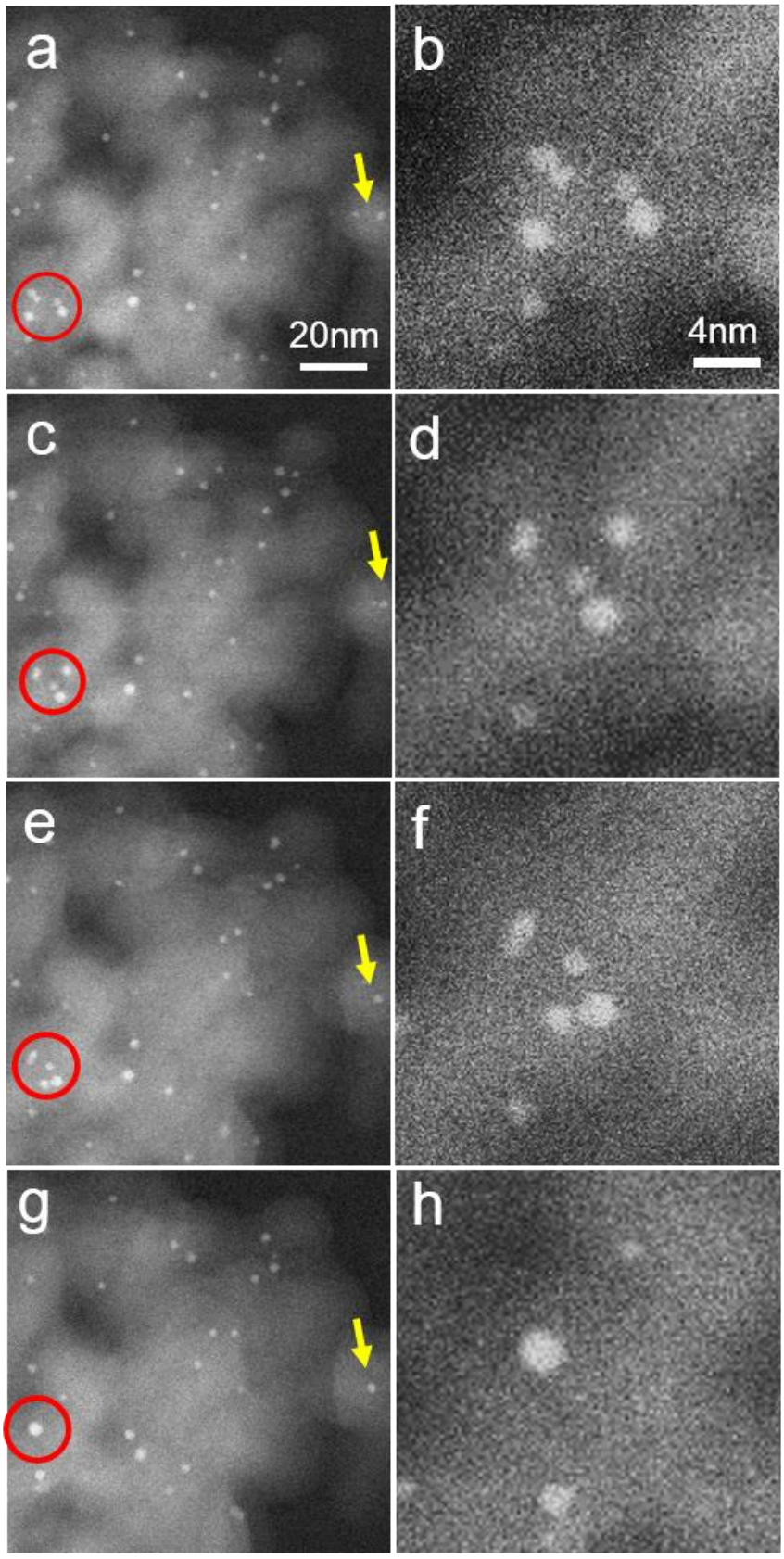

Figure 4.11 Sequential HAADF images (a, c, e, g) and zoom-in areas (b, d, f, h) indicated by the red circles showing an area of the small NP sample with relatively high ($20x10^{-4}$ nm^{-2}) NP density. (a,c,e,g) were acquired at 0 (at the end of 700 °C), 1, 3.5, and 5 hours at 800 °C. (Images are from Journal of Catalysis, **2016**, 337, 240-247).

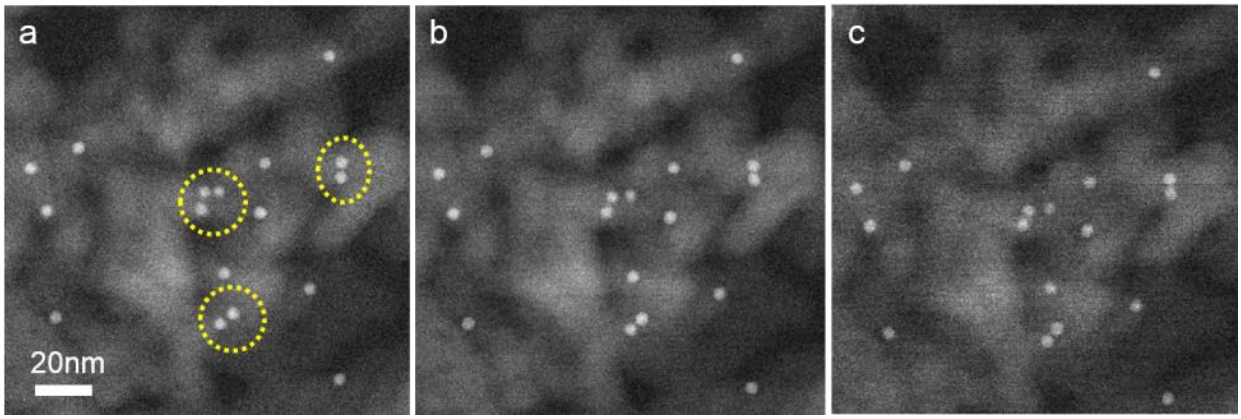

Figure 4.12 Sequential HAADF images showing an area of the large NP sample at initial stage (a), at the end of 700 °C (b) and 800 °C (c) aging. (Images are from Journal of Catalysis, **2016**, 337, 240-247)

Chapter V

Atomic-scale insight into the self-regenerative process of precious metal in $CaTiO_3$

5.1 Introduction

Several years ago, researchers at Daihatsu Motor Company proposed an intriguing idea, involving cyclical precipitation and dissolution of precious metal nanoparticles (NPs), for suppressing NP coarsening in novel perovskite-based three-way catalysts (TWCs) for automotive emissions control, thereby allowing for more efficient precious metal utilization[1-3]. The idea is based on the thermodynamically-motivated expectation, supported by x-ray absorption measurements, that a precious-metal-doped perovskite, with precious-metal atoms occupying B sites in the perovskite (ABO_3) lattice, will be stable under oxidizing conditions, that a mixture of precious-metal NPs and B-site-deficient perovskite will be more stable under reducing conditions, and that a transformation between these two states will occur in response to an imposed change in oxygen chemical potential. Obtaining an understanding of the mechanisms by which the transformation occurs was not the focus of the x-ray absorption measurements, however, nor was providing a clear picture of the actual morphology of the so-called 'intelligent catalyst'.

We thus initiated investigations of the atomic-scale processes underlying the self-regenerating catalyst concept and the structures generated, using spherical aberration (Cs) corrected scanning

transmission electron microscopy (STEM). The major finding of our previous studies was that most of the precious-metal NPs that initially precipitate upon reduction are located within the perovskite matrix, making them unavailable for gas-phase catalysis. We also found that the reverse process, dissolution of the metal NPs into the perovskite upon re-oxidation, is generally not as facile as precipitation, depending on the particular metal, perovskite, NP size, and location (surface versus matrix of the perovskite) [4-7]. Here, we expand upon some of our previous observations of the Pt-$CaTiO_3$ system, made on thin single-crystalline films of Pt-doped $CaTiO_3$ grown by pulsed laser deposition (PLD). In particular, we employ a small-angle STEM tilting technique to (1) confirm that Pt atoms are randomly dispersed throughout the as-grown film, most often occupying Ti sites, (2) show that the smallest Pt-rich clusters appearing upon reduction have a structure consistent with metallic Pt, and (3) demonstrate that upon re-oxidation, the Pt atoms from these clusters occupy mainly Ca sites, in the form of ordered Pt-atom arrays. These findings provide new insight into the atomic-scale structure and transformation reversibility that may offer clues about the detailed mechanisms involved. Our application of the small-angle tilting technique in this material system also serves to illustrate its value as a simple but effective technique to enhance the contrast and resolution of foreign atoms and small clusters of atoms in a matrix of dissimilar material.

5.2 Experimental Methods

5.2.1 Materials Synthesis and Thin Film Growth*

Pulsed laser deposition (PLD) targets were constructed from $Ca_{1.1}Ti_{0.9}Pt_{0.1}O_3$ powders, which were synthesized using the citrate method. Stoichiometric amounts of $Ca(NO_3)_2{\cdot}4H_2O$, $Ti[O(CH_2)_3CH_3]_4$, and $PtC_{10}H_{14}O_4$ (Alfa Aesar) were dissolved in de-ionized water with citric

acid, with nitric acid used to control the solution pH. The solution was dehydrated at 100 °C and held at 60 °C until gelation, after which it was calcined at 800 °C in flowing oxygen. The resultant powder was then pressed and sintered at 1200-1300 °C to form a dense PLD target. Film growth was performed in an ultra-high vacuum growth chamber using a KrF excimer laser operated at 248 nm, with Pt:$CaTiO_3$ films grown at 750 °C on $SrTiO_3$ (100) single crystal substrates supplied by MTI Corporation.

The thin film samples were synthesized by Kui Zhang and Minghao Fang.

5.2.2 Sample Preparation Methods

Cross-sectional STEM specimens were fabricated by mechanical thinning and polishing on diamond lapping media, followed by Ar-ion milling (Gatan PIPS, model 691) at 3kV, 3° to electron transparency and sample thickness are typically controlled around 20nm measured by plasma peak of Electron Energy Loss Spectroscopy (EELS), as shown in Figure 5.1. Specimens were examined in a Cs-corrected JEOL JEM-2100F STEM operated at 200 kV. Thermal processing was performed in a quartz tube in a tube furnace. Dry air was flowed through the tube at 450 sccm and 10% H_2 (balance N_2) at 100 sccm for oxidation and reduction treatments, respectively. These conditions mimic those in the original work.[2]

5.2.3 Multi-Slice Simulation

Based on the physical optics theory of Cowley and Moodie, the multi-slice method is a numerical integration method to solve the Schrodinger equation 1 by assuming that the wave function $\Psi(\vec{r})$ can be represented by a modulated plane wave shown in equation 2

$$\nabla^2\Psi(\vec{r}) + \frac{2m|e|}{\hbar^2}[E + V(\vec{r})]\,\Psi(\vec{r}) = 0 \quad (1)$$

$$\Psi(\vec{r}) = \exp(2\pi i k \cdot \vec{r})\Phi(\vec{r}) \quad (2)$$

Considering the high-energy approximation and assuming that the electron beam is normal to the crystal surface, we end up with

$$\frac{d\Phi(\vec{r})}{dz} = \frac{i\nabla_t^2}{4\pi k_z}\Phi(\vec{r}) + \frac{2m|e|i}{4\pi k_z\hbar^2}V(\vec{r})\Phi(\vec{r}) \quad (3)$$

The first order differential equation in t can be integrated numerically by "cutting" the sample in many thin slices parallel to its surface, reducing the potential in each slice to a 2-dimentional one through integration over the slice thickness which separates the scattering process into a kinematic scattering process and a Fresnel propagation through "vacuum" over the thickness of the slice, relating the wave function $\Phi(t+\Delta t)$ to $\Phi(t)$. Doing this for every slice will yield the wave function at the exit surface of the crystal, which becomes exact for $\Delta t \to 0$.

Image simulations were carried out using QSTEM based on a multi-slice algorithm developed by Christoph Koch[9] with the parameters shown in Table 5.1.

$CaTiO_3$ of orthorhombic structure was used for the image simulation with a=5.3789 Å, b=5.4361 Å, c= 7.6388 Å. The Pt-doped CTO thin film was grown on [001] $SrTiO_3$, and due to epitaxy relationship between cubic $SrTiO_3$ and orthorhombic $CaTiO_3$, $[110]_{CTO}$ // $[001]_{STO}$. So we defined a'=b'=$\sqrt{a^2+b^2}/2$=3.823 Å, c'=c/2=3.819 Å for simplicity, where $[100]'_{CTO}$// $[001]_{STO}$, a 2×4×54 supercell was used for simulation, and images are viewed from [100]' axis.

5.2.4 Experimental Tilting Methods

Due to epitaxy relationship, the direction normal to the film surface is [001]. It' important to align [001] direction of the sample either along x axis or y axis of the sample holder. After the specimen is well loaded on the sample holder, align the sample in [100] zone axis of STO substrate and then take several pictures of the thin film in zone. Remember several locations, especially locations with unique feature like dislocation or inclusions, and then slowly tilt the sample by 0.1 degree per step each time when looking at the image of the sample not diffraction until preferred tilting is achieved. Patience is needed in this step.

5.2.5 *In-situ* Microscopy

A small quantity of this powder was suspended in methanol with sonication and drop cast onto the heater chip of the MEMS-based gas cell of a Protochips Atmosphere system, as described in previous chapters.

5.3 Result and Discussion

In the present study, 50-60 nm thick $Ca_{0.96}Ti_{0.91}Pt_{0.09}O_{2.97}$ (CTO) thin films were grown by PLD on (001) $SrTiO_3$ substrates. One of the as-grown films was subjected to a reduction treatment (in 10% H_2 balanced with N_2) at 800 °C for 1 h, and a portion of this film was then subjected to a re-oxidation treatment (in dry air) at 800 °C for 1 h. Cross-sectional TEM specimens of all three samples were prepared by conventional methods and an overview of the high-angle annular dark field (HAADF) images obtained from all three samples are shown in Figure 5.2.

Figure 5.2a shows an image of the as-grown film. Since HAADF imaging provides Z contrast, it is tempting to associate the randomly distributed brighter spots in this image with single Pt atoms.

As shown more clearly in Figure 5.2b, most of these brighter spots are on Ti sites (red arrow), though some are on Ca sites (yellow arrow). Corresponding images of the reduced film are shown in Figures 5.2 c-d. Here, instead of the brighter spots, a number of diffuse areas, 1-2 nm in diameter, of higher intensity are apparent. Previously, these areas were identified as Pt-rich clusters, embedded in the perovskite matrix, but their structure and exact composition could not be determined [4]. Finally, Figures 5.2e and f show images of the reduced film following re-oxidation. As in our previous study, it is clear that the density of the smallest embedded clusters has decreased [4], but another kind of feature, characterized by ordered arrays of 3-5 very bright spots, is present throughout the film. As shown in Figure 5.2f, these spots are mostly located on Ca cites.

A HAADF image is generally regarded as a convolution between a point spread function and an object function, assuming incoherent scattering, and the brightness of a feature in the image should be proportional to $Z^{1.7-2}$ when the specimen thickness is uniform. This atomic number sensitivity usually provides ease of data interpretation. However, when the beam spreads significantly due to scattering, and channeling along atomic columns occurs, the probe changes when it encounters foreign atoms or clusters embedded in a crystalline material in a way that leads to greater complexity in the interpretation of the images. Previous theoretical study has shown that a 2° tilt away from the zone axis can successfully suppress beam channeling while still preserving some information about the lattice of the host material [8]. To better understand the distribution of Pt atoms within the CTO films, we have thus conducted a series of multi-slice image simulations of orthorhombic Pt-doped CTO thin film with 20nm thickness using QTEM [9], both along the [001] zone axis in a pseudocubic coordination and for low-angle tilted conditions, as shown in Figure

5.3. We found that one or two Pt substitutional atoms in one collumn will not generate enough contrast enhancement to be observed under the on-zone-axis condition for our specimen thickness, but a significant enhancement in brightness can be achieved with the sample rotated slightly off the zone axis, as shown in Figure 5.3a(a') and f(f'). The brightness of a Pt-containing column, viewed along the zone axis, increases with the number of Pt atoms within the given Ca or Ti column, and when viewed off-axis, multiple Pt atoms within the same column appear as an elongated region with brightness enhancement.

Simulation result of sample with different thicknesses are shown in Figure 5.4. A single Pt atom was substituted for No. 5 Ca site counting from the top surface in the $CaTiO_3$ lattice to illustrate the effect of specimen thickness variation. According to Figure 5.4, peak intensity enhancement induced by a single Pt atom decreases as specimen thickness increases. A single Pt atom is visible when the specimen is less than 10 nm thick, which is extremely challenging for typical thin film specimen preparation.

The influence of Pt location along atomic column is also shown in Figure 5.5. A single Pt atom replaced the No. 5, 27, or 50 Ca atom, representing top surface, middle and bottom surface Pt substitution with a total thickness of 54 unit cell. In the in-zone axis image, the contrast doesn't change much when Pt changes from top surface to bottom surface, indicating the entire column is in focus under channeling condition. However, after 2 degree tilting from zone axis, depth resolution can be restored due to elimination of channeling effect, and therefore Pt in the middle or bottom surface can't be visualized.

HAADF images of samples that were rotated by 2° away from the [001] zone axis are shown in Figure 5.6. The brighter of the relatively uniform stripes correspond to Ti columns, and the darker correspond to Ca columns. In the image of the as-grown film, shown in Figure 5.6a, numerous brighter spots appear, most of which are on Ti sites, though a significant minority fraction (30-40%) are on Ca sites. Based on the simulation results, we may reasonably conclude that these spots arise from Pt atoms. Tilting also significantly enhances the contrast from the Pt-rich clusters that appear in the film after reduction, as shown in Figure 5.6b, and these images thus provide an indication of the atomic structure of these clusters. Similarly, a hint of the structure responsible for the very bright spots that appear within small ordered arrays in the reduced, then re-oxidized film is apparent in the image shown in Figure 5.6c. More examples of the atom arrays can be found in Figure 5.7.

More quantitative and detailed information can be extracted through a comparison of on-axis and off-axis pairs of images taken from the same area of the sample, as shown in Figure 5.8. Several sub-nanometer Pt-rich clusters that are not visible in the on-axis image of a reduced film, shown in Figure 5.8a, are quite apparent (indicated by green arrows) in the off-axis image of the same area, shown in Figure 5.8b. By contrast, there is much less disparity in the number of Pt-rich clusters in a comparison of corresponding images of a reduced, then re-oxidized film, as shown in Figures 5.8c and 5.8d. The difference, as shown by the accompanying particle size distribution histograms, generated from tilted-sample images, reflects the disappearance of the majority of sub-nanometer Pt-rich clusters in the reduced, then re-oxidized film. This, in turn, suggests there is a connection between the disappearance of the sub-nanometer Pt-rich clusters and the formation of the small ordered arrays of very bright spots in the reduced, then re-oxidized film.

Atomic-scale information, not obtainable from on-axis images, can be further extracted from off-axis images for both the reduced and the reduced, then re-oxidized films, as shown in Figure 5.9. In the reduced film, although it is not visible within the area marked by the yellow dashed rectangular in Figure 5.9a (enlarged in Figure 5.9c), a Pt cluster can be clearly seen in Figure 5.9b. The projected distance between Pt atoms in this cluster (enlarged in Figure 5.9d) is about 0.2 nm, very close to the spacing between [10] planes in metallic Pt. We believe such clusters are typical of the early stage of Pt NP precipitation within the CTO matrix,[10] which begins with diffusive extraction of oxygen from the Pt-doped CTO lattice, driven by partial reduction of oxide at the free surface of the film. This process is necessarily disruptive of the perovskite lattice, since some of the original CTO is displaced by the Pt NPs that form. The size of the Pt NPs could depend on several factors, including local Pt concentration and the rates of interdiffusion of the four atomic species present. We have found that the separation between Pt NPs in our studies is generally consistent with ion diffusivities reported in the literature [11]. Relatively large (2-5 nm) Pt NPs, present throughout the CTO matrix at internal crystalline defects and on free surfaces, adopt the Pt FCC structure and typically exhibit cube-on-cube epitaxy with the CTO [4].

In the reduced, then re-oxidized film, our focus is on the small ordered arrays of very bright spots. As shown by the in-zone and tilted-sample pairs of images in Figures 5e and 5f (enlarged in Figures 5g and 5h, respectively), an elongation of the very bright spots occurs in the off-axis images. According to the simulation results, such an elongation results from the arrangement of a small number of Pt atoms, each separated by one or three unit cells, along the zone axis. Quantitatively, the elongation (0.1-0.2 nm) corresponds to a length along the zone axis that is comparable with the in-plane length of the array of very bright spots (~2-3 nm), suggesting that the ordered array

exists in three dimensions. A corresponding simulation results based on a 3-D model are shown in Figure 5 i-j. From A to C, 4, 3 and 4 Ca sites are replaced by Pt. (And their location in the beam direction counting from top surface are: A, No. 7, 9, 11, 15 Ca sites; B, No. 7, 11, 15 Ca sites; C, No. 7, 9, 11, 15 Ca sites) Significantly, these spots are exclusively on Ca sites. It thus appears that if these small ordered arrays of Pt atoms are formed as a result of the dissolution of the sub-nanometer Pt-rich clusters, as argued above, the Pt must not be fully oxidized at this stage. The significantly smaller size of Pt^{2+} (94 pm) than Ca^{2+} (126 pm) should tend to further stabilize the orthorhombic structure of CTO, possibly favoring the Pt occupation of only a subset of the possible Ca sites. This apparent atomic-scale irreversibility, likely related to the well-known kinetic barrier for Pt oxidation, could contribute to the observed asymmetry in the precipitation-dissolution redox cycle of the Pt-CTO system.

In-situ microscopy study was conducted on a similar material system, Rh-CTO in power form, to directly visualize the precipitation and dissolution processes of Rh particles. The series of high-angle annular-dark-field (HAADF) images shown in Figure 5.10 provide both an impression of the morphology of the Rh-doped CTO powder and an overview of the effects of time and temperature on what we believe to be the process of Rh NP precipitation during the initial reduction treatment in 760 Torr of forming gas (5%H_2 in Ar). As shown by the image in Figure 5.10a, the grain size of CTO support is generally 10-20 nm across, and some nanometer-size regions of brighter intensity, presumably due to Rh, already appear at 250 °C. When the temperature is raised to 355 °C for 10mins, more sub-nanometer-size regions become apparent, as shown by the image in Figure 5.10b. Both the number and clarity of the sub-nanometer regions increase when the temperature is raised to 500 °C, as shown in Figure 5.10 c and d. For the most part, the larger

bright regions remain stable, but small changes in the number or distribution of the smallest bright regions appear to occur with the passage of time, as shown in Figure 5.10.d. Unfortunately, neither the CTO nor Rh is in zone axis in this figure, but an in-zone atomic scale image is shown in Figure 5.11, taken on another region after 12 minutes of reduction at 500 °C. The fuzziness of the bright features is likely due to the channeling effect as we discussed in the case of Pt/CTO thin film. Those bright spots (one of which is marked by an arrow, another of which is enclosed within the rectangular box on the image and the corresponding line profile is shown on the right), are likely due to the presence of atomically dispersed Rh atoms.

To test the reversibility of the precipitated metal particles, we did another experiment with two complete redox cycles. Both reducing and oxidizing treatments were conducted in 760 Torr of forming gas (5%H_2 in Ar) and pure O_2, respectively, at 600 °C. Again, pre-existing nanometer-size regions of bright intensity, already apparent in the HAADF image at the beginning of the observation, and many more start to appear during reduction as shown in Figure 5.12. Upon subsequent heating to 600 °C in 760 Torr of pure O_2, most of the smaller regions disappear within 10 minutes but particles larger than 2nm still stay but become dimmer, suggesting oxidation of Rh particles. Significant changes in the CTO, pointed by the red arrow were also observed, which is likely due to a combination effect of electron beam irradiation and disruption caused by Rh NP precipitation and dissolution. Both a clear difference in the distribution of brighter intensity regions between this and a second reduction-oxidation cycle and the apparent sintering of CTO supports are apparent in the comparative images shown in Figure 5.13. Another point of interest is that both transitions (changes in bright intensity regions from first oxidation to second reduction and from

second reduction to second oxidation) took place faster (within a minute) than in the initial reduction-oxidation cycle, probably due to the destructive structure created by the first cycle.

5.4 Summary

To explore the precipitation and dissolution processes of precious metal particle in perovskite lattice, we conducted both *ex-situ* detailed analysis on Pt-CTO thin film sample an *in-situ* direct observation on Rh-CTO powder sample.

Our comparison of in-zone and tilted images (Pt-CTO thin film) has provided new information about the Pt-CTO system: (1) the presence of single Pt atoms on both Ti and Ca (to a lesser extent) sites in as-grown films was confirmed, (2) aspects of the atomic-scale structure of sub-nanometer Pt clusters in reduced films were revealed, and (3) the structure of small ordered arrays of Pt atoms in reduced, then re-oxidized films was probed and analyzed. Through the application of this small-angle tilting STEM technique, we have thus provided unprecedented detail about the precipitation and dissolution of Pt NPs in Pt-doped CTO.

We believe this method can be easily applied to other material systems that include single atom dopants or embedded nanoclusters. For example, a few years after Daihatsu's self-regenerating catalyst concept appeared, another group showed that the single process of precipitation (exsolution) of transition metal NPs from metal-doped oxides may be employed to create supported metal catalysts for solid oxide fuel cells (SOFCs) [12,13]. Since then, others have suggested that exsolution of metal NPs, as a general method for preparing supported metal catalysts, may provide unprecedented control over NP size, concentration, and stability [14,15]. We expect that there

will continue to be interest in the NP formation mechanisms and resulting structure of catalysts prepared in this fashion, and we anticipate that the approach we have used in our work will be useful for future research into these topics.

Looking beyond the field of heterogeneous catalysis, single dopants and nanoclusters embedded in a host material often exhibit unique electronic, optical, magnetic and thermal properties, and thus they have been widely used in novel functional materials like semiconductors, photovoltaics, and thermoelectrics [11-16]. For example, as the size of semiconductor devices continues to shrink, the number of dopant atoms in the channel region becomes small, and their random distribution may become an invalid assumption. It has been found that an ordered array of dopant atoms, well-controlled in number and position, exhibit superior uniformity, and that a device containing them shows remarkable performance compared with a device with an uncontrolled distribution [12]. In another example, however, randomly distributed 2 nm ErAs nanoclusters embedded in an $In_{0.53}Ga_{0.47}As$ matrix are more effective in reducing thermal conductivity than particles arranged in a super-lattice structure, presumably due to scattering of mid- and long- wavelength phonons [15]. Since ideal functionality can only be achieved with specific size, distribution, and structure relationships, direct visualization of the foreign species is crucial to the understanding of structure-property relationships needed to further improve material or device performance. We believe the approach, involving a comparison of in-zone and tilted-sample images can be easily implemented for a variety of different systems, providing more valuable fundamental observations for mechanistic understanding and property improvement.

The present *in-situ* STEM observations provide new, real time information about the Rh NP precipitation and dissolution processes in CTO, which are central to the 'intelligent catalyst' concept. Although the observations do not lend much support to the idea that Rh NP coarsening can be limited through reduction-oxidation cycling, the conditions under which these observations were performed still do not reproduce those that would exist in the exhaust gas passing over a three-way catalyst in use, and it is thus possible that exposure to more realistic conditions might lead to a different outcome. The effects of much smaller variations in oxygen chemical potential, imposed at higher frequency could, in principle, be explored in future experiments using this *in-situ* STEM technique

5.5 References

1. Nishihata, Y.; Mizuki, J.; Akao, T.; Tanaka, H.; Uenishi, M.; Kimura, M.; Okamoto, T.; Hamada, N. *Nature* **2002,** 418, 164-167.

2. Tanaka, H.; Taniguchi, M.; Uenishi, M.; Kajita, N.; Tan, I.; Nishihata, Y.; Mizuki, J. i.; Narita, K.; Kimura, M.; Kaneko, K. *Angew. Chem. Int. Ed.* **2006,** 45, 5998-6002.

3. Tanaka, H.; Uenishi, M.; Taniguchi, M.; Tan, I.; Narita, K.; Kimura, M.; Kaneko, K.; Nishihata, Y.; Mizuki, J. i. *Catal. Today* **2006,** 117, 321-328.

4. Katz, M. B.; Zhang, S.; Duan, Y.; Wang, H.; Fang, M.; Zhang, K.; Li, B.; Graham, G. W.; Pan, X. *J. Catal.* **2012,** 293, 145-148.

5. Katz, M.; Duan, Y.; Graham, G.; Pan, X.; Allard, L. *Microsc. Microanal.* **2012,** 18, (S2), 1120-1121.

6. Zhang, S.; Du, X.; Fang, M.; Katz, M.; Graham, G.; Pan, X. *Microsc. Microanal.* **2013,** 19, (S2), 1624-1625.

7. Li, B.; Katz, M. B.; Duan, Y.; Du, X.; Zhang, K.; Chen, L.; Van der Ven, A.; Graham, G. W.; Pan, X. *Chem. Mater.* **2014,** 27, 18-28.

8. Xin, H. L.; Intaraprasonk, V.; Muller, D. A. *Appl. Phys. Lett.* **2008,** 92, 013125.

9. Koch, C. T., *Determination of core structure periodicity and point defect density along dislocations*. 2002.

10. Such sub-nm clusters, which are almost invisible in on-axis images, may be largely responsible for the very small metal-metal average coordination numbers observed by EXAFS after the reduction treatments, as reported in Refs. 1-3.

11. Koenraad, P. M.; Flatté, M. E. *Nature materials* **2011,** 10, 91-100.

12. Shinada, T.; Okamoto, S.; Kobayashi, T.; Ohdomari, I. *Nature* **2005,** 437, 1128-1131.

13. Atwater, H. A.; Polman, A. *Nature materials* **2010,** 9, 205-213.

14. Wang, D. H.; Park, K. H.; Seo, J. H.; Seifter, J.; Jeon, J. H.; Kim, J. K.; Park, J. H.; Park, O. O.; Heeger, A. J. *Advanced Energy Materials* **2011,** 1, 766-770.

15. Kim, W.; Zide, J.; Gossard, A.; Klenov, D.; Stemmer, S.; Shakouri, A.; Majumdar, A. *Phys. Rev. Lett.* **2006,** 96, 045901.

16. Liu, Y.; Sahoo, P.; Makongo, J. P.; Zhou, X.; Kim, S.-J.; Chi, H.; Uher, C.; Pan, X.; Poudeu, P. F. *J. Am. Chem. Soc.* **2013,** 135, 7486-7495.

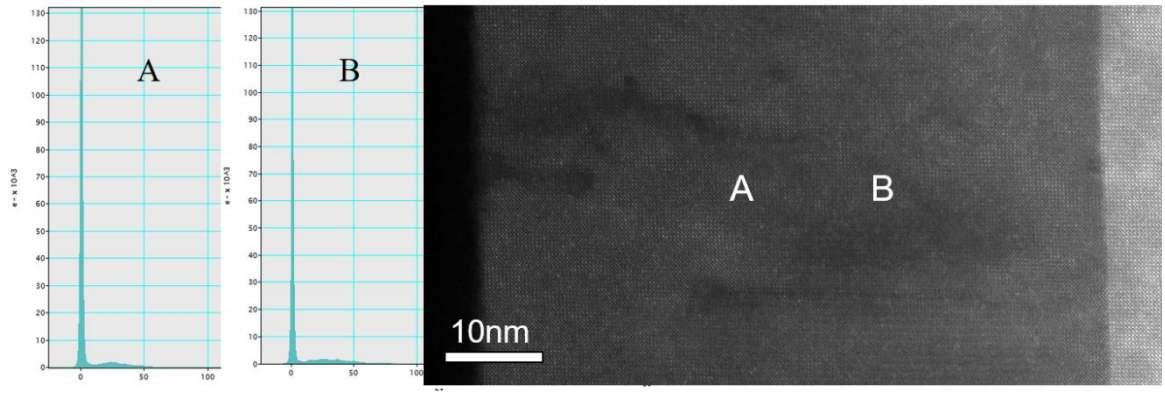

Figure 5.1 Plasma absorption spectra acquired from A and B in the STEM image on the right. The convergence angle is 14 mrad, the collection angle is 50 mrad, and effective mass is 19.2. The thickness at point A is about 20 nm, and thickness at point B is about 22 nm.

Table 5.1 Detailed parameters used for multi-slice image simulation

Acceleration voltage: 200 kV	Convergence angle: 14 mrad
Detector inner and outer angle: 80-240 mrad	Spherical aberration Cs:1um
Defocus: -2 nm from the top surface	Slice thickness 1.90 Å

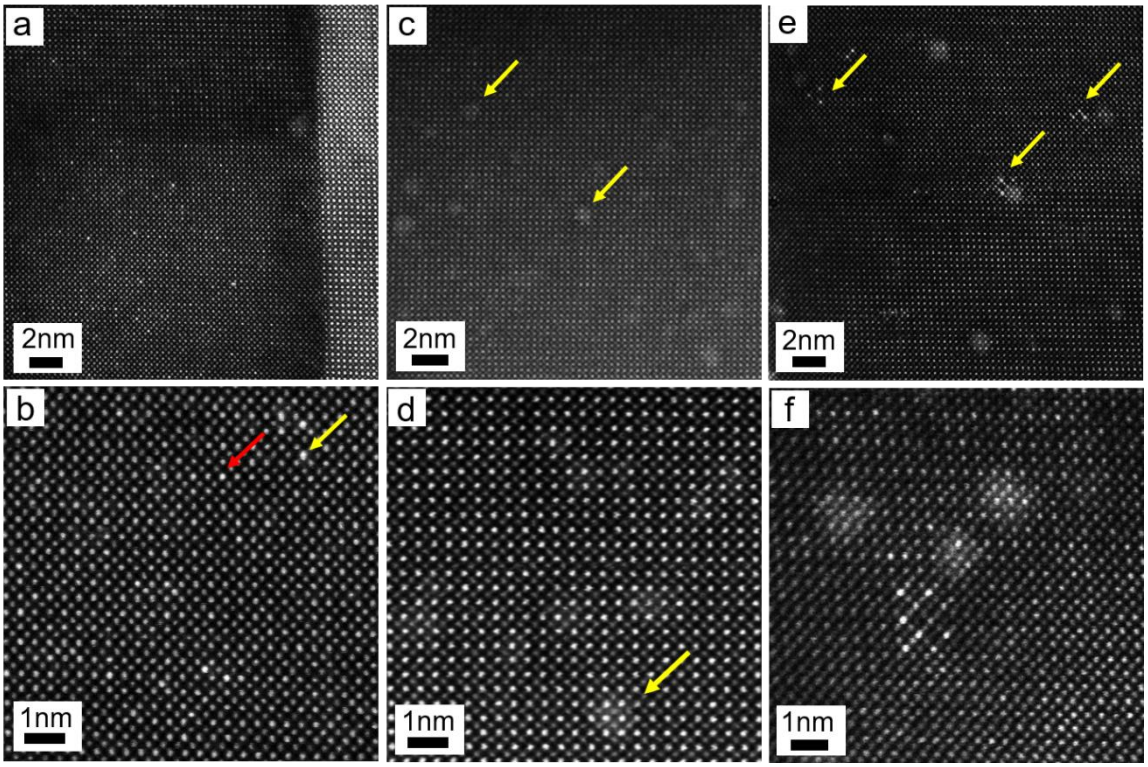

Figure 5.2 In-zone axis HAADF images of the as-grown film (a,b), the reduced film (c,d) and the reduced, then re-oxidized film (e,f).

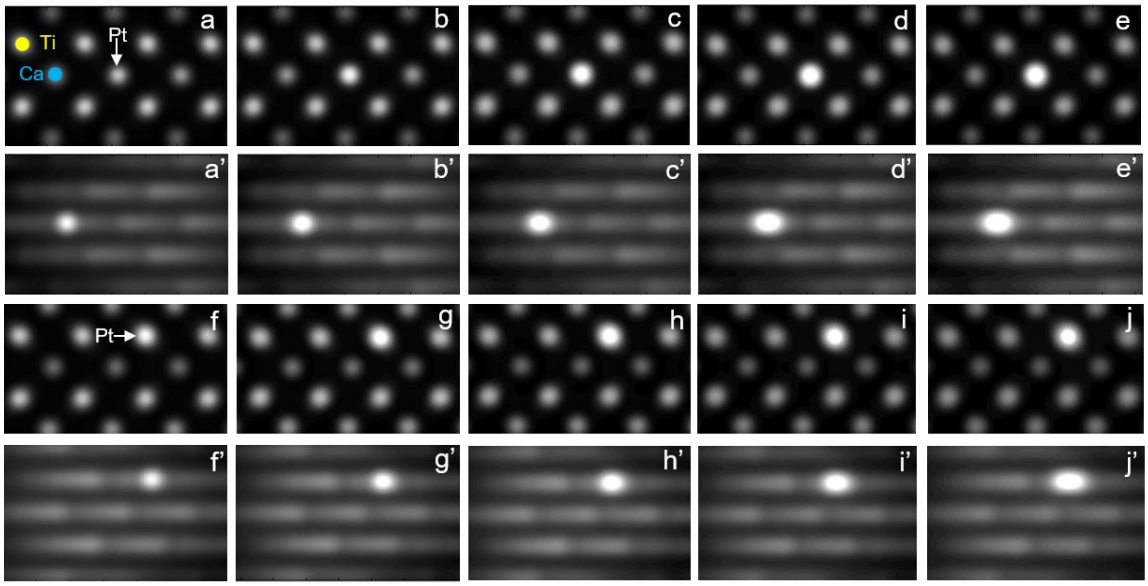

Figure 5.3 Multi-slice simulation of different numbers of Pt atoms substituted into a $CaTiO_3$ lattice with a total thickness (along the beam direction) of 20 nm. a(a')-e(e') simulated results showing 1-5 Pt atoms substituted onto Ca sites (center location) from the in-zone axis orientation (and a 2° tilted orientation). f(f')-j(j') corresponding simulated results showing 1-5 Pt atoms substituted onto Ti sites (upper right location) from in-zone axis orientation (and a 2° tilted orientation).

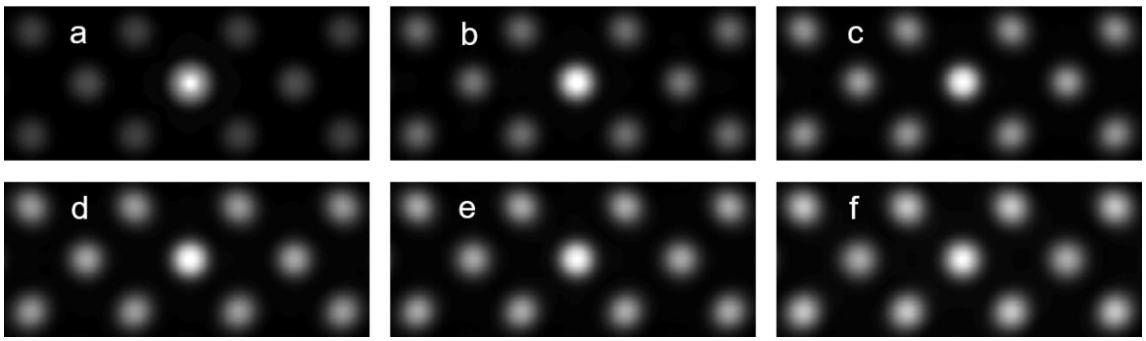

Figure 5.4 Multi-slice simulation results showing the brightness enhancement of one Pt atom in specimens of different thickness. (a) 3.64 nm, (b) 5.56 nm, (c) 7.47 nm, (d) 9.39 nm, (e) 11.31 nm, (f) 13.22 nm

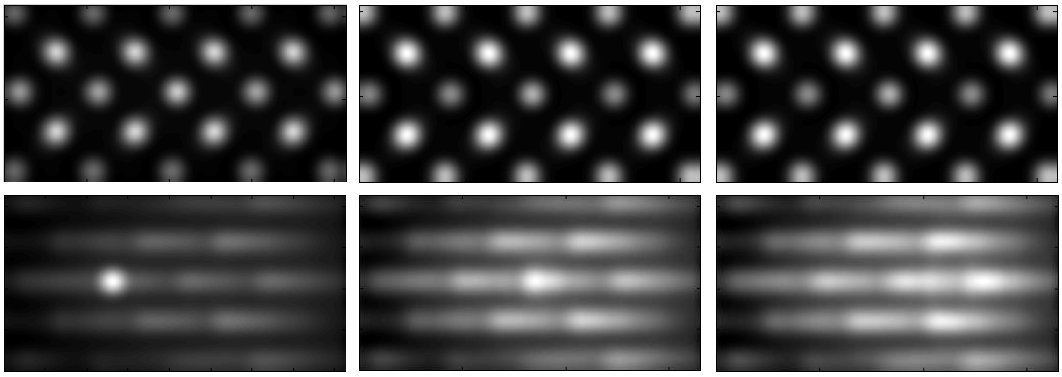

Figure 5.5 Multi-slice simulation showing that brightness enhancement changes with the Pt atom's location along the beam direction. In-zone images are shown in the first row and 2-degree tilted images are shown in the second row. Panels from left to right correspond to a Pt atom located at top, middle and bottom of the specimen.

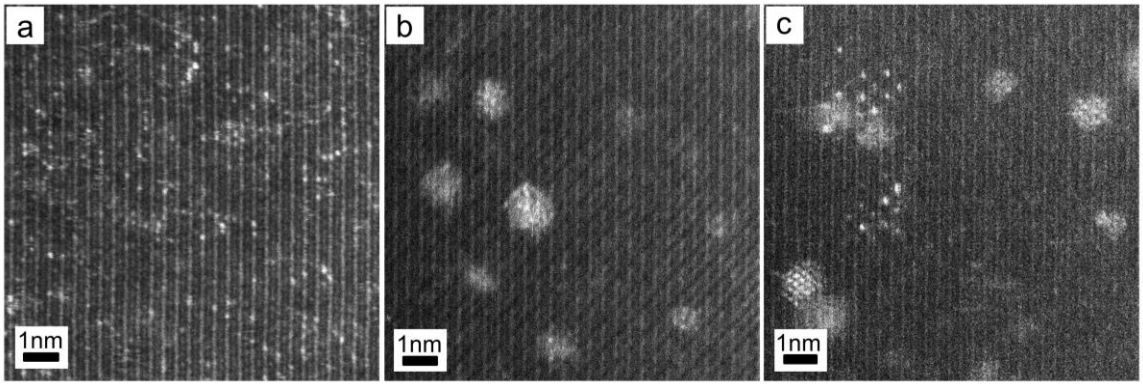

Figure 5.6 HAADF images of the as-grown film (a), the reduced film (b), and the reduced, then re-oxidized film (c) taken with the samples rotated by 2° away from the [001] zone axis.

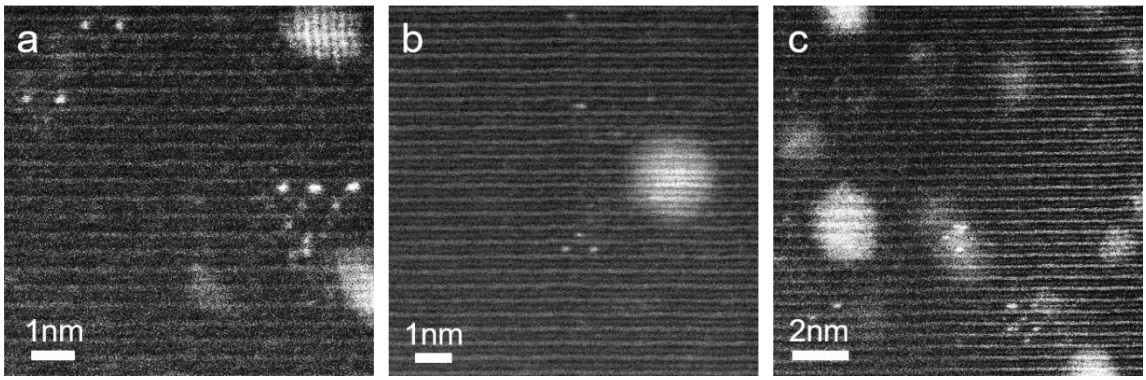

Figure 5.7 Low angle tilted STEM images showing that Pt atoms predominantly occupy Ca sites in the $CaTiO_3$ lattice.

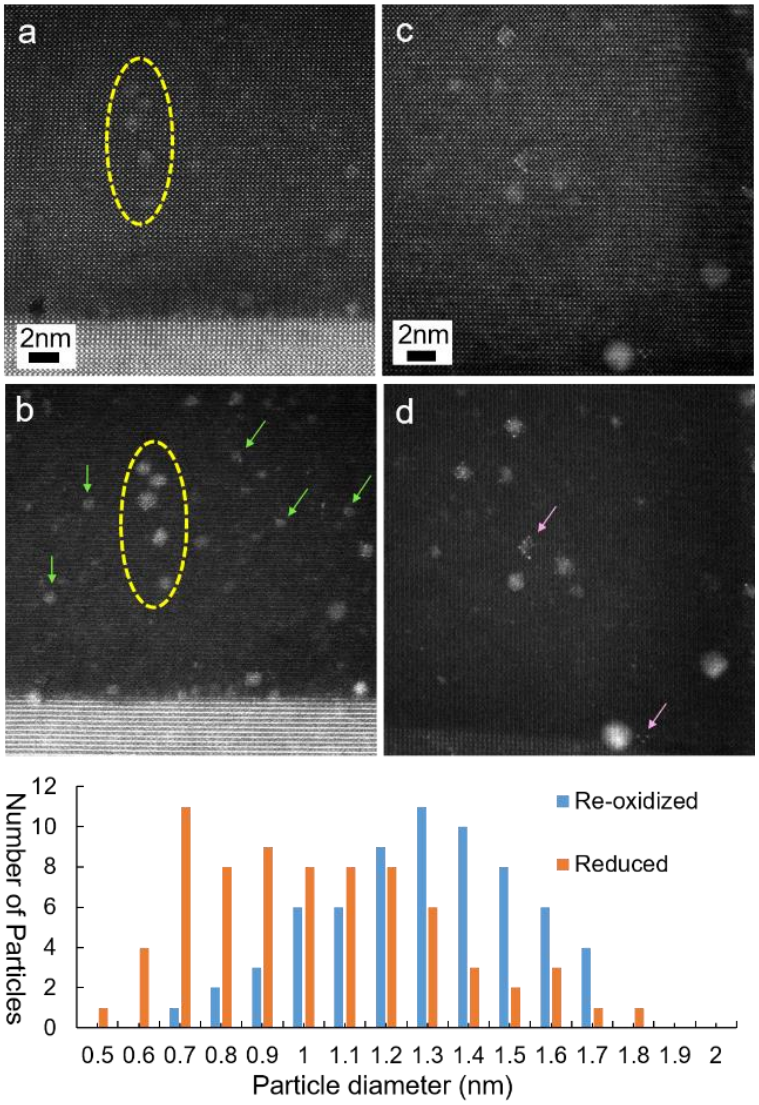

Figure 5.8 In-zone and tilted-sample HAADF images (a and b, respectively) from the same area of the reduced film, in-zone and tilted-sample HAADF images (c and d, respectively) from the same area of the reduced, then re-oxidized film, and particle size distributions of Pt-rich clusters taken from tilted-sample images of both films.

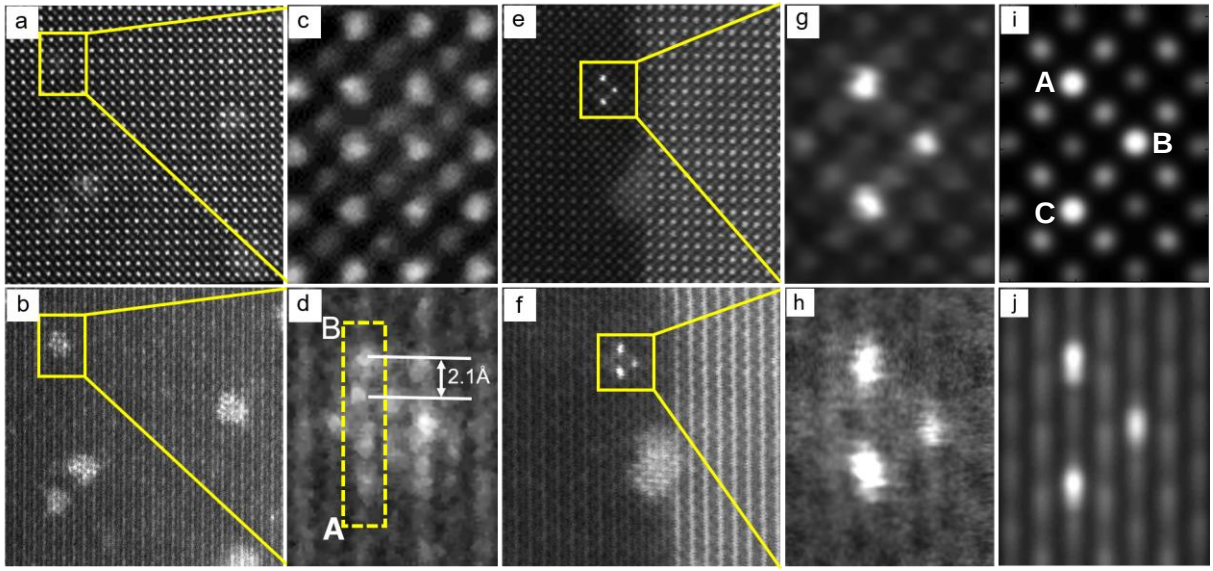

Figure 5.9 In-zone and tilted-sample HAADF images of the reduced film (a,c and b,d, respectively) and the reduced, then re-oxidized film (e,g and f,h, respectively). i an j are corresponding simulation results of the atom arrays in shown in g and h. From A to C, 4, 3 and 4 Ca sites are replaced by Pt. And their location in the beam direction counting from top surface are: A, No. 7, 9, 11, 15 Ca sites; B, No. 7, 11, 15 Ca sites; C, No. 7, 9, 11, 15 Ca sites

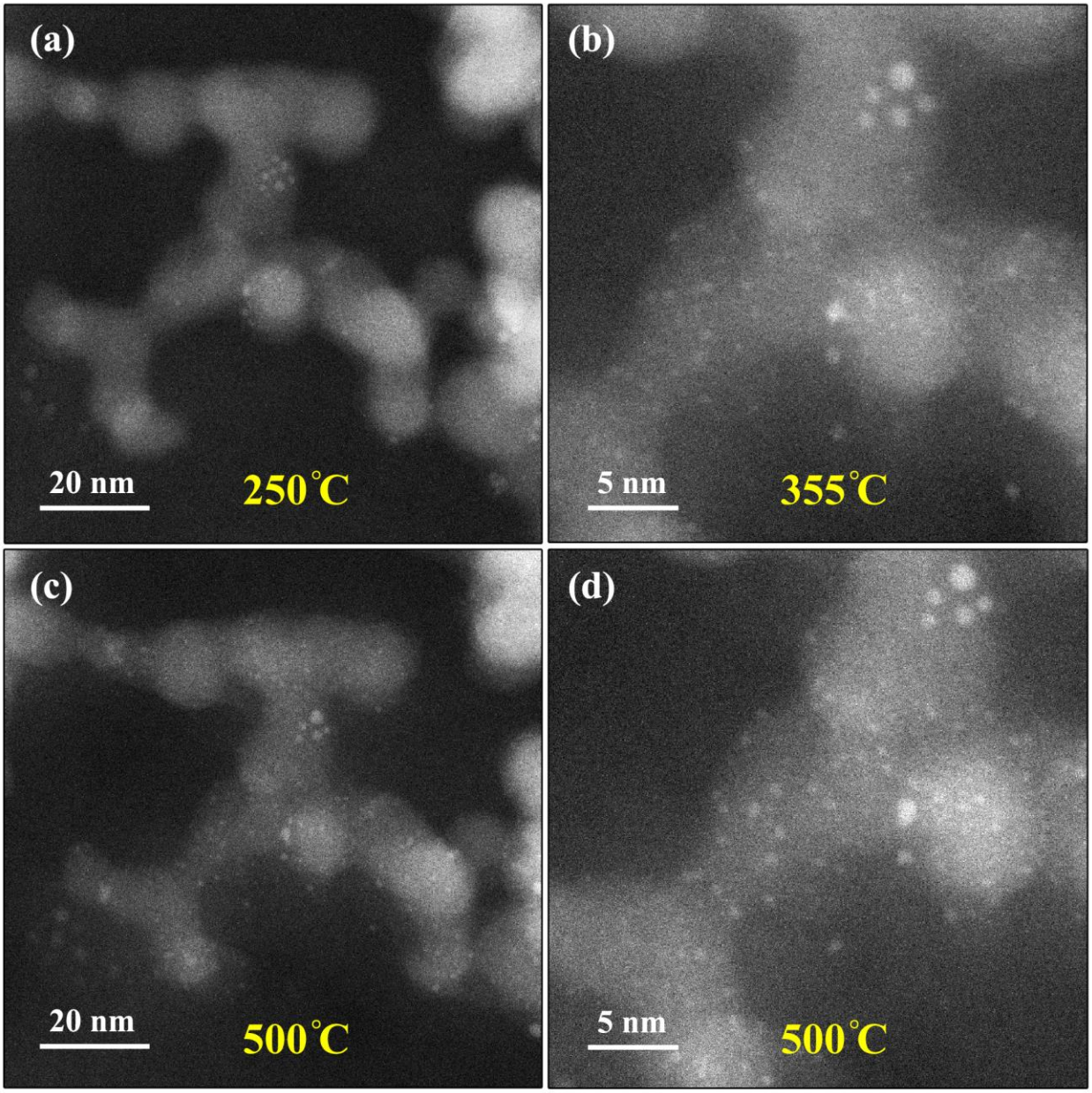

Figure 5.10 HAADF images of Rh-CTO powder in 760 Torr of 5%H_2/Ar at various temperatures and time lapses. (a) 250°C (b) 355°C 10min (c) 500C °C (d) 500 °C 2min.

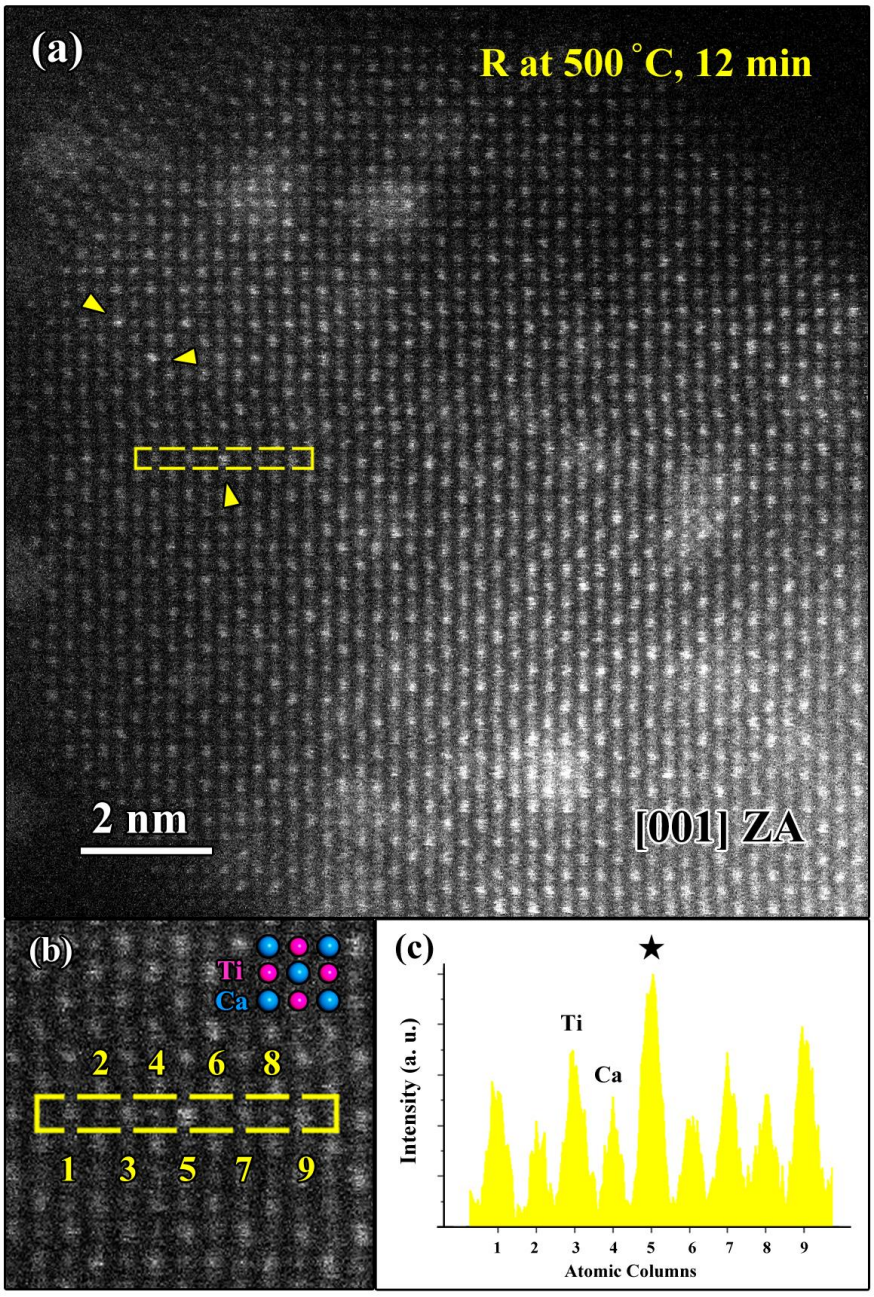
(a)
R at 500 °C, 12 min
2 nm
[001] ZA
(b)
Ti
Ca
2 4 6 8
1 3 5 7 9
(c)
Ti
Ca
Intensity (a. u.)
1 2 3 4 5 6 7 8 9
Atomic Columns

Figure 5.11 High-resolution HAADF image of Rh-CTO powder in 760 Torr of 5%H_2/Ar after 12 minutes at 500 °C. The intensity along a line scanned from left to right within the small rectangular box is also shown.

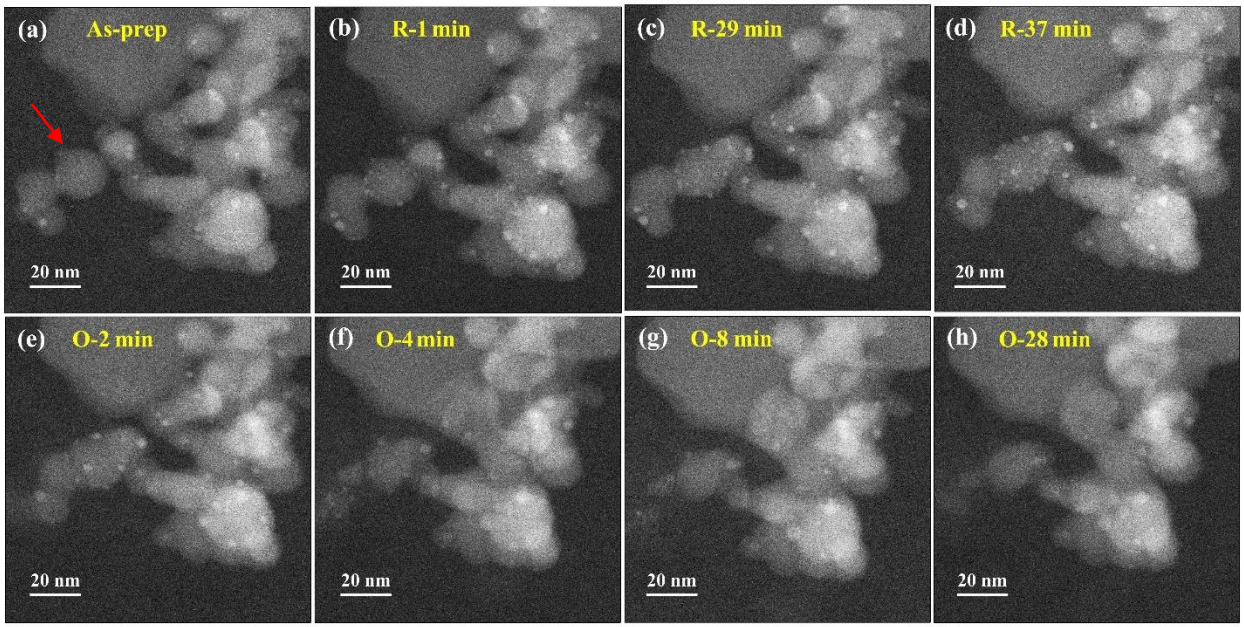

Figure 5.12 HAADF images of Rh-CTO powder in 760 Torr of 5%H_2/Ar (labeled by R) or pure O_2 (labeled by O) at 600 °C and various time lapses.

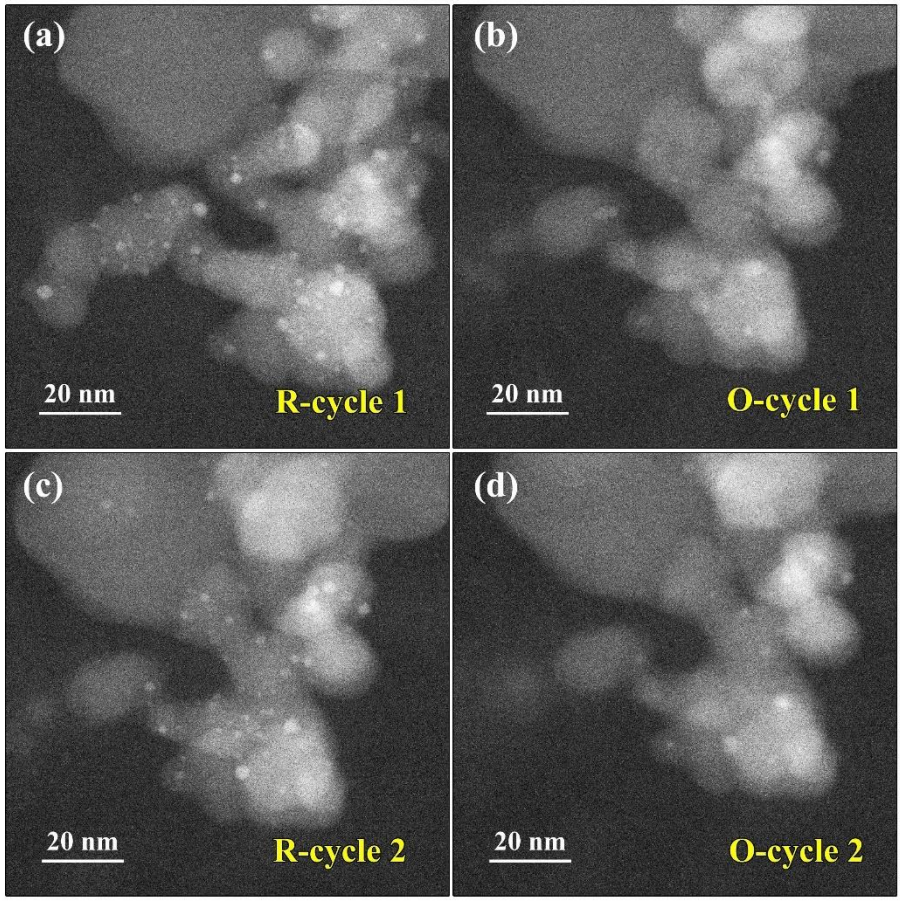
(a)
20 nm
R-cycle 1
(b)
20 nm
O-cycle 1
(c)
20 nm
R-cycle 2
(d)
20 nm
O-cycle 2

Figure 5.13 Comparison of HAADF images of Rh-CTO powder in 760 Torr of 5%H_2/Ar (labeled by R) or pure O_2 (labeled by O) at 600 °C taken at the conclusion of the first (labeled by cycle 1) and second (labeled by cycle 2) reduction-oxidation cycles.

Chapter VI

Summary and Future Outlook

6.1 Summary of Work

In this dissertation, *in-situ* microscopy and spectroscopy techniques have been applied to a variety of material systems to provide information that can't be known without real time direct observation at atomic scale.

In the case of SMSI, a complete structural transformation during classical SMSI state was visualized and the dependence of the surface structure on the surrounding atmosphere was explained by experimental evidence and DFT calculationsa. The shape change of the particle as a consequence of the surface layer formation was first time proposed and explained. Furthermore, through a combination of advanced *in-situ* microscopy and spectroscopy techniques, we discovered a new state of SMSI, where the existence of HCO_x-functionalized surface layer result in significant change of the selectivity of Rh particles supported on TiO_2.

In another application of $Pd@CeO_2$ core shell catalysts, an unexpected structural transformation of this novel catalyst is unarguably presented which cast doubt on the relation between the proposed core shell structure and the exceptional methane combustion property. Instead, the newly discovered structure in which ceria, palladium, and silica are all present in a very highly dispersed

form is likely to be the origin of the catalytic performance and deserves more attention and investigation.

This technique has also been applied to a catalyst system widely used in industry, Pt NPs supported on high-surface-area alumina, where energetic and kinetic parameters of Ostwald Ripening and Particle Migration and Coalescence have been extracted through tracking of individual particles under working condition. We therefore provide useful general guidelines for the preservation of high catalyst dispersion with extended time in use.

'Intelligent catalyst' catalyst system has been systematically studied by previous students in our group. Through a novel low angle tilting technique, we provided further information of the structure of the 1-2nm embedded nanoclusters, thus we are able to answer some of the unknown questions before. *In-situ* direct observation of the precipitation and dissolution processes of Rh-CTO system provides a more realistic perspective of this process, even though some very small particles, ~1nm in diameter, can undergo a few reversible cycles under large variation of oxygen potential and slow cycles but most of particle are still likely to suffer from coarsening in real exhaust stream.

The dynamical and detailed structural information provided by the above *in-situ* TEM study dramatically illustrates the value of this new technique for furthering the understanding of more subtle changes in other nanomaterial systems of interest.

6.2 Future Outlook

The research and development of gas cell technique for in-situ gas reaction has just started in the past several years and now we are happy to see a significant growing interest in this field. Instrumental improvement is still likely to be the primary driving force, ex., some catalytic processes happen very fast, thus incorporation of a camera that is fast enough to record individual steps of a complete transformation process with enough signal to noise ratio will definitely be very exciting.

Furthermore, it would be highly desirable to measure the product quantitatively while observing the structural change at atomic scale., so that a complete structure–property relation can be determined. This approach gives rise to the so-called operando methods where high efficiency spectrometer is surly needed. Vendelbo et al. provided a remarkable demonstration using a nanoreactor equipped with calorimeter and mass spectrometer to correlate the periodic faceting of the Pt nanoparticles with the periodic changes in the CO oxidation.[1] A significant implication of this study is that dynamic structure–functionality relationships in heterogeneous catalysis can now be directly determined at the atomic level under relevant reaction conditions. Crozier et al. proposed another method of using a compressed pellet in a heating holder to generate enough signal to be detected by residual gas analyzer equipped with ETEM.[2] But quantitative analysis of the mass spectrometry data from RGA in an ETEM is still limited due to inaccurate calibration and nonlinear dependence on gas concentration. EELS can also be used to quantify the gas composition in an ETEM but not in a closed cell due to the limited volume. For example, Chenna et al. used EELS core loss edge to distinguish between CO and CO_2 and further quantify the product of CO oxidation on Ru catalyst.[3] However, there's an inherent contradiction between TEM

observation and reaction product measurement since the former usually focus on individual particle while the latter is the result of the ensemble. Therefore, the correlation of the observed structural changes with the reactivity changes need to be carefully considered especially in a highly heterogonous sample. High electron dose during image acquisition my also alter the reaction in some extent that extra attention need to be paid. M. Picher et al. also demonstrate that Raman and Cathodoluminescence (CL) can also be incorporated in ESTEM.[4] The high resolution CL can be acquired simultaneously with EELS from the same area. These complementary measurements, obtained at the same time, from the same area, under controlled pressure and temperature, enable a complete characterization approach.

Besides incorporating everything into TEM where some of the functionality needs to be compromised, the combination of *in-situ* microscopy with other *in-situ* spectroscopy techniques that is conducted in a different chamber, Ex. XAS, FTIR and Raman, can also provide tremendous information of the structural and chemistry changes during a specific catalytic processes and thus cast light on the mechanisms underneath.

With the contribution of researchers from different fields, the capability of *in -situ* and operando methods to study catalysts or other nanomaterials under reaction conditions will continue to evolve and improve in the very near future.

6.3 References

1. Vendelbo, S.; Elkjær, C.; Falsig, H.; Puspitasari, I.; Dona, P.; Mele, L.; Morana, B.; Nelissen, B.; van Rijn, R.; Creemer, J. *Nature materials* **2014,** 13, 884-890.

2. Miller, B. K.; Crozier, P. A. **2014**.

3. Chenna, S.; Crozier, P. A. *ACS Catalysis* **2012,** 2, 2395-2402.

4. Picher, M.; Mazzucco, S.; Blankenship, S.; Sharma, R. *Ultramicroscopy* **2015,** 150, 10-15.

Appendix A

Improved Thermal Stability of Pd/ Al_2O_3 Catalysts by Atomic Layer Deposition

A.1 Introduction and Background

Stability issues are of great importance in emissions-control catalysis, in which high temperatures and redox cycling can lead to severe deactivation due to sintering of metal catalyst particles. A conceptually related approach to stabilizing metal catalysts involves depositing overlayers of an oxide onto a supported metal catalyst by atomic layer deposition (ALD).[1, 2] ALD can be used to prepare uniform, atomic-scale, oxide films by repeated reaction of an organometallic precursor with the substrate of interest, followed by oxidation of the surface compound.[3-5] The thickness of the oxide film is controlled by the number of deposition cycles. Sintering of Pd/Al_2O_3[4] and Ni/Al_2O_3[5] catalysts was suppressed by depositing a relatively thick alumina coating then heating the overlayers to introduce pores in the ALD overlayers. It is noteworthy that the deposited material in these two examples, along with most of the examples reported in the literature, was an inert oxide similar to the support oxide.

In our work, dissimilar functionally active oxides including zirconia and ceria overlayers were explored to stabilize the support material and further improve their catalytic performance. Zirconia overlayers were employed to stabilize the surface area of perovskite cathodes in solid oxide fuel

cells (SOFC).[6] Nanostructured cathodes exhibit better electrode performance because of the increased area for oxygen adsorption on the perovskite component, but nanostructure is difficult to maintain at the high operating temperatures. Zirconia overlayers deposited by ALD can prevent degradation of electrode performance, presumably by maintaining the initial high surface area of the perovskite. Furthermore, zirconia is already an important component in modern three-way catalysts. The high methane oxidation activity and good thermal stability of Pd@ZrO_2 catalysts also suggests that ZrO_2 may act as a promoter for Pd when there is contact between the phases. Therefore, ZrO_2 overlayer was used to coat the surface of alumina through ALD to suppress Pd sintering after high temperature calcination and enhance methane oxidation property. Ceria is well known for its exceptional Oxygen Storage Capacity (OSC) in automotive, three-way catalysts.[7-9] Therefore, the present study examined the effect of depositing thin layer of ZrO_2 onto a PdO/Al_2O_3 catalyst. The redox properties are also responsible for promotion of rates on ceria-supported metals for the CO-oxidation,[10] water-gas-shift,[11-13] methane-steam-reforming,[14, 15] and methane-oxidation reaction[16]. For CO oxidation, the rate enhancements were shown to depend on the interfacial contact between the ceria and the metal, implying that direct contact between the two phases is essential. Unfortunately, the OSC property deteriorate with sintering and crystallization through time in use.[17] Hydrothermal aging and the resulting increase in ceria crystallinity have also been shown to change the thermodynamics of CeO_2 reduction, increasing the magnitude of the heat of oxidation by as much as 50%.[18] Thus, CeO_2 was also employed to coat the surface of alumina which is approved to have comparable catalytic property with high-surface-area CeO_2 with enhanced stability. ZrO_2−PdO/Al_2O_3 related work was published in ACS Catalysis, **2015**, 5, 5696-5701. $Pd/20CeO_2$-Al_2O_3 related work was published in Catalysis B: Environmental 201, 430-437.

A2. Experimental Methods

A2. 1 Synthesis and Catalytic Measurements of $50ZrO_2{-}PdO/Al_2O_3$*

The Pd/Al_2O_3 catalysts were prepared by incipient wetness onto a γ-Al_2O_3 (Strem Chemicals, Inc.) that had been stabilized by calcining in air at 1173 K for 24 h. The aqueous Pd salt solution was prepared from 0.61 mL of $Pd(NO_3)_2$ (Sigma Aldrich, 10 wt % in 10 wt % nitric acid) and 0.60 g of citric acid (Sigma-Aldrich) in 10 mL of deionized H_2O. This Pd solution was added dropwise onto 3.0 g of the Al_2O_3, and the resulting mixture was then evaporated at 333 K until the sample was dry. Finally, the catalyst was calcined at 673 K in air for 6 h to remove any organics and nitrates. The above procedure results in a catalyst that is 1 wt % Pd.

ALD of ZrO_2 was performed using a home-built deposition system that has been described in detail in a previous publication.[19] The system consists of two heated chambers, one for the catalyst sample and one for the organometallic precursor, which could be evacuated to $\sim 10^{-3}$ Torr using a mechanical vacuum pump. High-temperature valves separated the two chambers from each other and from both the vacuum pump and a source of water vapor. In a typical experiment, the ZrO_2 precursor, (tetrakis (dimethylamino)-zirconium (TDMZ, Sigma-Aldrich)), was first evacuated then heated to 363 K to produce a TDMZ vapor pressure of ~2 Torr. The TDMZ vapor was then allowed to flow into the evacuated sample chamber, which was held at 453 K, a temperature high enough to avoid condensation of the TDMZ but low enough to prevent chemical vapor deposition. The Pd/Al2O3 samples, in either oxidized or reduced form, were exposed to TDMZ vapor for 300 s. In some cases, the samples were evacuated and exposed to TDMZ vapor multiple times to ensure that reaction with the surface was complete. After TDMZ exposure, the samples were again

evacuated and exposed to water vapor (~100 Torr) for 300 s. This procedure was repeated as often as desired. Finally, the amount of ZrO_2 deposited on the sample was determined gravimetrically. The Pd dispersions were determined volumetrically using CO adsorption uptakes at room temperature. In all cases, the samples were pretreated by oxidation in 200 Torr O_2 at 673 K, followed by reduction in 200 Torr H_2 at 423 K. Surface areas were determined from Brunauer−Emmett−Teller (BET) isotherms using N_2 adsorption at 78 K. X-ray diffraction (XRD) patterns were recorded from a Rigaku Smartlab diffractometer equipped with a Cu Kα source. The powdered samples were dispersed thoroughly onto the glass slides using acetone.

Steady-state methane oxidation rates were determined in a 0.25-in. quartz tubular reactor using 100 mg of catalyst. Helium was used as a carrier gas with the partial pressures of CH_4 and O_2 fixed at 3.8 Torr (0.5%) and 38 Torr (5%), respectively. The total flow rate was kept at 110 mL/min. The products were analyzed using a gas chromatograph (SRI8610C) equipped with a Hayesep Q column and a TCD detector. All rates in this study were normalized to the amount of Pd in the catalyst. Differential conversions were maintained in all cases.

*All the samples were synthesized and tested by Tzia Ming.

A2.2 Synthesis and Catalytic Measurement of Pd/20CeO_2-Al_2O_3

Similarly, CeO_2 precursor, Tetrakis (2,2,6,6-tetramethyl-3,5-heptanedionato) cerium, (Ce(TMHD)4, Strem Chemicals, Inc.), was heated to 453 K to produce a vapor pressure of approximately 2 Torr. During the deposition cycle, the $Ce(TMHD)_4$ vapor was introduced to the evacuated sample chamber containing approximately 0.5-g Al_2O_3. The alumina powder was exposed to the precursor vapor at 503 K for 300 s to ensure that the reaction with the surface was

complete. Because a previous study showed that the $Ce(TMHD)_4$ precursor may not be completely oxidized at 503 K,[19] in the present study, we removed the sample from the ALD systemafter evacuation and then heated it to 673 K in a muffle furnace for 5 min between exposures to the $Ce(TMHD)_4$ precursor.

To compare with the CeO_2 deposited by ALD, 0.28 g CeO_2 were added by infiltration with aqueous solutions of cerium (III) nitrate hexahydrate (10 g, $Ce(NO_3)_3 \cdot 6H_2O$, Sigma Aldrich) (Referred to here as $CeO_2(IMP)/Al_2O_3$.), and a bulk CeO_2 powder. The $CeO_2(IMP)/Al_2O_3$ was calcined to 673 K for 6 h to remove any nitrates. The CeO_2 powder was prepared by precipitating an aqueous solution of $Ce(NO_3)_3 \cdot 6H_2O$ with excess ammonium hydroxide (NH_4OH, FisherScientific).

1-wt% Pd/Al_2O_3 was prepared by similar methods as in the case of $50ZrO_2–PdO/Al_2O_3$, The elemental compositions of the samples were were measured by Inductively Coupled Plasma-Optical Emission spec-trometry (ICP-OES) performed on a Spectro Genesis spectrometerwith a concentric nebulizer. For the ICP-OES measurement, eachsample (~50 mg) was dissolved in a 5 mL solution of Aqua Regiaovernight. The solutions were then diluted with a 10 wt.%. HNO_3 solution to the appropriate concentration before the ICP analysis.

Steady-state water-gas-shift reaction rates were measured ina 0.25-inch, quartz, tubular reactor as the carrier gas with partial pressures of CO and H_2O both at 25 Torr (3.3%). The total flowrate of He was kept at 60 mL/min. Before testing, each sample was activated by heating the catalysts to 673 K in the reaction mixturebefore cooling back to the desired reaction temperature. The light-off profile CO-oxidation rates were also determined in the same flow reactor with CO and O_2 being

25 and 12.5 Torr, respectively, and the balance being He. The total flow rate of the gas mixturewas maintained at 120 mL min^{-1}. The samples tested for CO oxidation were previously heated to 1073 K in air before testing. The mass of catalyst used in every rate measurement was 0.10 g and the products were analyzed using a gas chromatograph (SRI8610C) equipped with a Hayesep Q column and a TCD detector. All rates in this study were normalized to the mass of the catalyst. Differential conversions were maintained in all cases.

*All the samples were synthesized and tested by Tzia Ming.

A2.3 Electron Microsocpy Characterization

Ex-situ transmission electron microscopy (TEM) was performed on powder specimens that had been sonicated in methanol and dropped onto carbon support films on copper TEM grids (Ted Pella, Inc.) for TEM examination. *In-situ* TEM was performed on a fresh ALD powder specimen under 150 Torr of O_2 at elevated temperature with Protochips Atmosphere system. Specimens were examined with a JEOL 3100R05 electron microscope with double spherical aberration correctors operated at 300 kV in scanning mode. The microscope is equipped with a horizontal ultrathin Window JEOL SDD X-ray detector capable of detecting elements with Z > 5 and Gatan # 965 Quantum imaging filter (GIF) for electron energy loss spectroscopy.

A.3 Results and Discussion

A3.1 50ZrO_2−PdO/Al_2O_3

To determine the growth rate for ZrO_2 films on PdO/Al_2O_3, the weight of the catalyst was measured as a function of the number of TDMZ− H_2O cycles, with the results shown in Figure A.1. It is important to note that the Al_2O_3 support used in this study had been calcined to 1173 K for

stabilization and had a surface area of only 100 m^2/g. Previous studies of an essentially identical Al_2O_3 treated in this way showed that this treatment gave rise to a material with an average pore diameter of 20 nm.[20] Because this is much greater than the size of the TDMZ precursor, the surface can be considered "flat" with respect to deposition. For the data in Figure A.1, the catalyst was removed from the ALD system after every 10th TDMZ−H_2O cycle and then calcined in flowing air at 673 K to ensure complete removal of all carbon. The data demonstrate that the mass increased linearly with the number of cycles in this coverage range, increasing by 21% after 50 cycles. Assuming that the ZrO_2 film deposits uniformly and with a density equal to that of tetragonal ZrO_2, the film growth was 0.02 nm/cycle (10 Zr atoms/nm^2 after 50 cycles).

The samples were also characterized using BET. As shown in Table 1, the surface area decreased from 100 m^2/g to 66 m^2/g after 50 deposition cycles. Also, the surface area was essentially unaffected by increasing the calcination temperature from 773 to 1073 K. The addition of 0.21 g ZrO_2/g catalyst would be expected to decrease the specific surface area from 100 to 83 m^2/g simply due to the change in mass of the sample. An additional loss in specific surface area would come from changing the average pore size of the Al_2O_3 from 20 nm to 18 nm due to the ZrO_2 coating, decreasing the expected surface area 10% so that the specific surface area would be 74 m^2/g. Since smaller pores have a disproportionally larger impact on surface area of a material with a distribution of pore sizes, coating of those smaller pores could explain the decrease to 66 m^2/g.

Scanning transmission electron microscopy (STEM) and EDS mapping also offered insights into the surface coverage of ZrO_2 on PdO/Al_2O_3. A comparison of the ALD-coated and uncoated sample after 773- and 1073-K calcination is shown in Figure A.2 a-d The PdO particles are of

comparable sizes, about 5 nm in diameter, in both the ZrO_2-coated (Figure A.2(a)) and uncoated (Figure A.2 (c)) samples after 773-K calcination. However, the sizes of PdO particles with the ZrO_2 protective layer remained unaffected after heating to 1073 K in air (Figure A.2 (b)). In contrast, the size of particles almost doubled in the uncoated PdO/Al_2O_3 sample after the same treatment. This observation is consistent with previous TEM analysis after ALD of a metal oxide was carried out.[3] In addition, sintering or signs of aggregation were frequently observed by TEM for PdO/Al_2O_3 calcined at 1073 K while these events were rarely observed with $50ZrO_2$-PdO/Al_2O_3. High angle annular dark field (HAADF) imaging, where ZrO_2 appears brighter than Al_2O_3 due to the atomic number difference between Zr and Al, allows the ZrO_2 surface layer to be distinguished from Al_2O_3, as shown in Figure A.2 (e)-(f). Here, the Al_2O_3 support appears to be covered by a uniform ZrO_2 surface layer with thickness of around 1 nm in the fresh sample without calcination. EDS elemental maps, including Pd, Zr and O, on the same sample, shown in Figure A.3, confirm that the brightness variation on Al_2O_3 is due to the presence of Zr; and they further confirm that the PdO particles are fully covered by the ZrO_2 layer, due to the coincidence of Zr and Pd in the spectra. It should be noted that Zr species, when observed under the TEM, appeared in three different forms: a thin ZrO_2 layer on the Al_2O_3 surface, a thin layer around the PdO particle, and sometimes small chunks throughout the sample.

XRD patterns from Figure A.4 confirmed that the ZrO_2 layers were initially amorphous and not crystalline. We observe that, upon heating to 773 K and 1073 K (Figure A.4(b) and 4(c) respectively), there were no observable features due to crystalline ZrO_2 from the ALD ZrO_2 samples. However, when the sample was heated to 1173 K in air (Figure A.4(d)), we observe small peaks near 30 and 50 degrees 2θ, aligned with the characteristic diffraction patterns of a tetragonal

ZrO_2 phase. The corresponding size of ZrO_2 crystallites was calculated to be around 5 nm based on the width of the peak at around 30 degrees at half maximum from the Scherrer equation. This result is consistent with the formation of thin ZrO_2 layer that forms particles upon high temperature calcination.

In-situ TEM observations revealed that the thin ZrO_2 layer on the Al_2O_3 surface actually begins to migrate and form into nano-particles at much lower temperature, 773 K, as shown in Figure A.5. Here, since the area imaged clearly contains no PdO particles initially, the particles that are observed to form with increasing time and temperature are certainly zirconia. These observations provide direct evidence for the effect of calcination temperature on catalytic activity, presented below. Finally, we also note that the ZrO_2 surface layer was not observed in many areas examined by TEM, presumably because it was too thin to detect by either HAADF imaging or EDS.

Methane oxidation was used to probe the effect of ZrO_2 films on the catalytic performance of Pd/Al_2O_3 catalysts, prepared by ALD on both oxidized and reduced catalysts. Steady state rate measurements were carried out under differential conditions in 0.5% CH_4 and 5.0% O_2 with Helium as the carrier gas. Figure A.6 is an Arrhenius plot showing rates for the unmodified Pd/Al_2O_3 sample following calcination at 773 K, 973 K, and 1073 K. The activation energies are roughly the same, 90 kJ/mol, but the rates decrease noticeably as the calcination temperature increased. The catalyst calcined at 773 K exhibited rates that were approximately five times higher than the catalyst calcined at 1073 K. This decrease in rates is at least partially explained by the increase in Pd particle size with calcination temperature observed in the TEM measurements discussed earlier. Dispersion measurements, reported in Table 2, also indicate a decrease in the

available Pd surface area, decreasing from 33% to 24% after heating the catalyst from 773 K to 1073 K. Clearly, the decrease in rates was significantly greater than the decrease in dispersion, implying that other factors must also be involved. Methane-oxidation rates have been reported to depend on Pd crystallite size[21-23] and the presence of support hydroxyls on Al_2O_3,[24, 25] but increased calcination temperature appears to influence rates by changing more than just the metal surface area.[19, 22, 26]

Rates for the sample prepared with 50 ALD cycles of ZrO_2 deposited onto the oxidized PdO/Al_2O_3 catalyst are shown in Figure A.6(b). The catalyst calcined at 773 K, designated $50ZrO_2$-PdO/Al_2O_3 (773), showed very low rates. Whereas the unmodified Pd/Al_2O_3 catalyst calcined at 773 K exhibited a rate of 10^{19} $CH_4/(s \cdot g\ Pd)$ at a temperature of 500 K, the $50ZrO_2$-PdO/Al_2O_3 (773) sample was only able to achieve this rate at 530 K through extrapolation. However, the activity of this catalyst increased dramatically with increasing calcination temperature. After heating to 1073 K, the temperature at which the rate was 10^{19} $CH_4/(s \cdot g\ Pd)$ was 485 K, indicating that $50ZrO_2$-PdO/Al_2O_3(1073) catalyst was more active than even fresh Pd/Al_2O_3. Since the STEM results indicated that the Pd particles were covered by the ZrO_2 film following ALD, it is likely the increased rates are due to breaking up of that ZrO_2 film. Again, changes in the rates were not reflected by changes in the dispersions measured by CO adsorption, shown in Table 2. The relatively high activity of the $50ZrO_2$-PdO/Al_2O_3 (1073) catalyst must be due in part to interactions with ZrO_2.

Methane-oxidation rates for a catalyst prepared by 50 ALD cycles of ZrO_2 onto reduced Pd/Al_2O_3 are shown in Figure A.6 (c). Rates for the unmodified Pd/Al_2O_3 after calcination at 773 and 1073

K are shown for comparison. Interestingly, rates on the $50ZrO_2$-Pd/Al_2O_3 samples were the same when calcined at either 773 or 1073 K. Rates were somewhat lower than for the unmodified Pd/Al_2O_3 calcined at 773 K but were stable. The measured dispersions on this catalyst were higher than that measured on $50ZrO_2$-PdO/Al_2O_3 catalysts and did not change with calcination temperature. We suggest that, in this case, the ZrO_2 film did not grow on the metallic Pd, so that there was no need to "break up" the oxide film. However, the presence of the ZrO_2 film on the Al_2O_3 does appear to thermally stabilize the Pd particles.

The structure of the oxide films prepared by ALD is clearly very different from what could be achieved by adding an oxide promoter using infiltration or co-precipitation methods. While most other methods of adding oxides will tend to form oxide particles or are limited to forming a single oxide monolayer, ALD allows formation of thin films of varying thickness. The observation from this work that ZrO_2 films could grow on PdO but not on Pd also suggests that it may be possible to deposit promoters over only selected parts of the catalyst. The present study did not explore compositional changes, but ALD clearly allows deposition of a wide range of materials.

The reason for the enhanced methane oxidation rates on the zirconia-promoted catalysts is uncertain. The literature shows that methane oxidation on Pd is a complex reaction that likely involves C-H activation on sites in the vicinity of both metallic Pd and PdO.[27] Although there is strong evidence that C-H bond activation is structure sensitive in Pd, there is controversy over whether or not particle size influences reaction rates, with some reporting that larger particles exhibit higher specific rates[21, 22] and others reporting that rates are strictly proportional to the surface area of the Pd or PdO.[28] There is agreement that PdO must be present in the active phase;

but the stability of PdO, along with the reaction rate for methane, can be influenced by the oxide support.[24-26]

Another interesting observation from the present study is that the ZrO_2 films deposited by ALD were XRD-amorphous to high temperatures. There was some evidence from TEM for changes in the film at 773 K but the crystallization is clearly suppressed. One would normally expect that thin films would be highly unstable and that the zirconia would try to minimize its free energy by forming crystalline particles. Interactions with the alumina must somehow suppress this crystallization. One would expect these effects to be strongly dependent on the thickness of the zirconia film. How important the crystalline structure for zirconia might be is uncertain. With ceria, it is well established that reducibility is affected by the crystalline structure.[9]

The mechanism by which the zirconia films stabilize Pd sintering is not completely understood. Sintering is most severe when PdO decomposes to form Pd, which normally occurs above 1073 K. While the zirconia film may simply stabilize the particles through physically covering the particles, it is also possible that the proximity between the Pd and zirconia could stabilize the PdO phase. Although there have been many studies of catalyst preparation by ALD, we believe this area of work is still in its infancy. Even considering only applications where ALD is used to add promoters to metal catalysts, there are many variables that have yet to be explored, including composition of the deposits and thickness of the films. The present work provides an example to further demonstrate the promise of this approach.

A3.2 Pd/20CeO_2-Al_2O_3

The growth rates for the CeO_2 films on γ-Al_2O_3 were determined gravimetrically by measuring the sample mass after every 5 ALD cycles, with results shown in Figure A.7. Similar to what we reported earlier for growth of ZrO_2 films by ALD on a similar alumina substrate, we observed that the sample weight increased linearly with the number of cycles. After 20 cycles, the sample (Referred to here as 20CeO_2-Al_2O_3.) had a total weight gain of approximately 28 wt%. That this weight increase corresponded to CeO_2 was confirmed by ICP analysis. Assuming that ceria forms a uniform, dense film with the bulk properties of CeO_2 over the 130-m^2/g Al_2O_3 surface, a 28-wt% loading of CeO_2 corresponds to a film thickness of 0.4 nm. The growth rate calculated from thisloading, 0.02 nm/cycle, similar to what was observed previously for ZrO_2 film growth using a similar precursor on a similar alumina substrate.

In order to verify the presence of a thin CeO_2 film, high angle annular dark field (HAADF) imaging was used to characterize the 20CeO_2-Al_2O_3 sample, as shown in Figure A.8 (a) through (d). Due to the atomic number difference between Ce and Al, CeO_2 appears brighter so the surface layer is distinguishable. The images in Figure A.8 (a) and b were obtained on the fresh sample calcined at 673 K and show that the Al_2O_3 is covered by a relatively uniform CeO_2 film with a thickness close to the expected 0.5nm. Not surprisingly for deposition on curved surfaces, some slightly larger CeO_2 particles are observed at the higher magnification. The images in Figures A. 8c and 8d show the same sample after calcination to 1073 K. Under low magnification, Figure A.8c, the entire surface of the support still appears to be covered with CeO_2. However, small particles, less than 5-nm in size, were also observed at high magnification, Figure A.8d, along with areas that still show the presence of a CeO_2 film.

The morphology of the $20CeO_2$-Al_2O_3 sample was clearly different from that from the CeO_2/Al_2O_3(IMP) sample, obtained by infiltration with aqueous solutions $Ce(NO_3)_3$ onto the same Al_2O_3. The images in Figures A.8(e) and (f) were obtained on CeO_2/Al_2O_3(IMP), which had the same weight loading of CeO_2, after calcination to 673 K. The images show that the CeO_2 exists as 20-nm clusters of roughly 3-nm particles, even after this low calcination temperature. Furthermore, most of the Al_2O_3 remains uncovered by CeO_2. It should be acknowledged that we did not attempt to optimize the impregnation procedure maximize the CeO_2 dispersion.

XRD patterns of the $20CeO_2$-Al_2O_3 sample are shown as a function of calcination temperature in Figure A.9, together with the pattern for the untreated Al_2O_3, Figure A.9(a) and the pattern for the CeO_2/Al_2O_3(IMP) sample, Figure A.9(e). First, it is worth noting that the diffraction pattern of the infiltrated sample with the same CeO_2 loading and calcined to only 673 K, Figure A.9(e), is very different. The peaks associated with CeO_2 dominate on CeO_2/Al_2O_3(IMP), to the point that the peaks from Al_2O_3 are difficult to see on the same scale due to the larger X-Ray scattering cross section for Ce compared to Al. Even for this relatively low calcination temperature, the CeO_2 domain size, calculated using the Scherrer Equation and the peak width at 28 degrees 2θ, was already 10 nm. By comparison, there is no evidence for the presence of CeO_2 in the $20CeO_2$-Al_2O_3 from the diffraction results after calcination at 873 K, Figure A.9(b). This is consistent with the fact that the domain size for ceria in these samples is very small. Features associated with CeO_2 begin to appear near 28 and 58 degrees 2θ in the diffraction pattern of the sample calcined to 1073 K, Figure A.9(c), and become more prominent after calcination at 1173 K, Figure A.9(d). However, the intensity of the CeO_2 peaks remains weak, implying that much of the CeO_2 is not

contributing. Based on diffraction peak widths, the crystallite size of CeO_2 particles was only 8 nm, even after calcination to 1173 K.

To determine how modification of the Al_2O_3 support by CeO_2 ALD affects the catalyst-support properties, we examined a series of 1-wt% Pd catalysts prepared from the unmodified γ-Al_2O_3, from the CeO_2 powder, from the CeO_2/Al_2O_3(IMP) sample, and from the $20CeO_2$-Al_2O_3 sample. It is first interesting to compare the BET surface areas of 1-wt Pd/CeO_2 powder and 1-wt% $Pd/20CeO_2$-Al_2O_3 as a function of calcination temperature. These results are reported in Table A.3. Because the γ-Al_2O_3 used here was initially heated to 1173 K, its surface area was only 130 m^2/g. The addition of 20 cycles of CeO_2 by ALD and of 1-wt% Pd by infiltration reduced this to 82 m^2/g. Most of this decrease in specific surface area can be accounted for by the addition of 0.28-g CeO_2 and 0.01-g Pd per gram of catalyst (130 m^2/1.29 g = 100 m^2/g). The additional decrease in specific surface area is likely due to a decreased average pore diameter as the pores of the γ-Al_2O_3 are coated with a nonporous, 0.4-nm film. Calcination of this sample to 1073 K had essentially no effect on the surface area. By contrast, the specific surface area of the Pd/CeO_2 powder decreased from a value of 46 m^2/g after calcination to 673 K, to 42 m^2/g 773 K and 18 m^2/g at 1073 K.

Pd dispersion measurements were also performed as a function of calcination temperature on the Pd/γ-Al_2O_3, Pd/CeO_2, and $Pd/20CeO_2$-Al_2O_3 samples, with results shown Table A.4. The data indicate that there was a fairly significant loss of Pd dispersion with calcination temperature on the Pd/γ-Al_2O_3 sample, from 34% after 773 K and 24% after 1073 K. Given the significant loss in total surface area of Pd/CeO_2, the decrease in dispersion from 40% to 30% in this temperature

range is small, indicating that CeO_2 likely helps maintain dispersion.[29] The Pd dispersion on $Pd/20CeO_2$-Al_2O_3 was 65% following catalyst treatment at 773 K and did not change significantly with calcination.

It has been suggested that sites of contact between Pd and ceria are especially active for the WGS reaction due the ability of reduced ceria to be oxidized by water, then transfer either oxygen or OH to CO that is adsorbed on the Pd.[11, 12] Based on this picture, WGS rates provide information about whether Pd is in contact with CeO_2 in composite materials. Therefore, differential WGS rates were measured for the $Pd/20CeO_2$-Al_2O_3, Pd/CeO_2, Pd/Al_2O_3 and Pd/CeO_2(IMP)/Al_2O_3 catalysts. The data obtained following calcination of the catalysts 773 K are shown in Figure A.10(a). Rates on Pd/CeO_2 were almost 10 times higher than those on Pd/Al_2O_3, as expected. What is more interesting is that the differential rates on Pd/CeO_2 were nearly indistinguishable from rates on $Pd/20CeO_2$-Al_2O_3. Because the ALD-prepared sample is completely covered with CeO_2, its catalytic properties are nearly identical to those of a conventional CeO_2-supported catalyst. Since the Pd dispersions on Pd/CeO_2 and $Pd/20CeO_2$-Al_2O_3 are also reasonably close for 773-K calcination, the number of contact sites between Pd and ceria are also similar. Rates on Pd/CeO_2(IMP)/Al_2O_3 are approximately 2 times lower, probably because some of the Pd particles are not in contact with CeO_2. Larger differences in the WGS rates were observed between the samples after the samples were calcined at 1073 K, as shown in Figure A.10(b). Most significantly, rates on the $Pd/20CeO_2$-Al_2O_3 sample remain unchanged. This is consistent with the observations that increased calcination temperature did not affect either the surface area or the Pd dispersion. The fact that the rates remain unchanged implies that contact between Pd and ceria also remains good. Rates on Pd/CeO_2 decreased by a factor of about three after heating to higher temperatures,

an amount that is too large to be explained entirely by the lower Pd dispersion. Because loss in ceria surface area is associated with an increase in crystallite size and larger ceria crystallites are considered to be less reducible, it is possible that the decrease in rates is associated with a change in the ceria reducibility. An even larger drop in rates occurs with the $Pd/CeO_2(IMP)/Al_2O_3$ sample, possibly due to a loss in interfacial contact between the Pd and the ceria component of the support.

To further probe the catalytic properties of these catalysts, we measured light-off rates for CO oxidation on the $Pd/20CeO_2$-Al_2O_3, Pd/CeO_2 and Pd/Al_2O_3 samples after they had been calcined to 1073 K in air. These results are shown in Figure A.11. The light-off temperatures correspond reasonably well with the relative WGS rates. The $Pd/20CeO_2$-Al_2O_3 sample was by far the most active, followed by the Pd/CeO_2 and Pd/Al_2O_3 samples. Again, the higher rates on $Pd/20CeO_2$-Al_2O_3 are an indication of good contact between Pd and ceria.

The redox properties of $Pd/20CeO_2$-Al_2O_3, Pd/CeO_2 and Pd/Al_2O_3 samples were probed using alternating CO and O_2 pulses at 673 K. Figure A.12 shows a comparison of results for the $Pd/20CeO_2$-Al_2O_3 and Pd/Al_2O_3 catalysts, while a summary of the quantities of oxygen that could be added and removed from the samples is reported in Table A.5. In Figure A.12, the regions between the dashed lines correspond to when either 10% O_2 (m/e = 32) or 10% CO (m/e = 28) was added to the He passing over the catalyst. The observation of CO_2 (m/e =44) upon exposure of the catalyst to CO is due to reduction of the catalyst. Formation of CO_2 during the O_2 pulse on $Pd/20CeO_2$-Al_2O_3, but not on Pd/Al_2O_3, sample is due to decomposition of carbonates that form on reduced ceria.[12] In the calculation of oxygen capacitance, the CO_2 from both the CO and O_2 pulses were added in determining the capacitance. A sample with 1-wt% Pd can provide 94 μmol/g

of atomic oxygen by reduction of PdO. For bulk CeO_2, complete reduction to Ce_2O_3 removes 2900 μmol/g of oxygen. The amounts oxygen removed from the Pd/Al_2O_3 sample, 87 μmol/g of CO_2, are within experimental error of the amount expected. Results for $Pd/20CeO_2$-Al_2O_3 and Pd/CeO_2 were similar, forming 220 and 160 μmol/g of CO_2 respectively. In both cases, the ceria in contact with the Pd must be undergoing oxidation and reduction.

Finally, in order to compare the surface chemistry of $20CeO_2$-Al_2O_3 and bulk CeO_2, we performed FTIR measurements on the Pd/ceria and $Pd/20CeO_2$-Al_2O_3 catalysts after they had been reduced in 10% CO-He mixtures. As mentioned above, this treatment is expected to reduce the ceria surface and form carbonates. As shown by the spectra in Figure A.13, this is exactly what is observed on both samples. They both exhibit broad features between 1300 and 1700 cm^{-1} that correspond to the carbonates. Because absorption in the IR region is strong on bulk CeO_2, the spectrum on $Pd/20CeO_2$-Al_2O_3 is simpler. The results suggest that the ALD-modified sample could be convenient, model system for spectroscopic characterization.

The present results indicate that it is possible to prepare a support material with the catalytic, promotional properties of ceria by depositing a thin conformal layer of CeO_2 onto a high-surface-area Al_2O_3 using Atomic Layer Deposition. When used as a support for Pd, the thin CeO_2 film has a similar effect on the water-gas-shift and CO-oxidation reactions as bulk CeO_2. The ALD-modified support has advantages over bulk ceria in that the underlying Al_2O_3 provides surface area for the CeO_2 and stabilizes that area to high-temperature calcination.

The thin-film, CeO_2-coated Al_2O_3 morphology would be difficult to achieve using conventional methods. With normal infiltration of Ce salts onto Al_2O_3, particles tend to form clusters during the

drying or precipitation steps. Similarly, co-precipitation of alumina and ceria will tend to form a mixture of particles in which a large fraction of the surface will be Al_2O_3. As we have seen in the present study, these materials are not as effective as bulk CeO_2, probably because supported metals will distribute between the Al_2O_3 and CeO_2 phases. In this regard, ALD may be unique in providing this hierarchical structure.

The CeO_2 films that were formed by ALD showed surprising good thermal stability upon calcination. Even after calcination to 1173 K, the diffraction peaks for CeO_2 were weak compared to what was observed for a CeO_2/Al_2O_3 formed by infiltration with a similar CeO_2 loading. It is possible that spatial isolation is responsible for maintaining the small crystallites but surface energies may also be responsible. Although CeO_2 does not react with Al_2O_3, Ce^{+3} can form a $CeAlO_3$ perovskite structure. It is therefore possible that there could be bonding interactions at the CeO_2-Al_2O_3 interface. High-temperature reducing conditions could be a problem if compound formation were to occur.

Finally, it interesting to note that the ALD approach for making "coated" supports is quite general and could be used to make other high-surface-area, functional supports. This opens up a number of opportunities. An obvious extension to the work in this paper would be to prepare CeO_2-ZrO_2, mixed-oxide films. While the mixed oxides are used in today's automotive catalysts, the surface areas are reported to drop below 2 m^2/g.[30, 31] Maintaining a higher surface area could enhance the properties of the mixed oxide. In another example, researchers at Daihatsu reported that perovskite-supported catalysts can exhibit very attractive properties;[32, 33] however, because most perovskite powders have very low surface areas, it may not be possible to take full advantage of

this fact. Preparation of a perovskite film on a support could allow the attractive properties of the perovskite to be used to full advantage.

A.4 Summary

ALD can be used to form thin, conformal overlayers on porous Al_2O_3, and the composites formed in this way can be used as catalyst supports for Pd. In the case of $50ZrO_2{-}PdO/Al_2O_3$, the ZrO_2 overlay stabilize Pd against sintering at high temperatures and enhance the methane oxidation activity of these catalysts following high-temperature calcination. In the case of *Pd/20CeO₂-Al₂O₃*, the supported Pd catalysts prepared from the ALD-modified supports exhibit similar water-gas-shift rates to those obtained on conventional Pd/CeO_2 catalysts, implying that there is good contact between the Pd and the CeO_2. The ALD-prepared catalysts have much better thermal stability than conventional CeO_2 supports due to the underlying Al_2O_3.

So far, *Ex-situ* STEM imaging combined with EDS or EELS mapping is the best way to directly visualize the overlayer and confirm the uniformity of the deposition. It can also provide information regarding thickness and the chemical state of the elements present in the overlayer indicating the interaction with the support underneath. *In-situ* calcination is a powerful tool to direct visulize the structure transformation of the ALD coated catalyst upon high temperatrue calcination which can provide direct information of the role of the ALD layer in stablizing the catlayst system.

A.5 References

1. Johnson, R. W.; Hultqvist, A.; Bent, S. F. *Mater. Today* **2014,** 17, 236-246.

2. O'Neill, B. J.; Jackson, D. H.; Lee, J.; Canlas, C.; Stair, P. C.; Marshall, C. L.; Elam, J. W.; Kuech, T. F.; Dumesic, J. A.; Huber, G. W. *ACS Catalysis* **2015,** 5, 1804-1825.

3. O'Neill, B. J.; Jackson, D. H.; Crisci, A. J.; Farberow, C. A.; Shi, F.; Alba-Rubio, A. C.; Lu, J.; Dietrich, P. J.; Gu, X.; Marshall, C. L. *Angew. Chem.* **2013,** 125, 14053-14057.

4. Lu, J.; Fu, B.; Kung, M. C.; Xiao, G.; Elam, J. W.; Kung, H. H.; Stair, P. C. *Science(Washington)* **2012,** 335, 1205-1208.

5. Gould, T. D.; Izar, A.; Weimer, A. W.; Falconer, J. L.; Medlin, J. W. *Acs Catalysis* **2014,** 4, 2714-2717.

6. Gong, Y.; Palacio, D.; Song, X.; Patel, R. L.; Liang, X.; Zhao, X.; Goodenough, J. B.; Huang, K. *Nano Lett.* **2013,** 13, 4340-4345.

7. Bunluesin, T.; Gorte, R.; Graham, G. *Applied Catalysis B: Environmental* **1997,** 14, 105-115.

8. Gandhi, H.; Graham, G.; McCabe, R. W. *J. Catal.* **2003,** 216, 433-442.

9. Gorte, R. J. *AlChE J.* **2010,** 56, 1126-1135.

10. Bunluesin, T.; Putna, E.; Gorte, R. *Catal. Lett.* **1996,** 41, 1-5.

11. Bunluesin, T.; Gorte, R.; Graham, G. *Applied Catalysis B: Environmental* **1998,** 15, 107-114.

12. Wang, X.; Gorte, R. J.; Wagner, J. *J. Catal.* **2002,** 212, 225-230.

13. Kalamaras, C. M.; Americanou, S.; Efstathiou, A. M. *J. Catal.* **2011,** 279, 287-300.

14. Craciun, R.; Daniell, W.; Knözinger, H. *Applied Catalysis A: General* **2002,** 230, 153-168.

15. Feio, L.; Hori, C.; Damyanova, S.; Noronha, F.; Cassinelli, W.; Marques, C.; Bueno, J. *Applied Catalysis A: General* **2007,** 316, 107-116.

16. Cargnello, M.; Doan-Nguyen, V. V.; Gordon, T. R.; Diaz, R. E.; Stach, E. A.; Gorte, R. J.; Fornasiero, P.; Murray, C. B. *Science* **2013,** 341, 771-773.

17. He, B. J.-J.; Wang, C.-X.; Zheng, T.-T.; Zhao, Y.-K. *Johnson Matthey Technology Review* **2016,** 60, 196-203.

18. Zhou, G.; Shah, P. R.; Montini, T.; Fornasiero, P.; Gorte, R. J. *Surf. Sci.* **2007,** 601, 2512-2519.

19. Anthony, S. Y.; Küngas, R.; Vohs, J. M.; Gorte, R. J. *J. Electrochem. Soc.* **2013,** 160, 1225-1231.

20. Farrauto, R. J.; Hobson, M.; Kennelly, T.; Waterman, E. *Applied Catalysis A: General* **1992,** 81, 227-237.

21. Briot, P.; Primet, M. *Applied catalysis* **1991,** 68, 301-314.

22. Stakheev, A. Y.; Batkin, A.; Teleguina, N.; Bragina, G.; Zaikovsky, V.; Prosvirin, I.; Khudorozhkov, A.; Bukhtiyarov, V. *Top. Catal.* **2013,** 56, 306-310.

23. Müller, C. A.; Maciejewski, M.; Koeppel, R. A.; Baiker, A. *Catal. Today* **1999,** 47, 245-252.

24. Schwartz, W. R.; Ciuparu, D.; Pfefferle, L. D. *The Journal of Physical Chemistry C* **2012,** 116, 8587-8593.

25. Ciuparu, D.; Perkins, E.; Pfefferle, L. *Applied Catalysis A: General* **2004,** 263, 145-153.

26. Farrauto, R. J.; Lampert, J. K.; Hobson, M. C.; Waterman, E. M. *Applied Catalysis B: Environmental* **1995,** 6, 263-270.

27. Fujimoto, K.-i.; Ribeiro, F. H.; Avalos-Borja, M.; Iglesia, E. *J. Catal.* **1998,** 179, 431-442.

28. Zhu, G.; Han, J.; Zemlyanov, D. Y.; Ribeiro, F. H. *J. Am. Chem. Soc.* **2004,** 126, 9896-9897.

29. Jones, J.; Xiong, H.; DeLaRiva, A. T.; Peterson, E. J.; Pham, H.; Challa, S. R.; Qi, G.; Oh, S.; Wiebenga, M. H.; Hernández, X. I. P. *Science* **2016,** 353, 150-154.

30. Voorhoeve, R.; Johnson, D.; Remeika, J.; Gallagher, P. *Science* **1977,** 195, 827-833.

31. Singh, U. G.; Li, J.; Bennett, J. W.; Rappe, A. M.; Seshadri, R.; Scott, S. L. *J. Catal.* **2007,** 249, 349-358.

32. Nishihata, Y.; Mizuki, J.; Akao, T.; Tanaka, H.; Uenishi, M.; Kimura, M.; Okamoto, T.; Hamada, N. *Nature* **2002,** 418, 164-167.

33. Tanaka, H.; Tan, I.; Uenishi, M.; Kimura, M.; Dohmae, K. *Top. Catal.* **2001,** 16, 63-70.

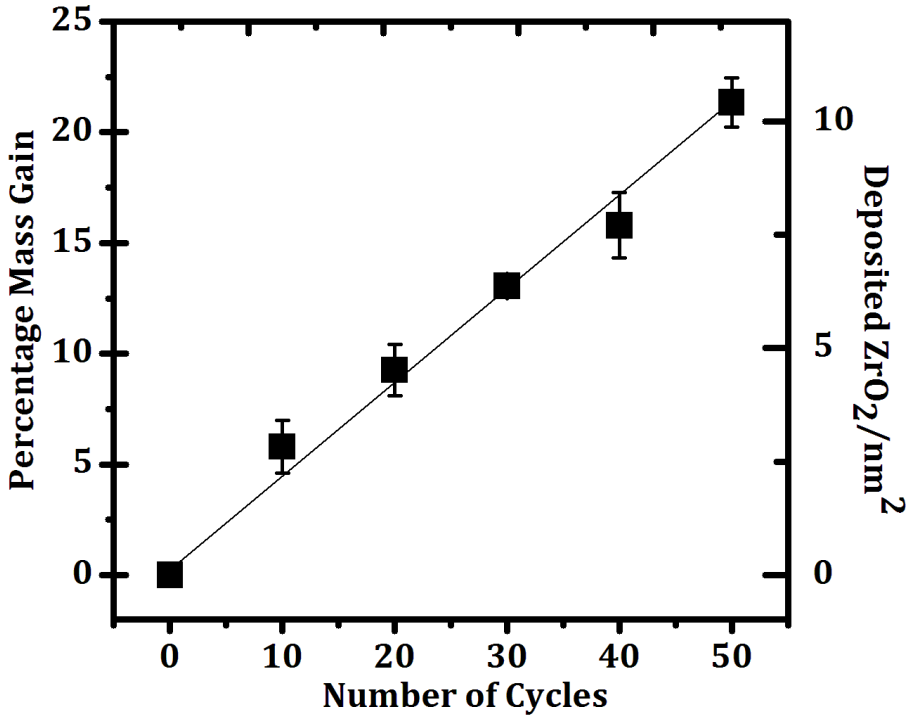

Figure A.1 Mass change as a function of the number of ALD cycles on a PdO/Al_2O_3 catalyst which had an initial surface area of 100 m^2/g. (Data is from ACS Catalysis, **2015**, 5, 5696-5701, taken by Tzia Ming Onn.)

Table A.1 BET surface areas of ZrO_2 ALD related samples

Support	**BET Surface Area (m^2/g)**	
Al_2O_3	100	
Calcination Temp	**PdO/Al_2O_3**	**$50ZrO_2$-PdO/Al_2O_3**
773 K	100	66
973 K	100	66
1073 K	100	70

(Data is from ACS Catalysis, **2015**, 5, 5696-5701, taken by Tzia Ming Onn)

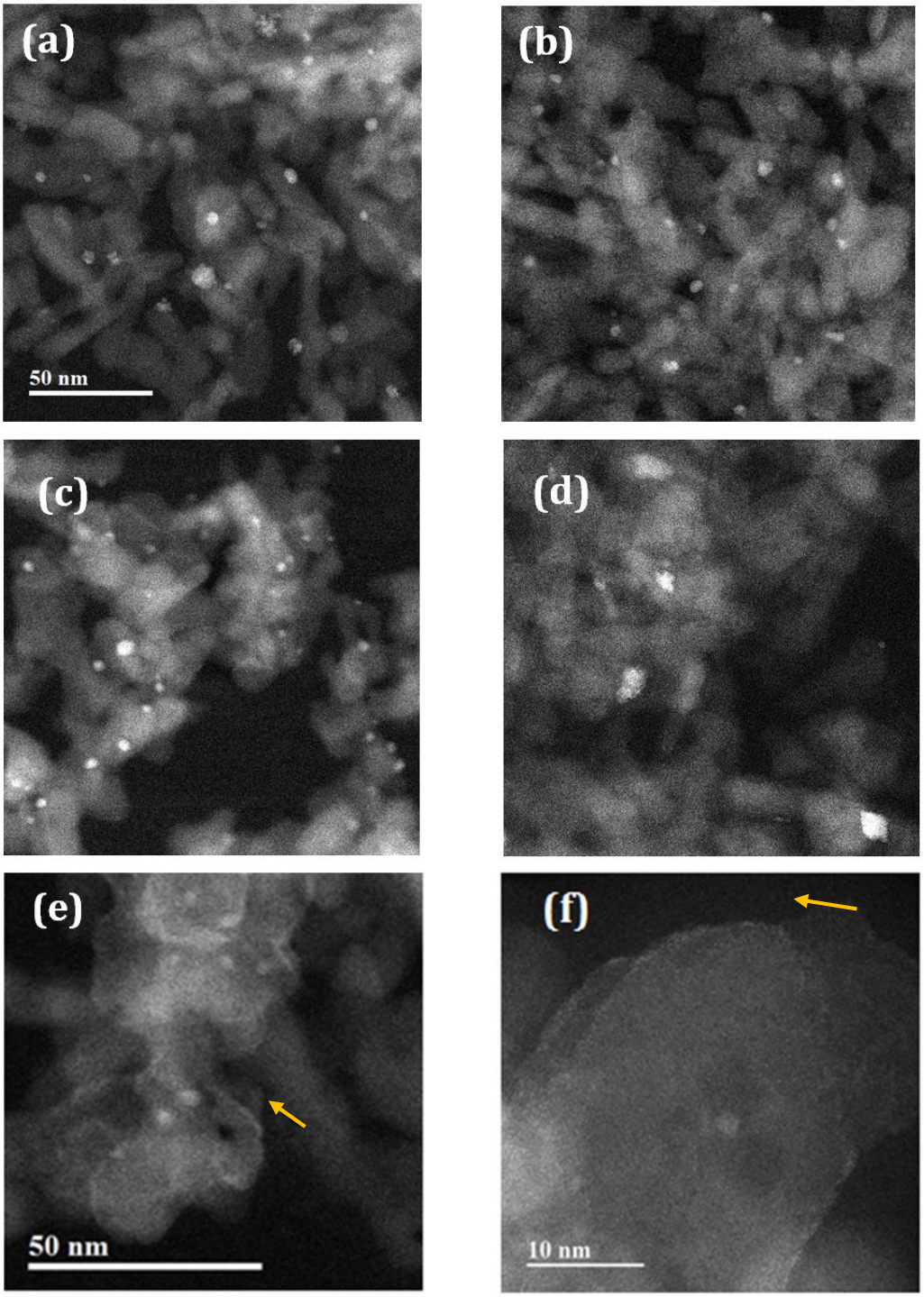

Figure A.2 STEM results for PdO/Al_2O_3 and $50ZrO_2$-PdO/Al_2O_3 catalysts after various pretreatments: (a) $50ZrO_2$-PdO/Al_2O_3 calcined at 773 K; (b) $50ZrO_2$-PdO/Al_2O_3 calcined at 1073 K; (c) PdO/Al_2O_3 calcined at 773 K; (d) PdO/Al_2O_3 calcined at 1073 K; (e) and (f) $50ZrO_2$-PdO/Al_2O_3 uncalcined (fresh). Arrows in (e) and (f) indicate regions of high contrast due to the ZrO_2 overlayer. (Data is from ACS Catalysis, **2015**, 5, 5696-5701.)

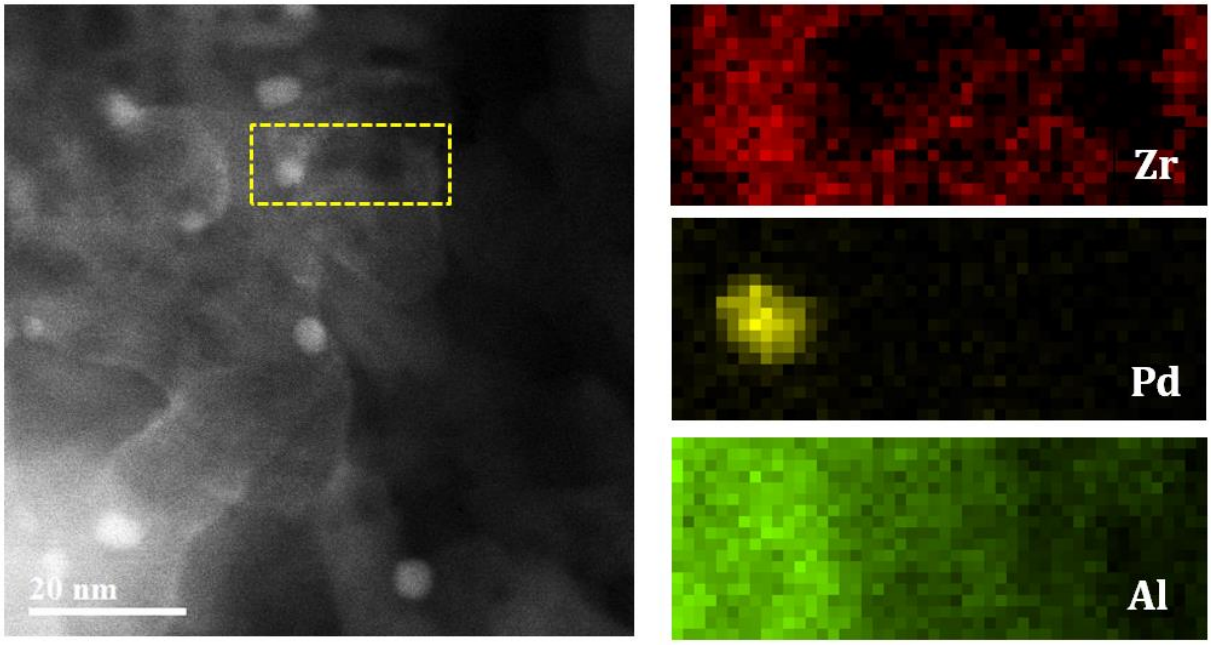

Figure A.3 STEM results for uncalcined (fresh) $50ZrO_2$-PdO/Al_2O_3 catalysts with EDS mapping of Al, Zr, and Pd. (Data is from ACS Catalysis, **2015**, 5, 5696-5701)

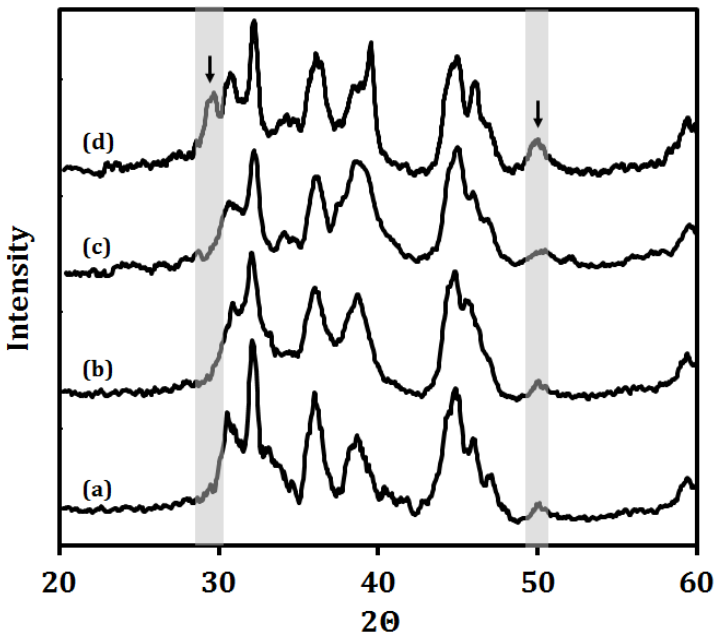

Figure A.4 XRD patterns of the ALD-coated, $50ZrO_2$-PdO/Al_2O_3 sample after calcination to various temperatures: (a) as deposited; (b) 773 K; (c) 1073 K; (d) 1173 K. Characteristic peaks for tetragonal ZrO_2 are marked by the grey lines. (Data is from ACS Catalysis, **2015**, 5, 5696-5701, taken by Tzia Ming Onn)

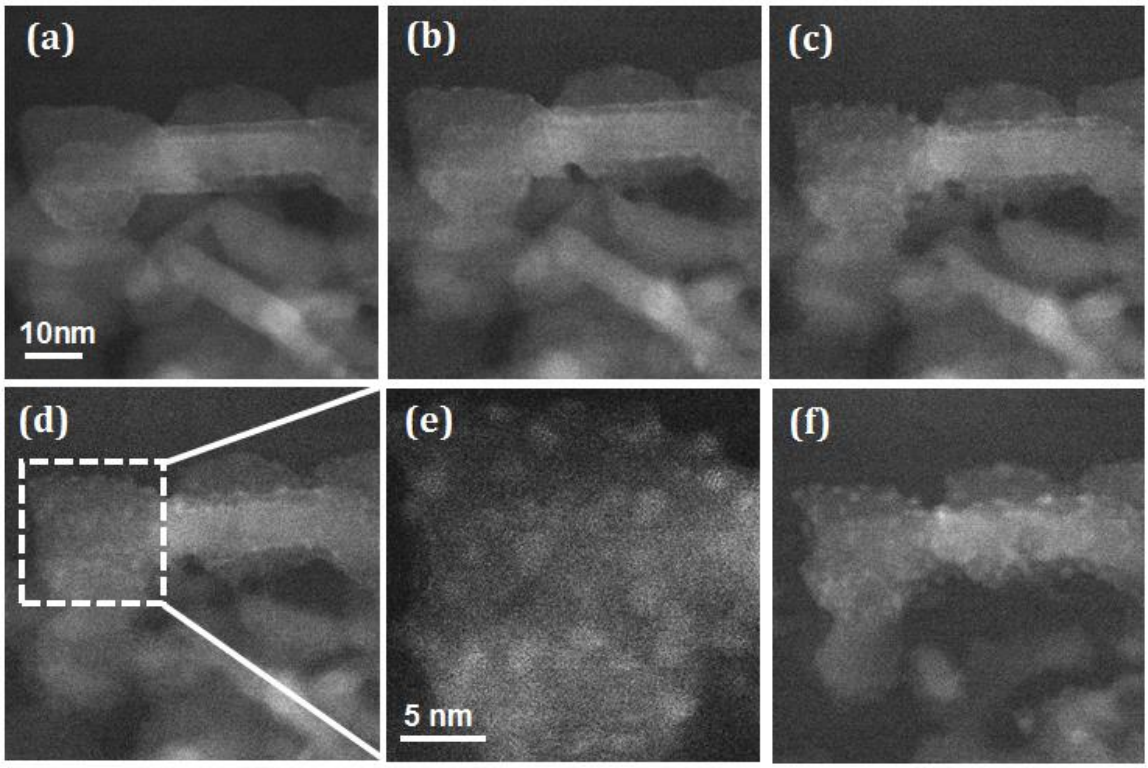

Figure A.5 Sequential STEM images of uncalcined (fresh) $50ZrO_2$-PdO/Al_2O_3 catalysts obtained in-situ under 150 Torr O_2 in the TEM gas cell at a temperature of: (a) 573 K, (b)-(c) 773 K for 0 and 3 min respectively, (d)-(e) 873 K, and (f) 973 K. (Data is from ACS Catalysis, **2015**, 5, 5696-5701.)

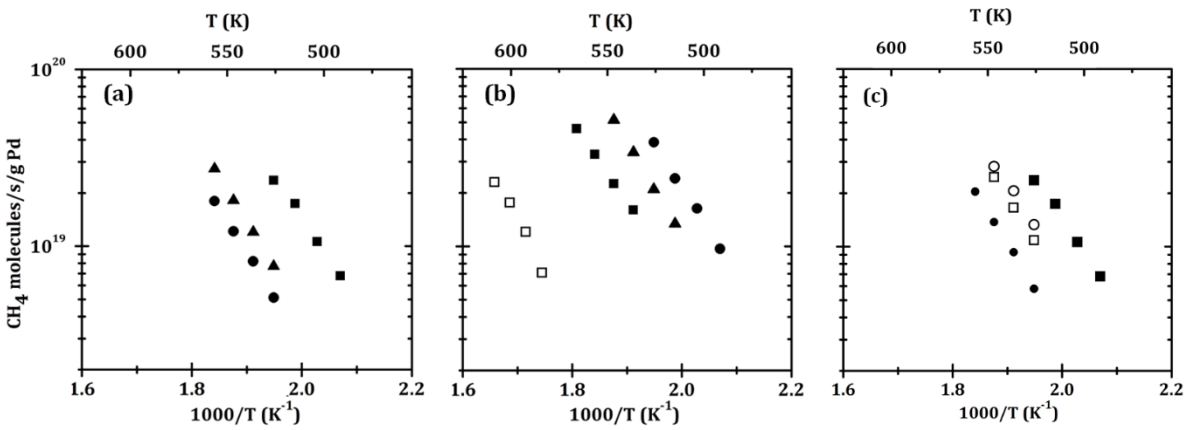

Figure A.6 Steady-state, differential reaction rates for methane oxidation in 0.5% CH_4 and 5% O_2. (a) Rates on PdO/Al_2O_3 after calcination to the following temperatures: (■) – 773 K, (▲) – 973 K, and (●) – 1073 K. (b) Rates on $50ZrO_2$-PdO/Al_2O_3 after calcination to the following temperatures: (□) – uncalcined, (■) – 773 K, (▲) – 973 K, and (●) – 1073 K. (c) Rates on $50ZrO_2$-Pd/Al_2O_3, in which ZrO_2 was deposited on the reduced catalysts by ALD, after calcination at (□) – 773 K and (○) – 1073 K. Data for PdO/Al_2O_3 calcined (■) – 773 K and (●) – 1073 K are shown for comparison. (Data is from ACS Catalysis, **2015**, 5, 5696-5701, taken by Tzia Ming Onn)

Table A.2: Pd metal dispersions of ZrO_2 ALD related samples

	Dispersion (%)		
Calcination Temp	**PdO/Al_2O_3**	**$50ZrO_2$-PdO/Al_2O_3**	**$50ZrO_2$-Pd/Al_2O_3**
773 K	32.9	10.6	18.5
973 K	29.8	10.8	
1073 K	24.2	13.2	18.6

(Data is from ACS Catalysis, **2015**, 5, 5696-5701, taken by Tzia Ming Onn)

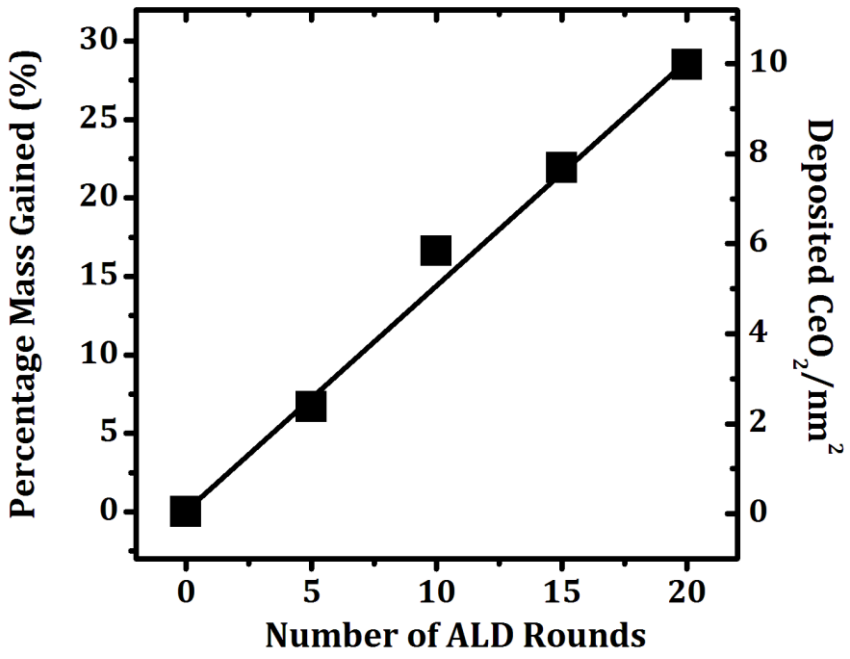

Figure A.7 Mass change as a function of the number of CeO_2 ALD cycles on an Al_2O_3 support which had an initial surface area of 130 m^2/g. (Data is from Applied Catalysis B: Environmental **2017**, 201, 430-437.)

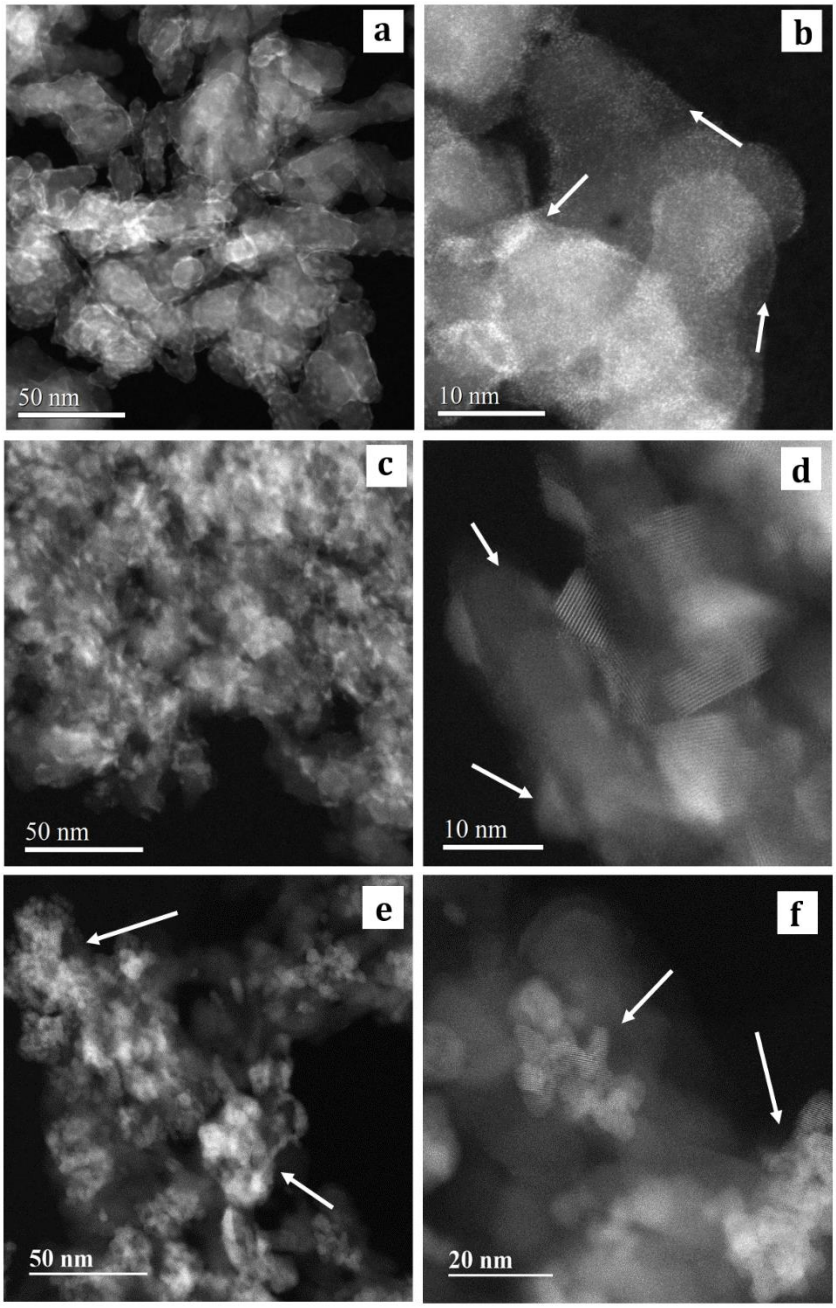

Figure A.8 HAADF image of ALD 20CeO_2-Al_2O_3 sample after calcination at 673 K (a-b) and 1073 K (c-d), showing that the uniform atomic CeO_2 layer made through ALD deposition evolved into a mixture of 5-nm CeO_2 particles and CeO_2 film after 1073 K calcination. Impregnated sample after calcination at 673 K (e-f) are shown for comparison. CeO_2 particles appear in chunks, ~20-nm in size, and they do not cover the surface uniformly. CeO_2 appear to be brighter features in all the six images. (Images are from Applied Catalysis B: Environmental **2017**, 201, 430-437.)

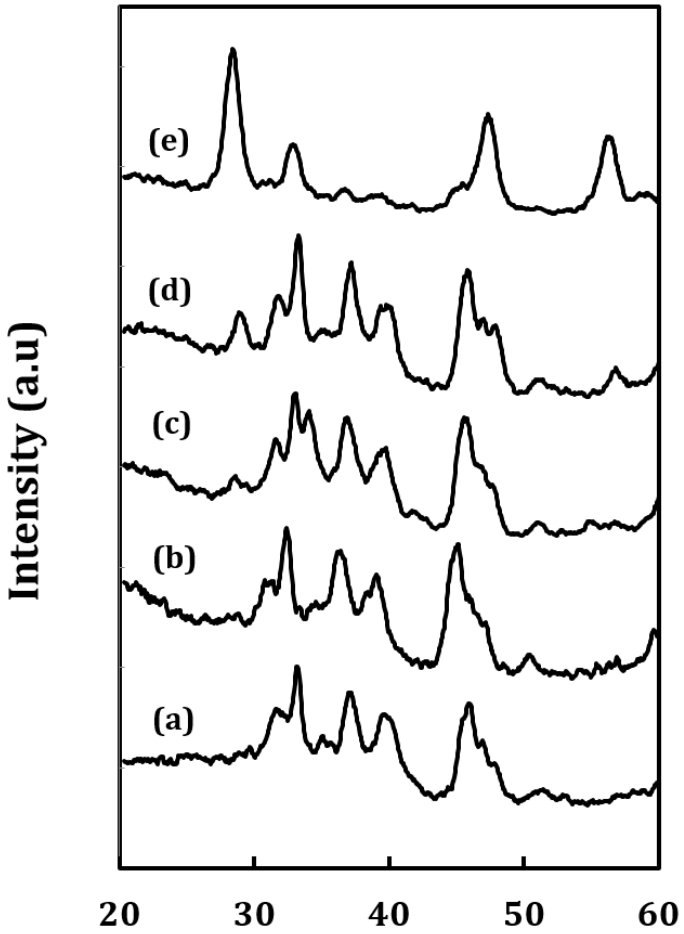

Figure A.9 XRD patterns of the (a) uncoated Al_2O_3 support heated to 1173 K ALD-coated, 20CeO_2 -Al_2O_3 sample after calcination to various temperatures: (b) 873 K; (c) 1073 K; (d) 1173 K, and (e) CeO_2(IMP)/Al_2O_3 heated to 673 K. Characteristic peaks for CeO_2 are marked by the grey line. (Data is from Applied Catalysis B: Environmental **2017**, 201 430-437, taken by Tzia Ming Onn)

Table A.3: BET Surface Area of CeO_2 ALD related samples as a function of Calcination Temperature. The surface area of the Alumina support is 130 m^2/g.

	BET Surface Area (m^2/g)		
Calcination Temperature (K)	**Pd/CeO_2**	**$Pd/20CeO_2$-Al_2O_3**	**Pd/CeO_2(IMP)/Al_2O_3**
773	42	82	110
973	30	78	100
1073	18	84	100

(Data is from Applied Catalysis B: Environmental **2017**, 201, 430-437, taken by Tzia Ming Onn)

Table A.4: Pd metal dispersions of CeO_2 ALD related samples

Calcination Temperature (K)	Pd/CeO_2	Pd/20CeO_2-Al_2O_3	Pd/Al_2O_3	Pd/CeO_2(IMP)/Al_2O_3
773	40	65	34	9
973	35	63	30	
1073	30	59	24	6

(Data is from Applied Catalysis B: Environmental **2017**, 201, 430-437, taken by Tzia Ming Onn)

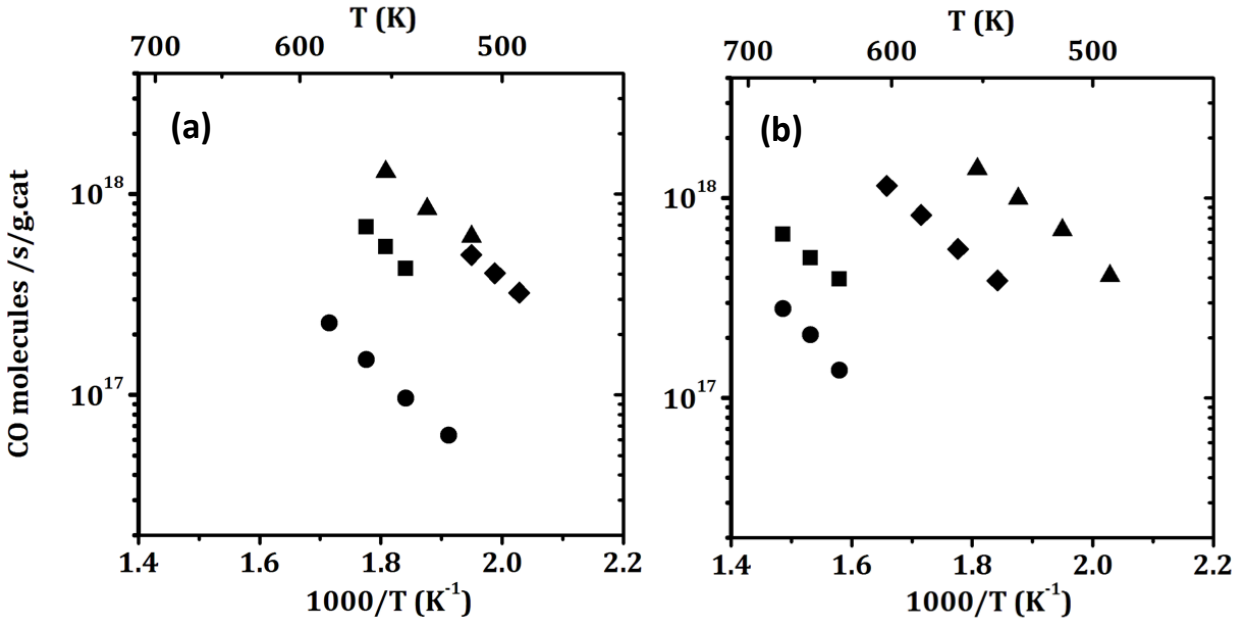

Figure A.10 Steady-state, differential reaction rates for water gas shift (WGS) reaction with partial pressure of CO and H_2O both at 25 Torr. The total flow rate, in this case, was kept at 60 mL/min. WGS rates after pretreatment calcination to (a) 773 K and (b) 1073 K were compared for the following catalysts: (▲) – Pd/2OCeO_2-Al_2O_3 (♦) – Pd/CeO_2, (■) Pd/CeO_2 (Impregnated) /Al_2O_3, and (●) – Pd/Al_2O_3. .(Data is from Applied Catalysis B: Environmental **2017**, 201, 430-437, taken by Tzia Ming Onn)

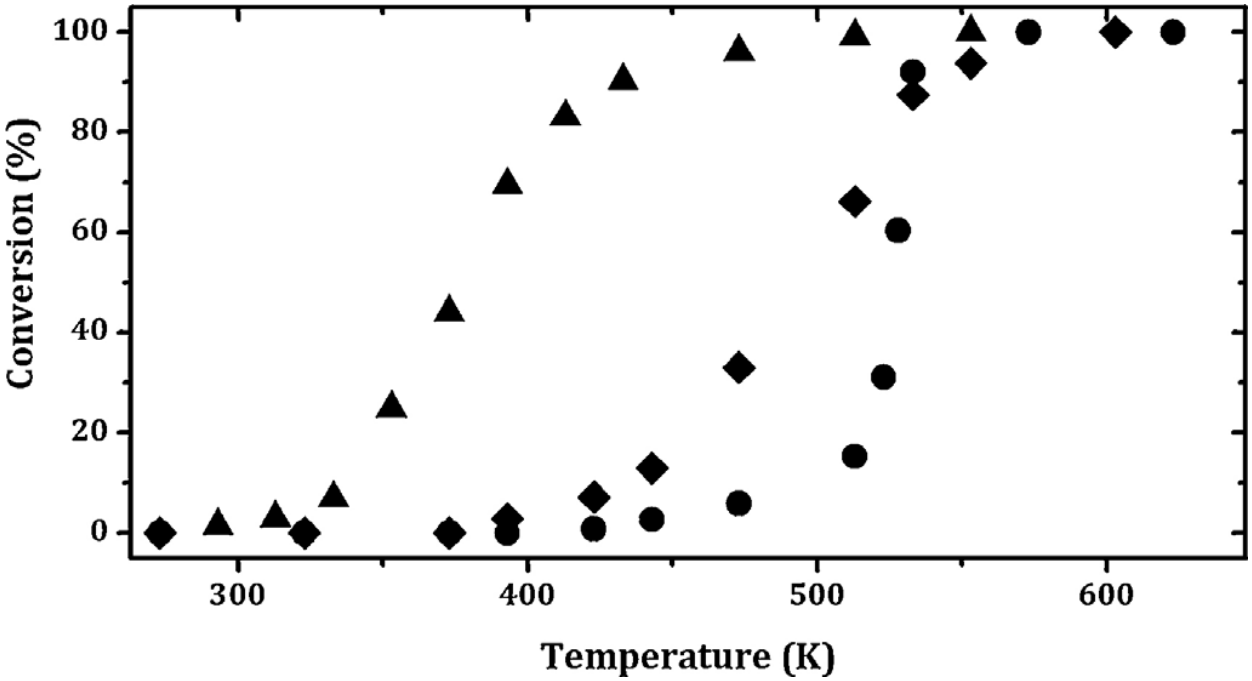

Figure A.11 Light-off curves of CO conversion against temperature for : (▲) – Pd/2OCeO_2-Al_2O_3, (♦) – Pd/CeO_2, and (●) – Pd/Al_2O_3 calcined at 1073 K. CO Oxidation reaction was carried out with partial pressure of CO and O_2 at 25 Torr and 12.5 Torr respectively. (Data is from Applied Catalysis B: Environmental **2017**, 201, 430-437, taken by Tzia Ming Onn)

Table A.5: Redox data for the pulse-reactor measurements performed at 673 K using CO-O_2 pulses over the samples.

Sample	**Average CO_2 (μmol/g) formed from CO pulse**
Pd/20CeO_2-Al_2O_3	220
Pd/CeO_2	160
Pd/Al_2O_3	87

(Data is from Applied Catalysis B: Environmental **2017**, 201, 430-437, taken by Tzia Ming Onn)

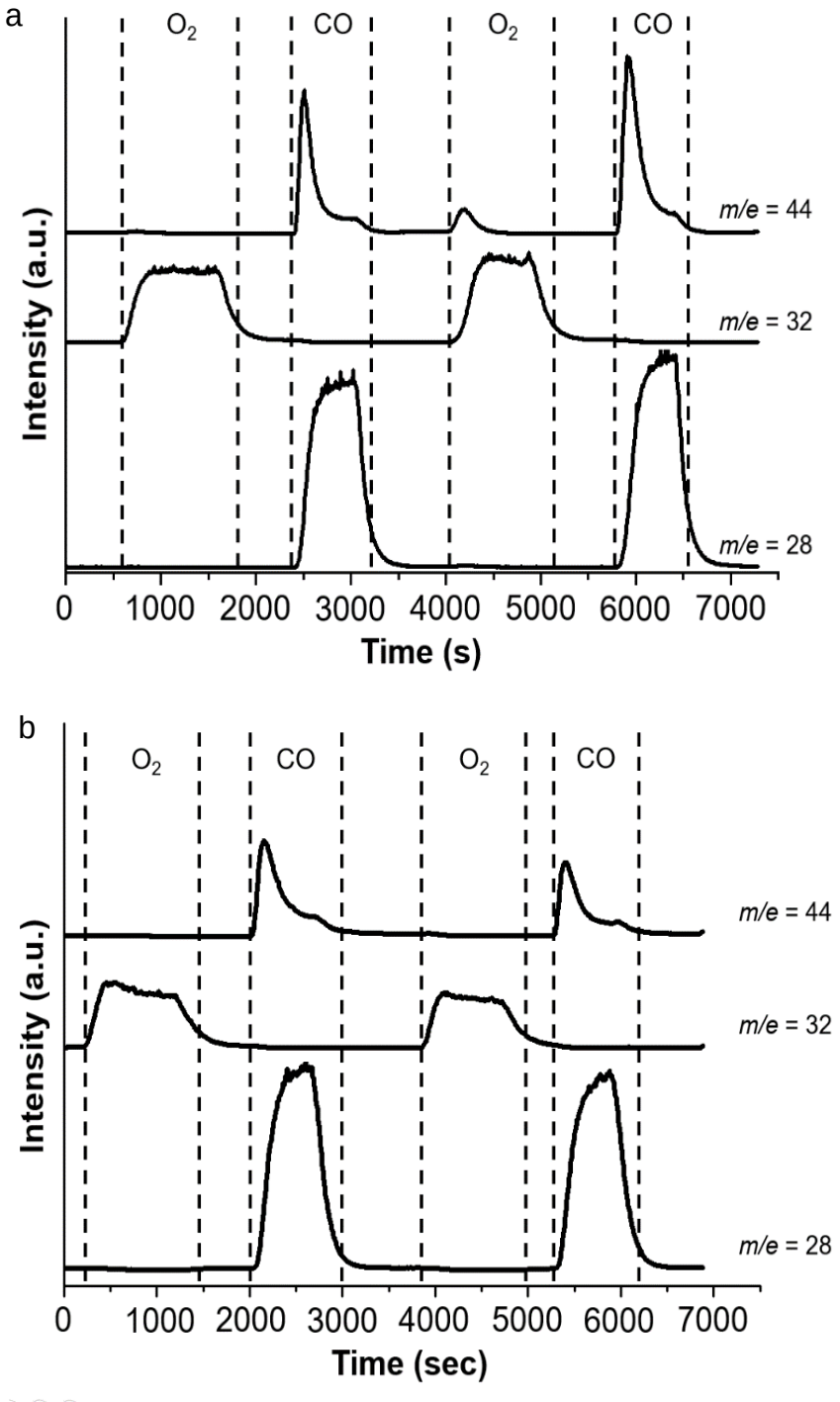

Figure A.12 Pulse measurements on a) Pd/20CeO_2-Al_2O_3, and b) Pd/Al_2O_3 catalysts at 673 K. The data are for two rounds of CO pulse (m/e = 28) and of O_2 pulse (m/e = 32). Formation of CO_2 (m/e = 44) is observed. (Data is from Applied Catalysis B: Environmental **2017**, 201, 430-437, taken by Tzia Ming Onn)

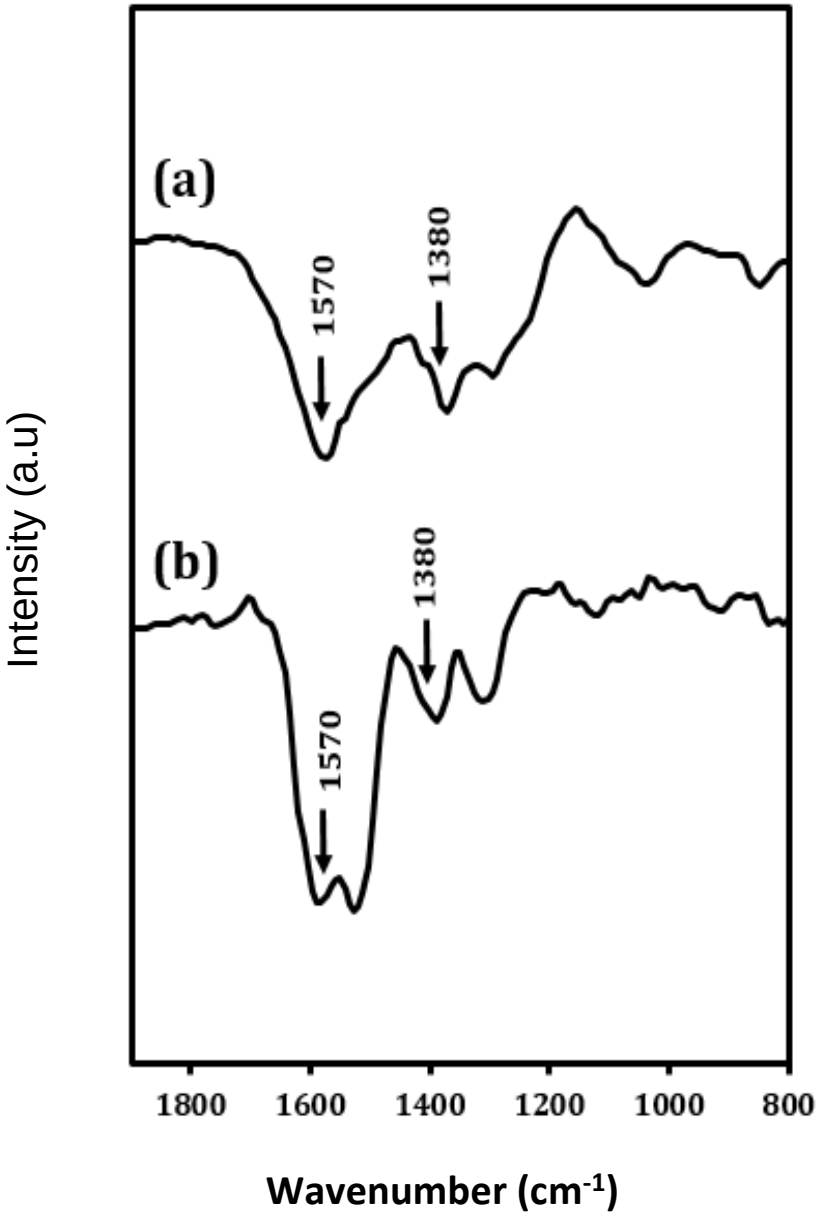

Figure A.13 DRIFTS spectra obtained for (a) Pd/CeO_2 and (b) $Pd/20CeO_2$-Al_2O_3, after exposure to 10% CO in flowing He at 573 K for 10 minutes. . (Data is from Applied Catalysis B: Environmental **2017**, 201, 430-437, taken by Tzia Ming Onn)

Appendix B Interesting Phenomena

Besides those finished work (published or manuscript finished) discussed in previous chapters, I also observed some interesting phenomena but couldn't gain a complete understanding based on current data. Since it might worth investigation of future students, I would like to document my observations here.

B.1 Triangle Pt Nanocluster Formation

Pt "mixed" sample (same sample used in Chapter IV) consisting 2nm and 4.5nm particles was heated under 150 Torr pure O_2 from 300 °C to 700°C, no obvious changes were found between 300-550°C and most of the particles exhibit in a spherical shape shown in Figure B.1a. But when temperature reached 600°C, faceting of the particles started to occur. For example, the particle pointed by the yellow arrow started to transform into triangle shape. With the passage of time, more and more particles changed to triangle shape as shown in Figure B.1 c-d. Some atomic resolution images taken at 650 °C are shown in Figure B.2, the lattice spacing is about 2.2 Å, consist with the lattice spacing of Pt (111) plane. These results would seem to be very relevant to the matter of transport of PtO2 via surface diffusion vs. the vapor phase.

Literature has reported that molecular oxygen can absorb onto Pt surface at temperature below 160K.[1] At higher temperature, α-PtO_2 oxide overlayer start to form and is most stable on Pt (111) surface.[2-5]. It is the stable bulk phase in oxygen at room temperature and atmospheric pressure,

and it consists of a layered structure similar to that of graphite, with sheets held together only by weak van der Waals forces. Ellinger et. al found that at an oxygen partial pressure of 500 mbar and at temperatures from 520 to 910 K, two atomic layers of α-PtO_2 form on Pt surfaces, oriented hexagon on hexagon with respect to the Pt(111) surface leading to a (8 × 8) superstructure surface unit cell.[6] Based on previous research and the data we have for now, the observed triangle shape Pt clusters might be Pt tetrahedron covered by α-PtO_2, and that the shape change of the Pt nano cluster from spherical to triangle is likely to accompanied with the formation of α-PtO_2 as a result of surface energy minimization. Assuming the surface α-PtO_2 layer formed on the bigger particle in the mixed sample originate from the dissociation of the smaller particles. These results would seem to be very relevant to the matter of transport of PtO_2 via surface diffusion vs. the vapor phase. If the diffusion happens in vapor phase, PtO_2 would have much higher chance to attach to the surface of the membrane rather than other Pt particles considering the low metal loading.

B.2 Stability of Pd Nanoparticles

7nm Pd particles (same sample a used in Chapter II for classical SMSI) were reduced under 5%H_2 /Ar from 300 ℃ to 500 ℃ followed by oxidation under 150Torr O_2 from 300 ℃ to 700 ℃. No obvious size change was observed when the sample was heated under forming gas but disappearance and shrinking of relatively smaller particles started to happen between 500 ℃-600 ℃ in 150 Torr O_2 as shown in Figure B. 3. When the temperature was raised to 650 ℃, most particles disappear and almost all of them were gone at 700 ℃.

A gradual size change of the two particles enclosed in the dashed rectangular in Figure B.3 is shown in Figure B.4. The average particle size in this sample is about 7nm. The upper one which

is originally 6.28nm started to shrink at 400 °C under 150 Torr O_2 accompanied by the growth of the lower one. Increasing temperature to 500 °C apparently accelerated this size transformation process as shown in Figure B.4 b-e. After 20mins at 500 °C, the upper one entirely disappeared and the lower one increased from 8.1nm to 9.36nm in diameter. A simple calculation of the size change shows that mass is conserved between the two particles. The dominant mechanism here is likely to be Ostwald Ripening. The two particles are still likely to be in metallic state.

Sequential images showing the gradual disappearance of another particle marked by the yellow arrow in Figure B.3 is shown in Figure B.5. Unlike the previous example, this particle doesn't have another particle in its close proximity. Obvious shrinking started at about 550 °C and accelerated at 650 °C as shown in Figure B.5 c-e. (No high magnification image was taken at 600 °C.) According to the fuzzy lattice fringes, the particle looks like oxidized. The instability of Pd NPs under oxidation condition has been reported by Kovarik et al. before.[7,8] The dominant mechanism of the disappearance of Pd NPs is not fully understood but is likely due to electron beam assisted PdO decomposition.[9,10] At relatively low temperature, ~500 °C, particles bigger than 8nm were stable and they acted as sink of the atoms from the smaller particles. But with increasing temperature, more and more bigger particles became unstable and started to dissociate. More studies and calculations are needed to further the understanding this phenomenon.

B.3 References

1. Steininger, H.; Lehwald, S.; Ibach, H. *Surf. Sci.* **1982,** 123, 1-17.

2. Seriani, N.; Pompe, W.; Ciacchi, L. C. *The Journal of Physical Chemistry B* **2006,** 110, 14860-14869.

3. Salmeron, M.; Brewer, L.; Somorjai, G. *Surf. Sci.* **1981,** 112, 207-228.

4. Li, W.; Hammer, B. *Chem. Phys. Lett.* **2005,** 409, 1-7.

5. Seriani, N.; Mittendorfer, F. *J. Phys.: Condens. Matter* **2008,** 20, 184023.

6. Ellinger, C.; Stierle, A.; Robinson, I.; Nefedov, A.; Dosch, H. *J. Phys.: Condens. Matter* **2008,** 20, 184013.

7. Kovarik, L.; Genc, A.; Karim, A.; Szanyi, J.; Kwak, J.; Peden, C. *Microsc. Microanal.* **2013,** 19, 1658-1659.

8. Kovarik, L.; Wei, Z.; Genc, A.; Arey, B.; Li, Y.; Wang, Y.; Szanyi, J.; Kwak, J.; Peden, C. *Microsc. Microanal.* **2014,** 20, 1574-1575.

9. McCarty, J. G. *Catal. Today* **1995,** 26, 283-293.

10. Zhang, H.; Gromek, J.; Fernando, G. W.; Marcus, H. L.; Boorse, S. *Journal of phase equilibria* **2002,** 23, 246-248.

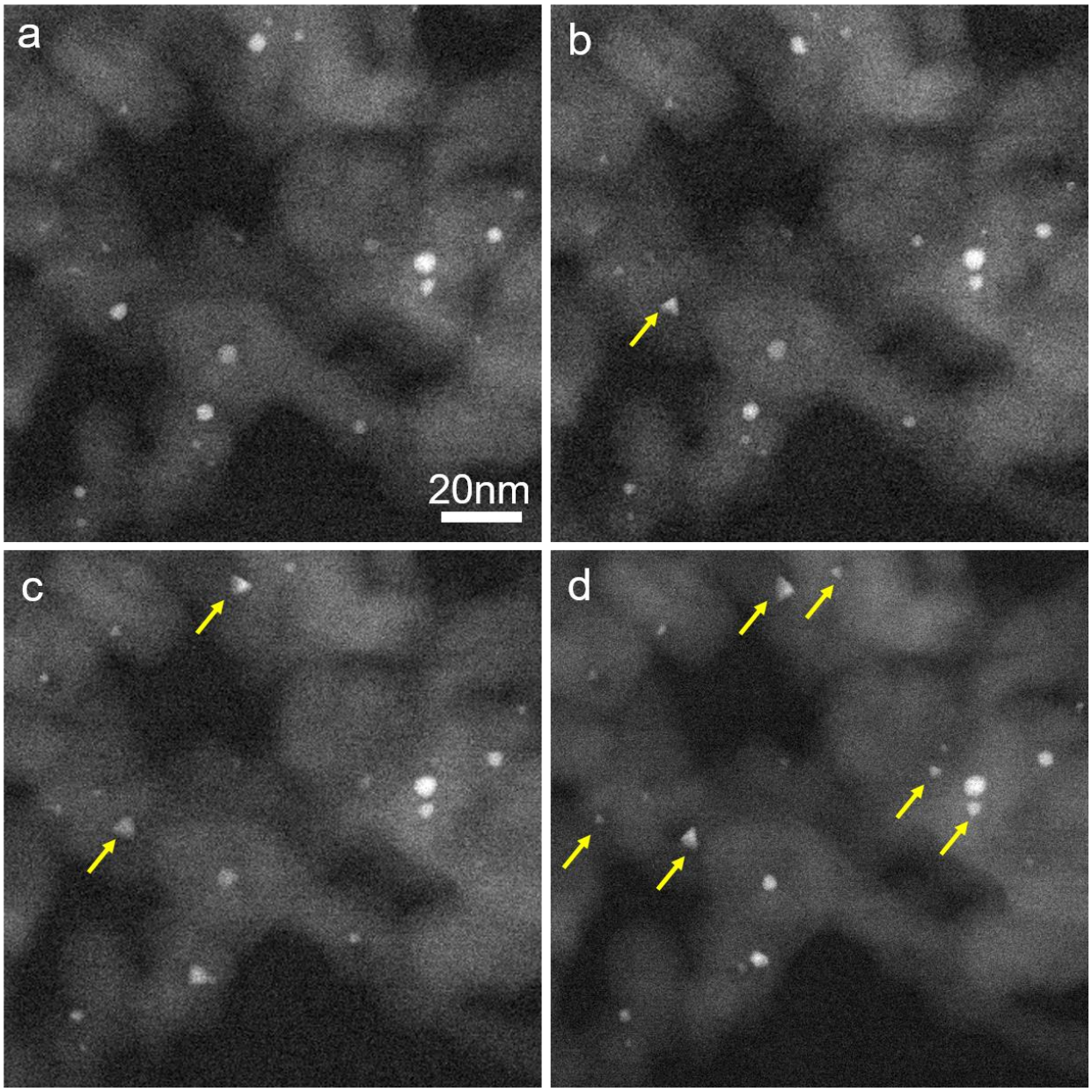

Figure B.1 Pt particles shape change under 150 Torr O2 at various temperature. (a) 550 °C 3min, (b) 600 °C 3min (c) 600 °C 15min (d) 600°C 25min

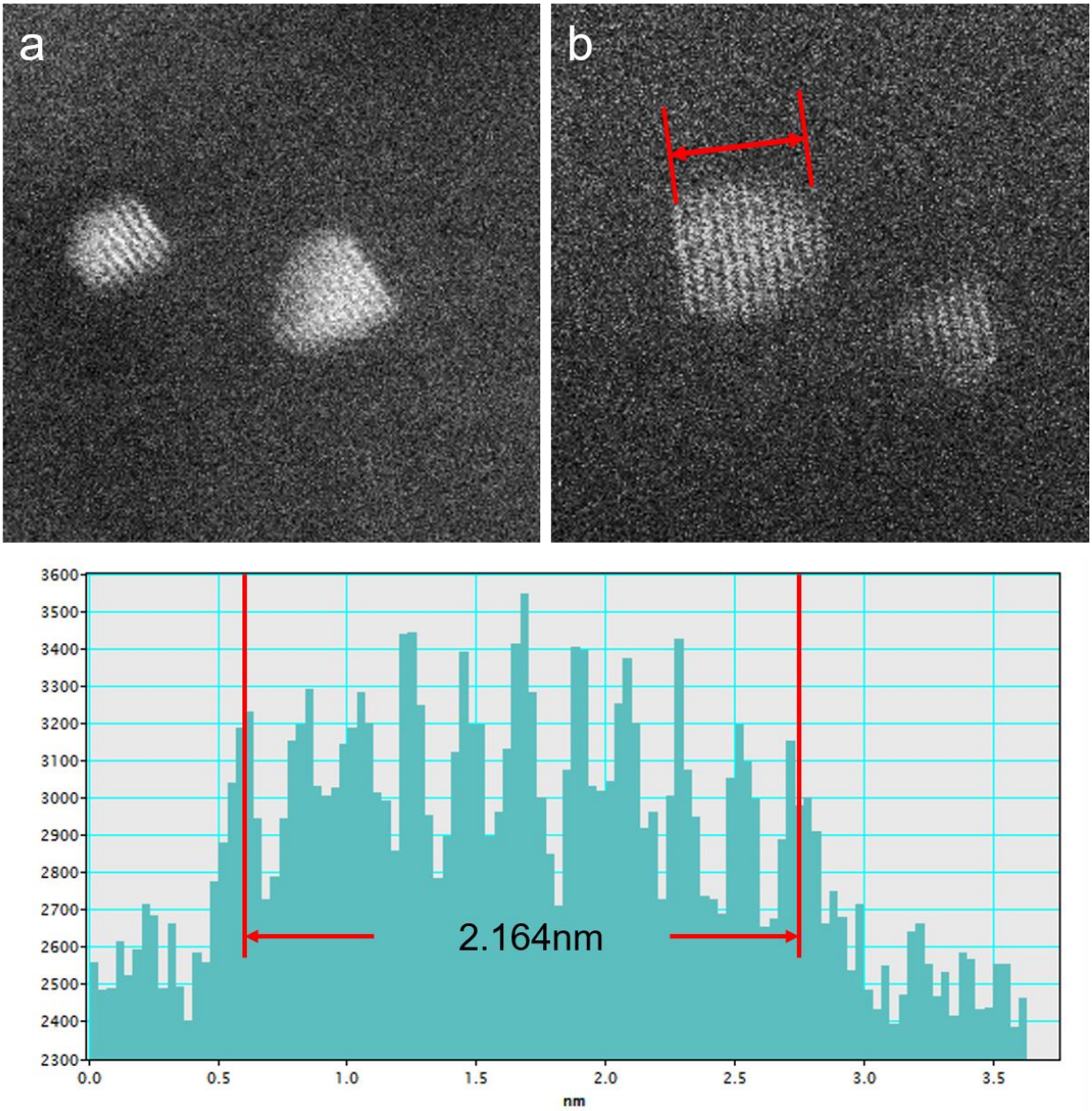

Figure B.2 HAADF image of Pt NPs taken under 150 Torr O_2 at 650 °C. The line profile corresponds to the particle shown in b.

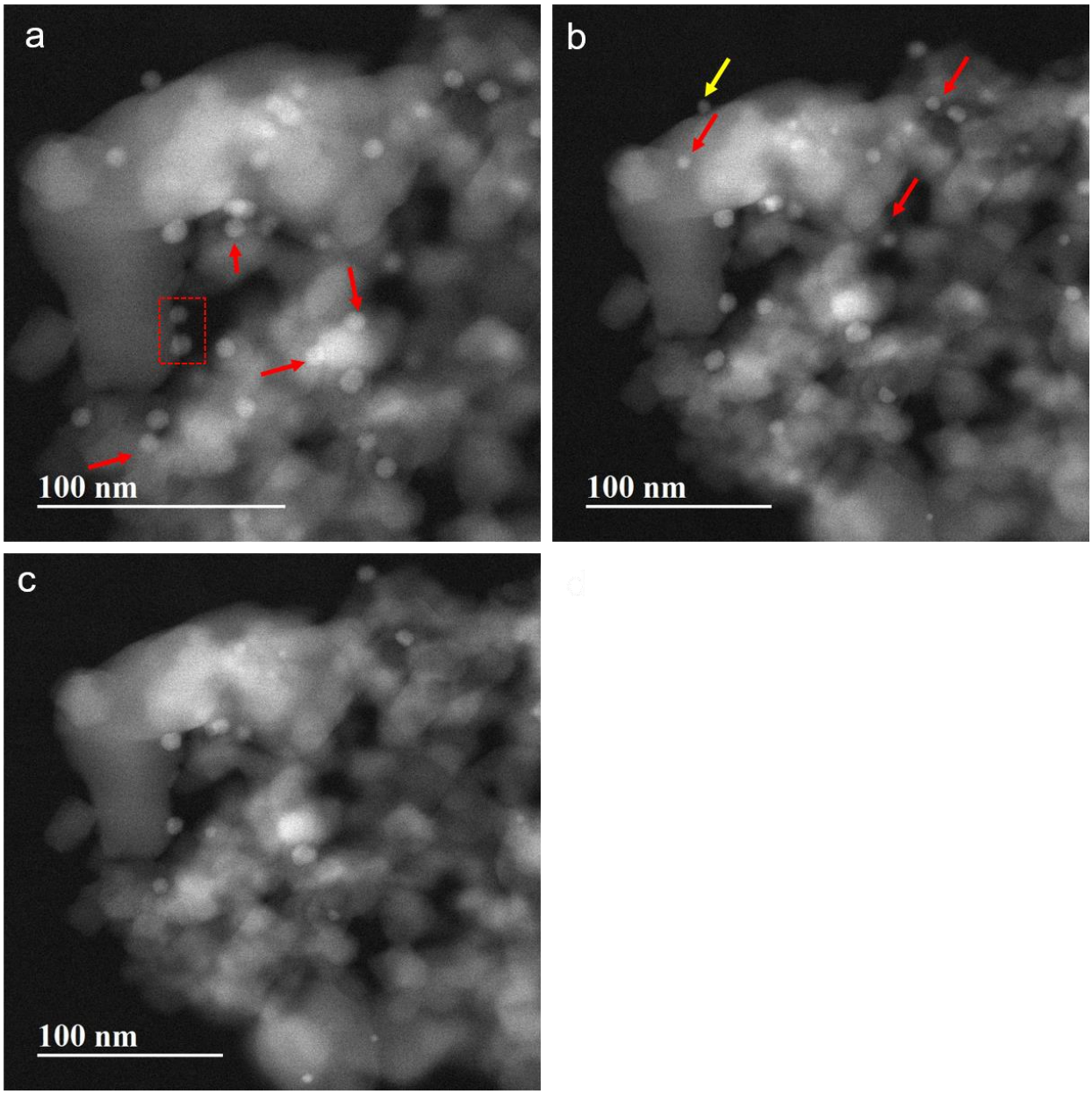

Figure B.3 HAADF images showing the disappearance of Pd NPs at elevated temperature. (a) was taken at 300 °C under 5%H_2/Ar , showing original particle distribution (b) 600 °C under 150 Torr O_2 (c) 650 °C 150 Torr O_2 (d) 700 °C 150 Torr O_2

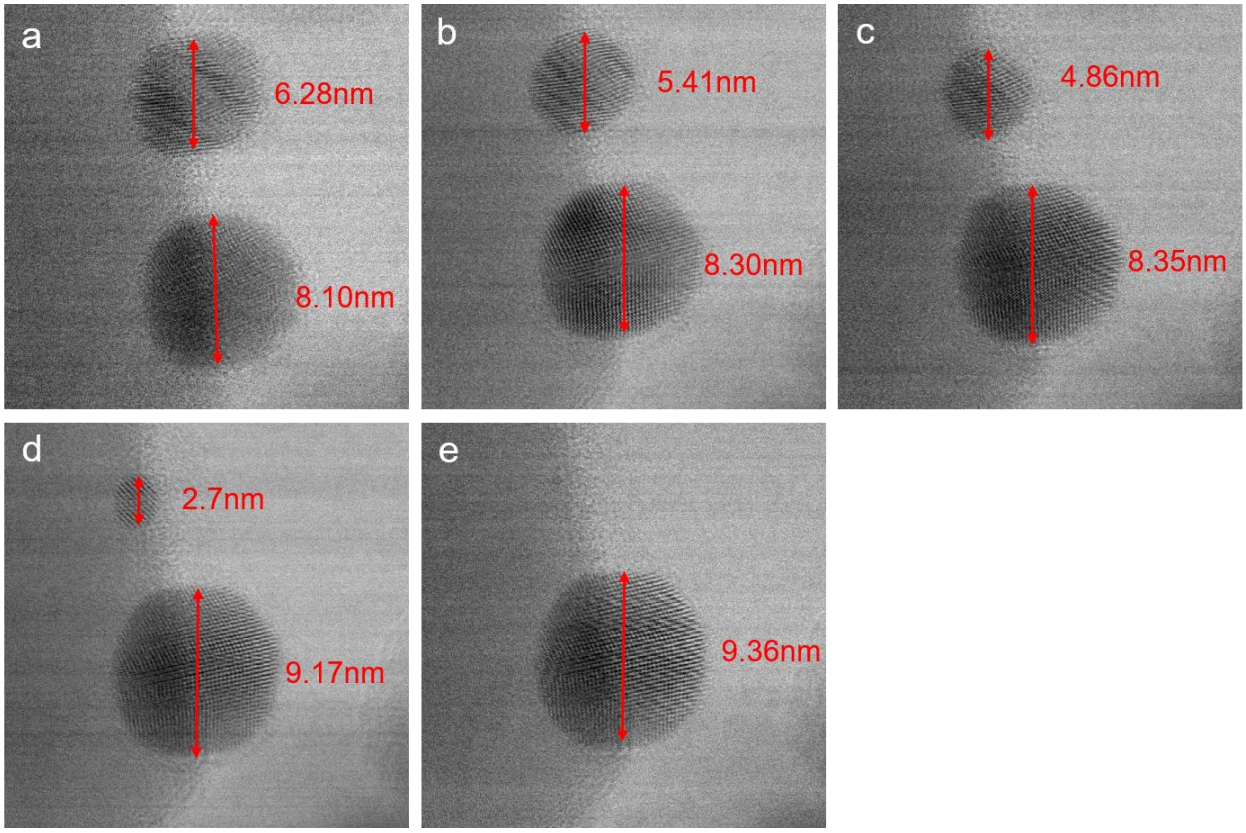

Figure B.4 Bright field images showing the size change of the two particles. (a) 500 °C, 5%H_2/ Ar (b) 400 °C O_2 (c) 500 °C 6min (d) 500 °C 18min (e) 500 ° C 20min

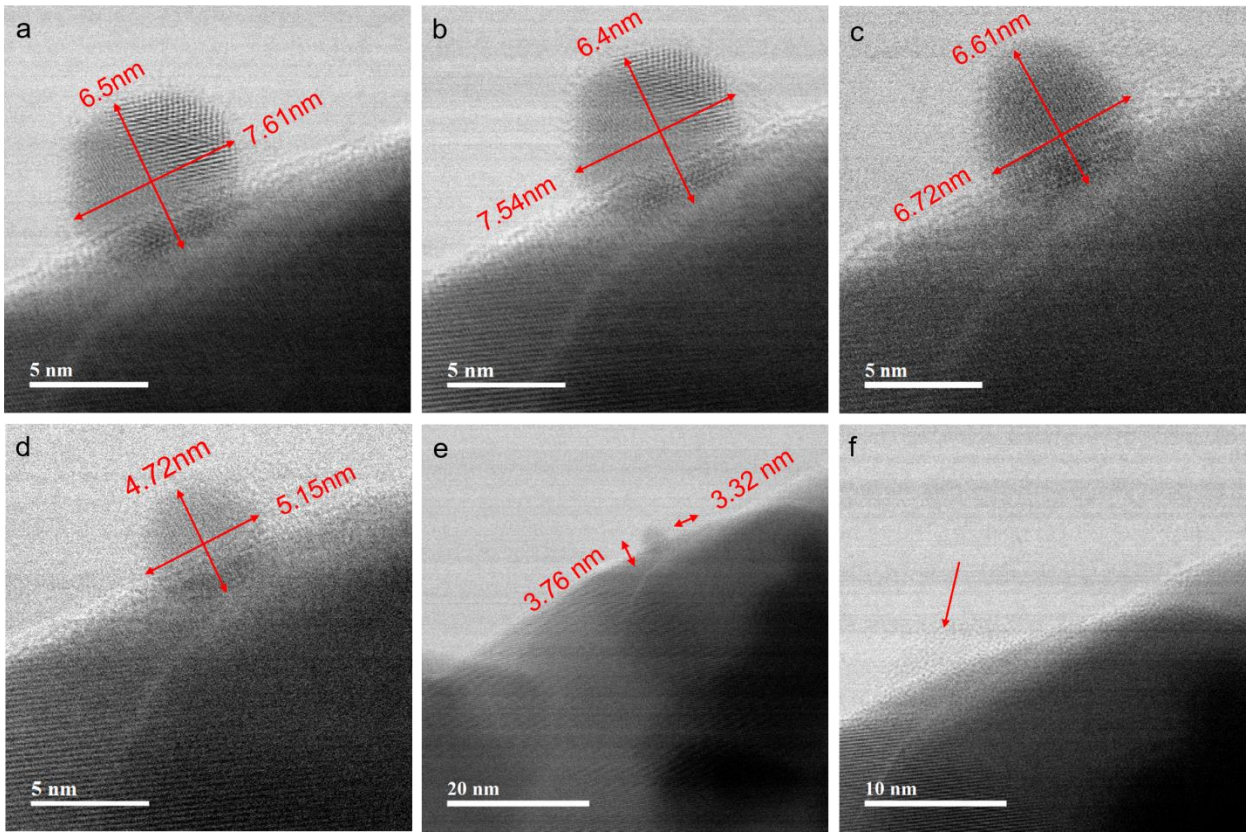

Figure B.5 Bright field images showing the gradual disappearance of Pd NP under 150 Torr O_2. (a) 500 °C (b) 550 °C (c) 650 °C 2min (d) 4min (e) 6min (f) 7min